U.S.NRC

United States Nuclear Regulatory Commission

Protecting People and the Environment

Crack Growth Rates and Fracture Toughness of Irradiated Austenitic Stainless Steels in BWR Environments

Office of Nuclear Regulatory Research

U.S.NRC

United States Nuclear Regulatory Commission

Protecting People and the Environment

Crack Growth Rates and Fracture Toughness of Irradiated Austenitic Stainless Steels in BWR Environments

Prepared by
O.K. Chopra and W.J. Shack

Argonne National Laboratory
Argonne, IL 60439

Office of Nuclear Regulatory Research

This page is intentionally left blank.

Abstract

In light water reactors, austenitic stainless steels (SSs) are used extensively as structural alloys in reactor core internal components because of their high strength, ductility, and fracture toughness. However, exposure to high levels of neutron irradiation for extended periods degrades the fracture properties of these steels by changing the material microstructure (e.g., radiation hardening) and microchemistry (e.g., radiation–induced segregation). Experimental data are presented on the fracture toughness and crack growth rates (CGRs) of wrought and cast austenitic SSs, including weld heat-affected-zone materials, that were irradiated to fluence levels as high as $\approx 2 \times 10^{21}$ n/cm^2 (E > 1 MeV) (≈ 3 dpa) in a boiling heavy water reactor at 288-300°C. The results are compared with the data available in the literature. The effects of material composition, irradiation dose, and water chemistry on CGRs under cyclic and stress corrosion cracking conditions were determined. A superposition model was used to represent the cyclic CGRs of austenitic SSs. The effects of neutron irradiation on the fracture toughness of these steels, as well as the effects of material and irradiation conditions and test temperature, have been evaluated. A fracture toughness trend curve that bounds the existing data has been defined. The synergistic effects of thermal and radiation embrittlement of cast austenitic SS internal components have also been evaluated.

Paperwork Reduction Act Statement

This NUREG does not contain information collection requirements and, therefore, is not subject to the requirements of the Paperwork Reduction Act of 1995 (44 U.S.C. 3501 et seq.).

Public Protection Notification

The NRC may not conduct or sponsor, and a person is not required to respond to, a request for information or an information collection requirement unless the requesting document displays a current valid OMB control number.

This page is intentionally left blank.

Foreword

This report presents the results of a study of simulated light-water reactor coolants, material chemistry, and irradiation damage and their effects on the susceptibility to stress-corrosion cracking of various commercially available and laboratory-melted stainless steels. This report is one of a series dating back about 8 years, describing such results, which are required to support analysis of the structural integrity of reactor internal components, many of which are subject to irradiation-assisted stress-corrosion cracking (IASCC).

The earlier reports detailed crack growth rates in heat-affected zones adjacent to stainless steel weldments, and they comprised the final publications based on specimens irradiated in Phase I (of two) in the Halden test reactor. Phase I irradiations principally involved stainless steels of wide-ranging chemistry (including commercial steels of typical chemistry) and conventional heat treatment and product form processing. By contrast, this report is the first to present data from specimens irradiated in Phase II, which featured a variety of innovatively fabricated and engineered alloys designed to be (possibly) more resistant to IASCC.

Irradiation levels in both Phase I and Phase II ranged up to about 3 displacements per atom (dpa), and the high-temperature water environment used in these tests contained dissolved oxygen concentrations ranging from 200 parts per billion (ppb) to 8 parts per million (ppm). The materials tested included several commonly used stainless steels, such as Types 304 and 316 (and their low-carbon counterparts), as well as CF-8M cast stainless steel. Taken together, these test conditions and materials make the study results most applicable to boiling-water reactor (BWR) internals.

This report presents additional crack growth rate data, which reinforce the earlier observation that when typical stainless steels are irradiated from >0.75 to 4.0 dpa, the growth rates of stress-corrosion cracks are elevated (by a factor of 2 to 7) above the reference line established in Revision 2 of NUREG-0313, "Technical Report on Material Selection and Processing Guidelines for BWR Coolant Pressure Boundary Piping: Final Report," dated January 1988. By contrast, for stainless steels irradiated to 0.45 dpa, or not irradiated at all, the growth rates of stress-corrosion cracks are comparable to, or slightly lower than, the NUREG-0313 reference line. Therefore, accumulated irradiation doses above 0.75 dpa can elevate crack growth rates in stainless steels. All tests conducted in simulated hydrogen water chemistry had substantially lower crack growth rates than the NUREG-0313 reference line. This result illustrates the beneficial effect of a low dissolved oxygen environment.

In addition, this report describes initial results of fracture toughness testing of sensitized and irradiated Type 304 stainless steel, heat-affected zone material, and CF-8M. The tests were conducted in simulated BWR environments by applying slowly-rising loads to specimens with stress-corrosion precracks (as opposed to air environment fatigue precracks). This approach is inherently more representative of the presumed failure mode of reactor internal components. However, these initial results exhibited little toughness degradation compared to comparable materials in high-temperature air environments. This finding suggests that the BWR environment may not substantially degrade the fracture toughness of irradiated stainless steels.

In part, the results of this NUREG/CR form the technical basis for Title 10 of the Code of Federal Regulations Part 50.55a (10 CFR 50.55a). In addition, the results of this research, including crack growth rates, may be reviewed, and if applicable, used as a basis for making a decision to approve or deny requests for relief or requests for reductions of inspection requirements of 10 CFR 50.55a.

This page is intentionally left blank.

Contents

Figures

xiii

Tables

Executive Summary

Background

In light water reactors (LWRs), austenitic stainless steels (SSs) are used extensively as structural alloys in the internal components of reactor pressure vessels because of their relatively high strength, ductility, and fracture toughness. However, exposure to neutron irradiation for extended periods changes the microstructure and degrades the fracture properties of these steels. Irradiation leads to a significant increase in yield strength and reduction in ductility and fracture resistance of austenitic SSs. Although radiation embrittlement was not considered in the design of LWR core internal components constructed of austenitic SSs, it has become an important consideration in addressing nuclear plant aging and license renewal issues. Also, irradiation exacerbates the corrosion fatigue and stress corrosion cracking (SCC) behavior of SSs by affecting the material microchemistry (e.g., radiation-induced segregation); material microstructure (e.g., radiation hardening); and water chemistry (e.g., radiolysis).

The factors that influence SCC susceptibility of materials include neutron fluence, cold work, corrosion potential, water purity, temperature, and loading. Although a threshold fluence level of 5×10^{20} n/cm^2 (E >1 MeV) (≈0.75 dpa) is often assumed for austenitic SSs in the boiling water reactor (BWR) environment, experimental data show that increases in susceptibility to intergranular cracking can occur at fluences greater than ≈2 $\times 10^{20}$ n/cm^2 (E >1 MeV) (≈0.3 dpa). At low enough fluences, reducing the corrosion potential of the environment has proved beneficial. However, low corrosion potential does not always provide immunity to irradiation-assisted stress corrosion cracking (IASCC). For example, intergranular SCC has occurred in cold-worked, irradiated SS baffle bolts in pressurized water reactors (PWRs) where the corrosion potential is very low.

Test Program

A program is being conducted at Argonne National Laboratory (ANL) on irradiated SSs to better understand the cracking of BWR core internal components. The susceptibility of austenitic SSs to IASCC and the resulting crack growth rates (CGRs) are being evaluated as a function of the fluence level, material composition, and water chemistry. The effect of neutron irradiation on the fracture toughness of wrought and cast austenitic SSs is also being evaluated.

Crack growth and fracture toughness tests have been completed on irradiated wrought and cast austenitic SSs, including weld heat-affected-zone (HAZ) materials, in BWR environments at 289°C. The present report presents experimental data on Type 316 SS irradiated to 0.3, 0.9, and 2.0 $\times 10^{21}$ n/cm^2 (0.45, 1.35, and 3.0 dpa); sensitized Type 304 SS and SS weld HAZ materials irradiated to 1.44 $\times 10^{21}$ n/cm^2 (2.16 dpa); and thermally aged CF-8M cast SS irradiated to 1.63 $\times 10^{21}$ n/cm^2 (2.46 dpa). The CGR tests on materials irradiated to 2.16 or 2.46 dpa were followed by a fracture toughness J-R curve test in the BWR environment. Tests have also been conducted in air at 289°C to obtain baseline data. Also compiled in this report are crack growth and fracture toughness data from earlier ANL studies on Types 304L and 316L SS irradiated up to 3.0 dpa and SS weld HAZ materials irradiated to 0.75 dpa in BWR environments, as well as fracture toughness data on Types 304 and 316L SS irradiated up to 3.0 dpa in air at 289°C. The results from the ANL studies are compared with the data available in the literature.

Crack Growth Rate Tests

The test results indicate that in normal water chemistry (NWC) BWR environment, the SCC CGRs of nonirradiated SSs or materials irradiated to $\approx$3 x 10^{20} n/cm^2 ($\approx$0.45 dpa) are either comparable to or slightly lower than the disposition curve in NUREG-0313 for sensitized SSs in water with 8 ppm dissolved oxygen (DO). Neutron irradiation to higher dpa increases the growth rates significantly. The SCC CGRs of SSs irradiated to 5 x 10^{20}-2.67 x 10^{21} n/cm^2 (0.75-4.0 dpa) are a factor of 2-7 higher than the NUREG-0313 disposition curve. For the same irradiation level, the CGRs for weld HAZ materials were higher than those for solution-annealed SSs. Results in the literature suggest that the CGRs of SSs irradiated to higher fluence levels (e.g., 8.67 x 10^{21} n/cm^2 or 13 dpa) strongly depend on the stress intensity factor (K) and can be up to a factor of 30 higher than the NUREG-0313 disposition curve.

The results for nonirradiated SSs and steels irradiated up to 2.67 x 10^{21} n/cm^2 (4.0 dpa) indicate a benefit from a low-DO environment. The SCC CGRs were decreased more than an order of magnitude when the environment was changed from a NWC BWR environment to hydrogen water chemistry (HWC) environment. It is known that at very high fluence levels, the beneficial effect of HWC is lost. The question of the maximum fluence level at which HWC is effective is of obvious importance. In our tests, a few specimens with less than 4.0 dpa did not show the benefit of the low-DO environment at higher values of K (greater than 20 MPa m$^{1/2}$). Because the loading conditions exceeded the proposed "effective yield stress" K/size criterion for irradiated SSs, it is not clear whether the specimen constraint had been lost for these tests. However, the adequacy of the current proposed K/size criterion is not well established, and the possible effects of a loss of specimen constraint on fracture morphology and crack growth behavior are discussed.

Although the data are limited, tests on SS weld HAZ materials indicate that neutron irradiation to $\approx$2.2 dpa has little or no effect on cyclic CGRs in air. The experimental CGRs are, in fact, slightly lower than those predicted by the previously published correlations for solution-annealed SSs.

In an NWC BWR environment, the cyclic CGRs of wrought SSs irradiated to $\approx$3 x 10^{20} n/cm^2 ($\approx$0.45 dpa) are the same as those for nonirradiated materials, whereas the cyclic CGRs of SSs irradiated to 5 x 10^{20}-2.67 x 10^{21} n/cm^2 (0.75-4.0 dpa) are higher. Limited data suggest that the growth rates of irradiated CF-8M cast SS are lower than those of solution-annealed materials irradiated to the same fluence level. At low frequencies, cyclic CGRs are decreased by more than an order of magnitude when the DO level is decreased by changing from NWC to HWC. A superposition model was used to represent the cyclic CGRs of austenitic SSs. The CGR in the BWR environments can be expressed as the superposition of the rate in air (mechanical fatigue) and the rates due to corrosion fatigue and SCC.

Fracture Toughness Tests

Neutron irradiation also decreases the fracture toughness of wrought and cast austenitic SSs and SS weld HAZ materials. For the same irradiation conditions, the fracture toughness of thermally aged cast SS is lower than that of HAZ material, which, in turn, is lower than that of solution-annealed materials. Limited data on irradiated SS weld HAZ materials indicate that an NWC BWR environment has little or no effect on the fracture toughness J-R curves of these materials (i.e., the fracture toughness J-R curves in air and NWC BWR environments are comparable). However, additional tests are needed to investigate the possible effects of LWR coolant environments on fracture toughness, e.g., the effect of the corrosion/ oxidation reaction during crack extension or using specimens with an intergranular crack rather than the transgranular fatigue crack generally used in nearly all fracture toughness tests.

The available fracture toughness data in the open literature on wrought and cast austenitic SSs and their welds have been reviewed. The data were analyzed to determine the effect of neutron irradiation on the fracture toughness of these steels, as well as the effect of material and irradiation conditions and test temperature. Most of the experimental data on neutron embrittlement of austenitic SSs are from materials irradiated in high flux fast reactors. Test results under irradiation conditions that are characteristic of LWRs, beyond those discussed in this report, are very limited. However, although the irradiation conditions differ, in general, the data trends to first order appear to be similar for the fast reactor and LWR irradiations.

The fracture toughness data on austenitic SSs indicate little or no change in toughness below 0.5 dpa, then a rapid decrease in toughness between 1 and 5 dpa to reach a saturation toughness value, and no further change beyond 10 dpa. There appear to be no significant differences in the fracture toughness data trends for the various grades of wrought austenitic SSs. For nonirradiated materials, it is well-established that the fracture toughness of weld metals and thermally aged cast SSs is lower than that of wrought materials. The fracture toughness of these materials also decreases more rapidly with irradiation than does that of wrought steels.

The data have been evaluated to define (a) a threshold neutron exposure for radiation embrittlement of austenitic SSs and a minimum fracture toughness of austenitic SSs irradiated to less than the threshold value, (b) a saturation irradiation level and saturation fracture toughness, and (c) a bounding curve for the changes in fracture toughness between the threshold and saturation irradiation levels. The results indicate that the fracture toughness properties exhibit (a) a threshold irradiation level of ≈ 0.3 dpa below which irradiation has little or no effect on fracture toughness and (b) a saturation irradiation level of ≈ 5 dpa. Conservatively, no ductile crack extension is assumed to occur at or above the saturation irradiation level. The available data indicate a J value for the onset of crack extension (J_{Ic}) of 15 kJ/m^2 (86 in.-lb/in.^{2}) for austenitic SSs irradiated to 5 dpa. A fracture toughness trend curve that bounds the existing data has been derived in terms of J_{Ic} vs. neutron dose as well as the coefficient C of the power-law J-R curve vs. dose.

The synergistic effects of thermal and radiation embrittlement of cast austenitic SS internal components have also been evaluated. Cast austenitic SSs have a duplex structure consisting of both ferrite and austenite phases and are susceptible to thermal embrittlement even in the absence of irradiation. Thermal aging affects primarily the ferrite phase and has little or no effect on the austenite phase. Below 2×10^{20} n/cm^2 (0.3 dpa), the minimum fracture toughness can be estimated from the correlations available for thermal embrittlement of cast SS. For fluences $>2 \times 10^{20}$ n/cm^2 (>0.3 dpa), the minimum fracture toughness of cast SSs can be assumed to be given by the lesser of the minimum predicted toughness for thermal aging or the lower bound curves for the fracture toughness of irradiated stainless steels.

This page is intentionally left blank.

Acknowledgments

This page is intentionally left blank.

Acronyms and Abbreviations

ANL	Argonne National Laboratory
ASTM	American Society for Testing and Materials
BWR	Boiling Water Reactor
CGR	Crack Growth Rate
CT	Compact Tension
CW	Cold Worked
DC	Direct Current
DO	Dissolved Oxygen
dpa	Displacements per atom
ECP	Electrochemical Potential
EPFM	Elastic-Plastic Fracture Mechanics
EPRI	Electric Power Research Institute
GG	Grand Gulf
GTA	Gas Tungsten Arc
HAZ	Heat-Affected Zone
HWC	Hydrogen Water Chemistry
IASCC	Irradiation-Assisted Stress Corrosion Cracking
IG	Intergranular
J-R	J Integral Resistance
LEFM	Linear-Elastic Fracture Mechanics
LWR	Light Water Reactor
MA	Mill Annealed
NDT	Nil-Ductility Transition
NRC	Nuclear Regulatory Commission
NWC	Normal Water Chemistry
PWR	Pressurized Water Reactor
RIS	Radiation-Induced Segregation
SA	Submerged Arc
SCC	Stress Corrosion Cracking
SHE	Standard Hydrogen Electrode
SMA	Shielded Metal Arc
SS	Stainless Steel
TG	Transgranular

This page is intentionally left blank.

Symbols

a	Crack length
a_i	Current value of crack length
$\dot{a}_{air}$	Crack growth rate in air
$\dot{a}_{env}$	Crack growth rate in the environment
$\dot{a}_{scc}$	Stress corrosion crack growth rate
A_{pl}	Plastic area under the load versus load-line displacement curve
b	Remaining ligament (distance from the physical crack front to the back edge of the specimen)
B	Specimen thickness
B_N	Net specimen thickness
da	Increment in crack length
dJ	Increment in J integral
E	Elastic modulus
J	J integral, a mathematical expression used to characterize the local stress-strain field at the crack tip region (parameter J represents the driving force for crack propagation)
J_{el}	Elastic component of J
J_{pl}	Plastic component of J
J_{Ic}	Value of J near the onset of crack extension
K	Stress intensity factor
K_{max}	Maximum stress intensity factor
K_{min}	Minimum stress intensity factor
P	Applied load
P_{max}	Maximum applied load
P_{min}	Minimum applied load
R	load ratio
T	Tearing modulus
t_r	Rise time
U	Current value of DC potential
U_0	Initial value of DC potential
V	Total load-line displacement
V_{pl}	Plastic component of loadline displacement
W	Specimen width
σ_f	Flow stress, defined as the average of yield and ultimate stress
σ_u	Ultimate stress
σ_y	Yield stress
υ	Poisson ratio

This page is intentionally left blank.

1   Introduction

In light water reactors (LWRs), austenitic stainless steels (SSs) are used extensively as structural alloys in the internal components of reactor pressure vessels because of their high strength, ductility, and fracture toughness. Fracture of these steels occurs by stable tearing at stresses well above the yield stress, and tearing instabilities require extensive plastic deformation. However, exposure to neutron irradiation for extended periods changes the microstructure and degrades the fracture properties of these steels.[1-4] Radiation embrittlement was not considered in the design of LWR core internal components constructed of austenitic SSs, but it is considered in addressing nuclear plant aging and license renewal issues. In addition to irradiation embrittlement, irradiation-assisted stress corrosion cracking (IASCC) is another degradation process that affects LWR internal components exposed to fast neutron radiation,[1,5,6] and needs to be considered in addressing nuclear plant aging and license renewal issues.

Neutron irradiation of austenitic SSs can produce damage by displacing atoms from their lattice position. This displacement creates point defects such as vacancies and interstitials. These point defects are unstable, and most of them are annihilated by recombination. The surviving defects rearrange into more stable configurations such as dislocation loops, network dislocations, precipitates, and cavities (or voids). Changes in the microstructure of austenitic SSs due to neutron irradiation vary with the irradiation temperature, neutron fluence, flux, and energy spectrum.

At temperatures below 300°C (572°F), neutron irradiation leads to the formation of a substructure with very fine defects that consist primarily of small (<5 nm) vacancy and interstitial loops ("black spots") and larger (>5 nm) faulted interstitial loops.[7-9] At irradiation temperatures above 300°C (572°F), the microstructure consists of larger faulted loops, network dislocations, and cavities that are three-dimensional clusters (voids) of vacancies and/or gas bubbles. The microchemistry of the material is also changed due to radiation-induced segregation (RIS). Regions that act as sinks for the point defects that are created by neutron irradiation are enriched with Ni, Si, and P, and depleted in Cr and Mo. Such changes in microchemistry can result in the formation of various precipitates. Cavities are often associated with these precipitates, as well as dislocations and grain boundaries.

The point defect clusters and precipitates act, to varying extent, as obstacles to a dislocation motion that leads to matrix strengthening, resulting in an increase in tensile strength and a reduction in ductility and fracture toughness of the material. In general, cavities (or voids) are strong barriers, large faulted Frank loops are intermediate barriers, and small loops and bubbles are weak barriers to dislocation motion.[1] For austenitic SSs, the greatest increase in yield strength for a given irradiation level occurs at irradiation temperatures near 300°C (572°F), which is in the temperature range of LWR operation. In boiling water reactors (BWRs), the temperature of core internal components is nearly constant at ≈ 288°C (550°F). Most pressurized water reactor (PWR) core internals operate nominally at ≈ 300°C (572°F), the temperature where the rate of increase in yield strength with irradiation is the greatest.

As the yield strength approaches the ultimate strength of the material, deformation by a planar slip mechanism is promoted.[10] This process is also termed "dislocation channeling," whereby dislocation motion along a narrow band of slip planes clears the irradiation-induced defect structure, creating a defect-free channel that offers less resistance to subsequent dislocation motion or deformation. The enhanced planar slip leads to a pronounced degradation in the fracture toughness of austenitic SSs.[3] Such effects of irradiation on the fracture toughness of austenitic SSs appear to be strongly influenced by minor differences in the chemical composition of the steels;[1] the chemical composition can influence the

1

stacking fault energy and/or irradiation-induced microstructure. In general, a higher stacking-fault energy enhances, and cold work inhibits, dislocation channeling.[1]

As discussed above, neutron irradiation can decrease the fracture toughness of austenitic SSs significantly, and failure may occur without general yielding. In such instances, a fracture mechanics methodology such as elastic-plastic fracture mechanics (EPFM) or linear-elastic fracture mechanics (LEFM) is needed for analysis of structural integrity and development of inspection guidelines. The former involves the J integral-resistance (J-R) curve approach and is used where failure involves plastic deformation. The J integral is a mathematical expression used to characterize the local stress-strain field at the crack tip region (parameter J represents the driving force for crack propagation), and the J-R curve characterizes the resistance of the material to stable crack extension. The fracture toughness of such materials is represented by fracture mechanics parameters such as J_{Ic}, the value of J near the onset of crack extension, and the tearing modulus, T, which characterizes the slope of the J-R curve:

$$T = \frac{dJ}{da} \frac{E}{\sigma_f^2} ,$$ (1)

where E is the elastic modulus, a is the crack length, and σ_f is the flow stress defined as the average of the yield stress (σ_y) and ultimate stress (σ_u). The LEFM methodology is used where failure involves negligible plastic deformation. The fracture toughness of such materials is represented by the parameter K_{Ic} (i.e., plane strain fracture toughness), which characterizes the resistance of the material to unstable crack extension. Under EPFM conditions, an equivalent K can be determined from the relationship

$$K_{Jc} = \left(E' J_{Ic} \right)^{1/2} ,$$ (2)

where $E' = E / \left(1 - \upsilon^2 \right)$, E is the elastic modulus, and υ is the Poisson ratio.

Most published experimental data on neutron embrittlement of austenitic SSs have been obtained on materials irradiated in high-flux fast reactors.[11-26] In these studies, the embrittlement of the materials has been characterized in terms of tensile properties, Charpy-impact properties, and fracture toughness. Irradiation damage is characterized by either the neutron fluence in neutrons per square centimeter (n/cm^2) or the average number of displacements experienced by each atom, i.e., displacements per atom (dpa).[*] Similar test results under LWR conditions are limited.[2,27]

The effect of neutron exposure (in dpa) on the fracture toughness J_{Ic} of austenitic SSs irradiated at 350-450°C (662-842°F) up to ≈ 25 dpa in fast reactors and BWRs is shown in Figs. 1a and b, respectively.[2,3,11-27] The fast reactor data show a rapid decrease in fracture toughness at a neutron dose of 1-2 dpa (Fig. 1a); the neutron dose at the onset of the rapid decrease varies with the chemical composition and heat treatment of the steel. The effects of irradiation may be divided into three regimes: little or no loss of toughness below an exposure of ≈ 1 dpa, substantial decrease in toughness at exposures of 1-10 dpa, and no further reduction in toughness above a saturation exposure of 10 dpa. The degradation in fracture properties saturates at a J_{Ic} value of ≈ 30 kJ/m^{2} (171 in.-lb/in.[2]) [or equivalent

---

[*]In this study, unless otherwise noted, when neutron dose in dpa was not available, the values of neutron fluence (n/cm^2) were converted to dpa as follows: for LWRs, E>1 MeV and 10^{22} n/cm^2 ≈15 dpa; and for fast reactors, E>0.1 MeV and 10^{22} n/cm^2 ≈5 dpa.

critical stress intensity factor K_{Jc} of 75 MPa m$^{1/2}$ (68.2 ksi in.$^{1/2}$)]. Also, the failure mode changes from dimple fracture to channel fracture.

The limited data from BWR irradiations (Fig. 1b) show fracture toughness trends similar to those observed for fast reactor irradiations. Most of the fracture toughness J_{Ic} values for austenitic SSs irradiated in BWRs fall within the scatter band of the data obtained on materials irradiated in fast reactors at temperatures higher than 288°C (550°F).[27] However, some tests on BWR irradiated materials report K_{Ic} values of 45-60 MPa m$^{1/2}$ (41-55 ksi in.$^{1/2}$), corresponding to J_{Ic} of 11-20 kJ m^2.
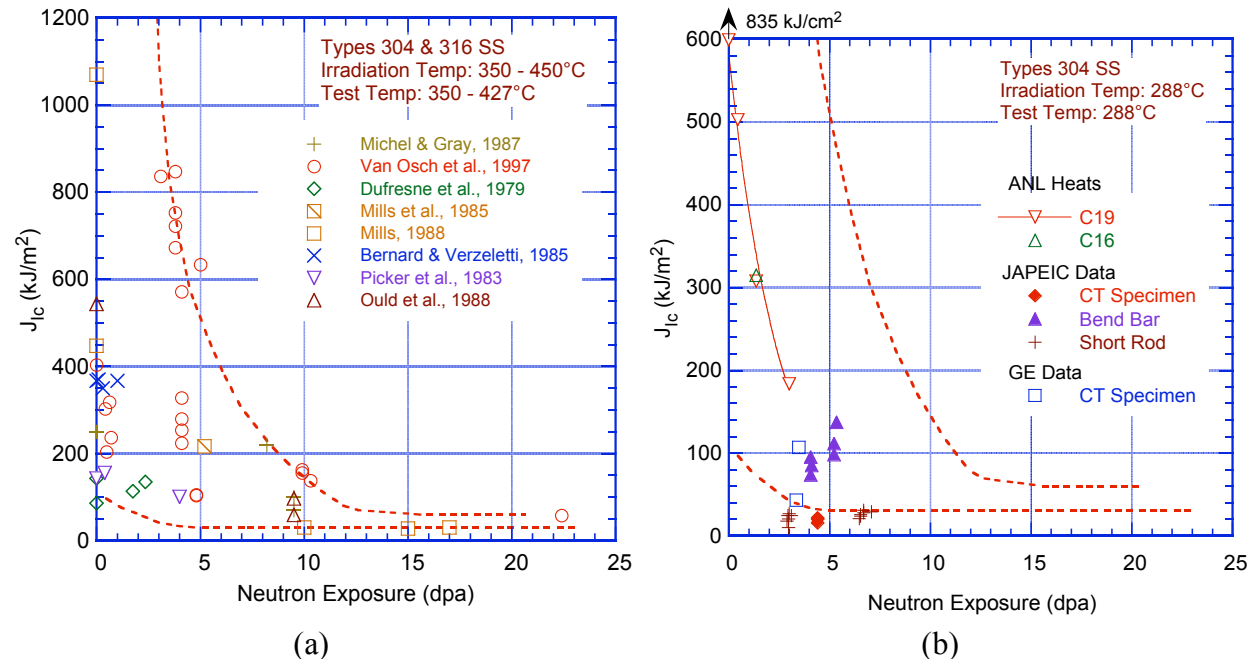
Figure 1. Fracture toughness J_{Ic} as a function of neutron exposure for austenitic Types 304 and 316 stainless steels irradiated in (a) fast reactors and (b) BWRs. Dashed lines represent upper and lower bounds for change in J_{Ic} for austenitic SSs irradiated at 350–450°C in fast reactors.

Another issue that has been a concern for reactor core internal components is the possibility of a synergistic interaction between irradiation and thermal embrittlement of cast austenitic SSs and SS weld metals.[28-32] Although wrought SSs are typically completely austenitic, welded and cast SSs have a duplex microstructure consisting of austenite and ferrite phases. The ferrite phase increases the tensile strength and improves resistance to SCC, but it is susceptible to thermal embrittlement after extended service at reactor operating temperatures. Thermal aging of cast SSs at 250-400°C (482-752°F) leads to precipitation of additional phases in the ferrite (e.g., formation of Cr-rich α' phase by spinodal decomposition; nucleation and growth of α'; precipitation of a Ni- and Si-rich G phase, $M_{23}C_6$ carbide, and γ_2 austenite; and additional precipitation and/or growth of existing carbides at the ferrite/austenite phase boundaries).[33-36] The formation of the Cr-rich α' phase by spinodal decomposition of ferrite is the primary mechanism for thermal embrittlement; it strengthens the ferrite phase by increasing strain hardening and the local tensile stress. Thermal aging has little or no effect on the austenite phase. Thus, thermal aging of cast SSs leads to the development of a material with a brittle phase dispersed in a ductile matrix.

Embrittlement of the ferrite phase due to neutron irradiation occurs much faster than for austenitic SSs; at reactor operating temperatures of 288-343°C (550-650°F) a shift in the nil-ductility transition

3

(ΔNDT) temperature of up to 150°C (302°F) has been observed in pressure vessel steels after neutron exposures of 0.07-0.15 dpa (0.5-1.0 x 10^{20} n/cm^2).[37] The irradiation temperature is an important factor in establishing the extent of embrittlement of ferritic steels. Although both the thermal aging embrittlement of ferrite and the neutron irradiation embrittlement of ferrite are well characterized, the synergistic effect of thermal aging and neutron irradiation on the embrittlement of SS welds and cast SSs has not been investigated yet.

Neutron irradiation increases the susceptibility of austenitic SSs to IASCC by changing the material microchemistry (e.g., radiation-induced segregation); material microstructure (e.g., radiation hardening); and water chemistry (e.g., radiolysis).[1,5,6] The factors that influence the IASCC susceptibility of materials include neutron fluence, cold work, material composition, corrosion potential, water purity, temperature, and loading. The effects of neutron fluence on the IASCC of SSs have been investigated for BWR control blade sheaths[38-40] and in laboratory tests on BWR-irradiated material.[5,41-46] The results indicate that the extent of intergranular (IG) SCC increases with fluence. The percent IGSCC measured in various irradiated SS specimens is plotted as a function of fast neutron fluence in Fig. 2. Although a threshold fluence level of 5 x 10^{20} n/cm^2 (E >1 MeV)∗ (≈0.75 dpa) has been proposed for austenitic SSs in BWR environments,[5,47] the results in Fig. 2 indicate an increase in IG cracking susceptibility in some commercial-purity SSs at fluence levels of ≈2 x 10^{20} n/cm^2 (≈0.3 dpa) and in high-purity heats of SSs at even lower fluence levels.
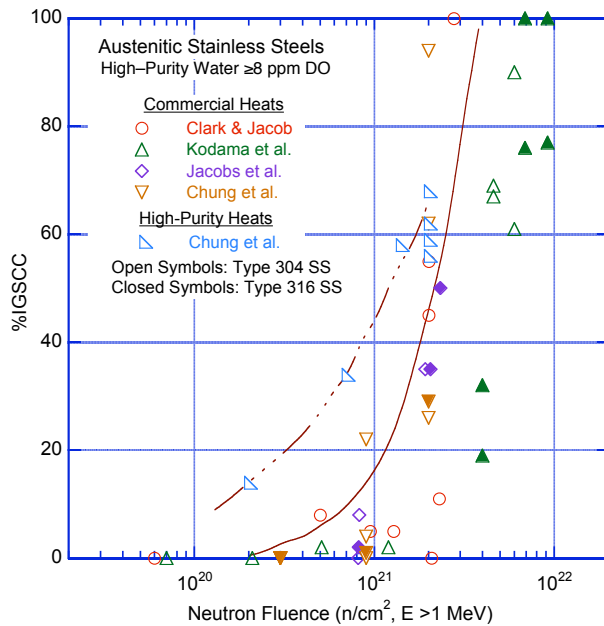
Figure 2.
Susceptibility of irradiated austenitic SSs to IGSCC as a function of fluence in high-DO water. From slow-strain-rate tensile tests (Refs. 41,43-45).

Constant extension rate tests on Types 304 and 316 SS irradiated to 0.3-4.0 x 10^{21} n/cm^2 (0.45-6.0 dpa) in a commercial BWR show a beneficial effect of reducing the corrosion potential of the environment.[6,48] This finding suggests that the threshold fluence for IASCC is higher under low potential conditions such as BWR hydrogen water chemistry (HWC) or PWR primary water chemistry. However, low corrosion potential does not provide immunity to IASCC if the fluence is high enough. For example, IGSCC has been observed in cold-worked, irradiated SS baffle bolts in PWRs.

∗All references to fluence levels are calculated for E ≥1 MeV.

The work at Argonne National Laboratory (ANL) on irradiated SSs sponsored by the Nuclear Regulatory Commission (NRC) is intended to provide a better understanding of the cracking and fracture toughness of BWR core internal components. The effect of neutron irradiation on the fracture toughness and IASCC behavior of austenitic SSs is being evaluated as a function of the fluence level, material composition, and water chemistry. Experimental data are being obtained on fracture toughness, corrosion fatigue, and SCC of Types 304 and 316 SS base metal and weld heat-affected zone (HAZ) as well as cast SSs that were irradiated to fluence levels up to 2.0×10^{21} n/cm^2 (3.0 dpa) at $\approx$288°C. Fracture toughness J-R curve tests are being conducted in air and normal water chemistry (NWC) BWR environment at 289°C, and the crack growth rate (CGR) tests are being conducted in NWC and HWC BWR environments at $\approx$289°C.

This report presents the following:

- CGR data for Type 316 SS irradiated to 0.3, 0.9, and 2.0×10^{21} n/cm^2 (0.45, 1.35, and 3.0 dpa),

- CGR and fracture toughness data for sensitized Type 304 SS and SS weld HAZ materials irradiated to 1.44×10^{21} n/cm^2 (2.16 dpa), and

- CGR and fracture toughness data for cast CF-8M SS irradiated to 1.63×10^{21} n/cm^2 (2.46 dpa).

The weld HAZ specimens were obtained from a Type 304L submerged arc (SA) weld and a Type 304 SS shielded metal arc (SMA) weld.

This page is intentionally left blank.

2   Experimental

2.1   Alloys and Specimen Preparation

Crack growth rate and fracture toughness J-R curve tests have been conducted on 1/4-T compact tension (CT) specimens of irradiated austenitic SSs in simulated BWR environments at 289°C. A standard CT specimen geometry (Fig. 3) was used in the present study. Tests have been completed on Types 304L, 304, 316L, and 316 SS (Heats C3, C19, C16, and C21, respectively), sensitized Type 304 SS (Heat 10285), HAZ of SA and SMA weld, and thermally aged cast CF-8M SS (Heat 75). The compositions of the various materials that are being investigated in the ANL study are presented in Table 1.

All irradiations were carried out in the Halden heavy boiling water reactor in a helium environment. The CT specimens from Heats C3, C16, C19, and C21 were irradiated in the reactor from April 1992 to November 1999. Six Type 304 SS capsules, each containing four CT specimens, were irradiated to fluence levels of 0.3, 0.9, and 2.0 x 10^{21} n/cm^2 (0.45, 1.35, and 3.0 dpa) at 288±2°C. Several spacers made of Type 304 SS wires were used to maintain a fixed gap between the specimens and the inner surface of the capsule during irradiation. To allow a uniform irradiation temperature, the gap was filled with helium. The specimens irradiated to 0.45, 1.35, and 3.0 dpa were discharged from the reactor in October 1992, November 1996, and November 1999, respectively.

A similar dry helium-filled capsule design was used for irradiating the specimens from sensitized SS, weld HAZ material, and cast SS. The neutron dose was monitored by Al/1% Co wire (for thermal neutrons) and by Fe and Ni wires (for fast neutrons) attached to the external surface of the irradiation capsules. Also, each irradiation capsule contained two sets of melting alloy temperature monitors (MATMs) to estimate the specimen temperature. The specimens irradiated to 0.5 x 10^{21} n/cm^2 (0.75 dpa) were discharged from the reactor in September 2002, and those irradiated to 1.44 x 10^{21} n/cm^2 (2.16 dpa) or 1.63 x 10^{21} n/cm^2 (2.46 dpa) were discharged in October 2004. The MATM results indicate that the specimen temperature was greater than 290°C and less than 305°C; i.e., irradiation temperature ≈297°C.

Figure 3.   Configuration of compact-tension specimen for this study (dimensions in mm).

The SA weld was obtained from the H5 weld of the core shroud from the Grand Gulf (GG) reactor. The top and bottom shroud shells for the GG H5 weld were fabricated from SA 240 Type 304L hot-rolled plate and welded by the SA method with ER308L filler metal using a double-V joint design. The SMA weld was prepared in the laboratory by welding two 70 x 178 mm (2.75 x 7.0 in.) pieces of 30-mm thick

Table 1.   Composition (wt.%) of austenitic stainless steels being investigated.

Steel Type	Heat ID	Analysis	Ni	Si	P	S	Mn	C	N	Cr	Mo	O
304L	C3	Vendor	8.91	0.46	0.019	0.004	1.81	0.016	0.083	18.55	-	-
		ANL	9.10	0.45	0.020	0.003	1.86	0.024	0.074	18.93	0.12	0.014
304	C19	Vendor	8.08	0.45	0.031	0.003	0.99	0.060	0.070	18.21	-	-
		ANL	8.13	0.51	0.028	0.008	1.00	0.060	0.068	18.05	0.09	0.020
316L	C16	Vendor	12.90	0.38	0.014	0.002	1.66	0.020	0.011	16.92	-	-
		ANL	12.32	0.42	0.026	0.003	1.65	0.029	0.011	16.91	2.18	0.016
316	C21	Vendor	10.24	0.51	0.034	0.001	1.19	0.060	0.020	16.28	2.08	-
		ANL	10.45	0.61	0.035	0.002	1.23	0.060	0.016	16.27	2.10	0.014
304	10285	Vendor	8.40	0.51	0.032	0.006	1.64	0.058	-	18.25	0.41	-
		ANL	8.45	0.60	0.015	0.007	1.90	0.070	0.084	18.56	0.51	0.013
304L	GG Top Shell	ANL	9.05	0.53	0.027	0.016	1.84	0.013	0.064	18.23	0.44	0.010
	GG Bottom Shell	ANL	8.95	0.55	0.023	0.008	1.80	0.015	0.067	18.62	0.31	0.014
CF-8M	75	ANL	9.12	0.67	0.022	0.012	0.53	0.065	0.052	20.86	2.58	-

(1.18-in. thick) plate of Type 304 SS (Heat 10285). The weld had a single-V joint design and was produced by 31 weld passes using E308 filler metal. Passes 1-5 were produced with 3.2-mm (0.125-in.) filler metal rod and 178-mm/min (7-ipm) travel speed, and passes 6-31 were produced with 4.0-mm (0.156-in.) filler metal rod and 216-mm/min (8.5-ipm) travel speed. Between passes the laboratory weld surfaces were cleaned by wire brush and grinding and were rinsed with de-mineralized water or alcohol. The corresponding details of the GG weld procedure are not known to the authors.

There are two potential differences between the GG SA weld HAZ and laboratory-prepared SMA weld HAZ: microstructure and residual strain. The HAZ of high-C austenitic SS welds typically consists of a sensitized microstructure. The low-C grades of SSs are considered to be resistant to weld sensitization. A transmission electron microscopy study of the GG Type 304L weld HAZ in the core shroud vertical weld revealed a few, very small Cr-rich precipitates at the grain boundaries about 1 and 3 mm (0.04 and 0.12 in.) from the fusion line; however, most boundaries showed no precipitates.[49] Thus, only the laboratory-prepared weld HAZ is likely to have a sensitized microstructure. The residual strain in various SS weld HAZs has been measured by the electron back-scattered pattern technique.[49-52] The results indicate that the peak strains typically extend up to 5 mm from the fusion line and range from 8 to 20%. Residual strains up to 10% have been measured in the GG Type 304L weld HAZ of core shroud vertical weld.[49] Because the heat input per pass for SA welds is typically higher than that for SMA welds of comparable geometry, the HAZ associated with an SA weld is wider than that associated with an SMA weld. However, because the total number of passes is less in an SA weld than an SMA weld, residual strains associated with SA welds are smaller.

The specimens were machined from 9.5-mm (0.37 in.) thick slices of the weld; some slices were thermally treated for 24 h at 500°C to simulate low-temperature sensitization. For all specimens, the machined notch was located in the HAZ of the weld. Each slice was etched, and the specimen orientation and notch location relative to the weld were clearly identified. In all cases, the machine notch was located ≈1 mm (0.04 in.) from the fusion zone in a region where the fusion zone was relatively straight.

Metallographic examination of weld HAZ materials showed that the base metal of Heat 10285 of Type 304 SS and the GG Type 304L core shroud shells contain stringers of ferrite (Fig. 4). Heat 10285 appears to have the most ferrite and the GG bottom shell, the least. The grain sizes for the GG top and bottom shell materials are comparable and are larger than those for Heat 10285; for example, the grain size in the HAZ region of the GG shell is ≈110 μm, and that of Heat 10285 is ≈80 μm. In all welds, the fusion line extends into the base metal along the ferrite stringers (Fig. 5). In other words, the ferrite stringers intersecting the fusion line appear to have melted and re-solidified during the welding process.

8
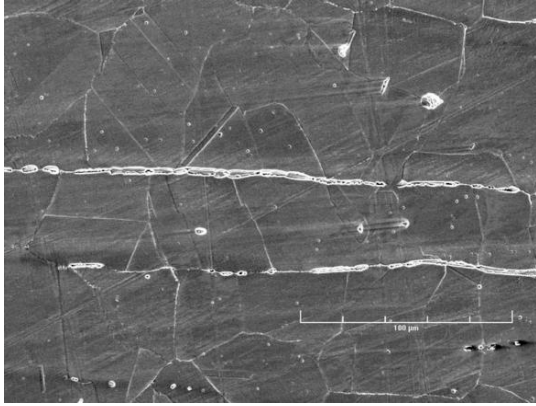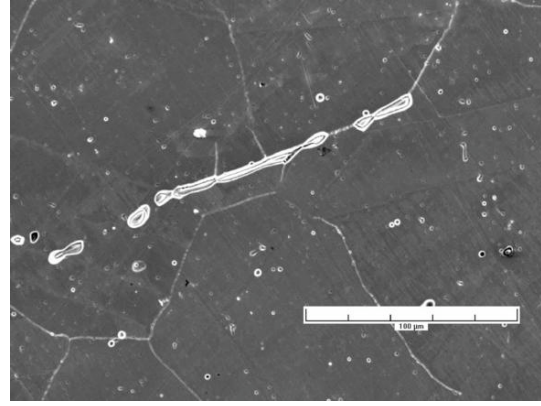
(a)   (b)

Figure 4.   Micrographs of the structure of (a) Heat 10285 of Type 304 SS and (b) Type 304L from the top shell of the H5 weld of the GG core shroud.
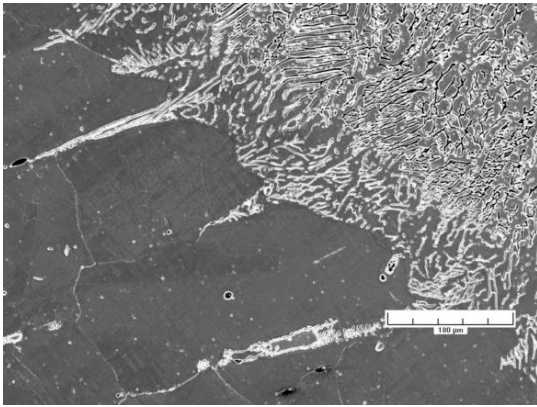
Figure 5.
Micrographs of the interface between the weld metal and top shell of the H5 weld of the GG core shroud.

The cast CF-8M SS was obtained from a static cast plate, ≈ 610 x 610 x 76 mm (24 x 24 x 3 in.). The cast SS material has a duplex ferrite-austenite structure consisting of lacy ferrite morphology. Figure 6 shows a photograph of the interlaced network of ferrite islands. The ferrite content, measured by a ferrite scope, was ≈ 28%. Prior to irradiation, the cast SS material was aged for 10,000 h at 400°C (752°F), and Heat 10285 of Type 304 SS was sensitized for 10.5 h at 600°C (1112°F).
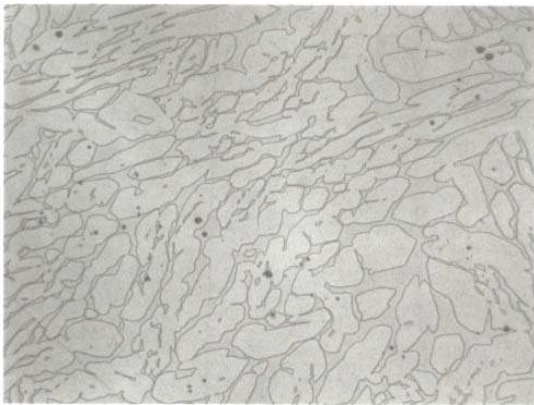
Figure 6.
Ferrite morphology for the CF-8M cast SS.

Table 2 gives the tensile yield and ultimate stress, determined from slow-strain-rate-tensile tests in high-dissolved oxygen (DO) water, for Types 304L, 304, 316L, and 316 SS (Heats C3, C19, C16, and

C21, respectively), irradiated to the three fluence levels and in the nonirradiated condition.[53] For the few materials that were tested in air and water environments, the experimental tensile stress was 10-20% higher in air than in water. Table 3 lists the tensile properties of nonirradiated Type 304L SS from the GG core shroud shell, Heat 10285 of Type 304 SS in the mill-annealed condition and after sensitization at 600°C for 10.5 h,[54] and the thermally aged cast CF-8M SS.[28] For these steels, the tensile properties of the irradiated materials have not been measured and were therefore estimated. The ultimate stresses for the irradiated steels were estimated from the data in Ref. 53, and the yield stress was estimated from the correlation developed by Odette and Lucas.[55] The increase in yield stress (MPa) is expressed in terms of the fluence (dpa) by the relationship

$$\Delta\sigma_y = 670 \, [1 - \exp(-dpa/2)]^{0.5}. \tag{3}$$

The estimated tensile yield and ultimate stresses for the irradiated SSs are given in Table 3. For Heat 10285 and the GG core shroud, the tensile properties of the sensitized material were used to determine the "K/size criterion" (discussed in Section 2.3.1) for nonirradiated and irradiated HAZ specimens, both in the as-welded and as-welded plus thermally-treated conditions.

Table 2.   Tensile properties[a] at 289°C of austenitic stainless steels from Halden Phase I irradiations.

Steel Type (Heat)	Nonirradiated		0.3×10^{21} n/cm^2 (0.45 dpa)		Fluence (E >1 MeV) 0.9×10^{21} n/cm^2 (1.35 dpa)		2.0×10^{21} n/cm^2 (3.00 dpa)	
	Yield (MPa)	Ultimate (MPa)	Yield (MPa)	Ultimate (MPa)	Yield (MPa)	Ultimate (MPa)	Yield (MPa)	Ultimate (MPa)
304L SS (C3)	(154)	(433)	338	491	632	668	796	826
304 SS (C19)	178	501	554	682	750	769	787	801
316L SS (C16)	(189)	(483)	370	527	562	618	766	803
316 SS (C21)	277	455	480	620	643	716	893	924

[a]Estimated values within parentheses.

Table 3.   Tensile properties[a] at 289°C of austenitic stainless steels from Halden Phase II irradiations.

Steel Type (Heat)	Material Condition	Yield (MPa)	Ultimate (MPa)	Yield (MPa)	Ultimate (MPa)	Yield (MPa)	Ultimate (MPa)
		Nonirradiated		0.5×10^{21} n/cm^2 (0.75 dpa)		1.44×10^{21} n/cm^2 (2.16 dpa)	
304 SS (10285)	Mill annealed	196	508	-	-		
	MA + 10.5 h at 600°C	156	501	(531)	(680)	(670)	(780)
304L SS GG Core Shroud	Mill annealed	158	411	-	-		
	MA + 10.5 h at 600°C	159	425	(533)	(610)	(702)	(720)
		Nonirradiated				1.63×10^{21} n/cm^2 (2.46 dpa)	
CF-8M (75)	As-cast + 10,000 h at 400°C	207	612			(740)	(780)

[a]Estimated values within parentheses.

2.2 Test Facility

The facility for conducting crack growth and fracture toughness tests on irradiated austenitic SSs is designed for in-cell testing, with the test frame, furnace, and other required equipment mounted on top of a portable wheeled cart that can be easily rolled into the cell. A 1-liter SS autoclave is installed inside the furnace for conducting tests in simulated BWR environments. The furnace is mounted on a pneumatic cylinder and can be raised to enclose the autoclave with the load cage and the specimen during the test. Water is circulated through a port in the autoclave cover plate that serves both as inlet and outlet. The hydraulic actuator is mounted on top of the test frame, with the load train components suspended beneath it. The 22-kN (5-kip) load cell is at the top of the pull rod. An Instron Model 8500+ Dynamic Materials

Testing System is used to load the specimen. A photograph of the test facility inside the hot cell is shown in Fig. 7.

The 1/4-T CT specimen is mounted in the clevises with 17-4 PH SS pins. Crack extensions are monitored by the reversing direct-current (DC) potential difference method. The specimen and clevises are kept electrically insulated from the load train by using oxidized Zircaloy pins and mica washers to connect the clevises to the rest of the load train. The Zircaloy pins were oxidized at 500°C for 24 h and air-cooled. Platinum wires are used for the current and potential leads. The current leads are attached to SS split pins that are inserted into the holes at the top and bottom of the specimen. The potential leads are attached by screwing short SS pins into threaded holes on the front face of the specimen and attaching the platinum wires with in-line SS crimps.

The recirculating water system consists of a storage tank, high pressure pump, regenerative heat exchanger, autoclave preheater, test autoclave, electrochemical potential (ECP) cell preheater, ECP cell, regenerative heat exchanger, Mity Mite™ back-pressure regulator, an ion-exchange cartridge, a 0.2 micron filter, a demineralizer resin bed, another 0.2 micron filter, and return line to the tank. A schematic diagram of the recirculating water system is shown in Fig. 8.

Figure 7.   Photograph of the test facility inside the hot cell.

The simulated BWR environments consist of high-purity deionized water that either contains 250-500 ppb DO (corresponding to NWC BWR water), or <30 ppb DO (corresponding to HWC BWR water). The resulting ECPs for SS are in the range of 160 to 240 mV versus a standard hydrogen electrode (SHE) for NWC and -200 to -500 mV (vs. SHE) for HWC. The feedwater is stored in a 135-L SS tank manufactured by Filpaco Industries. The tank is designed for vacuums and over-pressures up to 414 kPa (60 psig). The deionized water is prepared by passing purified water through a set of filters that comprise a carbon filter, an Organex-Q filter, two ion exchangers, and a 0.2-mm (8-mil) capsule filter. The DO level in water is established by maintaining a cover gas of nitrogen plus 1% oxygen above the supply tank and initially bubbling the gas mixture through the deionized water. The ECP of a Pt electrode and an SS sample located at the exit of the autoclave was monitored continuously during the test, and water samples were taken periodically to measure pH, resistivity, and DO concentration. The DO level was measured in the in-cell facility by the colorimetric technique using CHEMets sampling ampoules.

11

1. COVER GAS SUPPLY TANK	16. CHECK VALVE
2. HIGH-PRESSURE REGULATOR WITH FLASH ARRESTOR	17. RUPTURE DISK
	18. HEAT EXCHANGER
3. LOW-PRESSURE REGULATOR	19. SYSTEM BLEED PORT
4. FLOW METER	20. HIGH-PRESSURE GAUGE
5. GAS PURIFIER	21. AUTOCLAVE PREHEATER
6. PRESSURE GAUGE	22. PARR AUTOCLAVE
7. PRESSURE RELIEF VALVE	23. THERMOCOUPLE WELL
8. VENT TO AIR WITH FLASH	24. ECP CELL PREHEATER
9. FEEDWATER STORAGE TANK	25. ECP CELL
10. SPARGE TUBE	26. ECP CELL BYPASS LINE
11. FEEDWATER FILL PORT	27. BACK-PRESSURE RELIEF
12. WATER SAMPLE PORT	28. ION EXCHANGE
13. SOLENOID VALVE	29. RECIRCULATING PUMP
14. 0.2-MICRON FILTER	30. DEMINERALIZER
15. HIGH-PRESSURE PUMP	31. DEMINERALIZER BYPASS
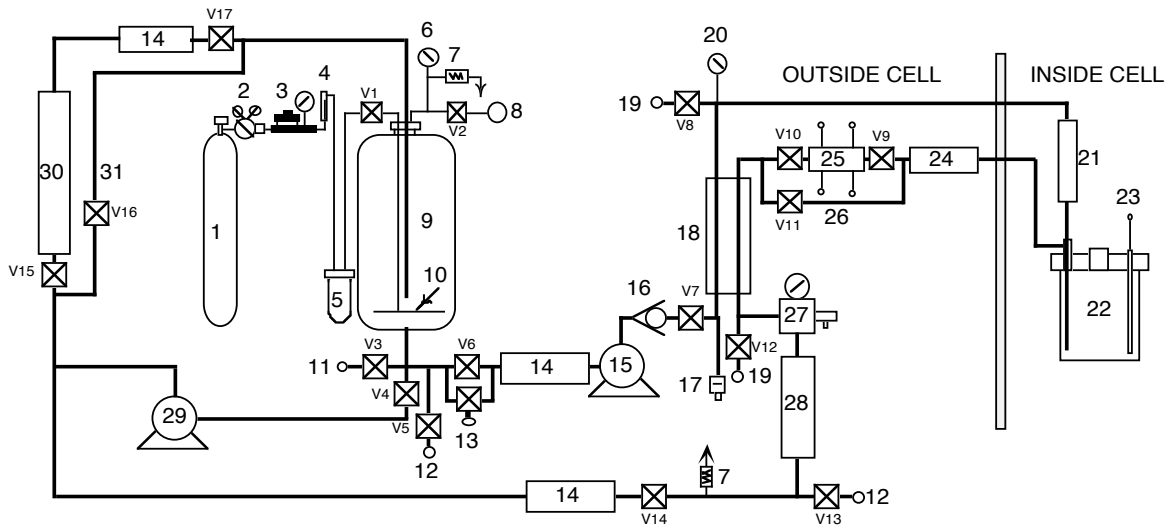
Figure 8. Schematic diagram of the water system.

All tests in simulated BWR environment were started in high-purity water that contained 250-500 ppb DO. After data were obtained for high-DO water, the DO level in the feedwater was decreased to <30 ppb by sparging it with a gas mixture of N_2 + 5% H_2. Because of the very low water flow rates, it took several days for the environmental conditions to stabilize for the in-cell tests. In general, the changes in ECP were slower in the SS sample than in the Pt electrode.

The autoclave, but without the water, was also used as the test chamber for conducting CGR and fracture toughness tests in air. The specimen temperature was monitored with a thermocouple located near the specimen and by measuring the temperatures of the top and bottom clevis.

2.3 Test Procedure

2.3.1 Crack Growth Rate Tests

The CGR tests were performed in accordance with American Society for Testing and Materials (ASTM) E-647, "Standard Test Method for Measurement of Fatigue Crack Growth Rates," and ASTM E-1681, "Standard Test Method for Determining a Threshold Stress Intensity Factor for Environment-Assisted Cracking of Metallic Materials under Constant Load."   The tests were conducted in the load-control mode using a triangular or sawtooth waveform with load ratio R of 0.2-0.7. All specimens were fatigue precracked in the test environment at R = 0.2-0.3, frequency of 1-5 Hz, and maximum stress intensity factor (K_{max}) of 13-16 MPa $m^{1/2}$.   After 0.3-0.5 mm crack extension, a prescribed loading

sequence was followed to facilitate the transition of a transgranular (TG) fatigue crack to an IG stress corrosion crack. To achieve this transition, R was increased incrementally to 0.7, and the loading waveform changed to a slow/fast sawtooth with rise times of 30-1000 s. The SCC growth rates were measured under constant load with or without periodic partial unloading to R = 0.7 every 1 or 2 h; the unload/reload period was 24 s. During individual test periods, K_{max} was maintained approximately constant by periodic load shedding (less than 2% decrease in load at any given time); K_{max} at the end of the test period is reported in the results.

In the present study, crack length "a" was calculated from the following correlation, which was developed from the best fit of the experimental data for normalized crack length and normalized DC potential:

$$\frac{a}{W} = \left[0.28887 \left(\frac{U}{U_0} - 0.5 \right) \right]^{0.34775} , \tag{4}$$

where W is the specimen width, and U and U_0 are the current and initial potentials, respectively. Equation 4 is comparable to the ASTM E 1737 correlation for a CT specimen with current inputs at the W/4 position and DC potential lead connections at the W/3 position. Also, the stress intensity factor range ΔK was calculated from the correlations for a CT specimen as follows:

$$\Delta K = \frac{\Delta P}{\left(BB_N W \right)^{1/2}} \frac{\left(2 + \frac{a}{W} \right)}{\left(1 - \frac{a}{W} \right)^{3/2}} f \left(\frac{a}{W} \right) , \tag{5}$$

$$\Delta P = \Delta P_{max} - \Delta P_{min} \qquad \text{for R > 0,} \tag{6}$$

$$f \left(\frac{a}{W} \right) = 0.886 + 4.64 \left(\frac{a}{W} \right) - 13.32 \left(\frac{a}{W} \right)^2 + 14.72 \left(\frac{a}{W} \right)^3 - 5.60 \left(\frac{a}{W} \right)^4 , \tag{7}$$

where P_{max} and P_{min} are maximum and minimum applied load, respectively; B is the specimen thickness; B_N is the net specimen thickness (or distance between the roots of the side grooves).

In an earlier report,[27] experimental J-R curve data were obtained at ANL on irradiated Types 304 and 316L SS (Heats C19 and C16, respectively), and K values were calculated using the correlations for a disc-shaped specimen instead of a standard CT specimen. The earlier data have been corrected using Eqs. 5-7; the corrected data are given in Appendix B of this report. The difference between the J-R curves based on the correlations for a disc-shaped specimen and standard CT specimen is minimal.

In the present test facility, the Bal-seal™ between the pull rod and the autoclave cover plate exerts a frictional load on the pull rod. In earlier tests, the frictional load typically varied in the range of ±22-44 N (±5-10 lb). However, the pull rod was replaced for the tests being performed on Halden Phase II specimens, and the frictional load on the new pull rod is in the range of ±111-133 N (±25-30 lb). Therefore, the measured values of P_{max} and P_{min} are first corrected for the frictional load before calculating the ΔK for the various test periods. The applied K and load ratio for each test period are

determined by subtracting the frictional load from the measured maximum load and adding it to the measured minimum load. The most significant effect of this correction is on the waveform for the cyclic tests; although the tests were intended to be conducted with either triangular or sawtooth waveforms, the actual loading waveforms for the test specimen are trapezoidal because the load did not change during the initial 40-50% of the loading or unloading cycles. For example, for a test intended to be conducted at R = 0.7 and a sawtooth waveform with 300-s rise time and 12-s return time, the actual loading waveform was trapezoidal with 112-s hold at minimum load, 188-s rise time, 6-s hold at maximum load, and 6-s return time. Because the autoclave, including the Bal-seal in the cover plate, was used as the test chamber for tests in air, the experimental data for the air tests were also corrected for frictional load.

During each test period, the CGR was determined from the slope of the corrected crack length vs. time plots; for cyclic loading, only the rise time was used to determine growth rate. The crack extension during each test period was at least 10 times the resolution of the DC potential drop method (i.e., typically 5 μm). Thus, crack extensions were at least 50 μm; for test periods with very low CGRs (e.g., less than 1×10^{-11} m/s), smaller crack extensions were used to reduce testing time.

The CGR test results were validated in accordance with the specimen size criteria of ASTM E 1681 and E 647. Fracture mechanics is a correlative technology, i.e., it does not attempt to describe the mechanisms that are occurring at the crack tip. It correlates the behavior of components with that of specimens through the use of the K parameter. If two cracks have the same K, then they have the same strains and stresses in a region near the crack tip. For this correlation between specimen and component to work, K has to control the stresses and strains at the crack tip in the process zone. Mathematically it can be shown that this is true if the plastic zone size is "small enough". The K/size criteria are combined theoretical and empirical results that have been found to ensure the plastic zone is small enough and K is controlling.   The ASTM specifications for specimen K/size criteria are intended to ensure the applicability and transferability of the cracking behavior of a component or specimen of a given thickness under a specific loading condition to a crack associated with a different geometry, thickness, and loading condition. For constant load tests, ASTM E 1681 requires that

$$B_{eff} \text{ and } (W - a) \geq 2.5 \ (K/\sigma_y)^2, \tag{8}$$

and for cyclic loading, ASTM 647 requires that

$$B_{eff} \text{ and } (W - a) \geq (4/\pi) \ (K/\sigma_y)^2, \tag{9}$$

where K is the applied stress intensity factor, σ_y is the yield stress of the material, a is crack length, and the B_{eff} is the specimen effective thickness, defined as $(B \ B_N)^{0.5}$. For high strain-hardening materials, i.e., $(\sigma_u/\sigma_y) \geq 1.3$, both criteria allow the use of the flow stress defined as $\sigma_f = (\sigma_u + \sigma_y)/2$ rather than the yield stress.

However, the database for defining the K/size criteria for irradiated materials is inadequate. The K/size criteria were developed for materials that show work hardening and, therefore, may not be applicable for materials irradiated to fluence levels where, on a local level, they do not strain harden. This lack of strain hardening, termed "strain softening," is most dramatic when dislocation channeling occurs but may also occur at lower fluences. For moderate to highly irradiated material, Andresen[56] has suggested an effective yield stress, defined as the average of the nonirradiated and irradiated yield stresses [$\sigma_{eff} = (\sigma_{yirr} + \sigma_{ynonirr})/2$]; this discounts the irradiation-induced increase in yield stress by a factor of 2.

14

Jenssen et al.[57] obtained crack growth data in simulated BWR environment on Type 304L SS irradiated to ≈13 dpa and investigated the specimen K/size criterion for CGR testing of irradiated austenitic SSs. They performed a finite element study that indicated that if the strain softening found in highly irradiated materials is taken into account, there is a significant amount of plastic deformation in the plane of the growing crack if the K/size criterion is defined as $\sigma_{eff} = (\sigma_{yirr} + \sigma_{ynonirr})/2$. The authors argue that as a result of an increased tendency for "highly irradiated material" to deform by dislocation channeling, a K/size criterion based on the sum of irradiated and nonirradiated yield stress divided by 3 [i.e., $\sigma_{eff} = (\sigma_{yirr} + \sigma_{ynonirr})/3$] fits the crack growth behavior better.[57]

In the present study, because the ultimate-to-yield stress ratio was generally less than 1.3, the effective yield stress was used to determine the allowed K_{max} for the irradiated specimens. The only exception was austenitic SSs irradiated to ≈0.45 dpa, where effective flow stress was used to determine allowed K_{max} for this specimen. Also, because the materials that have been investigated in the present study were irradiated only up to ≈3 dpa, the effective yield stress was defined as $(\sigma_{yirr} + \sigma_{ynonirr})/2$.

Under cyclic loading, the CGR (m/s) can be expressed as the superposition of the rate in air (i.e., mechanical fatigue) and the rates due to corrosion fatigue and SCC, given as

$$\dot{a}_{env} = \dot{a}_{air} + \dot{a}_{cf} + \dot{a}_{scc} . \tag{10}$$

The CGRs in air, $\dot{a}_{air}$ (m/s), were determined from the correlations developed by James and Jones:[58]

$$\dot{a}_{air} = C_{SS}\, S(R)\, \Delta K^{3.3}/t_r , \tag{11}$$

where R is the load ratio (K_{min}/K_{max}), ΔK is $K_{max} - K_{min}$ in MPa m$^{1/2}$, t_r is the rise time (s) of the loading waveform, and the function S(R) is expressed in terms of the load ratio R as follows:

$$
\begin{aligned}
S(R) &= 1.0 & R &< 0 \\
S(R) &= 1.0 + 1.8R & 0 &< R < 0.79 \\
S(R) &= -43.35 + 57.97R & 0.79 &< R < 1.0.
\end{aligned}
\tag{12}
$$

Function C_{SS} is given by a third-order polynomial of temperature T (°C), expressed as

$$C_{SS} = 1.9142 \times 10^{-12} + 6.7911 \times 10^{-15}\,T - 1.6638 \times 10^{-17}\,T^2 + 3.9616 \times 10^{-20}\,T^3. \tag{13}$$

Environmental effects on fatigue crack growth of nonirradiated austenitic SSs have been investigated by Shack and Kassner.[59] In the absence of any significant contribution of SCC to growth rate, the CGRs in water with ≈0.3 ppm DO are best represented by the expression

$$\dot{a}_{env} = \dot{a}_{air} + 4.5 \times 10^{-5}\, (\dot{a}_{air})^{0.5}, \tag{14}$$

and in water with ≈8 ppm DO by the expression,

$$\dot{a}_{env} = \dot{a}_{air} + 1.5 \times 10^{-4}\, (\dot{a}_{air})^{0.5}. \tag{15}$$

The CGR (m/s) under SCC conditions is represented by the correlation given in the U.S. NRC report NUREG-0313, Rev. 2:[60]

$$\dot{a}_{SCC} = A\,(K)^{2.161}, \tag{16}$$

where K is the stress intensity factor (MPa m$^{1/2}$), and the magnitude of the constant A depends on the water chemistry and composition and structure of the steel. A value of 2.1 x 10^{-13} has been proposed in NUREG-0313 for sensitized SS in water with 8 ppm DO. For water with 0.2 ppm DO, the CGR is taken as one-third that of the value given in NUREG-0313; in this case A is 7.0 x 10^{-14}. The value of constant A is smaller in low-DO environments, such as HWC BWR or PWR environments.

2.3.2 Fracture Toughness J-R Curve Tests

After the CGR test, a J-R test was performed on the specimen at 289°C in high-DO water. The test was conducted at a constant extension rate of ≈0.43 μm/s (0.017 mil/s) in accordance with ASTM specification E-1737 for "J-Integral Characterization of Fracture Toughness." The test was interrupted periodically (by holding the specimen at constant extension) to measure the crack length. For most steels, load relaxation occurs during the hold period, which may influence the DC potential readings. Consequently, before measuring the DC potential drop at each and every hold point, the specimen was held for ≈30 min to allow relaxation.

Specimen extension was monitored and controlled outside the high-temperature zone. The actual displacement of load points was determined by subtracting the extension of the load train from the measured extension. The load train displacement was determined as a function of applied load with a very stiff specimen. The J-integral was calculated from the load vs. load-line displacement curves according to the correlations for a CT specimens in ASTM Specification E 1737. The total J is the sum of the elastic and plastic components, J_{el} and J_{pl}, respectively,

$$J = J_{el} + J_{pl}. \tag{17}$$

The total area and plastic component of the area $A_{pl(i)}$ at each recorded deflection are computed during the test by summing the increase in areas for each increment in deflection; the elastic component of deflection is calculated from the specimen load-line elastic compliance at each step and subtracted from the total deflection to obtain plastic deflection. The elastic component of J, at a point corresponding to a_i, V_i, and P_i on the specimen load vs. load-line displacement record, is given by

$$J_{el(i)} = \frac{\left(K_{(i)}\right)^2 \left(1 - \upsilon^2\right)}{E_{ef}}, \tag{18}$$

where the stress intensity $K_{(i)}$ is calculated from Eqs. 5 and 7. The plastic component of J is given by

$$J_{pl(i)} = \left[J_{pl(i-1)} + \left(\frac{\eta_{(i-1)}}{b_{(i-1)}}\right)\frac{A_{pl(i)} - A_{pl(i-1)}}{B_N}\right]\left[1 - \gamma_{(i-1)}\frac{a_{(i)} - a_{(i-1)}}{b_{(i-1)}}\right], \tag{19}$$

where the factors that account for limited crack growth $\gamma_{(i)}$ and for the tensile component of the load $\eta_{(i)}$ are expressed as

$$\eta_{(i-1)} = 2.0 + 0.552 \frac{b_{(i-1)}}{W} , \tag{20}$$

$$\gamma_{(i-1)} = 1.0 + 0.76 \frac{b_{(i-1)}}{W} . \tag{21}$$

In the above equation $b_{(i-1)}$ is the remaining ligament (distance from the physical crack front to the back edge of the specimen) at a point i-1.

The quantity $A_{pl(i)}$ - $A_{pl(i-1)}$ is the increment of plastic area under the load vs. load-line displacement record between lines of constant displacement at points i-1 and i. The quantity $J_{pl(i)}$ represents the total crack-growth-corrected plastic J at point i and is obtained by first incrementing the existing $J_{pl(i-1)}$ and then by modifying the total accumulated result to account for the crack growth increment. Accurate evaluations of $J_{pl(i)}$ require small uniform increments in crack growth. The plastic area under the load vs. load-line displacement record is given by

$$A_{pl(i)} = A_{pl(i-1)} + \frac{\left[P_i + P_{i-1} \right] \left[V_{pl(i)} - V_{pl(i-1)} \right]}{2} , \tag{22}$$

where the total and plastic components of the load-line displacement, $V_{(i)}$ and $V_{pl(i)}$, respectively, are expressed as

$$V_{pl(i)} = V_{(i)} - P_i C_{LL(i)} , \tag{23}$$

where $C_{LL(i)}$ is the compliance, $(\Delta V / \Delta P)_i$, required to give the current crack length a_i. For test methods that do not use the elastic compliance techniques, $C_{LL(i)}$ can be determined from knowledge of a_i/W, as follows:

$$C_{LL(i)} = \frac{\left[1.62 + 17.80\left(a_i/W\right) - 4.88\left(a_i/W\right)^2 + 1.27\left(a_i/W\right)^3 \right]}{E' B_e \left[1 - \left(a_i/W\right) \right]^2} , \tag{24}$$

where B_e is specimen effective thickness given by $B - (B - B_N)^2/B$ and $E' = E/(1 - \upsilon^2)$.

After the test the final crack size was marked by fatigue cycling in air at room temperature. The specimens were then fractured, and the fracture surface of both halves of the specimen was photographed with a telephoto lens through the hot cell window. The final crack length of each half of the fractured specimen was determined from the optical photograph by the 9/8 averaging technique. In this technique, nine measurements were taken across the width of the specimen at equal intervals, the two near-surface measurements were averaged, and the resultant value was averaged with the remaining seven measurements. The crack extensions determined from the DC potential drop method were proportionately scaled to match the final optically measured crack length.

The experimental results from the J-R curve test were analyzed in accordance with ASTM E-1737 to obtain the fracture toughness J-R curve. The DC potential data were corrected to account for the

17

effects of plasticity on the measured potential, since large crack-tip plasticity can increase the measured potentials due to resistivity increases without crack extension. As per ASTM E1737, the change in potential before crack initiation was ignored, and the remainder of the potential change was used to establish the J-R curve. The normalized potential varies linearly with load-line displacement until the onset of crack extension. For all data prior to the loss in linearity, crack extension was expressed as $a_o + \Delta a_B$, where a_o is the initial crack length, and the crack extension Δa_B is calculated from the blunting line relationship $\Delta a = J/(4\sigma_f)$. For all data after this point, crack length was calculated from Eq. 4, in which U_0 is considered to be the potential at the onset of crack extension in the potential vs. load-line-displacement plot (i.e., at Δa_B crack extension).

The use of the blunting line given by $\Delta a = J/(4\sigma_f)$ is not consistent with ASTM E 813, which specifies a slope of two times the effective yield stress (or flow stress) for the blunting line. However, for high-strain-hardening materials, such as austenitic SSs, a slope that is four times the flow stress ($4\sigma_f$) represents the blunting line better than the slope of $2\sigma_f$ defined in ASTM E 1737.[61,62] In irradiated materials, the increase in yield stress is primarily due to a high density of barriers to dislocation motion. During deformation, as dislocations sweep through the irradiated matrix, they annihilate the very fine scale of barriers, thus creating a "channel" for easy dislocation motion. As discussed in Section 4.3.1, this condition may result in marked work softening and produce a distinctive change in fracture mode. As discussed in Section 2.3.1, to account for the possible strain softening that may occur in irradiated materials, an effective flow stress, defined as the average of the nonirradiated and irradiated flow stress,[56] was used in the J-R curve data analysis. Because the effective flow stress discounts the irradiation-induced increase in flow stress by a factor of two, the slope of the blunting line was defined as $4\sigma_f$ even for the irradiated materials.

3 Test Results

In earlier ANL studies, CGR tests were completed in simulated BWR environments at 289°C with the following: Types 304L and 316L SS (Heats C3 and C16, respectively) irradiated to 0.45, 1.35, and 3.0 dpa and Types 304 and 304L weld HAZ irradiated to 0.75 dpa. The CGR data from earlier studies are given in Appendix A of this report, Tables A1-A12.

Fracture toughness tests were also completed in air on Types 304 and 316L SS (Heats C19 and C16, respectively) irradiated 3.0 dpa. However, as discussed in Section 2.3.1, because the experimental data from the J-R curve tests performed earlier[27] were analyzed by using the correlations for a disc-shaped specimen instead of a standard CT specimen, the earlier data have been corrected using Eqs. 5-7. The corrected fracture toughness J-R curve data are compiled in Appendix B of this report, Tables B1-B4.

3.1 Types 304 and 316 Stainless Steel

Crack growth tests have been completed in BWR environments at 289°C on 1/4-T CT specimens of Type 316 SS (Heat C21) irradiated to ≈0.45, 1.35, and 3.00 dpa, as well as sensitized Type 304 SS (Heat 10285) irradiated to ≈2.16 dpa. The test on sensitized Type 304 SS included a fracture toughness J-R curve test conducted in high-DO water at 289°C, after the CGR test. The significant results for the various tests are summarized below.

3.1.1 Specimen C21-A of Type 316 SS, Test CGRI-25

The test on Specimen C21-A of Type 316 SS irradiated to 0.45 dpa was started in high-purity water with ≈350 ppb DO and a flow rate of ≈20 mL/min. The specimen was fatigue precracked at R = 0.35, K_{max} = 15.5 MPa m$^{1/2}$, triangular waveform, and 1-Hz frequency. After ≈0.20-mm crack advance, R was increased incrementally to 0.7, and the waveform was changed to a slow/fast sawtooth with rise times of 30-1000 s. Finally, the specimen was subjected to a constant load with and without periodic partial unloading. At ≈162 h the test was interrupted because of a power bump that tripped the autoclave temperature control unit and the water pump. The cessation of water flow caused overheating of the ECP-cell unit, which damaged the reference electrode. The test was restarted with the ECP cell bypassed; ECP measurements were not obtained for the remainder of the test. There was no chloride intrusion during the interruption, and test conditions prior to the interruption were restored.

After the test the final crack size was marked by fatigue cycling in air at room temperature. The specimen was then fractured; a photograph of the fracture surfaces is shown in Fig. 9. The final crack length measured from the photograph of each half of the specimen was ≈23% greater than the value determined from the DC potential measurements. The experimental crack extensions were scaled proportionately. The environmental and loading conditions, corrected CGRs, and the allowed K_{max} based on the K/size criterion are given in Table 4; the changes in crack length, CGR, and K_{max} with time during the various test periods are plotted in Fig. 10.
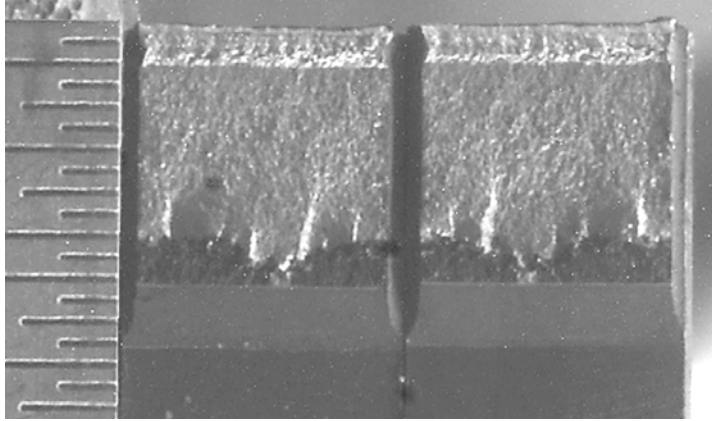
Figure 9.
Photograph of the fracture surfaces of the two halves of the fractured specimen C21-A.

Table 4. Test conditions and results for Specimen C21-A[a] of Type 316 SS in BWR water at 289°C.

Test Period	Test Time, h	ECP[b] mV (SHE) Pt	Steel	O_2 Conc.,[b] ppb	R Load Ratio	Rise Time, s	Return Time, s	Hold Time, s	K_{max}, MPa m$^{1/2}$	ΔK, MPa m$^{1/2}$	Growth Rate, m/s	Allowed K_{max},[c] MPa m$^{1/2}$	Crack Length,[d] mm
													6.000
Pre a	95	-	-	350	0.35	0.5	0.5	0	15.5	10.1	1.10E-08	22.2	6.138
Pre b	112	249	103	350	0.34	5	5	0	15.7	10.3	5.69E-09	22.0	6.244
1	157	246	116	350	0.51	30	4	0	16.0	7.9	1.33E-09	21.7	6.410
2	232	e	e	350	0.53	300	12	0	16.1	7.6	3.82E-10	21.5	6.497
3	331	e	e	350	0.69	300	12	0	16.2	5.0	1.10E-10	21.4	6.544
4	474	e	e	350	0.70	1,000	12	0	16.3	4.9	5.84E-11	21.3	6.571
5	570	e	e	350	0.70	12	12	3600	16.5	5.0	1.51E-10	21.2	6.622
6	695	e	e	350	0.70	12	12	3600	21.8	6.5	2.46E-10	21.0	6.748
7	835	e	e	350	1.00	-	-	-	22.7	-	2.56E-10	20.7	6.883

[a]Type 316 SS Heat C21, irradiated to 0.3 x 10^{21} n/cm^2 (0.45 dpa) at ≈288°C.
[b]Represents values in the effluent. Conductivity and DO were ≈0.07 µS/cm and 500 ppb, respectively, in the feedwater.
[c]Based on effective flow stress, defined as the average of irradiated and nonirradiated flow stresses.
[d]Actual crack extension was 23% greater than the value determined from the DC potential drop measurements.
[e]ECP not measured, the ECP cell was damaged due to a power bump at 162 h. The test was restarted and experimental conditions were restored; there was no chloride intrusion during the interruption.

(a)
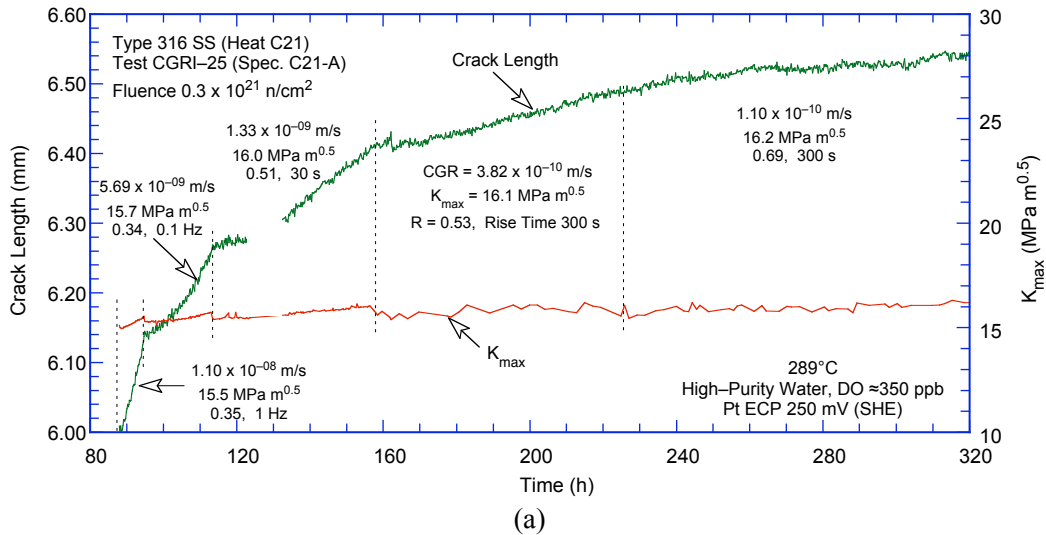
Figure 10. Crack-length-vs.-time plot for Type 316 SS in BWR water at 288°C during test periods (a) precracking-3, (b) 4-5, and (c) 6-7.

20
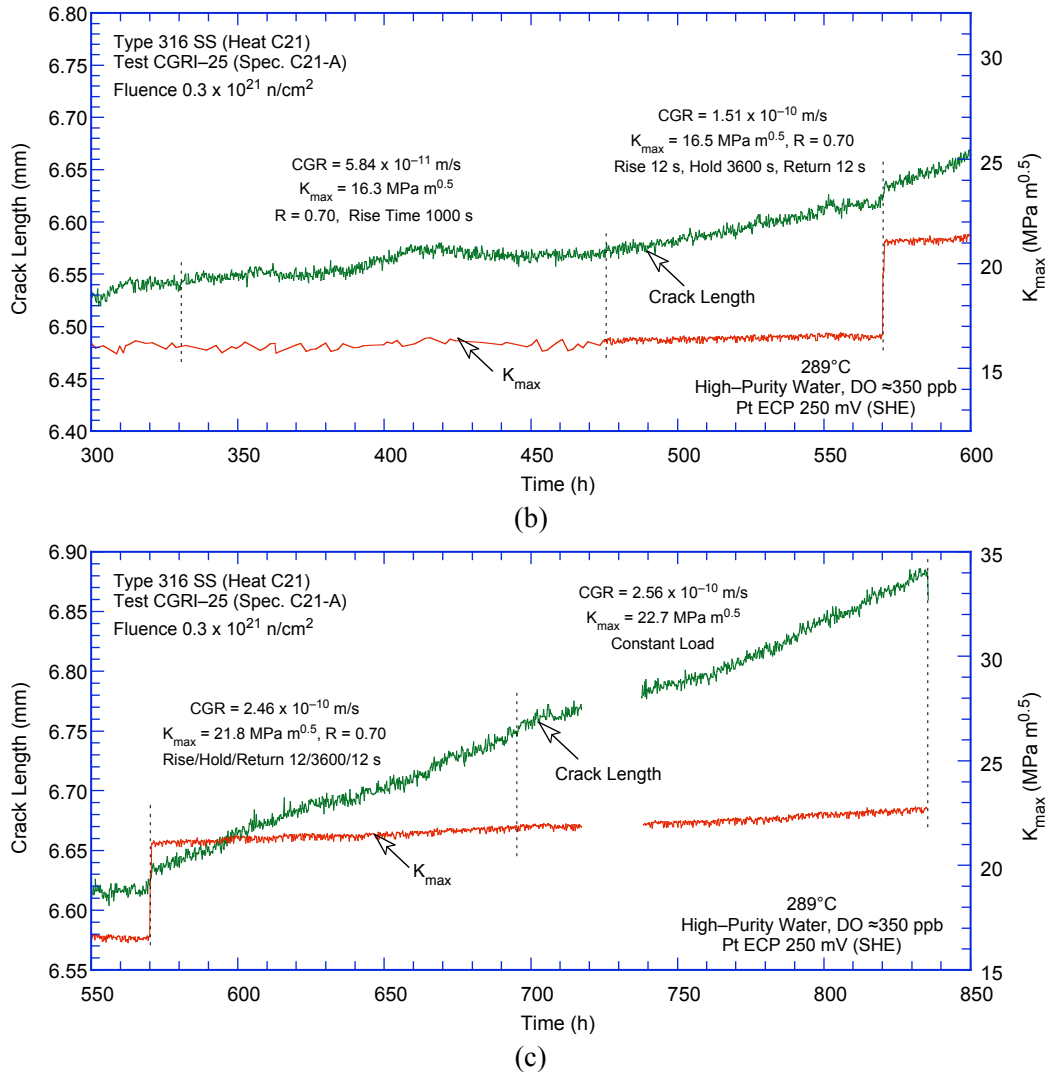
Figure 10.   (Contd.)

3.1.2   Specimen C21-B of Type 316 SS, Test CGRI-24

The test on Specimen C21-B of Type 316 SS irradiated to 1.35 dpa was started in high-purity water with ≈350 ppb DO and a flow rate of ≈34 mL/min. The specimen was fatigue precracked at R = 0.33, K_{max} = 15.9 MPa m$^{1/2}$, triangular waveform, and 1-Hz frequency. Initially, the crack length data were lost for about 24 h because of a malfunction in the DC potential drop system. After ≈0.3-mm crack advance, R was increased incrementally to 0.7, and the waveform was changed to a slow/fast sawtooth with rise times of 300 or 1000 s and a return time of 12 s.

At ≈245 h the DO level in the feedwater was decreased from ≈350 ppb to <30 ppb by purging the feedwater tank with a mixture of N_2 + 5% H_2. The change in crack length and ECP of the Pt and SS electrodes during the transient period is shown in Fig. 11. The ECP of the Pt electrode decreased to below -450 mV (SHE) within 3-4 h, while the ECP of the SS electrode took nearly 20 h to decrease to -200 mV (SHE), although it eventually decreased to less than -400 mV. Crack growth rates dropped significantly in the low DO environment. The test was terminated after 557 h.

21
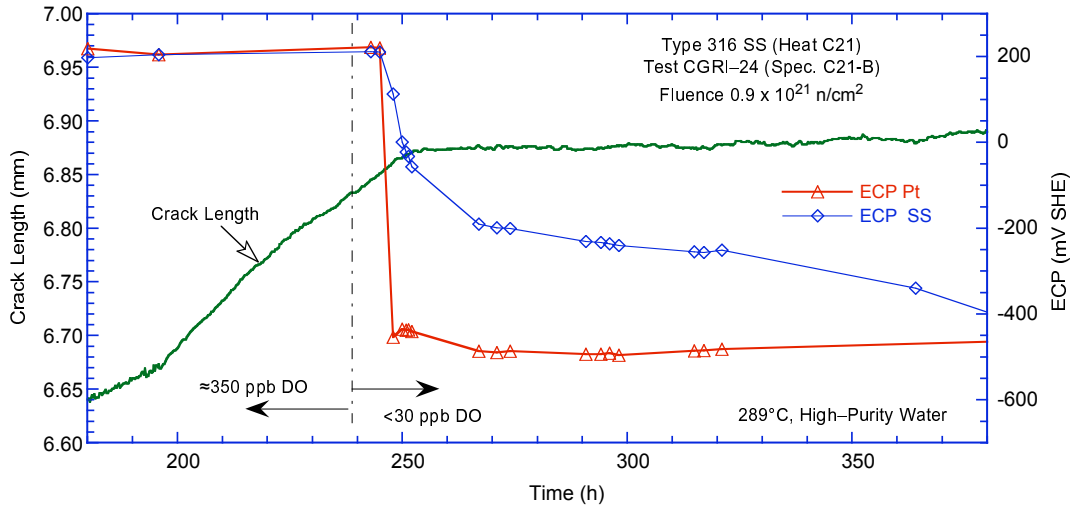
Figure 11. Change in crack length and ECP of Pt and SS electrodes during test periods 5-6 and the intermediate transition period.

After the CGR test, the final crack front was marked by fatigue cycling at room temperature in air. The specimen was then fractured; a photograph of the fracture surface is shown in Fig. 12. The final crack length, measured from the photograph, showed good agreement with the values estimated from the DC potential drop measurements; the difference in measured and estimated crack lengths was <5%. The environmental and loading conditions, corrected CGRs, and the allowed K_{max} based on the K/size criterion are given in Table 5; the changes in crack length, CGR, and K_{max} with time during the various test periods are plotted in Fig. 13. For this specimen, the K/size criterion was satisfied for all loading conditions.
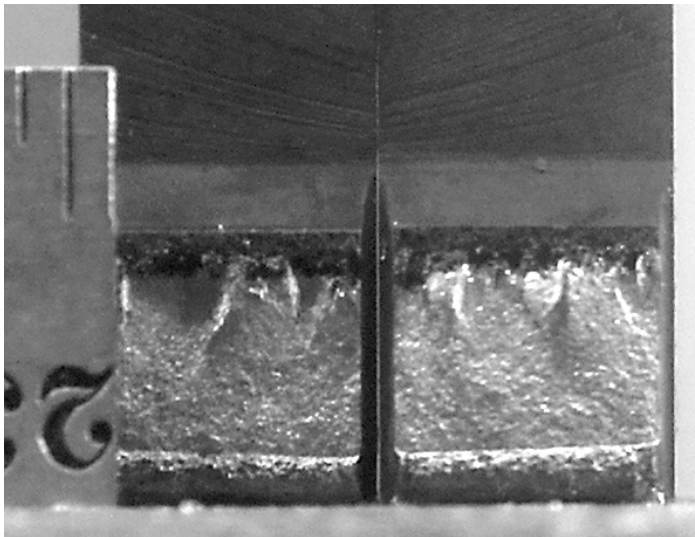
Figure 12.
Photomicrographs of the fracture surface of Specimen C21-B.

22

Table 5.   Test conditions and results for Specimen C21-B[a] of Type 316 SS in BWR water at 289°C.

Test Period	Test Time, h	ECP[b] mV (SHE) Pt	ECP[b] mV (SHE) Steel	O$_2$ Conc.,[b] ppb	R Load Ratio	Rise Time, s	Return Time, s	Hold Time, s	K_{max}, MPa m$^{1/2}$	ΔK, MPa m$^{1/2}$	Growth Rate, m/s	Allowed K_{max},[c] MPa m$^{1/2}$	Crack Length,[d] mm
													6.000
Pre	7	-	-	350	0.33	0.5	0.5	0	15.9	10.6	2.63E-08	21.9	6.312
1[e]	24	268	151	350	0.52	300	12	0	-	-	-	-	-
2a[e]	30	267	166	350	0.50	12	2	0	-	-	-	-	-
2b	77	231	185	350	0.50	300	12	0	16.0	8.0	5.85E-10	21.7	6.458
3	124	221	191	350	0.71	300	12	0	16.3	4.7	5.40E-10	21.5	6.551
4	196	204	204	350	0.70	1000	12	0	16.2	4.9	4.91E-10	21.2	6.670
5	255	221	211	350	1.00	-	-	0	16.2	-	9.67E-10	20.8	6.872
6	395	-485	-452	<30	1.00	-	-	0	16.3	-	3.32E-11	20.8	6.889
7	557	-512	-551	<30	1.00	-	-	0	19.6	-	1.24E-11	20.8	6.914

[a]Type 316 SS Heat C21, irradiated to 0.9 x 10^{21} n/cm^2 (1.35 dpa) at ≈288°C.
[b]Represents values in the effluent. Conductivity was ≈0.07 μS/cm in the feedwater.
[c]Based on effective yield stress, defined as the average of irradiated and nonirradiated yield stresses.
[d]The difference between the measured crack extension and that determined from the DC potential drop measurements was <5%.
[e]Crack length could not be determined because of a malfunction in the DC potential system.

(a)

(b)
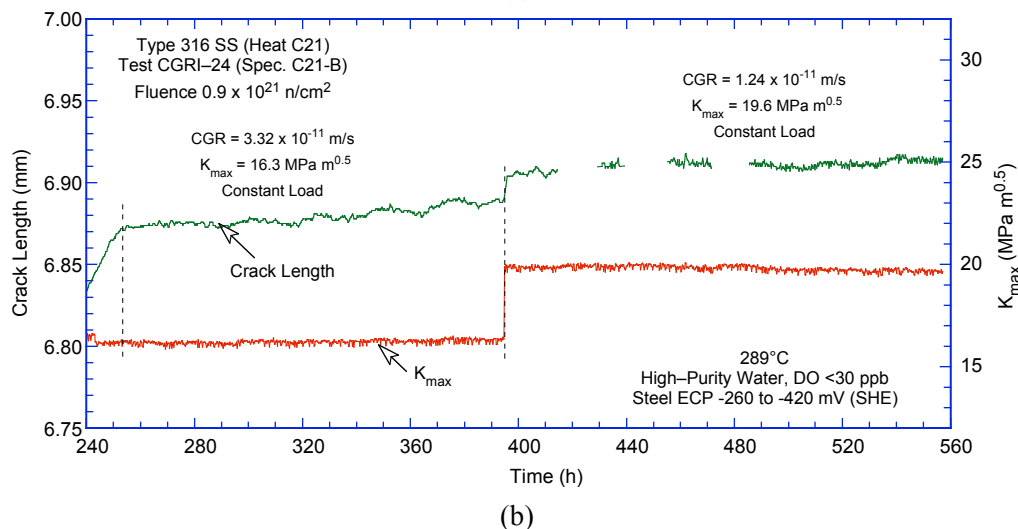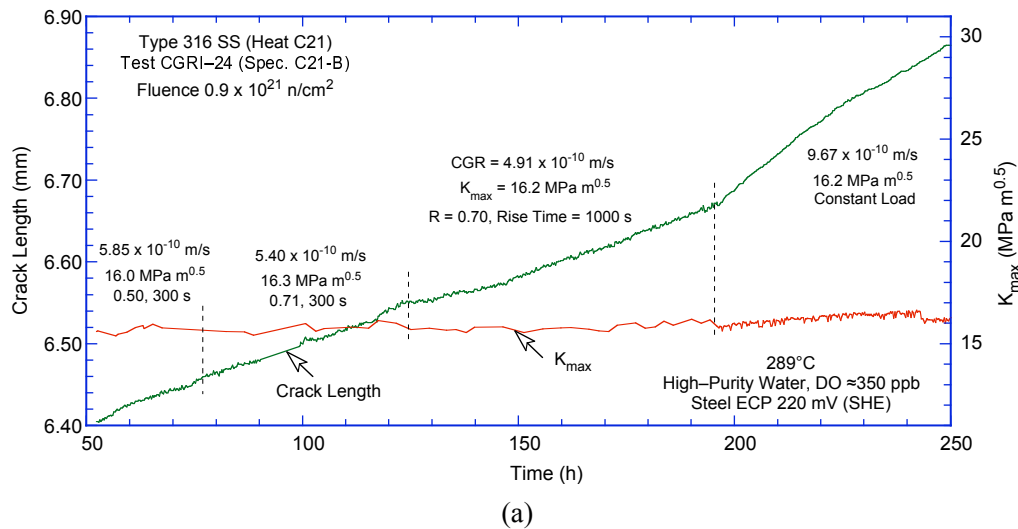
Figure 13.   Crack-length-vs.-time plot for Type 316 SS in BWR water at 288°C during test periods (a) precraking-5 and (b) 6-7.

3.1.3   Specimen C21-C of Type 316 SS, Test CGRI-26

The test on Specimen C21-C of Type 316 SS irradiated to 3.0 dpa was started in high-purity water with ≈500 ppb DO and a flow rate of 27 mL/min. The specimen was fatigue precracked at R = 0.33, K_{max} = 15.5 MPa m$^{1/2}$, triangular waveform, and 1-Hz frequency. After ≈0.4-mm crack advance, R was increased incrementally to 0.7, and the waveform was changed to a slow/fast sawtooth with rise times of 30-1000 s. Finally, the specimen was subjected to a constant load. At 450 h, the CGR increased rapidly by a factor of ≈6 (Fig. 14b); considering that the applied K_{max} for the test period may have exceeded the specimen size criterion, the test was terminated at 510 h.

The DO level in the effluent was decreased after 96 h from ≈500 ppb to <20 ppb, then at 192 h it was increased to ≈450 ppb, and finally at 318 h it was again decreased below 20 ppb. The change in crack length and ECP of the Pt and SS electrodes during the transient periods is shown in Fig. 14. During the first change, the ECP of the Pt electrode decreased to below -450 mV (SHE) rather rapidly while the ECP of the SS electrode took nearly a day to decrease below -200 mV (SHE); it eventually decreased to about -400 mV. The CGR decreased significantly in the low-DO water (Fig. 14a); the change in CGR is abrupt and appears to have occurred when the ECP of the SS electrode decreased to about -200 mV. Similarly, when the DO content was increased from <20 ppb to ≈400 ppb, although the ECP of the Pt

(a)

(b)
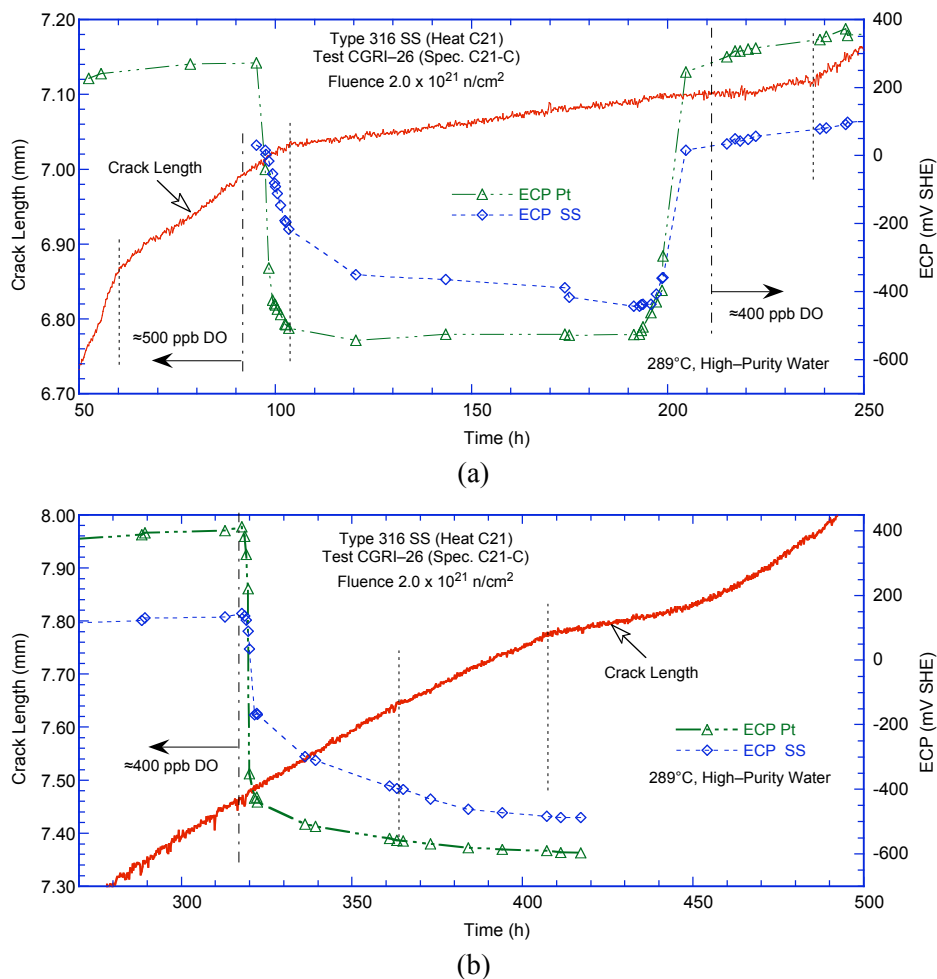
Figure 14.   Change in crack length and ECP of Pt and SS electrodes during test periods (a) 3-5 and (b) 7-9.

24

electrode had increased above 250 mV at ≈200 h, the CGR increased at 238 h when the ECP of the SS electrode increased above ≈100 mV (Fig. 14a).

The crack growth behavior during the second decrease in the DO level at 318 h (Fig. 14b) was different from that during the first decrease in DO level. The CGR did not decrease for nearly 100 h, even after the SS ECP had decreased below -400 mV (SHE). The reason for the different behavior during the second decrease in the DO level is not clear. The applied K_{max} during the change in DO (from ≈270-360 h) was 23.6-24.9 MPa m$^{1/2}$, which is equal to or marginally above the value allowed by the K/size criterion based on effective flow stress. To ensure compliance with the K/size criterion, K_{max} was gradually decreased from ≈25.0 to 20.0 MPa m$^{1/2}$. The CGR decreased for about a day (Fig. 14b) and then increased back to approximately the growth rate prior to the decrease in K_{max}.

After the test the final crack size was marked by fatigue cycling in air at room temperature. The specimen was then fractured; a photograph of the fracture surfaces is shown in Fig. 15. The final crack length was ≈69% greater than the value determined from the DC potential measurements. The experimental crack extensions were scaled proportionately. The environmental and loading conditions, corrected CGRs, and allowed K_{max} based on the K/size criterion are given in Table 6; the changes in crack length, CGR, and K_{max} with time during the various test periods are plotted in Fig. 16.
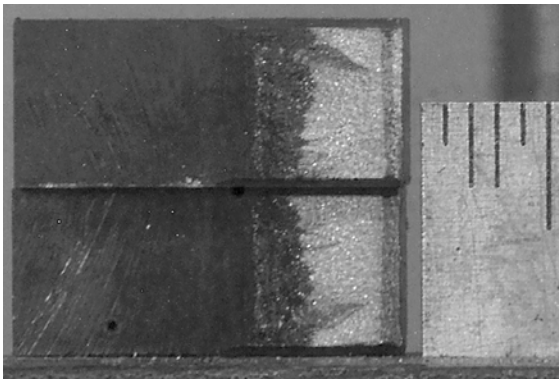
Figure 15.
Photograph of the fracture surfaces of the two halves of the fractured specimen C21-C.

Table 6. Test conditions and results for Specimen C21-C[a] of Type 316 SS in BWR water at 289°C.

Test Period	Test Time, h	ECP[b] mV (SHE) Pt	ECP[b] mV (SHE) Steel	O_2 Conc.,[b] ppb	R Load Ratio	Rise Time, s	Return Time, s	Hold Time, s	K_{max}, MPa m$^{1/2}$	ΔK, MPa m$^{1/2}$	Growth Rate, m/s	Allowed K_{max},[c] MPa m$^{1/2}$	Crack Length,[d] mm
													6.000
Pre	7	e	e	500	0.33	0.5	0.5	0	15.5	10.4	4.87E-08	27.7	6.404
1	29	249	e	500	0.52	30	5	0	15.7	7.5	3.12E-09	27.4	6.528
2	48	227	e	500	0.51	300	4	0	16.5	8.1	2.84E-09	26.9	6.708
3	56	241	e	500	0.71	1000	12	0	17.0	4.9	3.22E-09	26.7	6.797
4	103	241	e	500	1.00	-	-	-	17.6	-	1.06E-09	26.1	7.025
5	237	-507	-216	<30	1.00	-	-	-	17.9	-	1.77E-10	25.9	7.116
6	266	379	114	450	1.00	-	-	-	18.1	-	9.18E-10	25.6	7.212
7	321	328	124	450	1.00	-	-	-	23.6	-	1.21E-09	24.9	7.480
8	360	-551	-389	<30	1.00	-	-	-	24.9	-	1.06E-09	24.5	7.631
9a	409	-590	-483	<30	1.00	-	-	-	23.3[f]	-	7.85E-10	24.1	7.774
9b	442	-596	-487	<30	1.00	-	-	-	20.8[f]	-	3.12E-10	23.9	7.814
9c	506	-	-	<30	1.00	-	-	-	22.1	-	1.80E-09	23.1	8.097

[a]Type 316 SS Heat C21, irradiated to 2.0 x 10^{21} n/cm^2 (3.0 dpa) at ≈288°C.
[b]Represents values in the effluent. Conductivity and DO were ≈0.07 µS/cm and 600 ppb, respectively, in the feedwater.
[c]Based on effective yield stress, defined as the average of irradiated and nonirradiated yield stresses.
[d]Actual crack extension was 69% greater than the value determined from the DC potential drop measurements.
[e]Not measured.
[f]K_{max} was decreased during the test period; the listed value represents the average value for the period.

25
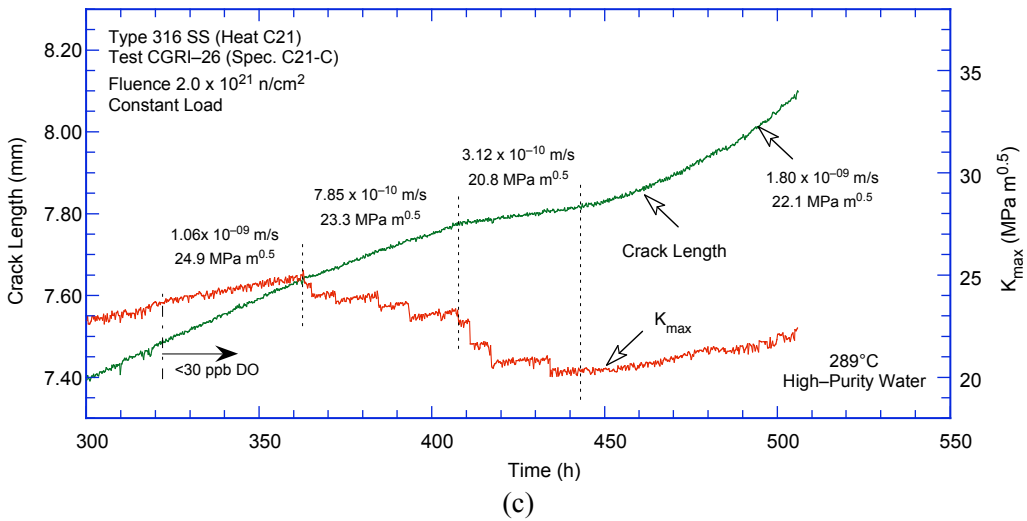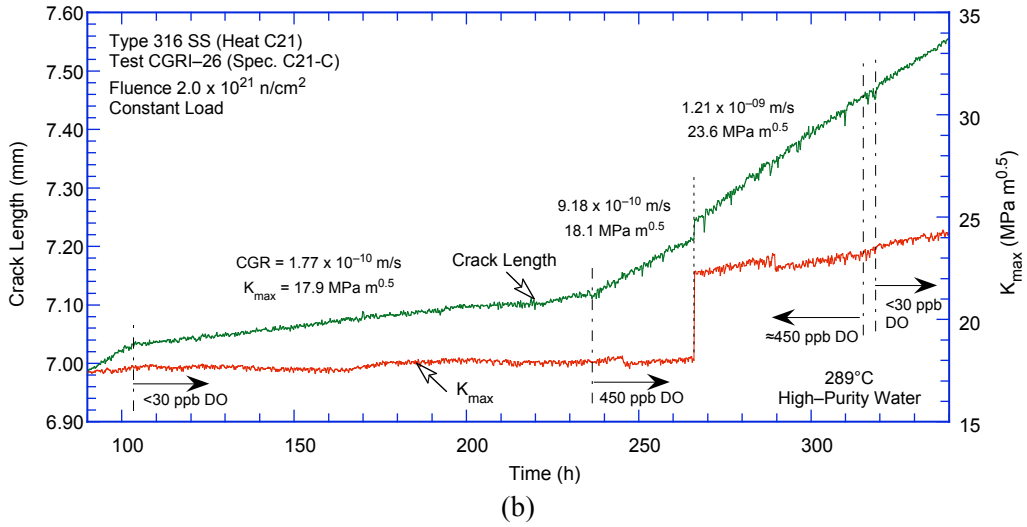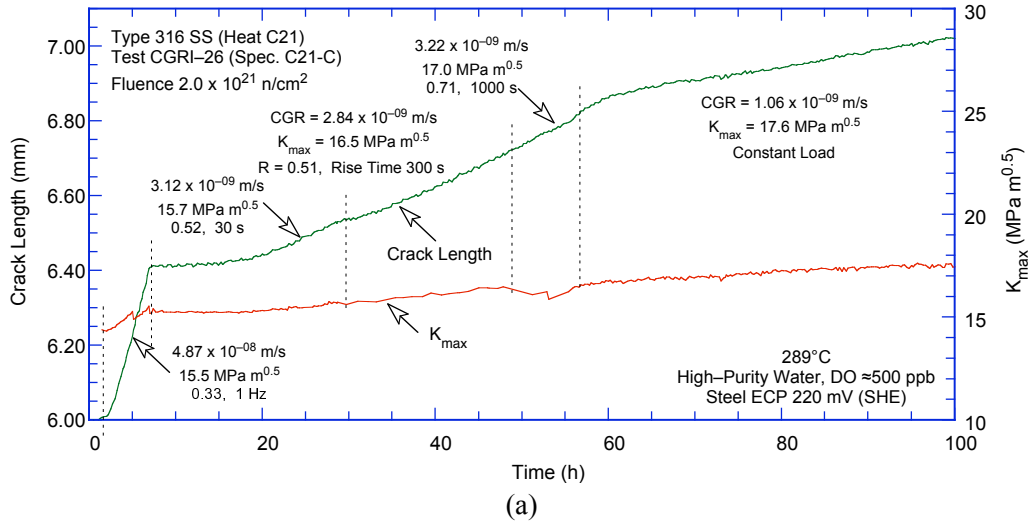
Figure 16. Crack-length-vs.-time plot for Type 316 SS in BWR water at 288°C during test periods (a) precracking-3, (b) 4-7, and (c) 8-9.

3.1.4   Specimen 85-3TT of Sensitized Type 304 SS, Test CGRI JR-31

The test on Specimen 85-3TT of sensitized Type 304 SS (Heat 10285) irradiated to 2.16 dpa was started in high-purity water with 300-350 ppb DO and a flow rate of 22 mL/min. The frictional load was measured to be ±156 N (±35 lb); the results presented here have been corrected to account for this frictional load.   Fatigue precracking was carried out at R ≈ 0.42, K_{max} ≈ 14.9 MPa m$^{1/2}$, triangular waveform, and frequency of 1 Hz. After ≈0.1-mm crack extension, to transition the TG fatigue crack to an IG crack, the loading waveform was changed to a sawtooth, and the load ratio was increased to 0.7 with rise times of 30-1000 s and return times of 4 or 12 s. Finally, the specimen was subjected to a constant load (K_{max} = 15.7 MPa m$^{1/2}$) to obtain the SCC growth rate.

After the CGR test, the DC potential measuring system was reinitialized, and a J-R test was performed on the specimen at 289°C in high-DO water (≈350 ppb DO). The test was conducted at a constant extension rate of ≈0.43 μm/s (0.017 mil/s). The test was interrupted periodically to measure the crack length by the DC potential drop measurements. The measured load vs. extension curve and the load vs. load-line displacement curve for Specimen 85-3TT are shown in Fig 17.
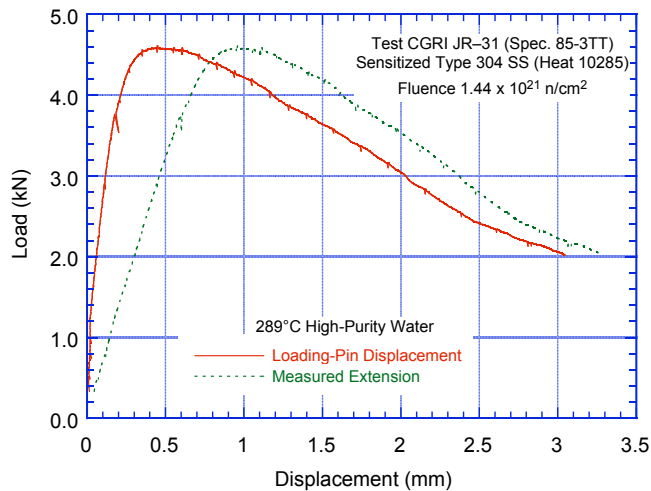
Figure 17.

Load vs. load-line displacement curve for sensitized Type 304 SS tested in high-purity water at 289°C.

The final crack size was marked by fatigue cycling at room temperature. The specimen was then fractured; a photograph of the fracture surface is shown in Fig. 18. The actual crack extension, measured from a photograph, was ≈28% greater than the value determined from the DC potential measurements. Crack extensions estimated from the DC potential method were adjusted accordingly. The results for the test, including the allowed K_{max} from the K/size criterion, are given in Table 7; the changes in crack length, CGR, and K_{max} with time are given in Fig. 19.

The DC potential data during the J-R curve test were also corrected to account for the effects of plasticity on the measured potential. The fracture toughness J-R curve for Specimen 85-3TT in high-DO water is shown in Fig. 20; the actual data for the J-R curve test are given in Appendix B, Table B5. The results yield a J_{Ic} value of 176 kJ/m^2.

27
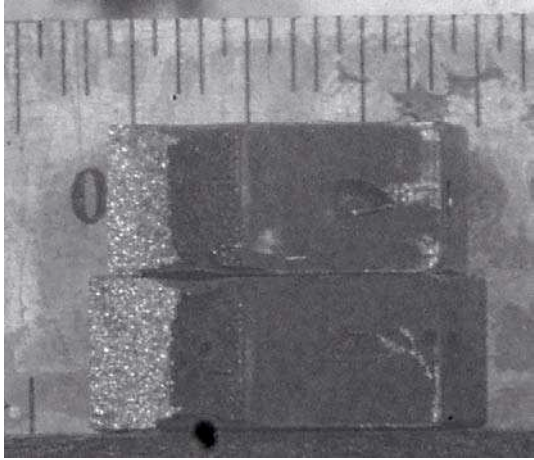
Figure 18.
Photograph of the fracture surface of for sensitized Type 304 SS tested in high-purity water at 289°C.

Table 7. Test conditions and results for Specimen 85-3TT of sensitized Type 304 SS in high-purity water[a] at 289°C.

Test Period	Test Time, h	ECP[b] mV (SHE) Pt	ECP[b] mV (SHE) Steel	O_2 Conc.,[b] ppb	R Load Ratio	Rise Time, s	Return Time, s	Hold Time, s	K_{max}, MPa m$^{1/2}$	ΔK, MPa m$^{1/2}$	Growth Rate, m/s	Allowed K_{max},[c] MPa m$^{1/2}$	Crack Length,[d] mm
													5.812
Pre	29	-	-	500	0.42	0.33	0.33	0.17/0.17	14.9	8.7	1.64E-08	20.4	5.911
1	93	200	218	500	0.74	142	5.7	158/6.3	15.3	4.0	1.02E-09	20.3	5.986
2	102	196	e	500	0.75	13.7	1.8	16.3/2.2	15.4	3.8	3.16E-09	20.2	6.027
3	195	e	e	500	0.95	140	1.7	860/10.3	15.7	0.7	2.22E-10	20.1	6.098
4	285	e	e	500	1.00	-	-	-	15.7	-	1.97E-10	20.0	6.161

[a]Type 304 SS Heat 10285, sensitized 10.5 h at 600°C, irradiated to 1.44 x 10^{21} n/cm^2 (2.16 dpa) at ≈297°C.
[b]Represents values in the effluent. Conductivity was ≈0.07 and 0.3 μS/cm in feedwater and effluent, respectively.
[c]Based on effective yield stress, defined as the average of irradiated and nonirradiated yield stresses.
[d]Actual crack extension was 28% greater than the value determined from the DC potential drop measurements.
[e]Not measured.
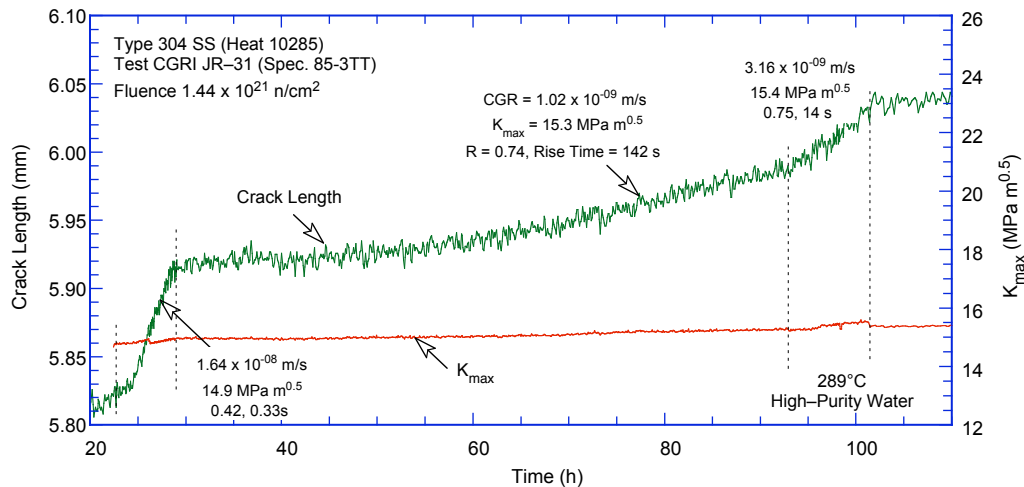
(a)

Figure 19. Crack-length-vs.-time plots for sensitized and irradiated Type 304 SS in high-purity water at 289°C during test periods (a) precracking-2 and (b) 3-4.
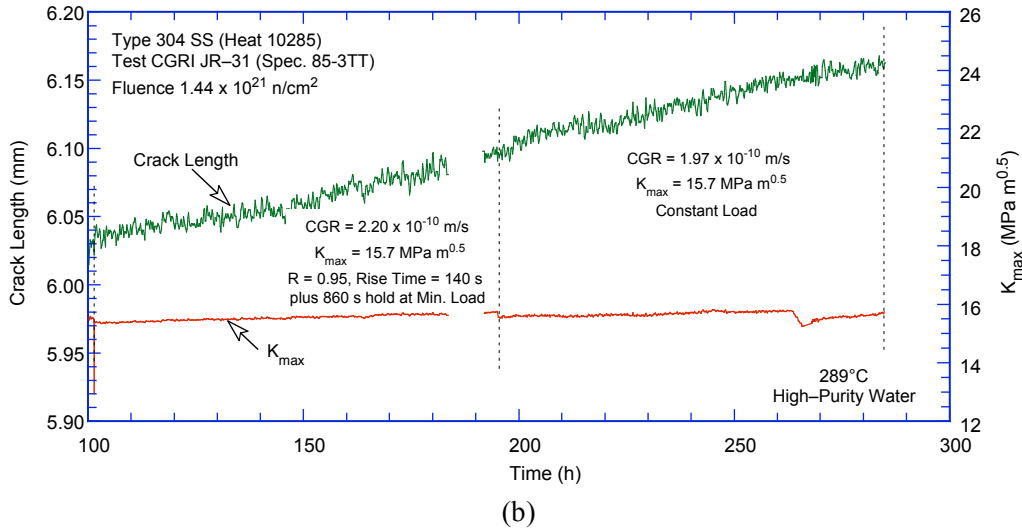
Figure 19. (Contd.)
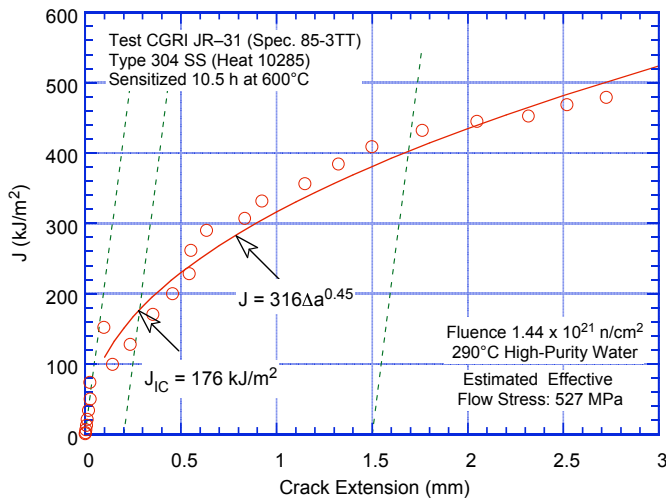
Figure 20.
Fracture toughness J-R curve for sensitized Type 304 SS irradiated to 2.16 dpa in high-DO water at 289°C.

3.2 Stainless Steel Weld HAZ Materials

Crack growth and fracture toughness J-R curve tests have been completed in air and simulated BWR environments at 289°C on 1/4-T CT specimens of Types 304 and 304L SS weld HAZ materials irradiated to ≈2.16 dpa. The significant results for the various tests are summarized below.

3.2.1   Simulated BWR Environment

3.2.1.1   Specimen 85-XA of Type 304 SS SMA Weld HAZ, Test CGRI JR-32

The test on Specimen 85-XA of Type 304 SS (Heat 10285) SMA weld HAZ irradiated to 2.16 dpa was started in high-purity water with ≈400 ppb DO and a flow rate of 21 mL/min. The frictional load was measured to be ±156 N (±35 lb); the results presented here have been corrected to account for this frictional load.   Fatigue precracking was carried out at R = 0.42, K_{max} = 13.3 MPa m$^{1/2}$, triangular waveform, and frequency of 2 Hz. After ≈0.11-mm crack extension, to transition the TG fatigue crack to an IG crack, the load ratio R was increased to ≈0.73, and the waveform changed from triangular to

sawtooth with rise times of 26 or 433 s and return times of ≈5 s. Finally, the specimen was subjected to a constant load (K_{max} ≈14.0 MPa m$^{1/2}$) to obtain the SCC growth rate.

After the CGR test, the DC potential measuring system was reinitialized, and a J-R test was performed on the specimen at 289°C in high-DO water (≈400 ppb DO). The test was conducted at a constant extension rate of ≈0.43 μm/s (0.017 mil/s). The test was interrupted periodically to measure crack length by the DC potential drop measurements. The measured load vs. extension curve and the load vs. load-line displacement curve for Specimen 85-XA are shown in Fig. 21.
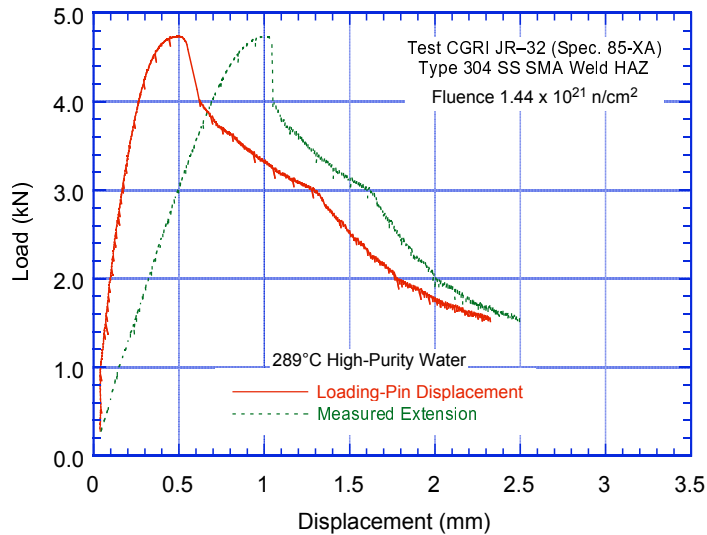
Figure 21.
Load vs. load-line displacement curve for Type 304 SS SMA weld HAZ tested in high-purity water at 289°C.

The final crack size was marked by fatigue cycling at room temperature. The specimen was then fractured, and the final crack length of both halves of the fractured specimen was measured from the photograph of the fracture surface of Specimen 85-XA (Fig. 22). The actual crack extension was ≈16% greater than the value determined from the DC potential measurements. Crack extensions estimated from the DC potential method were adjusted accordingly. The results for the CGR test, including the allowed K_{max} from the K/size criterion, are given in Table 8; the changes in crack length, CGR, and K_{max} with time are given in Fig. 23.
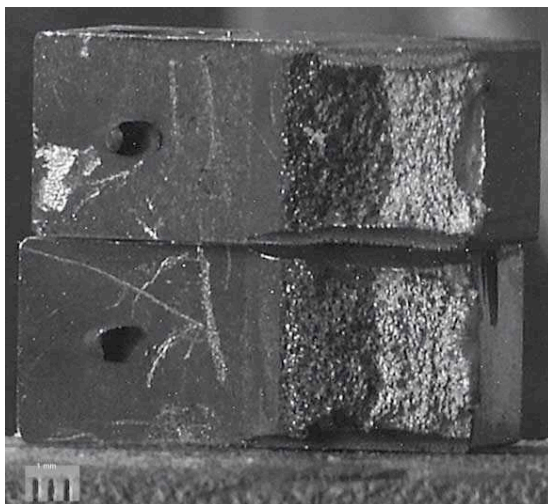
Figure 22.
Photograph of the fracture surface of Type 304 SS SMA weld HAZ tested in high-purity water at 289°C.

30

Table 8. Test conditions and results for Specimen 85-XA of Type 304 SS SMA weld HAZ in high-purity water[a] at 289°C.

Test Period	Test Time, h	ECP[b] mV (SHE) Pt	ECP[b] mV (SHE) Steel	O_2 Conc.,[b] ppb	R Load Ratio	Rise Time, s	Return Time, s	Hold Time, s	K_{max}, MPa m$^{1/2}$	ΔK, MPa m$^{1/2}$	Growth Rate, m/s	Allowed K_{max},[c] MPa m$^{1/2}$	Crack Length,[d] mm
													5.809
Pre	51	e	205	500	0.42	0.16	0.16	0.09/0.09	13.3	7.7	1.86E-08	20.3	5.920
1	93	e	240	500	0.74	26	5.2	34/6.8	13.9	3.6	2.21E-09	20.2	6.006
2	140	e	236	500	0.72	433	5.2	567/6.8	13.0	3.6	7.07E-10	20.1	6.061
3	190	e	235	500	1.00	-	-	-	13.9	-	1.98E-10	20.0	6.132
4	331	e	210	500	1.00	-	-	-	14.0	-	2.61E-10	19.8	6.263

[a]Type 304 SS Heat 10285, SMA weld HAZ irradiated to 1.44 x 10^{21} n/cm^2 (2.16 dpa) at ≈297°C.
[b]Represents values in the effluent. Conductivity was ≈0.07 and 0.3 µS/cm in feedwater and effluent, respectively.
[c]Based on effective yield stress, defined as the average of irradiated and nonirradiated yield stresses.
[d]Actual crack extension was 16% greater than the value determined from the DC potential drop measurements.
[e]Not measured.

(a)

(b)
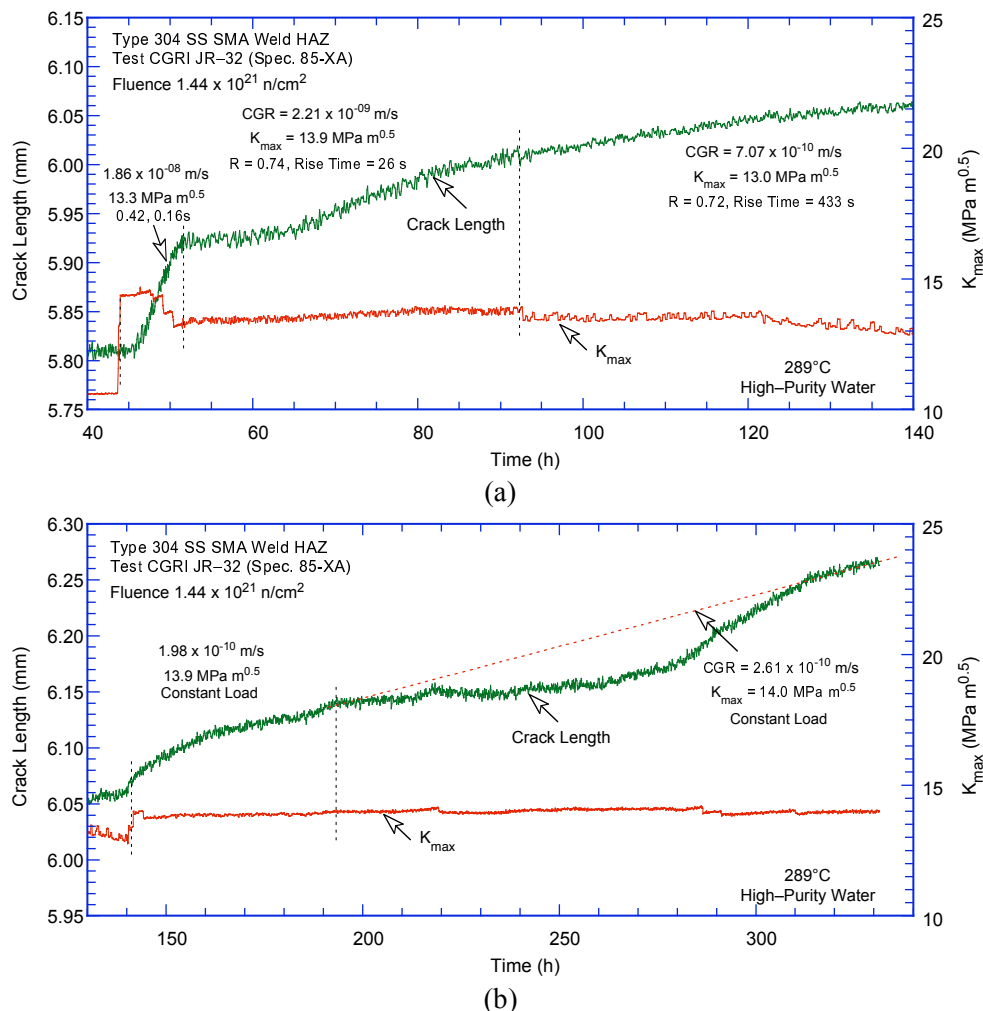
Figure 23. Crack-length-vs.-time plots for irradiated Type 304 SS SMA weld HAZ (Spec. 85-XA) in high-purity water at 289°C during test periods (a) precracking-2 and (b) 3-4.

The DC potential data during the J-R curve test were also corrected to account for the effects of plasticity on the measured potential. The fracture toughness J-R curve for Specimen 85-XA in high-DO

water is shown in Fig. 24; the actual data for the J-R curve test are given in Appendix B, Table B6. The results yield a J_{Ic} value of 128 kJ/m^2.

The results indicate that the fracture toughness of the SMA weld HAZ material is significantly lower than that of the sensitized material from the same heat of Type 304 SS (e.g., compare J-R curve for Specimen 85-3TT in Fig. 20). However, examination of the fracture surface through the hot cell window by telescope indicated that the fracture surface might not have been in the HAZ of the specimen. The fracture plane might have moved away from the HAZ region and into the weld metal, as indicated by Fig. 25. The sharp drop in load (Fig. 21) most likely is associated with this change in the fracture plane.
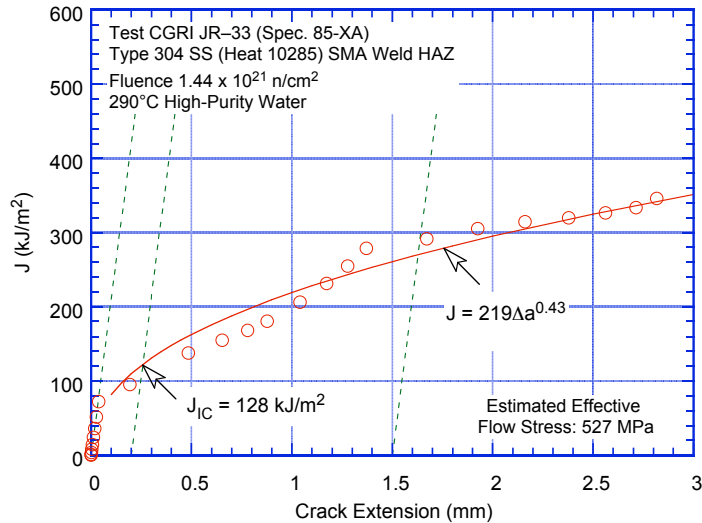
Figure 24.
Fracture toughness J-R curve for Type 304 SS SMA weld irradiated to 2.16 dpa in high-DO water at 289°C.
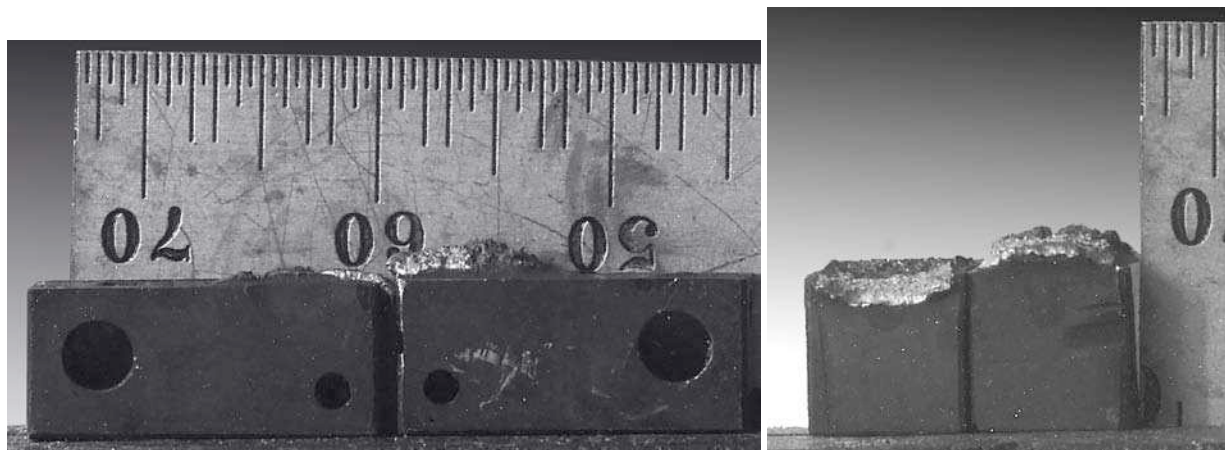
Figure 25.   Fracture pieces of Type 304 SS SMA weld HAZ: (a) side view and (b) end view.

3.2.1.2   Specimen GG6T-A of Type 304L SS SA Weld HAZ, Test CGRI JR-35

The test on Specimen GG6T-A of the GG Type 304L SA weld HAZ irradiated to 2.16 dpa was started in high-purity water with ≈600 ppb DO and a flow rate of 20 mL/min. The measured frictional load on the pull rod was ±133 N (±30 lb) during the test; the results presented here have been corrected to account for this frictional load. Fatigue precracking was carried out at R = 0.26, K_{max} ≈ 15.2 MPa m$^{1/2}$, triangular waveform, and 2-Hz frequency. After ≈0.26-mm crack extension, to transition the TG fatigue crack to an IG crack, the loading waveform was changed to sawtooth with a load ratio of ≈0.5, a rise time

of 38 s, and a return time of 2.5 s. However, the crack actually stalled under these loading conditions, and no crack growth was observed even after ≈3 days. The above steps were repeated but with one difference, the rise time was increased gradually. Environmental enhancement was achieved during test period 2. Finally, the specimen was subjected to a constant load (four conditions with decreasing load corresponding to K_{max} = 16.0, 13.6, 10.9, and 7.0 MPa m$^{1/2}$) to obtain the SCC growth rates. The CGR test was terminated after ≈580 h.

After the CGR test, the DC potential measuring system was reinitialized, and a J-R test was performed on the specimen at 289°C in high-DO water (≈600 ppb DO). The test was conducted at a constant extension rate of ≈0.43 μm/s (0.017 mil/s). The test was interrupted periodically (by holding the specimen at constant extension) to measure crack length by the DC potential drop measurements. The load vs. extension curve and the load vs. load-line displacement curve for Specimen GG6T-A are shown in Fig. 26.
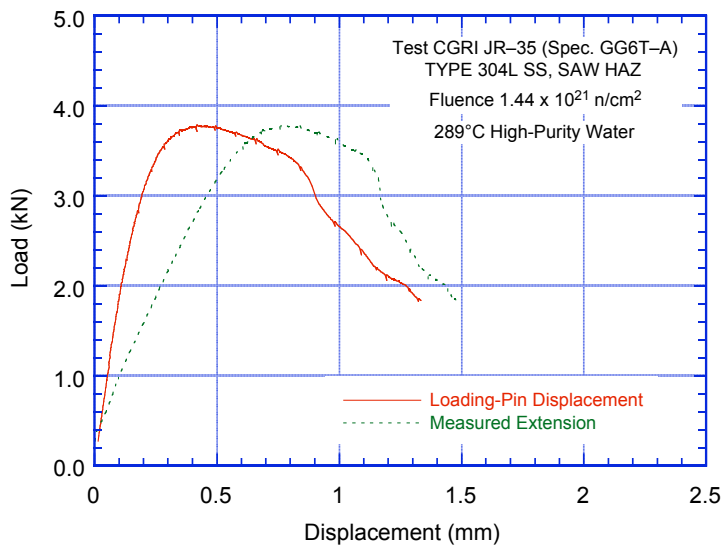
Figure 26.
Load vs. load-line displacement curve for Type 304L SS SA weld HAZ tested in high-purity water at 289°C.

The final crack size was marked by fatigue cycling at room temperature. The specimen was then fractured, and the final crack length was measured from photographs of the fracture surface of both halves of the fractured specimen (Fig. 27a). The actual crack extension was ≈30% greater than the value determined from the DC potential measurements; the measured crack extensions were scaled proportionately. The side view of the two broken halves of the specimen, Fig. 27b, indicates a relatively straight crack plane. The results for the CGR test, including the allowed K_{max} from the K/size criterion, are given in Table 9; the changes in crack length, CGR, and K_{max} with time are given in Fig. 28.
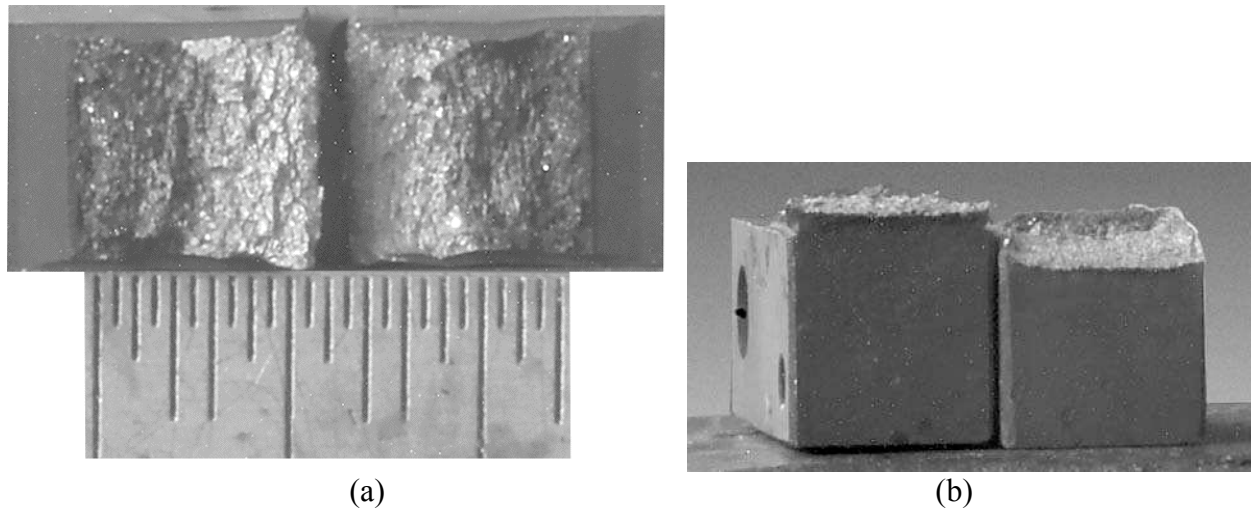
Figure 27. Photographs of the (a) fracture surface and (b) end view of Type 304L SS SA weld HAZ.

Table 9. Test conditions and results for Type 304L SS SA weld HAZ specimen GG6T-A[a] in BWR water at 289°C.

Test Period	Test Time, h	ECP,[b] mV (SHE) Pt	ECP,[b] mV (SHE) Steel	O_2 Conc.,[b] ppb	R Load Ratio	Rise Time, s	Return Time, s	Hold Time,[c] s	K_{max}, MPa m$^{1/2}$	ΔK, MPa m$^{1/2}$	Growth Rate, m/s	Allowed K_{max},[d] MPa m$^{1/2}$	Crack Length,[e] mm
													5.827
Pre	8	233	232	600	0.26	0.18	0.18	0.07/0.07	15.2	11.3	4.54E-08	20.8	6.179
1a	71	229	230	600	0.53	38	2.5	22/1.5	15.0	7.1	no growth	20.8	6.178
1b	79	228	229	600	0.29	0.18	0.18	0.07/0.07	15.3	11.0	5.93E-10	20.8	6.185
1c	101	224	223	600	0.29	7.3	7.3	2.7/2.7	15.5	11.0	3.91E-10	20.7	6.194
2	127	222	223	600	0.57	7.4	2.5	4.6/1.5	15.4	6.6	1.44E-09	20.6	6.249
3	151	221	222	600	0.57	37	2.5	23/1.5	15.4	6.6	6.29E-10	20.6	6.279
4	195	219	220	600	0.67	168	6.7	132/5.3	16.2	5.4	7.85E-10	20.5	6.345
5	238	221	222	600	0.67	559	6.7	441/5.3	16.1	5.4	6.08E-10	20.4	6.398
6	288	222	223	600	1.00	–	–	–	16.0	-	4.17E-10	20.2	6.482
7	412	223	224	600	1.00	–	–	–	13.6	-	4.04E-10	20.0	6.595
8	507	217	218	600	1.00	–	–	–	10.9	-	5.78E-10	19.8	6.711
9	575	217	218	600	1.00	–	–	–	7.0	-	1.66E-10	19.7	6.747

[a]Grand Gulf Type 304L SS core shroud shell, SA weld HAZ irradiated to 1.44 x 10^{21} n/cm^2 (2.16 dpa) at ≈297°C.
[b]Represents values in the effluent. Conductivity and DO were ≈0.07 μS/cm and 800 ppb, respectively, in the feedwater.
[c]Hold periods at maximum load during the unloading cycle and at minimum load during the loading cycle.
[d]Based on effective yield stress, defined as the average of irradiated and nonirradiated yield stresses.
[e]Actual crack extension was 30% greater than the value determined from the DC potential drop measurements.

The DC potential data during the J-R curve test were also corrected to account for the effects of plasticity on the measured potential. The fracture toughness J-R curve for Specimen GG6T-A in high-DO water is shown in Fig. 29; the actual data for the J-R curve test are given in Appendix B, Table B7. The results yield a J_{Ic} value of 121 kJ/m^2.
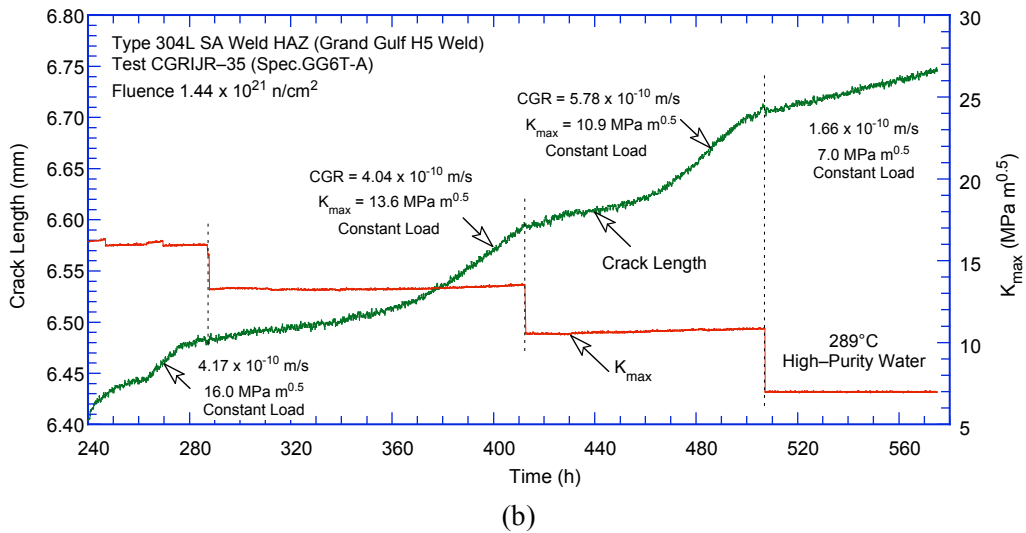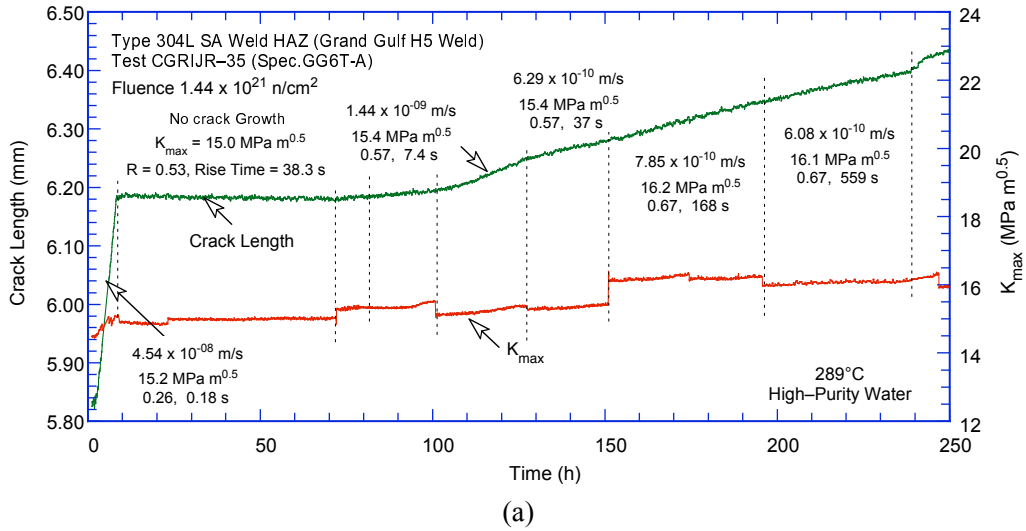
Figure 28. Crack-length-vs.-time plot for Type 304L SS SA weld HAZ in BWR water at 289°C for test periods (a) precracking-5 and (b) 6-9.
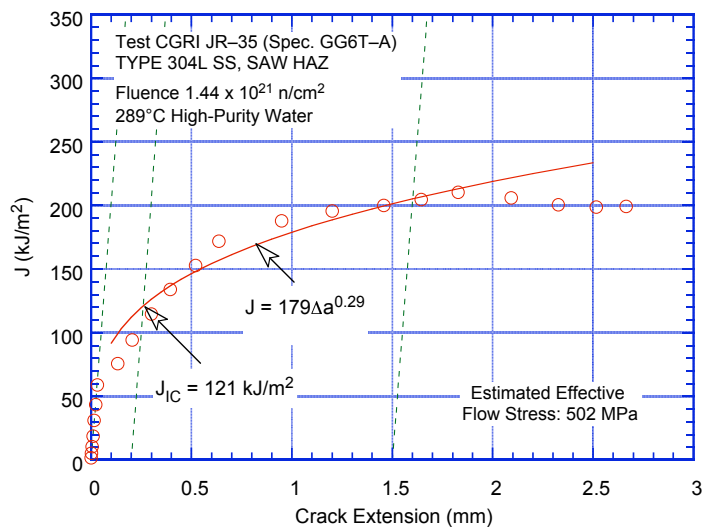
Figure 29. Fracture toughness J-R curve for Type 304L SS SA weld HAZ material in high-DO water at 289°C.

35

3.2.2   Air Environment

3.2.2.1   Specimen 85-XB of Type 304 SS SMA Weld HAZ, Test JRI-35

The test on Specimen 85-XB of Type 304 SS SMA weld HAZ irradiated to 2.16 dpa was initiated by fatigue precracking the specimen at R = 0.28, $K_{max} \approx 20.2$ MPa m$^{1/2}$, triangular waveform, and 2-Hz frequency in air at 289°C. As discussed in Section 2.3.1, because the autoclave, including the Bal-seal, was used as the test chamber for tests in air, the experimental data in air were also corrected for the frictional load between the pull rod and the Bal-seal. For this test, the frictional load was measured to be ±133 N (±30 lb); the results presented here have been corrected to account for this frictional load. After ≈0.31-mm crack advance, the waveform was changed to a slow/fast sawtooth, and CGRs were obtained at R = 0.3-0.5 and rise times = 5-50 s.

Fatigue loading was stopped after ≈0.7-mm crack extension, and a fracture toughness J-R curve test was performed on the specimen in air at 289°C. The test, conducted at a constant extension rate of ≈ 0.43 μm/s (0.017 mil/s), was interrupted periodically (by holding the specimen at constant extension) to measure crack length by the DC potential drop measurements. Unfortunately, a complete J-R curve could not be obtained for the specimen because of a large abrupt load drop (from 5.4 to <1.0 kN) at ≈0.5-mm load-line displacement. The crack advanced more than 3 mm during the load drop; the test was terminated. A sharp load drop, near the onset of crack extension, also occurred for a duplicate specimen of the same material tested in NWC BWR water. However, the crack extension was only ≈0.3 mm, and a stable crack extension was observed for the remainder of that test. The load vs. extension curve and the load vs. load-line displacement curve for Specimen 85-XB are shown in Fig. 30.
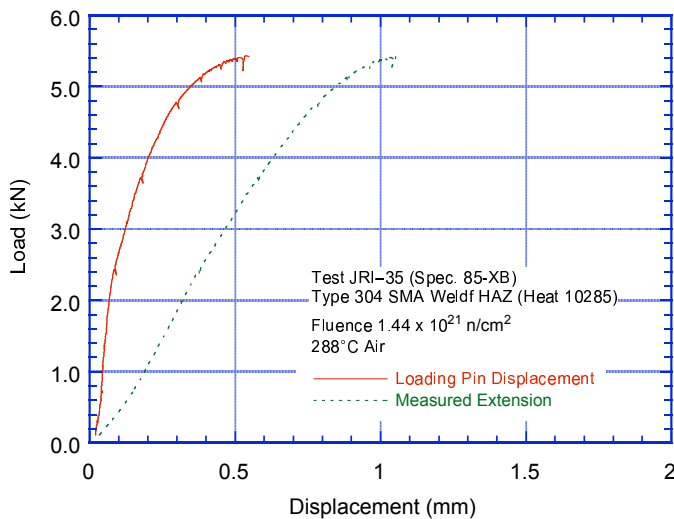
Figure 30.
Load vs. load-line displacement curve for Type 304 SS SMA weld HAZ tested in air at 289°C.

The specimen was then broken open, and crack extension during the CGR test and final crack length were measured from photographs of the fracture surface of the two broken halves (Fig. 31). The actual fatigue crack length was 25% greater than the values determined from the DC potential measurements; the measured crack extensions were scaled proportionately. The results for the CGR test, including the allowed K_{max} from the K/size criterion, are given in Table 10; the changes in crack length, CGR, and K_{max} with time are given in Fig. 32.

The side and end views of the two broken halves of the specimen are shown in Figs. 33 and 34, respectively. These photographs indicate that crack extension was along the normal plane during the

Figure 31.
Photograph of the fracture surface of the two halves of Type 304 SS SMA weld HAZ.

Table 10. Test conditions and results for Type 304 SMA weld HAZ specimen 85-XB[a] in air at 289°C.

Test Period	Test Time, h	R Load Ratio	Rise Time, s	Return Time, s	Hold Time,[b] s	K_{max}, MPa m$^{1/2}$	ΔK, MPa m$^{1/2}$	Growth Rate, m/s	Allowed K_{max}, MPa m$^{1/2}$	K_{max} - $K_{allowed}$,[c] %	Crack Length[d] mm
											5.747
Pre	3	0.28	0.20	0.20	0.05/0.05	20.2	14.6	8.15E-08	20.0	1	6.064
1c	23	0.55	40.8	8.2	19.2/3.8	18.7	8.5	2.23E-10	20.0	-6	6.094
2	47	0.44	4.4	0.72	1.6/0.28	19.8	11.0	2.83E-09	19.7	0	6.254
3	120	0.43	43.5	2.9	16.5/1.1	19.8	11.3	4.23E-10	19.6	1	6.338
4	143	0.39	8.8	2.9	3.2/1.1	19.8	12.1	2.60E-09	19.4	2	6.442

[a]Type 304 SS Heat 10285, SMA weld HAZ irradiated to 1.44 x 10^{21} n/cm^2 (2.16 dpa) at ≈297°C.
[b]Hold periods at maximum load during the unloading cycle and at minimum load during the loading cycle.
[c]Based on effective yield stress, defined as the average of irradiated and nonirradiated yield stresses.
[d]Actual crack extension was 25% greater than the value determined from the DC potential drop measurements.

fatigue crack growth test, but the abrupt 3-mm crack extension during the J-R curve test occurred away from the normal plane, particularly near the specimen sides. It is not clear whether the crack extended into the weld metal or base metal. Also, because the crack plane moved considerably away from the normal plane and away from the side groove, the specimen fractured along a plane nearly 2 mm away from the side groove.

(a)
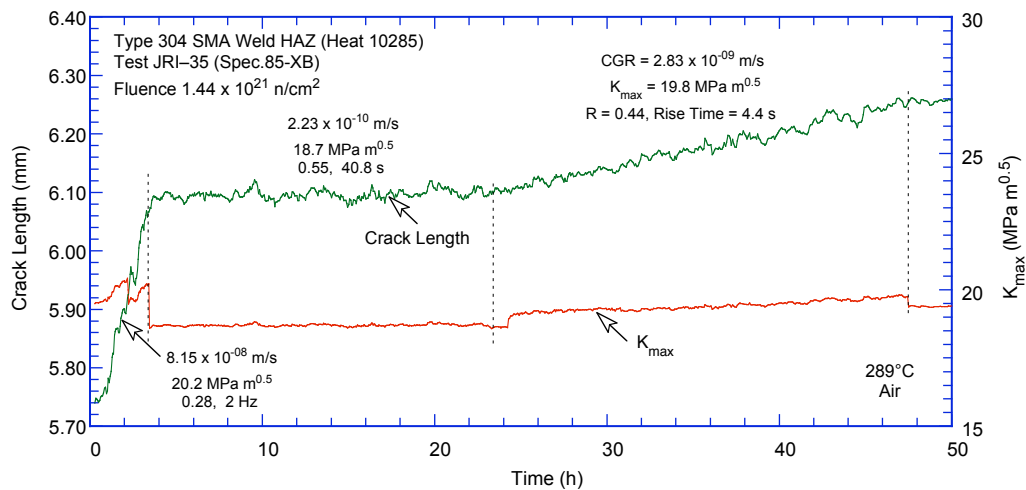
Figure 32. Crack-length-vs.-time plots for irradiated Type 304 SS SMA weld HAZ (Spec. 85-XB) in air at 289°C during test periods (a) precracking-2 and (b) 3-4.
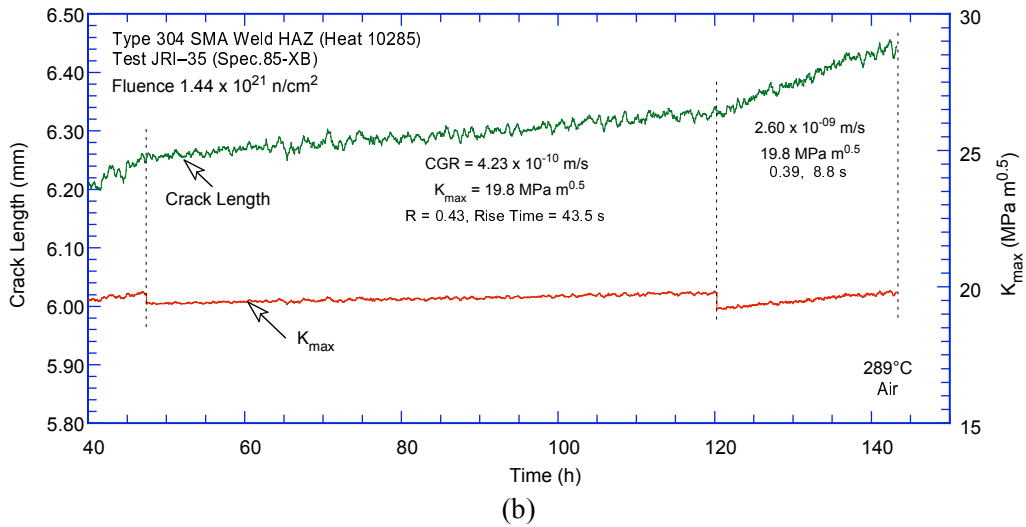
Figure 32. (Contd.)
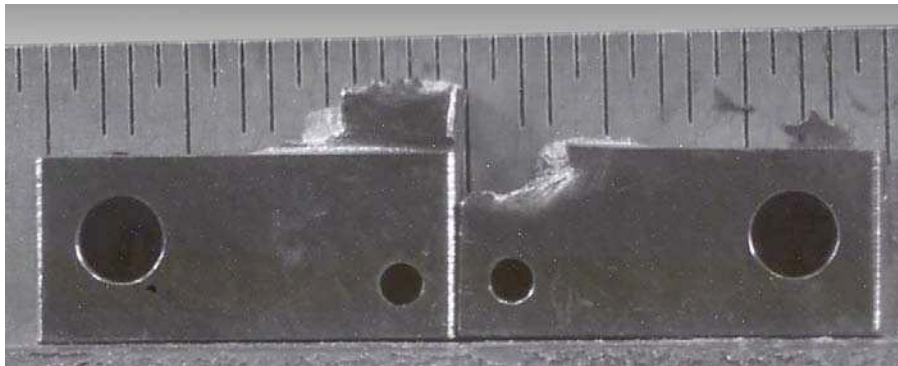
Figure 33.
Photograph of the side view of the two halves of Type 304 SS SMA weld HAZ.

The DC potential data during the J-R curve test were corrected to account for the effects of plasticity on the measured potential. The fracture toughness J-R curve for Specimen 85-XB in air is shown in Fig. 35; the actual data for the J-R curve test are given in Appendix B, Table B8. The J-R curve for a duplicate specimen of the same material (Specimen 85-XA) tested in the NWC BWR environment is also included in the figure for comparison. The limited data in air suggest that the fracture toughness J-R curve for this material may not be significantly different from that in NWC BWR water.
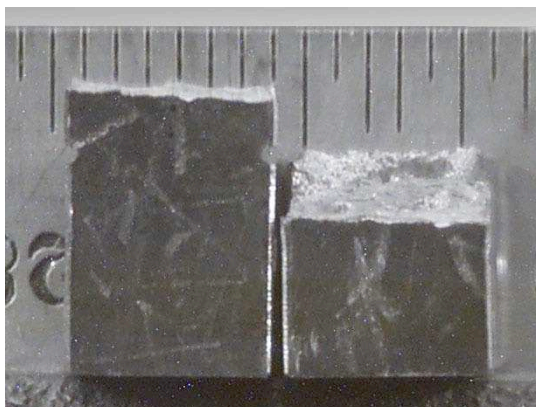
Figure 34.
Photograph of the end view of the two halves of Type 304 SS SMA weld HAZ.

38
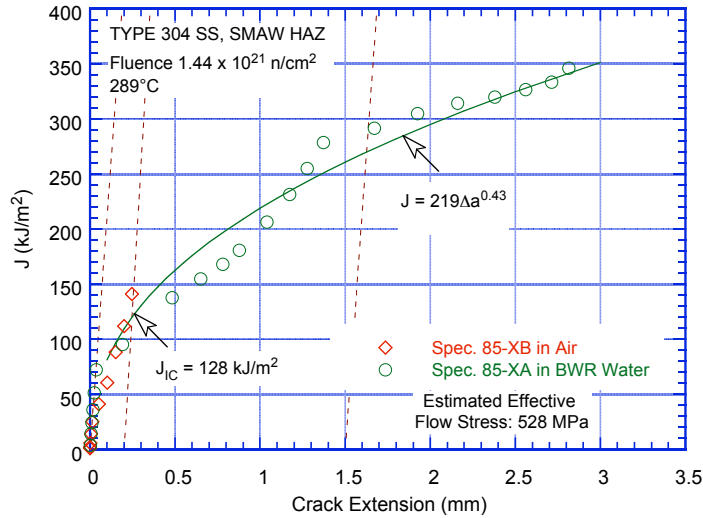
Figure 35.
Fracture toughness J-R curve for Type 304 SS SMA weld HAZ irradiated to 2.16 dpa tested in air and NWC BWR water at 289°C.

3.2.2.2   Specimen GG6T-B of Type 304L SS SA Weld HAZ, Test JRI-36

The test on Specimen GG6T-B of Type 304L SS SA weld HAZ irradiated to 2.16 dpa was initiated by fatigue precracking the specimen at R = 0.20, $K_{max} \approx 17.6$ MPa m$^{1/2}$, triangular waveform, and 2-Hz frequency in air at 289°C. The frictional load in the system was measured to be ±102 N (±23 lb); the results presented here have been corrected to account for this frictional load. After ≈0.43-mm crack advance, the waveform was changed to a slow/fast sawtooth, and CGRs were obtained at R ≈ 0.35 and rise times = 23 or 5 s.

Fatigue loading was stopped after ≈0.6-mm crack extension, and a fracture toughness J-R curve test was performed on the specimen in air at 289°C. The test, conducted at a constant extension rate of ≈ 0.43 μm/s (0.017 mil/s), was interrupted periodically (by holding the specimen at constant extension) to measure crack length by the DC potential drop measurements. The load vs. extension curve and the load vs. load-line displacement curve for Specimen 85-XB are shown in Fig. 36.
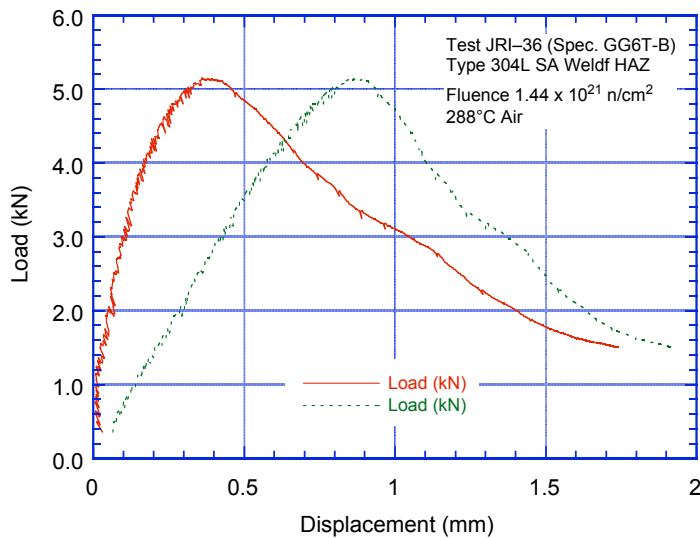
Figure 36.
Load vs. load-line displacement curve for Type 304L SS SA weld HAZ tested in air at 289°C.

The final crack size was marked by fatigue cycling at room temperature. The specimen was then fractured, and the final crack length of both halves of the fractured specimen was measured from the photograph of the fracture surface (Fig. 37). The actual crack extension was ≈27% greater than the value determined from the DC potential measurements. Crack extensions estimated from the DC potential method were adjusted accordingly. The side and end views of the two broken halves of the specimen, shown in Fig. 38, indicate a relatively straight crack plane. The results for the CGR test, including the allowed K_{max} from the K/size criterion, are given in Table 11; the changes in crack length, CGR, and K_{max} with time are given in Fig. 39.
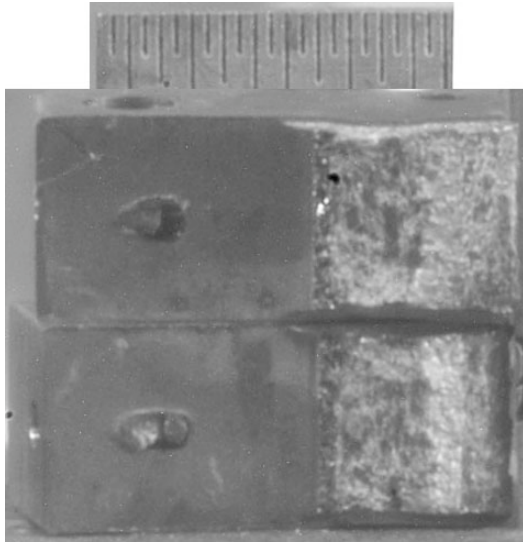
Figure 37.
Photograph of the fracture surface of Type 304L SS SA weld HAZ tested in air at 289°C.
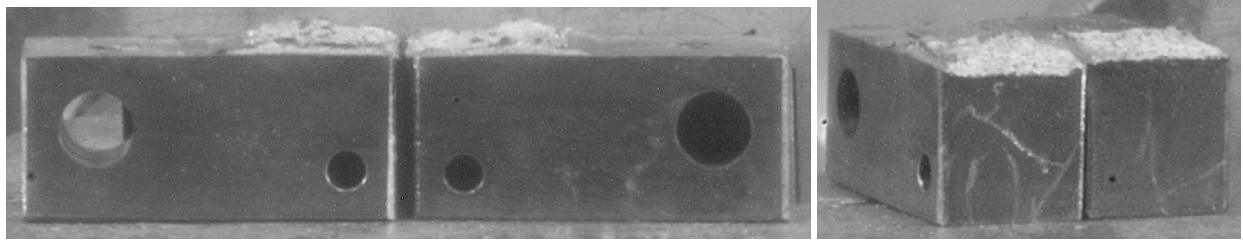
Figure 38. Fracture pieces of Type 304L SS SA weld HAZ: (a) side view and (b) end view.

Table 11. Test conditions and results for Type 304L SA weld HAZ specimen GG6T-B[a] in air at 289°C.

Test Period	Test Time, h	R Load Ratio	Rise Time, s	Return Time, s	Hold Time,[b] s	K_{max}, MPa m$^{1/2}$	ΔK, MPa m$^{1/2}$	Growth Rate, m/s	Allowed K_{max}, MPa m$^{1/2}$	K_{max} - $K_{allowed}$,[c] %	Crack Length[d] mm
											5.831
Pre a	2	0.19	0.21	0.21	0.04/0.04	17.7	14.3	9.10E-08	21.1	-16	5.988
Pre b	5	0.21	0.20	0.20	0.05/0.05	17.5	13.9	7.69E-08	20.6	-15	6.258
1	48	0.35	23.1	3.1	6.9/0.9	16.5	10.8	4.29E-10	20.5	-20	6.311
2	72	0.32	4.7	1.6	1.3/0.4	17.0	11.6	2.44E-09	20.3	-16	6.426

[a]Grand Gulf Type 304L SS core shroud shell, SA weld HAZ irradiated to 1.44 x 10^{21} n/cm^2 (2.16 dpa) at ≈297°C.
[b]Hold periods at maximum load during the unloading cycle and at minimum load during the loading cycle.
[c]Based on effective yield stress, defined as the average of irradiated and nonirradiated yield stresses.
[d]Actual crack extension was 27% greater than the value determined from the DC potential drop measurements.
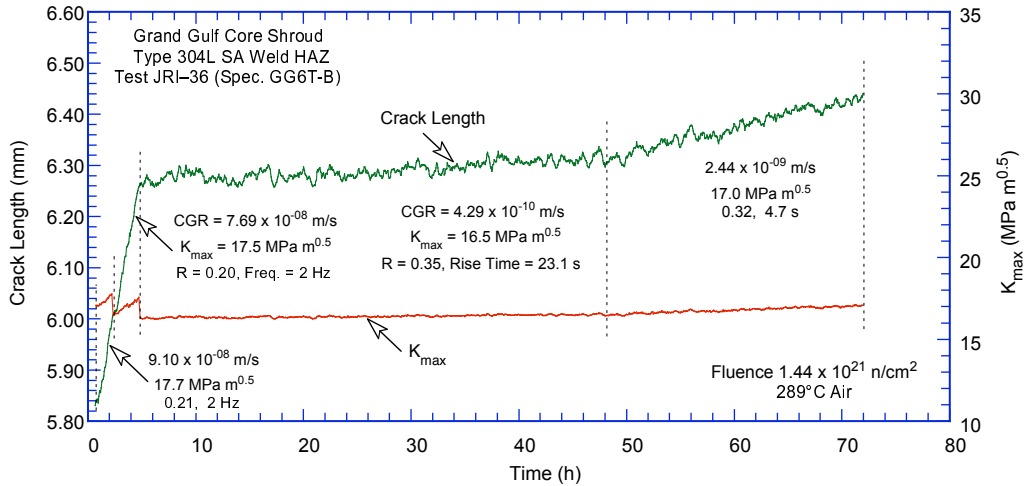
Figure 39. Crack-length-vs.-time plot for Type 304L SS SA weld HAZ in air at 289°C from precracking to test period 4.

The DC potential data during the J-R curve test were also corrected to account for the effects of plasticity on the measured potential. The fracture toughness J-R curve for Specimen GG6T-B in air is shown in Fig. 40; the actual data for the J-R curve test are given in Appendix B, Table B9. The results yield a J_{Ic} value of 125 kJ/m^2. For the GG core shroud SA weld HAZ material, the J-R curve in air is comparable to that in NWC BWR water (Fig. 29).
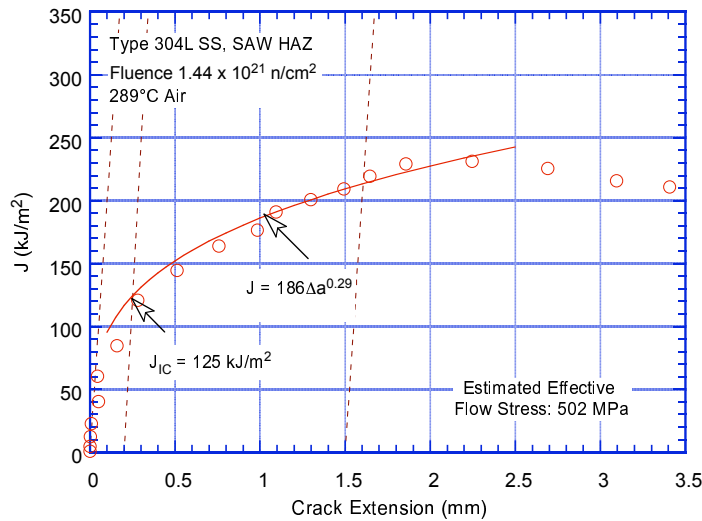
Figure 40.
Fracture toughness J-R curve for Type 304L SS SA weld HAZ irradiated to 2.16 dpa tested in air at 289°C.

3.3 Cast CF-8M Stainless Steel

Crack growth and fracture toughness J-R curve tests have been completed in BWR environments at 289°C on 1/4-T CT specimens of cast CF-8M SS that were thermally aged for 10,000 h at 400°C (752°F) and then irradiated to ≈2.46 dpa. The significant results for the various tests are summarized below.

3.3.1 Specimen 75-11TT of Thermally Aged CF-8M Cast SS, Test CGRI JR-33

The CGR test on Specimen 75-11TT was started in high-purity water at a flow rate of 21 mL/min. The system was operated for a few days to stabilize environmental conditions. The conductivity and DO

41

in the feedwater were 0.07 µS/cm and ≈ 800 ppb, respectively, and the DO content in the effluent was ≈ 600 ppb. The frictional load was measured to be ±156 N (±35 lb); the results presented here have been corrected to account for the frictional load.

Fatigue precracking was carried out at R = 0.45, K_{max} ≈ 11.5 MPa m $^{1/2}$, triangular waveform, and frequency of 2 Hz. After ≈ 0.05-mm (≈3.5-mil) crack extension, the load ratio was increased to 0.5-0.8 with rise times of 14-177 s and return times of 2-7 s. However, environmental enhancement was not readily achieved for this specimen; the loading conditions for most test periods yielded little or no enhancement in CGRs. Finally, the specimen was subjected to a constant load (K_{max} = 17.5 MPa) to obtain the SCC growth rate.

After determination of the SCC growth rate, a J-R test was performed on the specimen at 289°C (552°F) in high-DO water (≈ 600 ppb DO). The test was conducted at a constant extension rate of ≈ 0.43 µm/s (0.017 mil/s). The test was interrupted periodically (by holding the specimen at constant extension) to measure the crack length from the DC potential drop. The load vs. extension curve and the load vs. load-line displacement curve for Specimen 75-11TT are shown in Fig. 41. After the onset of crack extension, two large, abrupt load drops (≈ 1.2 and 0.7 kN) were observed. These load drops resulted in two large crack extensions of ≈ 0.9 and 0.6 mm, respectively.

The final crack size was marked by fatigue cycling at room temperature. The specimen was then fractured, and the final crack length of both halves of the fractured specimen was measured from photographs of the fracture surface for the two broken halves (Fig. 42). The actual crack extension was comparable to the value determined from the DC potential measurements; therefore, no correction was needed for the crack length measurements. The side view of the two broken halves of Specimen 75-11TT (Fig. 43) indicates a relatively straight crack plane. The results for the CGR test, including the allowed K_{max} from the K/size criterion, are given in Table 12; the changes in crack length, CGR, and K_{max} with time are given in Fig. 44.
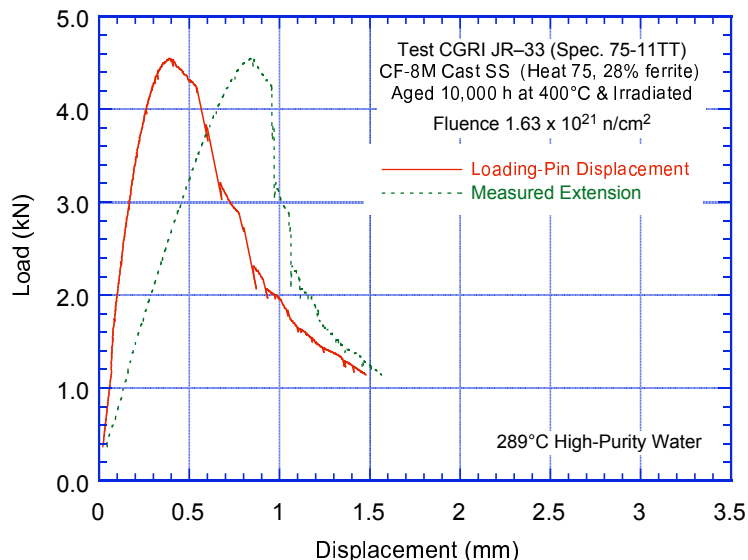
Figure 41.
Load vs. load-line displacement curve for CF-8M cast SS (Specimen 75-11TT) tested in high-purity water.
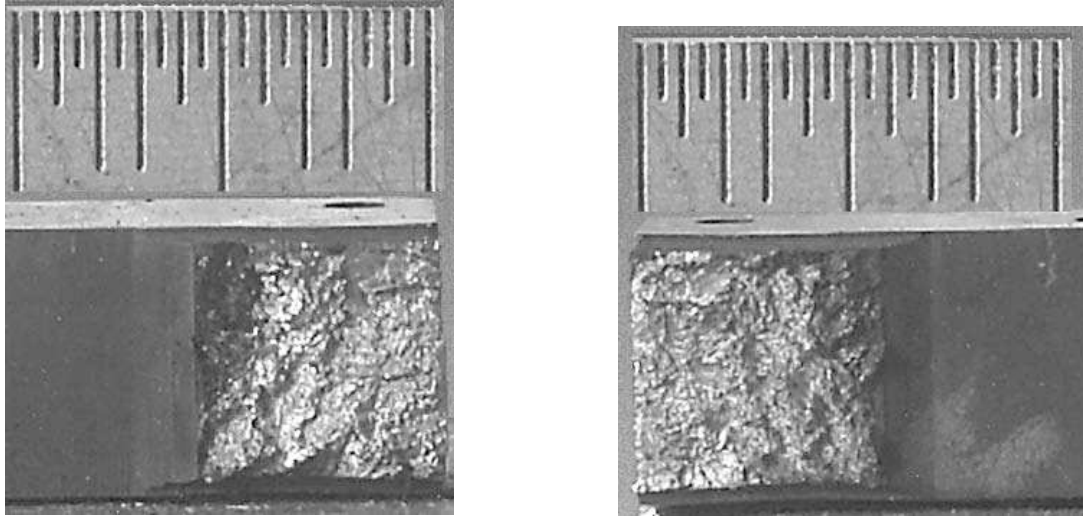
Figure 42.   Photographs of the fracture surface of the two halves of CF-8M cast SS (Specimen 75-11TT).
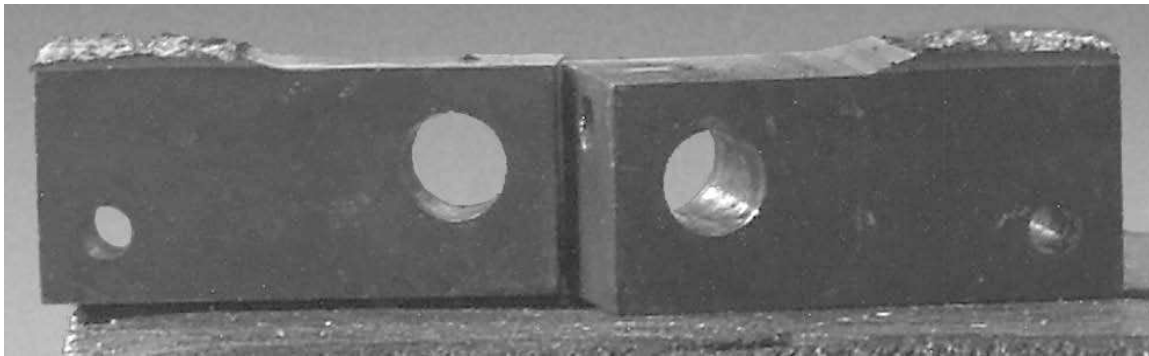
Figure 43.   Side view of the fractured pieces of CF-8M cast SS (Specimen 75-11TT).

Table 12.   Test conditions and results for thermally aged CF-8M Specimen 75-11TT[a] in BWR water at 289°C.

Test Period	Test Time, h	ECP[b] mV (SHE) Pt	ECP[b] mV (SHE) Steel	O_2 Conc.,[b] ppb	R Load Ratio	Rise Time, s	Return Time, s	Hold Time,[c] s	K_{max}, MPa m$^{1/2}$	ΔK, MPa m$^{1/2}$	Growth Rate, m/s	Allowed K_{max},[d] MPa m$^{1/2}$	Crack Length,[e] mm
													6.043
Pre a	78	169	201	600	0.46	0.14	0.14	0.11/0.11	11.3	6.1	2.70E-08	23.1	6.071
Pre b	102	213	234	600	0.45	0.14	0.14	0.11/0.11	11.2	6.2	2.69E-09	23.1	6.090
Pre c	118	212	232	600	0.45	14.3	14.3	10.7/10.7	11.2	6.1	5.35E-11	23.1	6.093
Pre d	126	216	236	600	0.58	0.13	0.13	0.12/0.12	11.2	4.7	3.52E-09	23.0	6.109
1a	142	213	232	600	0.82	18.0	4.0	42.0/8.0	10.8	1.9	1.48E-10	23.0	6.112
1b	150	214	233	600	0.53	17.2	2.3	12.8/1.7	13.4	6.3	4.38E-10	23.0	6.119
1c	216	213	229	600	0.53	34.8	7.0	25.2/5.0	13.5	6.3	5.69E-11	23.0	6.125
2	286	209	221	600	0.68	155	6.2	145/25.8	15.4	4.9	1.39E-11	23.0	6.128
3	312	211	222	600	0.50	7.7	1.3	4.3/0.7	17.1	8.5	8.55E-10	22.9	6.163
4	360	215	225	600	0.60	177	7.0	123/5.0	17.1	6.8	3.10E-11	22.9	6.167
5	405	216	225	600	0.50	7.7	1.3	4.3/0.7	17.1	8.5	9.64E-10	22.8	6.251
6	433	216	224	600	0.50	77.0	2.6	43.0/1.4	17.3	8.6	2.50E-10	22.7	6.302
7	550	210	217	600	1.00	–	–	–	17.5	0.0	1.24E-10	22.6	6.338

[a]Cast austenitic SS (Heat 75), thermally aged for 10,000 h at 400°C and then irradiated to 1.63 x 10^{21} n/cm^2 (2.46 dpa) at ≈297°C.
[b]Represents values in the effluent. Conductivity and DO were ≈0.07 µS/cm and 800 ppb, respectively, in the feedwater.
[c]Hold periods at maximum load during the unloading cycle and at minimum load during the loading cycle.
[d]Based on effective yield stress, defined as the average of irradiated and nonirradiated yield stresses.
[e]The difference between the measured crack extension and that determined from the DC potential drop measurements was <5%.

Figure 44. Crack-length-vs.-time plot for CF-8M cast SS (Specimen 75-11TT) in BWR water at 289°C for test periods (a) precracking-3, (b) 3-5, and (c) 6-7.

The DC potential data were corrected to account for the effects of plasticity on the measured potential. The fracture toughness J-R curve for Specimen 75-11TT in high-DO water is shown in Fig. 45; the actual data for the test are presented in Appendix B, Table B10. The results yield a J_{Ic} value of 84 kJ/m^2 (480 in.-lb/in.^{2}). As noted earlier, the two abrupt load drops (Fig. 41) resulted in uncontrolled crack extensions of ≈ 0.9 and 0.6 mm, respectively. However, the specimen showed controlled crack extension after these two load drops.
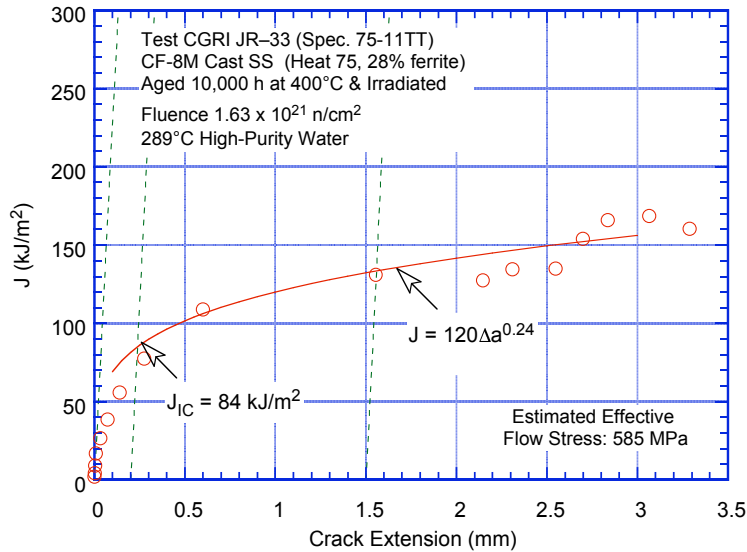
Figure 45.
Fracture toughness J-R curve for thermally aged and irradiated cast CF-8M SS (Specimen 75-11TT) in high-DO water at 289°C.

3.3.2   Specimen 75-11TM of Thermally Aged CF-8M Cast SS, Test CGRI JR-34

The CGR test on Specimen 75-11TM was started in high-purity water at a flow rate of 20 mL/min. The conductivity and DO in the feedwater were 0.07 μS/cm and ≈ 800 ppb, respectively, and the DO content in the effluent was ≈ 600 ppb. The frictional load was measured to be ± 120 N (± 27 lb); the results presented here have been corrected to account for the frictional load.

Fatigue precracking was carried out at R = 0.50, $K_{max} \approx 15.0$ MPa m$^{1/2}$, triangular waveform, and frequency of 2 Hz. After ≈ 0.14-mm (5.5-mil) crack extension, the load ratio was increased incrementally to 0.8 with rise times of 37-435 s and return times of 2-6 s. Environmental enhancement was readily achieved for this specimen of thermally aged cast SS. Finally, the specimen was subjected to a constant load (corresponding to $K_{max} = 14.7$, 10.7, and 7.6 MPa m$^{1/2}$) to obtain SCC growth rates.

After completion of the SCC growth rate test, a J-R test was performed on the specimen at 289°C (552°F) in high-DO water (≈ 600 ppb DO). The test was conducted at a constant extension rate of ≈ 0.43 μm/s (0.017 mil/s). The load vs. extension and the load vs load-line displacement curves for Specimen 75-11TM are shown in Fig. 46. After the onset of crack extension, a few large, abrupt load drops were observed. These load drops resulted in crack extensions of ≈ 0.4-0.5 mm (16-20 mil).

The final crack size was marked by fatigue cycling at room temperature. The specimen was then fractured, and the final crack length of both halves of the fractured specimen was measured from photographs of the fracture surface for the two broken halves (Fig. 47a). The actual crack extension was comparable to the value determined from the DC potential measurements; therefore, no correction was needed for the crack length measurements. The end view of the two broken halves of the specimen

45

(Fig. 47b) indicates a relatively straight crack plane. The results for the CGR test, including the allowed K_{max} from the K/size criterion, are given in Table 13; the changes in crack length, CGR, and K_{max} with time are given in Fig. 48.
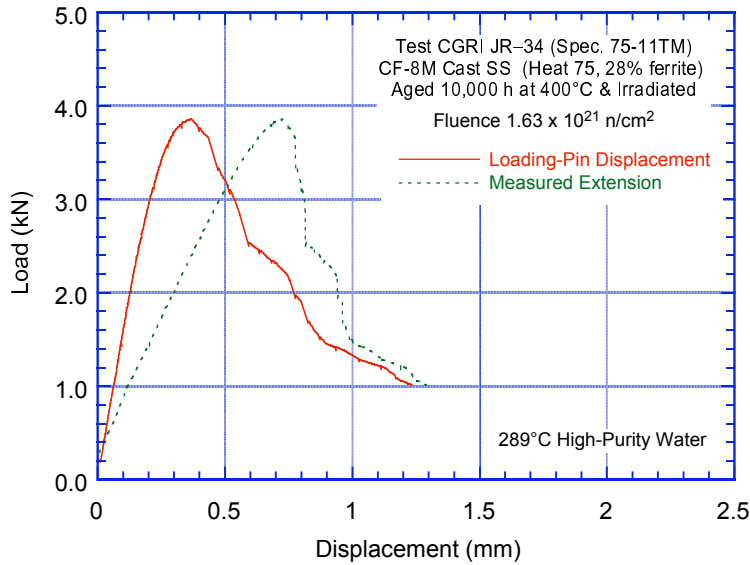
Figure 46.
Load vs. load-line displacement curve for CF-8M cast SS (Specimen 75-11TM) tested in high-purity water.

(a)   (b)
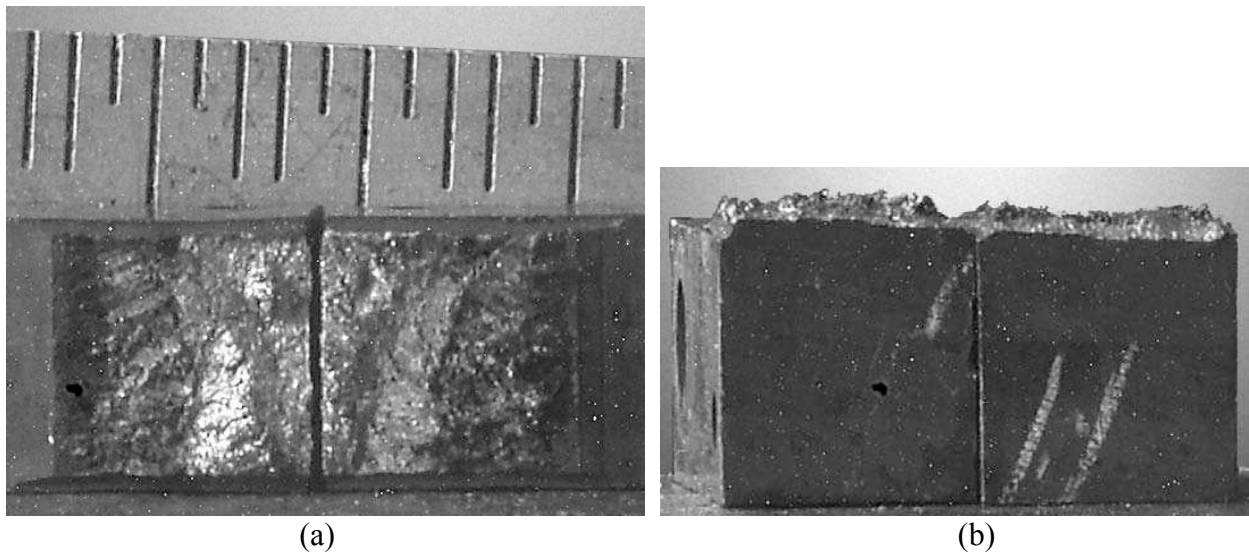
Figure 47.   Photographs of the (a) fracture surface and (b) end view of the two halves of CF-8M cast SS (Specimen 75-11TM).

The DC potential data were corrected to account for the effects of plasticity on the measured potential. The fracture toughness J-R curve for Specimen 75-11TM in high-DO water is shown in Fig. 49. The actual data for the test are presented in Appendix B, Table B11. The results yield a J_{Ic} value of 40 kJ/m^2 (228 in.-lb/in.^{2}) Note that the three abrupt load drops (Fig. 46) resulted in uncontrolled crack extensions of $\approx$ 0.4-0.5 mm. However, the specimen showed controlled crack extension after these load drops.

Table 13. Test conditions and results for thermally aged CF-8M Specimen 75-11TM[a] in BWR water at 289°C.

Test Period	Test Time, h	ECP[b] mV (SHE) Pt	ECP[b] mV (SHE) Steel	O$_2$ Conc.,[b] ppb	R Load Ratio	Rise Time, s	Return Time, s	Hold Time,[c] s	K$_{max}$, MPa m$^{1/2}$	ΔK, MPa m$^{1/2}$	Growth Rate, m/s	Allowed K$_{max}$,[d] MPa m$^{1/2}$	Crack Length,[e] mm
													6.030
Pre	72	226	229	600	0.49	0.17	0.17	0.08/0.08	15.0	7.6	3.02E-08	22.9	6.166
1	114	227	230	600	0.59	37	2.5	23/1.5	14.6	6.1	6.43E-10	22.8	6.224
2	162	226	229	600	0.72	159	6.4	141/5.6	14.8	4.2	3.61E-10	22.7	6.256
3	234	225	228	600	0.81	435	5.2	565/6.8	14.9	2.9	2.84E-10	22.7	6.289
4	264	224	226	600	1.00	–	–	–	14.7	0.0	4.27E-10	22.6	6.335
5	354	218	220	600	1.00	–	–	–	10.7	0.0	1.72E-10	22.5	6.376
6	450	209	209	600	1.00	–	–	–	7.6	0.0	2.84E-11	22.5	6.384

[a] Cast austenitic SS (Heat 75), thermally aged for 10,000 h at 400°C and then irradiated to 1.63 x 10^{21} n/cm^2 (2.46 dpa) at ≈297°C.
[b]Represents values in the effluent. Conductivity and DO were ≈0.07 μS/cm and 800 ppb, respectively, in the feedwater.
[c]Hold periods at maximum load during the unloading cycle and at minimum load during the loading cycle.
[d]Based on effective yield stress, defined as the average of irradiated and nonirradiated yield stresses.
[e]The difference between the measured crack extension and that determined from the DC potential drop measurements was <5%.

(a)

(b)

Figure 48. Crack-length-vs.-time plot for CF-8M cast SS (Specimen 85-3TM) in BWR water at 289°C for test periods (a) precracking-3, (b) 3-5, and (c) 6-7.
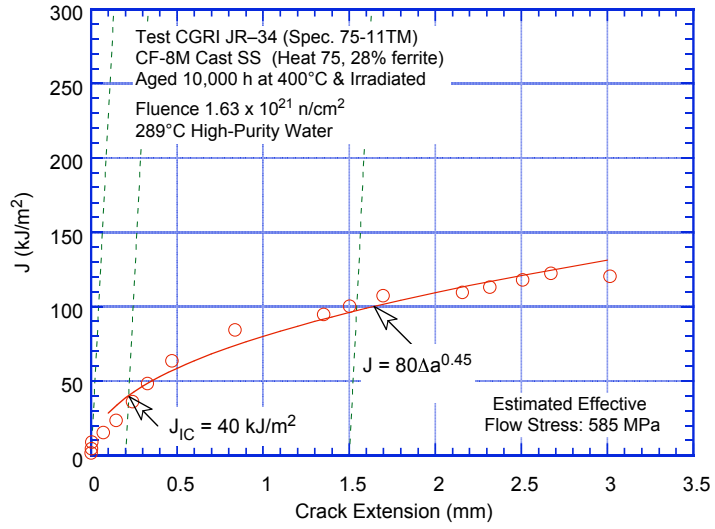
Figure 49.
Fracture toughness J-R curve for thermally aged and irradiated cast CF-8M SS (Specimen 75-11TM) in high-DO water at 289°C.

Content within the figure:

Test CGRI JR–34 (Spec. 75-11TM)
CF-8M Cast SS (Heat 75, 28% ferrite)
Aged 10,000 h at 400°C & Irradiated

Fluence 1.63 x 10^{21} n/cm^2
289°C High-Purity Water

$J = 80\Delta a^{0.45}$

$J_{IC} = 40$ kJ/m^2

Estimated Effective
Flow Stress: 585 MPa

J (kJ/m^2)

Crack Extension (mm)

4 Discussion

4.1 CGRs under Constant Load with or without Periodic Partial Unloading

The constant-load CGRs from the present study and those obtained earlier at ANL[27,54] are compiled in Table 14. Most of the tests were conducted under constant load with or without periodic partial unloading to R = 0.7 every 1-3 h. The unloading/reloading period was 24 s for all tests except for the test on Specimen C3-B, which used a 4-s unloading/reloading period. The results indicate that periodic partial unloading has little or no effect on constant-load CGRs. A few tests were conducted using a trapezoidal waveform having rise and return times of 300-500 and 12 s, respectively. For these tests, the experimental CGRs were adjusted for the contribution of corrosion fatigue by using the cyclic CGR data obtained with a saw-tooth waveform (i.e., without a hold period at peak stress). The adjusted values (i.e., constant-load CGRs) are listed within parentheses in Table 14. For the loading conditions used in these tests, the CGRs under cyclic loading were comparable to those under constant load; therefore, the difference between the experimental and adjusted CGRs is relatively small (less than 5%).

Table 14. Test conditions and constant-load crack growth data in BWR environment at 289°C.

Steel Type	Material[a]	Condition[b]	Heat[c]	Spec. ID	Dose, dpa	DO, ppb	ECP,[d] mV (SHE)	K_{max}, MPa m$^{1/2}$	CGR,[e] m/s	Waveform	$K_{max} - K_{allowed}$,[f] %
304L	Base	SA	C3	C3-A	0.45	300	197	17.9	8.65E-11 (9.22E-11)	Trapezoidal	4.2
304L	Base	SA	C3	C3-A	0.45	300	200	22.0	1.11E-10 (1.17E-10)	Trapezoidal	28.7
304L	Base	SA	C3	C3-A	0.45	300	203	22.3	1.13E-10 (1.15E-10)	Trapezoidal	30.9
304L	Base	SA	C3	C3-B	1.35	300	191	20.1	1.06E-09	Periodic Unload	13.5
304L	Base	SA	C3	C3-B	1.35	300	195	22.1	1.04E-09	Periodic Unload	26.9
304L	Base	SA	C3	C3-B	1.35	≈10	-595	22.3	4.02E-11	Periodic Unload	29.5
304L	Base	SA	C3	C3-B	1.35	≈10	-614	22.7	6.42E-12	Periodic Unload	32.5
304L	Base	SA	C3	C3-B	1.35	250	155	24.4	8.70E-10	Periodic Unload	48.9
304L	Base	SA	C3	C3-C	3.00	300	164	19.4	6.83E-10	Periodic Unload	-7.9
304L	Base	SA	C3	C3-C	3.00	100	150	23.7	5.07E-10	Periodic Unload	15.5
304L	Base	SA	C3	C3-C	3.00	≈10	-294	27.5	6.91E-10	Periodic Unload	43.9
304L	Base	SA	C3	C3-C	3.00	≈10	-502	34.7	2.04E-09	Periodic Unload	111.8
304L	Base	SA	C3	C3-C	3.00	≈10	-457	37.0	3.70E-09	Periodic Unload	133.9
316L	Base	SA	C16	C16-B	3.00	250	117	15.2	4.62E-10	Periodic Unload	-29.0
316L	Base	SA	C16	C16-B	3.00	<30	-298	15.3	1.90E-11	Periodic Unload	-28.4
316L	Base	SA	C16	C16-B	3.00	<30	-554	17.3	1.73E-11	Periodic Unload	-18.1
316L	Base	SA	C16	C16-B	3.00	<30	-597	19.7	4.11E-11	Periodic Unload	-6.9
316L	Base	SA	C16	C16-B	3.00	250	139	19.6	7.14E-10	Periodic Unload	-6.7
316L	Base	SA	C16	C16-B	3.00	250	148	21.9	1.10E-09	Periodic Unload	4.7
316	Base	SA	C21	C21-A	0.45	350	(160)	16.5	1.51E-10	Periodic Unload	-22.0
316	Base	SA	C21	C21-A	0.45	350	(160)	21.8	2.46E-10	Periodic Unload	3.8
316	Base	SA	C21	C21-A	0.45	350	(160)	22.7	2.56E-10	Const. Load	9.5
316	Base	SA	C21	C21-B	1.35	350	211	16.2	9.67E-10	Const. Load	-22.2
316	Base	SA	C21	C21-B	1.35	<30	-452	16.3	3.32E-11	Const. Load	-21.4
316	Base	SA	C21	C21-B	1.35	<30	-551	19.6	1.24E-11	Const. Load	-5.4
316	Base	SA	C21	C21-C	3.00	500	(230)	17.6	1.06E-09	Const. Load	-32.7
316	Base	SA	C21	C21-C	3.00	<30	-216	17.9	1.77E-10	Const. Load	-30.8
316	Base	SA	C21	C21-C	3.00	450	114	18.1	9.18E-10	Const. Load	-29.4
316	Base	SA	C21	C21-C	3.00	450	124	23.6	1.21E-09	Const. Load	-5.4
316	Base	SA	C21	C21-C	3.00	<30	-389	24.9	1.06E-09	Const. Load	1.5
316	Base	SA	C21	C21-C	3.00	<30	-483	22.9	7.85E-10	Const. Load	-5.0
316	Base	SA	C21	C21-C	3.00	<30	-487	20.2	3.12E-10	Const. Load	-15.6
316	Base	SA	C21	C21-C	3.00	<30	(-485)	22.1	1.80E-09	Const. Load	-4.5

Table 14.   (Contd.)

Steel Type	Material[a]	Condition[b]	Heat[c]	Spec. ID	Dose, dpa	DO, ppb	ECP,[d] mV (SHE)	K_{max}, MPa m$^{1/2}$	CGR,[e] m/s	Waveform	K_{max} - $K_{allowed}$,[f] %
304	Base	Sens.	10285	85-3TT	2.16	500	(230)	15.7	1.97E-10	Const. Load	-21.4
304L	SAW HAZ	AW	GG	GG5B-A	0.00	500	(230)	21.1	6.01E-11	Periodic Unload	14.4
304L	SAW HAZ	AW	GG	GG5B-A	0.00	500	(230)	26.5	1.72E-10	Periodic Unload	44.8
304L	SAW HAZ	AW	GG	GG5B-A	0.00	500	(230)	26.9	1.55E-10	Periodic Unload	47.6
304L	SAW HAZ	AW+TT	GG	GG3B-A-TT	0.00	400	68	16.4	4.34E-11	Periodic Unload	-12.4
304	SMAW HAZ	AW	10285	85-YA	0.00	300	(230)	19.7	1.50E-12	Const. Load	-5.6
304	SMAW HAZ	AW+TT	10285	85-3A-TT	0.00	600	106	21.2	6.60E-10	Periodic Unload	4.7
304	SMAW HAZ	AW+TT	10285	85-3A-TT	0.00	45	-633	21.4	9.13E-11	Periodic Unload	6.8
304	SMAW HAZ	AW+TT	10285	85-3A-TT	0.00	<40	-627	25.0	4.29E-11	Periodic Unload	25.4
304L	SAW HAZ	AW	GG	GG5T-B	0.75	350	176	14.7	6.75E-10 (7.11E-10)	Trapezoidal	-44.8
304L	SAW HAZ	AW	GG	GG5T-B	0.75	350	204	15.0	4.24E-10	Const. Load	-43.3
304L	SAW HAZ	AW	GG	GG5T-B	0.75	350	202	15.2	5.62E-10 (5.72E-10)	Trapezoidal	-41.7
304L	SAW HAZ	AW	GG	GG5T-B	0.75	<50	-285	14.9	1.50E-12	Trapezoidal	-42.7
304L	SAW HAZ	AW	GG	GG6T-A	2.16	600	223	16.0	4.17E-10	Const. Load	-21.0
304L	SAW HAZ	AW	GG	GG6T-A	2.16	600	224	13.6	4.04E-10	Const. Load	-32.3
304L	SAW HAZ	AW	GG	GG6T-A	2.16	600	218	10.9	5.78E-10	Const. Load	-45.1
304L	SAW HAZ	AW	GG	GG6T-A	2.16	600	218	7.0	1.66E-10	Const. Load	-64.6
304	SMAW HAZ	AW	10285	85-7A	0.75	500	212	18.6	9.51E-10 (1.10E-09)	Trapezoidal	-35.4
304	SMAW HAZ	AW	10285	85-7A	0.75	500	214	19.4	9.46E-10	Const. Load	-31.5
304	SMAW HAZ	AW	10285	85-7A	0.75	<50	-252	19.8	1.55E-11	Const. Load	-29.2
304	SMAW HAZ	AW	10285	85-XA	2.16	500	235	13.9	1.98E-10	Const. Load	-30.3
304	SMAW HAZ	AW	10285	85-XA	2.16	500	210	14.0	2.61E-10	Const. Load	-29.3
304	SMAW HAZ	AW+TT	10285	85-1A-TT	0.75	250	182	16.6	2.55E-10 (2.34E-10)	Trapezoidal	-43.6
304	SMAW HAZ	AW+TT	10285	85-1A-TT	0.75	250	188	16.7	1.74E-10 (1.64E-10)	Trapezoidal	-43.3
304	SMAW HAZ	AW+TT	10285	85-1A-TT	0.75	250	185	18.7	2.78E-10 (2.67E-10)	Trapezoidal	-35.7
304	SMAW HAZ	AW+TT	10285	85-1A-TT	0.75	<30	-258	19.3	5.73E-11 (3.89E-11)	Trapezoidal	-33.4
CF-8M	Cast SS	Aged	75	75-11TT	2.46	600	217	17.5	1.24E-10	Const. Load	-22.7
CF-8M	Cast SS	Aged	75	75-11TM	2.46	600	226	14.7	4.27E-10	Const. Load	-35.0
CF-8M	Cast SS	Aged	75	75-11TM	2.46	600	220	10.7	1.72E-10	Const. Load	-52.5
CF-8M	Cast SS	Aged	75	75-11TM	2.46	600	209	7.6	2.84E-11	Const. Load	-66.2

[a]SAW = submerged arc weld; SMAW = shielded metal arc weld; HAZ = heat affected zone.
[b]AW = as welded; TT = thermally treated.
[c]GG = Grand Gulf core shroud shell.
[d]Measured with a SS electrode located in the exit of the autoclave; the values within parentheses are estimated values.
[e]Values within parentheses are constant-load CGRs obtained after adjusting the experimental CGRs for the contribution of corrosion fatigue.
[f]$K_{allowed}$ based on effective yield stress, defined as the average of irradiated and nonirradiated yield stresses.

4.1.1   Solution-Annealed Materials

The constant-load CGRs obtained at ANL for irradiated Types 304L, 316L, and 316 SS in high- and low-DO environments (corresponding to NWC and HWC BWR environments, respectively) are shown in Fig. 50; symbols shown with a "+" represent loading conditions that did not satisfy the specimen K/size criterion (Eq. 8) based on effective yield stress (defined as the average of the irradiated and nonirradiated yield stresses). In the NWC BWR environment (Fig. 50a), the CGRs for SSs irradiated to ≈0.45 dpa are comparable to the CGRs predicted by the NUREG-0313 disposition curve (Eq. 16) for nonirradiated, sensitized SSs in water with 8 ppm DO. For SSs irradiated to ≈1.35 or 3.0 dpa, the CGRs are comparable and a factor of ≈6 higher than the NUREG-0313 disposition curve.[60]

The results in Fig. 50 also indicate a benefit from a low-DO environment. In general, for the materials and irradiation conditions investigated in the present study, the CGRs decreased more than an
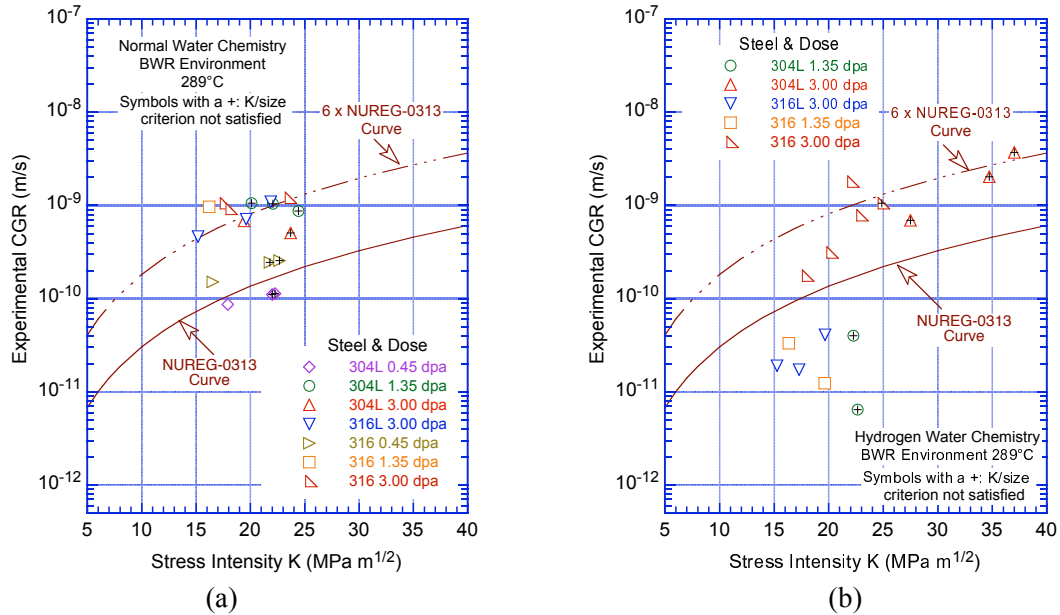
Figure 50. CGR data under constant load with periodic partial unloads for irradiated austenitic SSs in high-purity water at 289°C.

order of magnitude when the DO level was decreased from ≈350 to <30 ppb (i.e., by changing from NWC to HWC environments). A few specimens showed a different behavior. For example, no benefit of low-DO environment was observed for Heat C3 of Type 304L SS irradiated to 3.0 dpa (triangles in Fig. 50). It is not clear whether this behavior is genuine or caused by loss of specimen constraint because of the high applied load. For Heat C3, the applied K_{max} of ≈25 MPa m$^{1/2}$ (i.e., during periods 6 and 7, see Table A.3) was 53% greater than the value allowed by the K/size criterion. Under these conditions, the CGR remained constant at ≈5 x 10^{-10} m/s for ≈370 h when the DO level was decreased from ≈300 to <20 ppb. Later during test periods 8 and 9 (see Table A.3), both the CGR and applied K_{max} increased rapidly. As discussed in Section 4.1.5, the behavior during periods 8 and 9 can clearly be attributed to a loss of specimen constraint; the fracture plane deviated from the normal plane, and the crack propagated at an angle of 45° to the original fracture plane.

Similarly, a benefit of HWC was not observed for Heat C21 at K_{max} ≈25 MPa m$^{1/2}$. For Heat C21, all applied K_{max} values, except during period 8, satisfied the K/size criterion. The experimental CGRs for Heat C21 in BWR environments are plotted in Fig. 51; the numbers next to the data points represent test period. The CGR decreased by a factor of ≈8 when DO was decreased at ≈19 MPa m$^{1/2}$ (during test periods 4 and 5, see Table 6). It did not change when DO was decreased at ≈25 MPa m$^{1/2}$ (during test periods 7 and 8). The applied K_{max} during test periods 4 and 5 was ≈7% higher than the value allowed by the K/size criterion. It was decreased to a value that satisfied the K/size criterion (test period 9a); no significant change in CGR was observed even after ≈0.15-mm crack advance. The applied K_{max} was then decreased further to 21.4 MPa m$^{1/2}$; after an ≈50-h period of slightly lower CGR (test period 9b), the growth rate increased back to the value observed earlier during test periods 7 and 8. It is not clear whether this behavior should be attributed to a loss of constraint, or whether there are other threshold conditions, e.g., exceeding a threshold CGR, under which a low DO offers no benefit, and the temporary decrease of the rates was due to the relatively large decrease in K_{max} (≈12%). The possible effect of specimen size is discussed further in Section 4.1.5.

Metallographic examination of the fracture surfaces indicated a predominantly IG fracture under constant load. Micrographs of the fracture surface of Specimen C3-C are presented in Section 4.1.5.

51
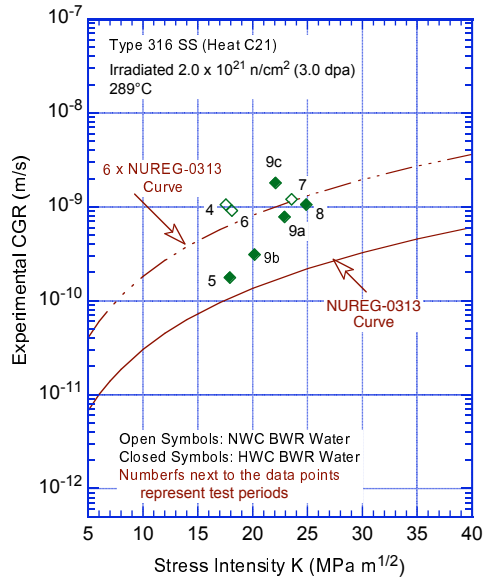
Figure 51.
Crack growth rates under constant load for irradiated Heat C21 of Type 316 SS in NWC and HWC BWR environments at 289°C.

4.1.2   Stainless Steel Weld HAZ Materials

Figure 52 shows the constant-load CGRs obtained at ANL for nonirradiated and irradiated Types 304L and 304 SS weld HAZ materials and sensitized Type 304 SS. These materials were tested in high-DO and low-DO environments at 289°C. For nonirradiated materials (Fig. 52a), because of relatively low values of flow stress, the applied K_{max} for all materials, except thermally treated Type 304L SA weld HAZ (squares in Fig. 52a), did not satisfy the K/size criterion of ASTM E-1681. In addition, for the Type 304 SS SMA weld HAZ specimen (right angle triangles in Fig. 52a), the fracture plane was not normal to the stress axis but at an angle of 45° to the stress axis, the CGR for this specimen is not included in Fig. 52a.

For nonirradiated GG Type 304L SA weld HAZ, although the data did not meet the K/size criterion of ASTM E-1681, the as-welded (triangles in Fig. 52a) and as-welded plus thermally-treated (squares in Fig. 52a) materials have comparable CGRs. For both conditions, the CGRs are a factor of ≈2 lower than the NUREG-0313 curve for nonirradiated, sensitized SSs in water with 8 ppm DO.[60] These results are in good agreement with the CGR of 1 x 10^{-10} m/s obtained by Andresen et al.[51] for the GG Type 304L weld HAZ in high-DO water (2000 ppb DO) at 288°C and K_{max} = 27.4 MPa m$^{1/2}$.

Irradiation increased the CGRs of all SS weld HAZ materials; the loading conditions for all data shown in Fig. 52b satisfied the K/size criterion (Eq. 8) based on the effective yield stress. The CGRs of HAZ specimens irradiated to ≈0.75 and 2.16 dpa are comparable and are a factor of 3-10 higher than those predicted by the NUREG-0313 disposition curve. Reducing the corrosion potential of the environment was beneficial for all materials that were tested in the HWC BWR environment. The growth rates of irradiated or nonirradiated Type 304 weld HAZ decreased by an order of magnitude or more when the DO was decreased from ≈350 ppb to <30 ppb (Fig. 52).

An IG fracture occurred for both nonirradiated and irradiated Type 304 SMA weld HAZ materials. However, the fracture morphology of nonirradiated Type 304L SA weld HAZ material was primarily TG with a well-defined river pattern. A TG fracture morphology is unusual in SS weld HAZ. The presence of residual strain in the material typically promotes IG crack growth even in nonsensitized SS.[49-52] An IG fracture is always observed in cold-worked SSs.
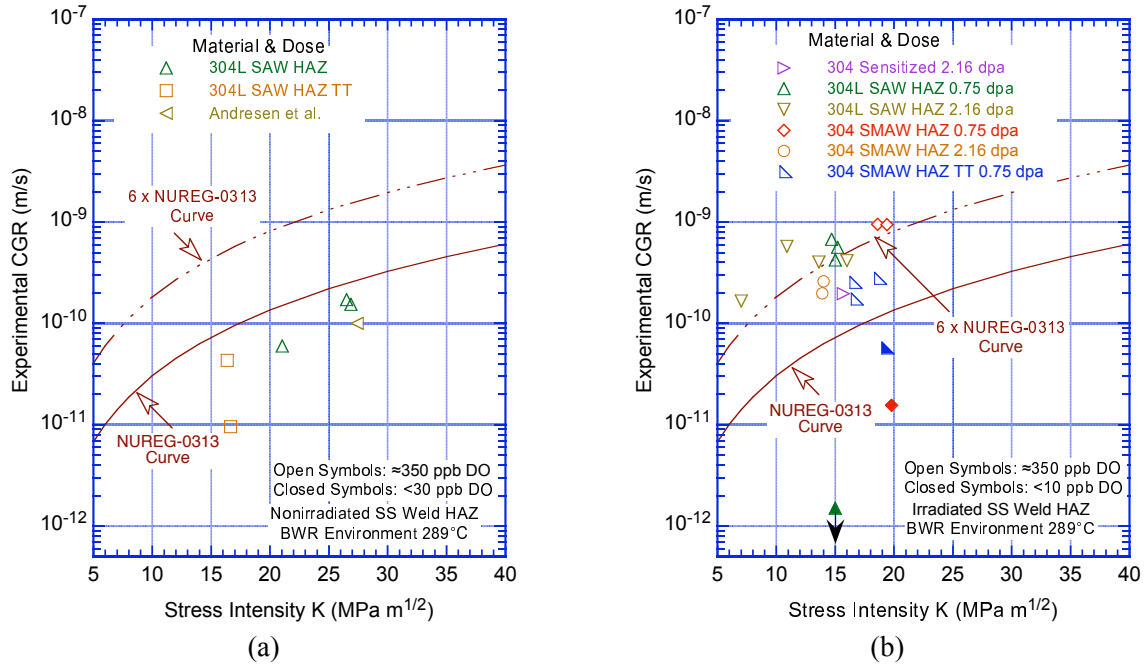
Figure 52.   CGR under constant load with periodic partial unloads for (a) nonirradiated and (b) irradiated SS weld HAZ specimens in high-purity water at 289°C.

4.1.3   Cast Austenitic Stainless Steel

Figure 53 gives the constant-load CGRs for two irradiated specimens of CF-8M cast SS in the NWC BWR environment. The specimens were aged for 10,000 h at 400°C before irradiation. Although the measured CGRs for the two specimens differ significantly, the results are comparable to the data obtained on solution-annealed SSs and weld HAZ materials irradiated to similar dose levels. The CGRs are a factor of 2-6 above the values predicted by the NUREG-0313 curve for nonirradiated austenitic SSs.[60]
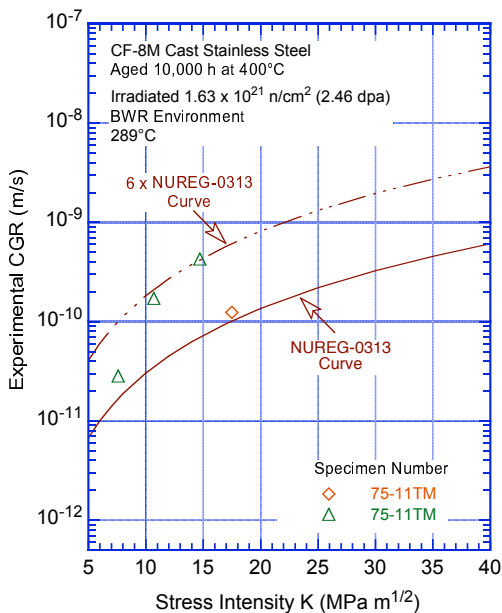
Figure 53.
CGR under constant load for thermally aged and irradiated CF-8M cast stainless steel specimens in BWR environment at 289°C.

4.1.4   Comparison with CGR Data in the Literature

Figure 54 shows the constant-load CGR data obtained in the present study for NWC and HWC BWR environments with austenitic SSs and weld HAZ materials irradiated to 0.75-2.2 dpa, along with the data available in the literature[63] for purposes of comparison. Most of the CGRs are a factor of 3-10 greater than the values predicted by the NUREG-0313 curve for nonirradiated sensitized SSs in water with 8 ppm DO.[60] For the same irradiation level, the CGRs for weld HAZ materials are higher than those for solution-annealed SSs. Also, at these irradiation dose levels a beneficial effect of reducing the corrosion potential by changing from the NWC to HWC BWR environment is observed for all materials; the growth rates in low-DO water are more than a factor of 10 lower than in high-DO water.
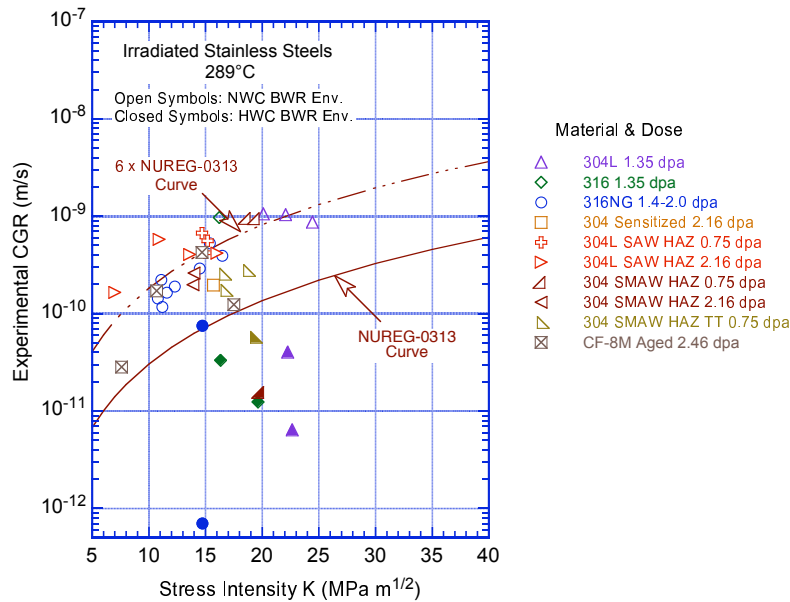
Figure 54.   CGR under constant load in NWC and HWC BWR environments at 289°C for austenitic stainless steels irradiated to 0.75-2.2 dpa (Ref. 63, present study).

The constant-load CGRs obtained in the present study in NWC and HWC BWR environments on austenitic SSs and weld HAZ materials irradiated to 3.0-4.0 dpa are compared with the data available in the literature[56,63] in Fig. 55. At these irradiation doses, the CGRs in NWC BWR environment are a factor of 3-10 greater than the values predicted by the NUREG-0313 curve for nonirradiated SSs. There is no apparent increase in CGR over the growth rates for material with lower fluence levels, although the number of heats of material is limited. A beneficial effect of low DO was not observed in these tests at higher values of K (greater than 20 MPa $m^{1/2}$). The Type 304 SS irradiated to 4.0 dpa and tested at $\approx$17 MPa $m^{1/2}$ (open and closed right angle triangles in Fig. 55) showed reduced CGRs in low-DO water. HWC was not beneficial at higher loads (e.g., K_{max} $\geq$30 MPa $m^{1/2}$); however, the specimen K/size criterion was not satisfied at these loads in either NWC or HWC environments. The specimen K/size criterion was also not satisfied for the Type 304L SS irradiated to 3.0 dpa (closed triangles) tested in the HWC environment at K_{max} $\geq$35 MPa $m^{1/2}$. Possible effects of specimen K/size criterion are discussed in the next section.

The constant-load CGR data from the present study and available in the literature[57,63] on austenitic SSs irradiated to $\approx$0.45 dpa and 13.0 dpa are presented in Figs. 56a and b, respectively. At 0.45 dpa, the CGRs are in good agreement with the values predicted by the NUREG-0313 curve for nonirradiated SSs.[60] The CGRs for SSs irradiated to 13 dpa show a strong dependence on K at less than 15 MPa $m^{1/2}$

54
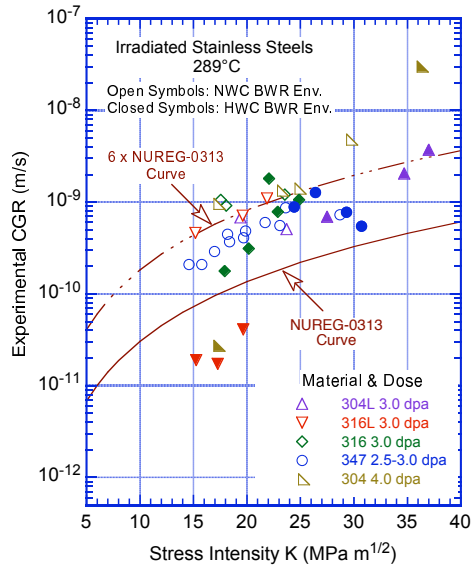
Figure 55.
CGR under constant load in NWC and HWC BWR environments at 289°C for austenitic stainless steels irradiated to 3.0-4.0 dpa (Refs. 56, 63, and present study).

(a)   (b)
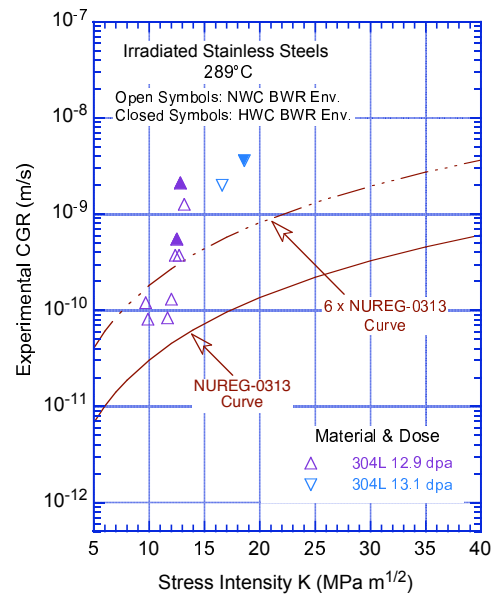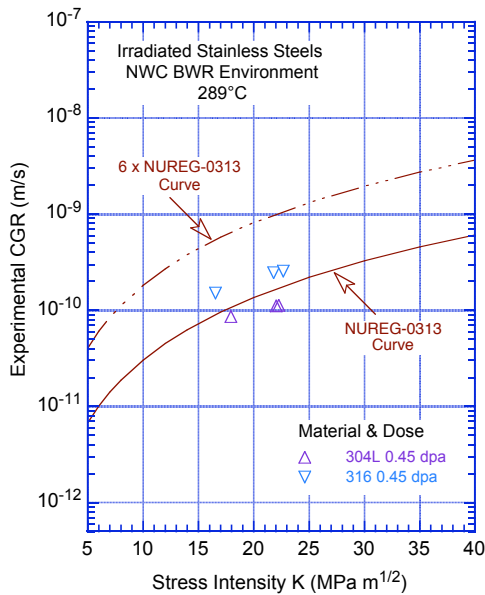
Figure 56. CGR under constant load in BWR environment at 289°C for austenitic stainless steels irradiated to (a) <0.5 dpa (present study) and (b) ≈13.0 dpa (Refs. 57, 63).

and are up to a factor of 30 higher than the NUREG-0313 curve. A beneficial effect of low corrosion potential was not observed for steels irradiated to 13.0 dpa.

The constant-load CGRs of austenitic SSs irradiated to 1.0-2.5, 3.0-4.0, and 13 dpa are plotted as a function of the steel ECP in Fig. 57. The effect of reduced corrosion potential on the CGRs of irradiated SSs is seen clearly in these figures. Decreasing the corrosion potential has a beneficial effect on growth rates for all steels irradiated to 1.0-2.5 dpa. A beneficial effect has been observed in a few cases for steels irradiated to 3.0-4.0 dpa, and in no cases for steels irradiated to 13 dpa. The fact that for some materials a beneficial effect is seen at one K level, but not at another higher K level, could be an indication of a loss of constraint or some kind of threshold phenomenon. The failure to see a benefit even at relatively low K levels at ≈13 dpa could be due to fluence effects on the constraint criteria or on the threshold effect.

55

(a)

(b)

(c)
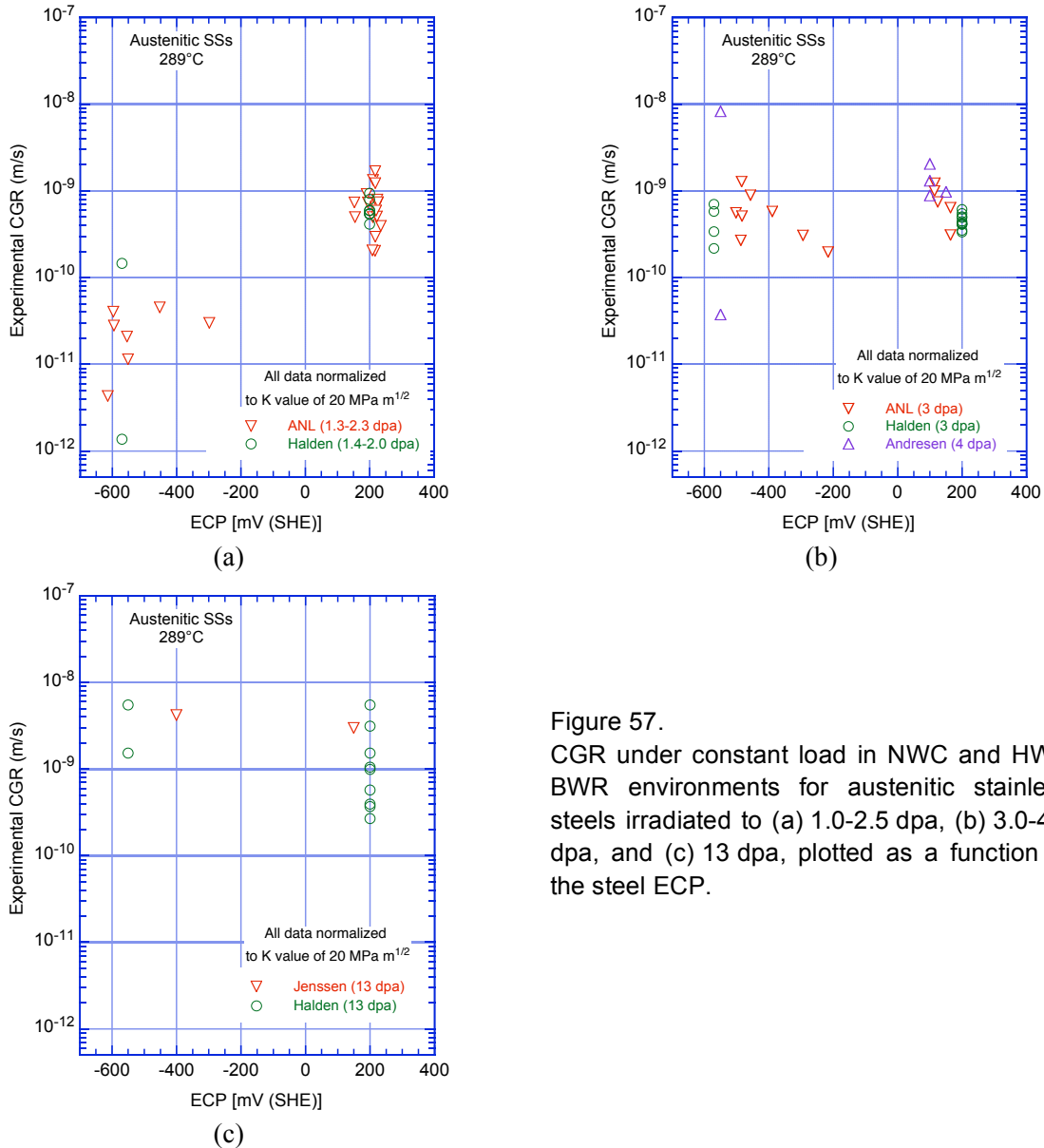
Figure 57.
CGR under constant load in NWC and HWC BWR environments for austenitic stainless steels irradiated to (a) 1.0-2.5 dpa, (b) 3.0-4.0 dpa, and (c) 13 dpa, plotted as a function of the steel ECP.

4.1.5 Specimen K/Size Criterion

For austenitic SSs irradiated to neutron dose levels of 3.0-4.0 dpa, there are only a few cases in the existing CGR data on irradiated austenitic SSs in simulated BWR environments that show a significant decrease in CGR when the DO is decreased from ≈300 ppb to <30 ppb. There are data for SSs irradiated to 3.0 dpa that show no decrease in CGR when the DO level is reduced to levels corresponding to HWC. However, it is not clear whether the loading conditions for these tests had satisfied the K/size validity criterion, because the appropriate criterion for K_{max} for highly irradiated materials is not clearly defined. The K/size validity issue is not well treated by the ASTM standards because irradiated materials undergo local (and macroscopic) work softening as the first dislocations sweep out the point defect damage (creating localized "channels" of high dislocation activity). Andresen has suggested a criterion based on the effective yield stress [defined as $(\sigma_{eff} = \sigma_{yirr} + \sigma_{ynonirr})/2$].[56] Jenssen et al.[57] proposed an even more restrictive criterion $\sigma_{eff} = (\sigma_{yirr} + \sigma_{ynonirr})/3$ for highly irradiated materials. Jenssen et al.[57] have

performed an FEM analysis of the plastic strain in front of a crack tip in a work softening material to help support their argument, but provide no criteria to determine how much plastic strain or what size plastic zone is acceptable, e.g, by comparison with plastic zones in specimens for nonirradiated materials that can be demonstrated to have sufficient constraint empirically by testing different specimen sizes. There appears to be an implicit assumption that if lowering the DO is effective at one K level and is not effective at another, higher K level, then it must be due to a loss of constraint without due consideration of the possibility of other effects. In this section, the current data are reviewed specifically in terms of the insight they can provide on the choice of specimen size criterion.

The experimental CGRs obtained in the present study under loading conditions that exceed the K/size criterion proposed by Andresen are shown in Fig. 58; the numbers next to the data points represent the value (in percentages) by which the applied K_{max} exceeded the allowed value. The significant results from these tests are summarized as follows:

(a)   For all tests in high-DO water, although the applied K_{max} exceeds the value allowed by the K/size criterion by up to ≈60%, the CGRs measured from these tests are consistent with the results from tests that meet the criterion. Also, the K dependence for these tests is consistent with that observed for valid tests (e.g., the data yield an exponent of ≈2.1). Furthermore, in high-DO water, the CGR did not increase during the test period (for up to 200 h). Typically, the CGR increases rapidly when the applied load exceeds the specimen K/size criterion; for a 1/2-T CT specimen of Type 304 SS irradiated to 4.0 dpa, the CGR increased by a factor 5 in a period of 40 h in high-DO water at 288°C and K_{max} of 29-34 MPa m$^{1/2}$.[56]

(b)   The two data points obtained in low-DO environment on Types 304L and 316 SS irradiated to 3.0 dpa and tested at 25-30 MPa m$^{1/2}$ (solid triangle and right-angle triangle in Fig. 58) did not show the expected decrease in CGR when the DO level in the environment was decreased. It is argued that because the expected decrease in growth rate is not observed for these tests, the loading conditions must have exceeded the specimen K/size criterion. For Type 304L SS irradiated to 3.0 dpa, Fig. 59 shows the change in crack length and K_{max} with time during periods 6 (≈200-311 h) and 7 (≈400-540 h). The results indicate no change in CGR during these test periods. A similar behavior was also observed for Type 316 SS. It is not clear whether this behavior should be
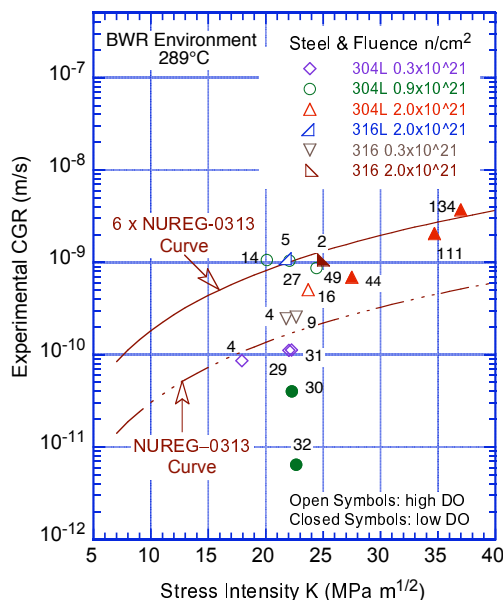
Figure 58.
Experimental CGRs for irradiated austenitic stainless steels obtained in high- and low-DO BWR environments under loading conditions that exceeded the K/size criterion. The numbers next to the data points represent the difference (percentages) between the applied and allowed K_{max}.

attributed to loss of specimen constraint. In both cases, the loading condition seems to have had no effect on growth rates until the DO level in the environment was decreased. If specimen constraint had been lost, the growth rate should have rapidly increased in high-DO water.
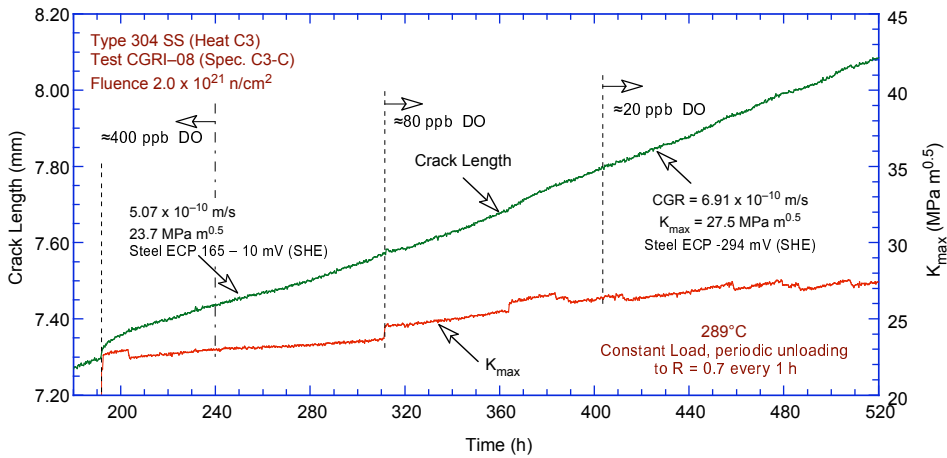
Figure 59. Crack length and K_{max} vs. time for Type 304L SS Specimen C3-C in high-purity water at 289°C during test periods 6 and 7.

(c)   The specimen constraints were lost for the irradiated Type 304L SS in low-DO water during test periods 8 and 9 at K_{max} >35 MPa m$^{1/2}$ (solid triangles in Fig. 58), as evidenced by unusually high growth rates. This behavior has been verified by fractographic examination of the specimen; under these loading conditions, the crack propagation was away from the normal plane.

A loss of specimen constraint can also influence the fracture mode and morphology. For example, if the thickness criterion is exceeded, the crack plane is typically out-of-normal near the edges of the specimen, and if the specimen ligament criterion is exceeded, the crack propagates away from the normal plane at an angle of 45°. The fracture surface of Specimen C3-C was examined to investigate any change in fracture morphology and/or change in the fracture plane. Figure 60 shows a side view of a 1-mm-wide slice of the fracture surface (along the entire crack advance) cut from Specimen C3-C. The fracture surface is towards the top, in a plane perpendicular to the picture. (Although precautions were taken to ensure that the specimen was square to the movement of the EDM wire, the cuts were not always straight; the bottom surface of this slice has an uneven cut.) The profile of the fracture surface indicates that the fracture plane is relatively straight and normal to the stress axis for the initial ≈3.5-mm crack extension. The DO level was decreased from ≈400 to 20 ppb at ≈1.7-mm crack extension, which is equivalent to the middle of the relatively straight crack extension. The fracture plane is out-of-normal for crack extensions greater than 3.5 mm. A secondary crack that propagated at an angle of ≈45° to the original fracture plane is also observed. This region corresponds to the crack advance during test period 9 (see Table A.3).
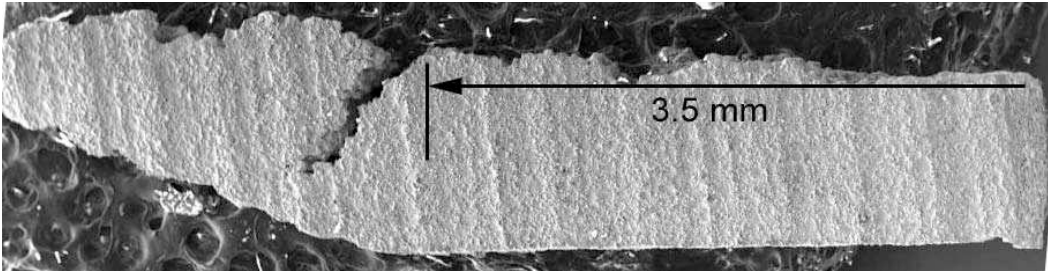
Figure 60.   Side view of the first slice cut from Type 304L SS Specimen C3-C.

58

These results indicate that the specimen ligament criterion, most likely, was exceeded during test periods 8 and 9; also, the CGRs during these periods were unusually high (Fig. 58).

A collage of images taken from the entire crack extension for the first slice is shown in Fig. 61a, and high-magnification photomicrographs of the surface at locations 2 and 1 are shown in Figs. 61b and c, respectively. After the initial ≈0.6-mm-long TG crack, the fracture morphology for the specimen is completely IG for the remainder of the test. The transition from a TG to IG fracture appears to have occurred at ≈80 h during test period 2. Locations 1 and 2 represent regions near the end of TG fracture and start of the IG fracture, respectively.

(a)

(b)

(c)
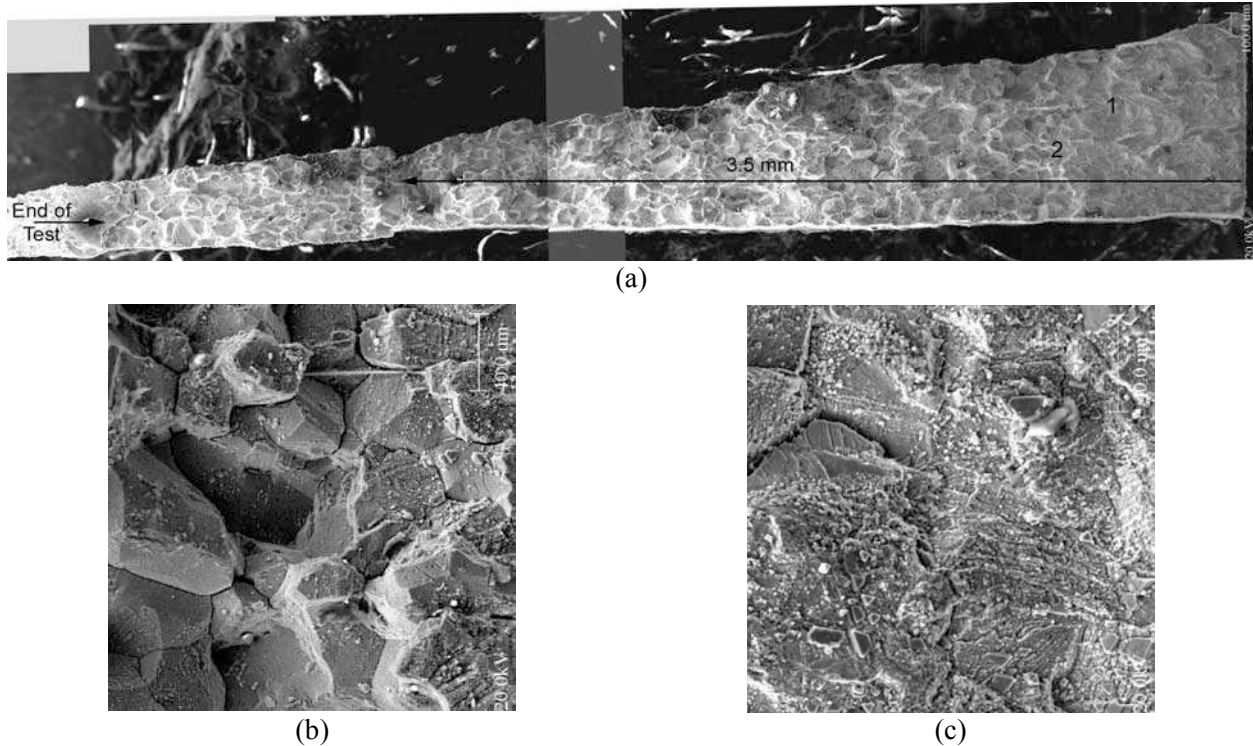
Figure 61. (a) A photograph of the entire crack extension for the first slice of Type 304L SS Specimen C3-C and high-magnification micrographs of the surface at locations 2 (b) and 1 (c).

A composite photograph of the fracture surface of a second slice from Specimen C3-C is shown in Fig. 62a, and high-magnification photomicrographs of the fracture surface at locations D, C, B, and A are shown in Figs. 62b, c, d, and e, respectively. These locations represent the fracture morphology during test periods 2, 3, 6, and 7, respectively. After the initial TG fracture during test period 1, the fracture morphology during all other test periods is completely IG. No fractographic indication of a change in fracture mode due to a loss in constraint is evident at the ≈1.6-mm crack extension. Also, the fracture morphology for test periods 6 and 7 (Figs. 62d and e) is the same.

Although the proposed specimen size criterion of Eq. 8 was not met for Specimen C3-C at the time when the DO level was decreased from ≈400 to 20 ppb (i.e., at ≈1.6-mm crack extension between test periods 6 and 7), there was no fractographic indication of a loss in constraint in the specimen (i.e., the fracture morphology did not change, and the fracture plane was straight and normal to the stress axis). Furthermore, the growth rate was constant in high-DO water during test period 6; if the applied K_{max} exceeded the specimen size criterion during periods 6 and 7, the CGR would be expected to have increased during test period 6.
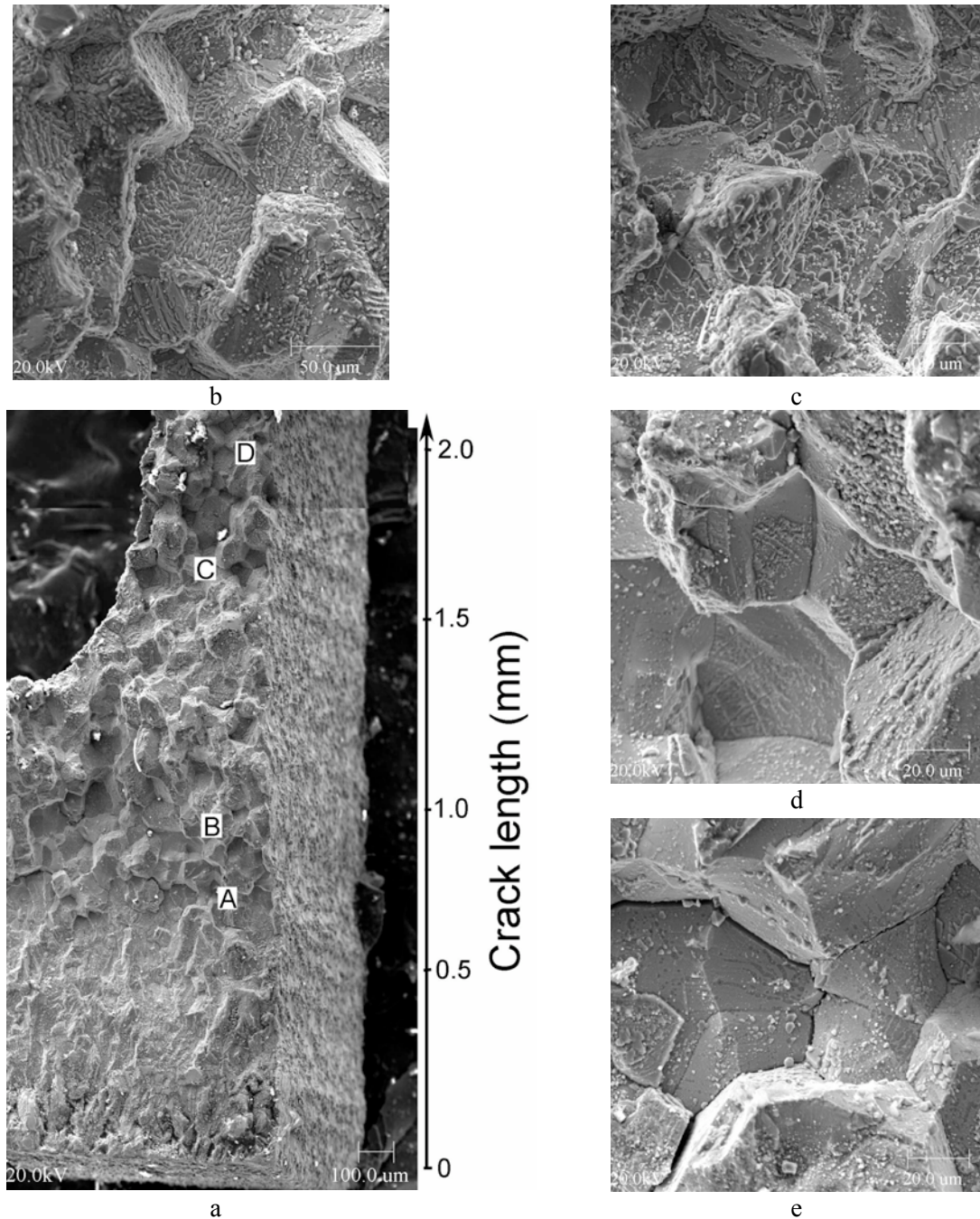
Figure 62.   (a) Photograph of the fracture surface of the second slice of Type 304L SS Specimen C3-C and high-magnification micrographs of the surface at locations (b) D, (c) C, (d) B, and (e) A.

The proposed K/size criterion is based on a weighted average of the irradiated and nonirradiated yield stress. The usual ASTM criteria consider only the yield strength of the actual material being tested. Pettersson[*] has presented three arguments against the proposed criterion.

---

[*]Kjell Pettersson, Matsafe AB, private communication, Nov. 2006, "Some Aspects of Specimen Size Validity and Crack Tip Strain Rate."

Firstly, Pettersson suggests that the strain softening in irradiated austenitic SSs is rarely more than 10-15%. This behavior is clearly demonstrated in the engineering stress vs. strain curves shown in Fig. 63 for Type 304 SS irradiated to 3.0 dpa in the Halden reactor at 288°C and tested in air at 289 and 325°C.[53] Secondly, in most of the plastic zone the plastic strains are so low that the material never passes the maximum tensile stress, so that it is effectively not a strain-softening material. Thirdly, finite element analyses indicate that the difference between the strain distributions ahead of an advancing crack, in a strain-hardening material versus a strain-softening material, is marginal (Fig. 64). These calculations do not support the suggestion that the nonirradiated yield strength should be involved in any calculations of specimen sizes for obtaining valid data.
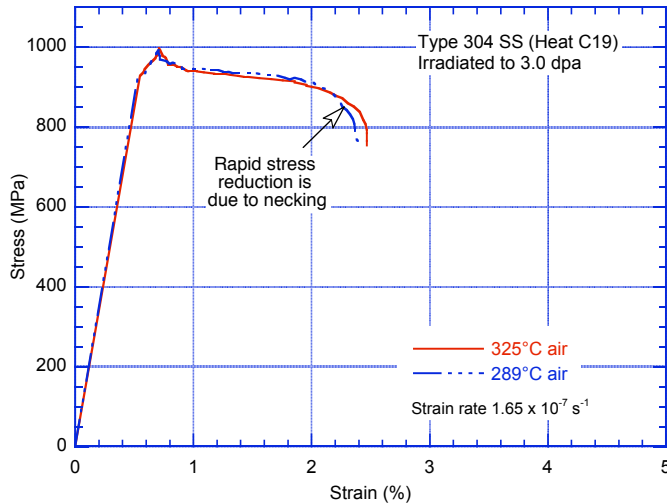
Figure 63.
Engineering stress vs. strain curve for Type 304 stainless steel irradiated to 3.0 dpa and tested in air at 289 and 325°C (Ref. 53).
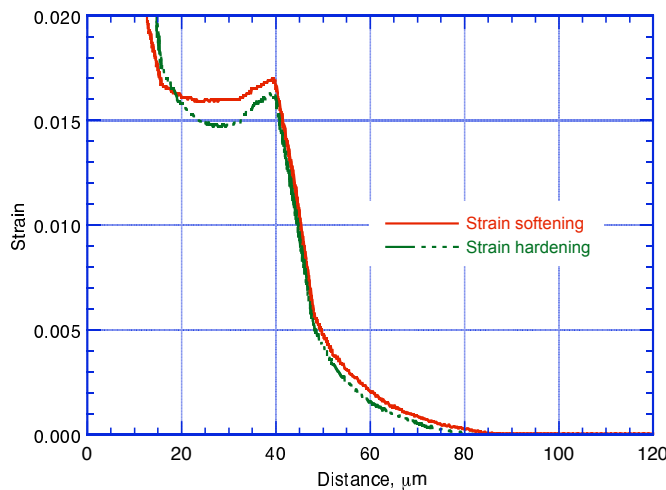
Figure 64.
Strain distribution of a moving crack in a strain-softening and a strain-hardening material.

The existing data for constant-load CGR in austenitic SSs irradiated up to 4.0 dpa indicate that all examples of unusually high growth rates, or lack of a benefit of HWC on growth rate, occur at a CGR of approximately 1×10^{-9} m/s. This growth rate seems to be necessary and possibly is associated with the mechanism responsible for the high rates in low-DO environments. Such a dependence of environmental effects on the rate of production of fresh surface has been observed in the enhancement of CGRs of carbon and low-alloy steels in low-DO environments.

4.2 CGRs under Continuous Cycling

The cyclic CGRs from the present study and those obtained earlier at ANL[27,54] are compiled in Table 15. The tests were conducted with either a triangular or slow/fast sawtooth waveform. The load ratio R was ≤0.3 for the triangular waveform and 0.3-0.7 for the sawtooth waveform. The rise time and return time for each loading waveform are listed in the table, as well as the stress intensity factors. The CGRs (da/dt) were determined by using only the rise time for the fatigue cycle. The CGRs in air, under the same loading conditions, were determined from the correlations developed by James and Jones[58] for solution-annealed SSs.

Table 15.   The cyclic crack growth data in BWR environment at 289°C.

Steel Type	Material[a]	Condition[b]	Heat[c]	Spec. ID	Dose, dpa	DO, ppb	ECP,[d] mV (SHE)	Rise Time, s	Return Time, s	K_{max}, MPa m$^{1/2}$	ΔK, MPa m$^{1/2}$	CGR, m/s	CGR$_{air}$, m/s
304L	Base	SA	C3	C3-A	0.45	300	166	0.5	0.5	14.0	9.8	8.37E-09	1.97E-08
304L	Base	SA	C3	C3-A	0.45	300	171	0.5	0.5	15.0	10.5	1.48E-08	2.51E-08
304L	Base	SA	C3	C3-A	0.45	300	171	1	1	15.9	11.1	1.39E-08	1.50E-08
304L	Base	SA	C3	C3-A	0.45	300	171	30	4	16.0	11.2	1.33E-09	5.17E-10
304L	Base	SA	C3	C3-A	0.45	300	177	300	4	15.9	11.3	3.29E-10	5.24E-11
304L	Base	SA	C3	C3-A	0.45	300	173	300	4	15.7	8.2	4.75E-11	2.17E-11
304L	Base	SA	C3	C3-A	0.45	300	188	12	12	17.6	5.3	6.23E-11	1.57E-10
304L	Base	SA	C3	C3-B	1.35	300	147	0.5	0.5	18.7	15.0	4.51E-08	7.07E-08
304L	Base	SA	C3	C3-B	1.35	300	148	0.5	0.5	17.6	14.1	4.17E-08	5.83E-08
304L	Base	SA	C3	C3-B	1.35	300	(148)	30	2	16.9	7.9	1.12E-10	2.09E-10
304L	Base	SA	C3	C3-B	1.35	300	(148)	0.5	0.5	17.9	14.3	3.41E-08	6.12E-08
304L	Base	SA	C3	C3-B	1.35	300	154	0.5	0.5	19.1	15.3	6.83E-08	7.63E-08
304L	Base	SA	C3	C3-B	1.35	300	189	60	2	19.0	9.3	1.75E-10	1.72E-10
304L	Base	SA	C3	C3-B	1.35	300	187	300	2	19.8	5.9	6.38E-10	9.26E-12
304L	Base	SA	C3	C3-B	1.35	≈10	-607	300	2	22.1	6.6	8.56E-11	1.33E-11
304L	Base	SA	C3	C3-B	1.35	≈10	-609	300	2	22.5	6.8	3.37E-11	1.42E-11
304L	Base	SA	C3	C3-B	1.35	≈10	-620	1000	2	23.0	6.9	1.20E-11	4.59E-12
304L	Base	SA	C3	C3-B	1.35	≈10	-624	30	2	22.9	6.9	5.17E-11	1.49E-10
304L	Base	SA	C3	C3-B	1.35	≈10	-617	300	2	23.1	6.9	1.55E-11	1.54E-11
304L	Base	SA	C3	C3-B	1.35	250	151	1000	2	24.2	7.3	5.93E-10	5.38E-12
304L	Base	SA	C3	C3-C	3.00	300	164	2	2	17.9	13.2	2.00E-08	1.27E-08
304L	Base	SA	C3	C3-C	3.00	300	155	30	2	18.4	8.7	2.22E-09	2.77E-10
304L	Base	SA	C3	C3-C	3.00	300	167	300	2	18.8	5.6	1.73E-09	7.83E-12
304L	Base	SA	C3	C3-C	3.00	300	164	1000	2	19.2	6.0	1.25E-09	2.79E-12
316L	Base	SA	C16	C16-B	3.00	250	(144)	1	1	14.3	9.8	1.75E-08	9.96E-09
316L	Base	SA	C16	C16-B	3.00	250	144	2	2	14.0	9.8	7.54E-09	4.94E-09
316L	Base	SA	C16	C16-B	3.00	250	144	2	2	14.2	9.8	8.94E-09	5.00E-09
316L	Base	SA	C16	C16-B	3.00	250	148	12	2	14.6	6.4	4.94E-10	2.67E-10
316L	Base	SA	C16	C16-B	3.00	250	147	30	2	14.8	4.0	8.65E-10	2.54E-11
316L	Base	SA	C16	C16-B	3.00	250	151	300	2	15.0	4.4	8.16E-10	3.34E-12
316L	Base	SA	C16	C16-B	3.00	250	153	1,000	12	15.0	4.5	7.33E-10	1.12E-12
316L	Base	SA	C16	C16-B	3.00	<30	-410	1,000	12	15.1	4.5	2.76E-11	1.15E-12
316L	Base	SA	C16	C16-B	3.00	<30	-449	30	2	15.2	4.1	6.07E-11	2.79E-11
316L	Base	SA	C16	C16-B	3.00	<30	-502	30	2	17.3	5.2	2.51E-10	5.92E-11
316L	Base	SA	C16	C16-B	3.00	<30	-545	1,000	12	17.2	5.3	3.59E-11	1.95E-12
316	Base	SA	C21	C21-A	0.45	350	(105)	0.5	0.5	15.5	10.1	1.10E-08	2.30E-08
316	Base	SA	C21	C21-A	0.45	350	103	5	5	15.7	10.3	5.69E-09	2.47E-09
316	Base	SA	C21	C21-A	0.45	350	116	30	4	16.0	7.9	1.33E-09	1.98E-10
316	Base	SA	C21	C21-A	0.45	350	(160)	300	12	16.1	7.6	3.82E-10	1.78E-11
316	Base	SA	C21	C21-A	0.45	350	(160)	300	12	16.2	5.0	1.10E-10	5.28E-12
316	Base	SA	C21	C21-A	0.45	350	(160)	1,000	12	16.3	4.9	5.84E-11	1.45E-12
316	Base	SA	C21	C21-B	1.35	350	(180)	0.5	0.5	15.9	10.6	2.63E-08	2.70E-08
316	Base	SA	C21	C21-B	1.35	350	185	300	12	16.0	8.0	5.85E-10	2.10E-11
316	Base	SA	C21	C21-B	1.35	350	191	300	12	16.3	4.7	5.40E-10	4.39E-12
316	Base	SA	C21	C21-B	1.35	350	204	1000	12	16.2	4.9	4.91E-10	1.44E-12

Table 15.   (Contd.)

Steel Type	Material[a]	Condition[b]	Heat[c]	Spec. ID	Dose, dpa	DO, ppb	ECP,[d] mV (SHE)	Rise Time, s	Return Time, s	K_{max}, MPa m$^{1/2}$	ΔK, MPa m$^{1/2}$	CGR, m/s	CGR$_{air}$, m/s
316	Base	SA	C21	C21-C	3.00	500	(230)	0.5	0.5	15.5	10.4	4.87E-08	2.47E-08
316	Base	SA	C21	C21-C	3.00	500	(230)	30	5	15.7	7.5	3.12E-09	1.74E-10
316	Base	SA	C21	C21-C	3.00	500	(230)	300	4	16.5	8.1	2.84E-09	2.18E-11
316	Base	SA	C21	C21-C	3.00	500	(230)	1000	12	17.0	4.9	3.22E-09	1.53E-12
304	Base	Sensitized	10285	85-3TT	2.16	500	(220)	0.33	0.5	14.9	8.7	1.64E-08	2.28E-08
304	Base	Sensitized	10285	85-3TT	2.16	500	218	142	4	15.3	4.0	1.02E-09	5.37E-12
304	Base	Sensitized	10285	85-3TT	2.16	500	(220)	13.7	4	15.4	3.8	3.16E-09	5.03E-11
304	Base	Sensitized	10285	85-3TT	2.16	500	(220)	140	12	15.7	0.8	2.22E-10	1.31E-13
304L	SAW HAZ	As welded	GG shroud	GG5B-A	0.00	580	(230)	0.25	0.25	16.7	12.9	7.57E-08	8.98E-08
304L	SAW HAZ	As welded	GG shroud	GG5B-A	0.00	580	(230)	0.25	0.25	15.0	11.5	3.42E-08	6.18E-08
304L	SAW HAZ	As welded	GG shroud	GG5B-A	0.00	590	(230)	7.5	7.5	14.2	11.0	3.59E-10	1.75E-09
304L	SAW HAZ	As welded	GG shroud	GG5B-A	0.00	590	(230)	0.5	0.5	15.7	12.1	3.40E-08	3.62E-08
304L	SAW HAZ	As welded	GG shroud	GG5B-A	0.00	485	(220)	30	2	15.5	7.4	5.85E-11	1.65E-10
304L	SAW HAZ	As welded	GG shroud	GG5B-A	0.00	440	(220)	30	2	17.0	4.9	1.50E-12	5.04E-11
304L	SAW HAZ	As welded	GG shroud	GG5B-A	0.00	450	(220)	30	2	17.0	4.9	1.52E-11	5.06E-11
304L	SAW HAZ	As welded	GG shroud	GG5B-A	0.00	465	(220)	30	2	20.6	5.8	3.15E-10	8.49E-11
304L	SAW HAZ	As welded	GG shroud	GG5B-A	0.00	460	(220)	300	2	20.8	6.0	1.81E-10	9.89E-12
304L	SAW HAZ	As welded	GG shroud	GG5B-A	0.00	500	(220)	1,000	2	20.9	6.1	1.26E-10	3.01E-12
304L	SAW HAZ	As welded	GG shroud	GG5B-A	0.00	500	(220)	1000	2	27.4	7.9	3.18E-10	7.32E-12
304L	SAW HAZ	AW + TT	GG shroud	GG3B-A-TT	0.00	450	(220)	0.5	0.5	14.3	9.9	7.71E-09	2.06E-08
304L	SAW HAZ	AW + TT	GG shroud	GG3B-A-TT	0.00	450	(220)	5	5	14.4	10.0	5.91E-09	2.10E-09
304L	SAW HAZ	AW + TT	GG shroud	GG3B-A-TT	0.00	450	(220)	1	1	15.0	7.4	1.34E-09	4.79E-09
304L	SAW HAZ	AW + TT	GG shroud	GG3B-A-TT	0.00	470	(220)	12	2	16.0	4.6	8.66E-10	1.03E-10
304L	SAW HAZ	AW + TT	GG shroud	GG3B-A-TT	0.00	470	(220)	12	2	16.3	4.7	2.50E-09	1.10E-10
304L	SAW HAZ	AW + TT	GG shroud	GG3B-A-TT	0.00	470	(220)	30	2	16.5	4.8	1.22E-09	4.57E-11
304L	SAW HAZ	AW + TT	GG shroud	GG3B-A-TT	0.00	450	(220)	300	2	16.7	5.0	2.80E-10	5.25E-12
304L	SAW HAZ	AW + TT	GG shroud	GG3B-A-TT	0.00	400	(220)	1,000	12	16.7	5.0	1.12E-10	1.57E-12
304	SMAW HAZ	As welded	10285	85-YA	0.00	300	(180)	0.5	0.5	16.2	10.8	4.73E-08	2.84E-08
304	SMAW HAZ	As welded	10285	85-YA	0.00	300	(180)	10	10	16.7	11.2	5.72E-09	1.60E-09
304	SMAW HAZ	As welded	10285	85-YA	0.00	300	(180)	300	12	16.7	8.0	2.19E-11	2.12E-11
304	SMAW HAZ	As welded	10285	85-YA	0.00	300	(180)	30	12	16.7	8.0	2.51E-10	2.15E-10
304	SMAW HAZ	As welded	10285	85-YA	0.00	300	(180)	30	12	19.2	9.2	6.21E-10	3.39E-10
304	SMAW HAZ	As welded	10285	85-YA	0.00	300	(180)	300	12	19.3	9.5	3.68E-10	3.66E-11
304	SMAW HAZ	As welded	10285	85-YA	0.00	300	(180)	1,000	12	19.8	9.7	1.85E-10	1.19E-11
304	SMAW HAZ	AW + TT	10285	85-3A-TT	0.00	690	(230)	0.5	0.5	16.1	12.7	5.46E-08	4.21E-08
304	SMAW HAZ	AW + TT	10285	85-3A-TT	0.00	650	(230)	0.5	0.5	15.0	11.9	5.00E-08	3.32E-08
304	SMAW HAZ	AW + TT	10285	85-3A-TT	0.00	600	(230)	30	2	14.6	7.2	5.61E-11	1.47E-10
304	SMAW HAZ	AW + TT	10285	85-3A-TT	0.00	600	(230)	30	2	16.7	8.2	5.50E-10	2.28E-10
304	SMAW HAZ	AW + TT	10285	85-3A-TT	0.00	600	(230)	30	2	16.9	4.9	3.16E-11	4.96E-11
304	SMAW HAZ	AW + TT	10285	85-3A-TT	0.00	600	(230)	30	2	19.8	5.8	8.85E-10	8.39E-11
304	SMAW HAZ	AW + TT	10285	85-3A-TT	0.00	600	(230)	300	2	19.8	5.7	2.75E-10	8.37E-12
304	SMAW HAZ	AW + TT	10285	85-3A-TT	0.00	600	(230)	300	2	20.2	5.9	7.91E-10	8.99E-12
304	SMAW HAZ	AW + TT	10285	85-3A-TT	0.00	600	(230)	1,000	2	20.5	6.2	4.57E-10	3.13E-12
304L	SAW HAZ	As welded	GG shroud	GG5T-A	0.75	250	205	0.5	0.5	12.4	10.3	1.71E-08	1.97E-08
304L	SAW HAZ	As welded	GG shroud	GG5T-A	0.75	250	205	0.5	0.5	12.3	8.9	3.11E-09	1.39E-08
304L	SAW HAZ	As welded	GG shroud	GG5T-A	0.75	250	201	0.5	0.5	12.8	8.9	2.70E-09	1.45E-08
304L	SAW HAZ	As welded	GG shroud	GG5T-A	0.75	250	201	0.5	0.5	13.5	9.2	1.06E-08	1.64E-08
304L	SAW HAZ	As welded	GG shroud	GG5T-A	0.75	250	195	60	4	14.3	6.9	4.30E-11	6.35E-11
304L	SAW HAZ	As welded	GG shroud	GG5T-A	0.75	250	195	60	4	15.3	7.4	1.61E-09	8.04E-11
304L	SAW HAZ	As welded	GG shroud	GG5T-A	0.75	250	196	300	4	14.7	4.6	3.34E-10	3.85E-12
304L	SAW HAZ	As welded	GG shroud	GG5T-A	0.75	250	196	1,000	12	14.7	4.6	3.89E-10	1.15E-12
304L	SAW HAZ	As welded	GG shroud	GG5T-A	0.75	250	196	60	12	15.3	4.6	3.10E-11	1.98E-11
304L	SAW HAZ	As welded	GG shroud	GG5T-A	0.75	250	199	60	12	16.6	4.8	8.03E-11	2.36E-11
304L	SAW HAZ	As welded	GG shroud	GG5T-A	0.75	250	193	30	4	16.6	8.1	8.57E-11	2.22E-10
304L	SAW HAZ	As welded	GG shroud	GG5T-B	0.75	400	211	0.5	0.5	13.8	11.0	7.24E-09	2.56E-08
304L	SAW HAZ	As welded	GG shroud	GG5T-B	0.75	400	200	0.5	0.5	13.0	9.1	4.59E-09	1.55E-08
304L	SAW HAZ	As welded	GG shroud	GG5T-B	0.75	350	206	60	4	12.8	6.4	1.50E-12	4.93E-11
304L	SAW HAZ	As welded	GG shroud	GG5T-B	0.75	350	199	30	4	14.4	7.1	9.13E-10	1.39E-10

Table 15.   (Contd.)

Steel Type	Material[a]	Condition[b]	Heat[c]	Spec. ID	Dose, dpa	DO, ppb	ECP,[d] mV (SHE)	Rise Time, s	Return Time, s	K_{max}, MPa m$^{1/2}$	ΔK, MPa m$^{1/2}$	CGR, m/s	CGR$_{air}$, m/s
304L	SAW HAZ	As welded GG shroud	GG5T-B	0.75	350	199	300	4	14.7	7.5	2.82E-10	1.67E-11
304L	SAW HAZ	As welded GG shroud	GG5T-B	0.75	350	200	300	4	14.8	4.4	2.35E-10	3.53E-12
304L	SAW HAZ	As welded GG shroud	GG5T-B	0.75	350	200	1,000	12	14.7	4.7	2.98E-10	1.26E-12
304L	SAW HAZ	As welded GG shroud	GG5T-B	0.75	<50	-530	300	122	15.0	4.6	1.50E-12	4.08E-12
304L	SAW HAZ	As welded GG shroud	GG6T-A	2.16	600	232	0.18	0.18	15.2	11.2	4.54E-08	8.20E-08
304L	SAW HAZ	As welded GG shroud	GG6T-A	2.16	600	230	38	2.5	15.0	7.1	1.50E-12	1.12E-10
304L	SAW HAZ	As welded GG shroud	GG6T-A	2.16	600	229	0.18	0.18	15.3	10.9	5.93E-10	7.68E-08
304L	SAW HAZ	As welded GG shroud	GG6T-A	2.16	600	223	7.3	7.3	15.5	11.0	3.91E-10	1.97E-09
304L	SAW HAZ	As welded GG shroud	GG6T-A	2.16	600	223	7.4	2.5	15.4	6.6	1.44E-09	4.79E-10
304L	SAW HAZ	As welded GG shroud	GG6T-A	2.16	600	222	37	2.5	15.4	6.6	6.29E-10	9.69E-11
304L	SAW HAZ	As welded GG shroud	GG6T-A	2.16	600	220	168	6.7	16.3	5.4	7.85E-10	1.15E-11
304L	SAW HAZ	As welded GG shroud	GG6T-A	2.16	600	222	559	6.7	16.1	5.3	6.08E-10	3.38E-12
304	SMAW HAZ	As welded	10285	85-7A	0.75	500	224	0.5	0.5	15.9	12.2	2.77E-08	3.77E-08
304	SMAW HAZ	As welded	10285	85-7A	0.75	500	225	60	4	15.8	7.9	1.50E-12	9.94E-11
304	SMAW HAZ	As welded	10285	85-7A	0.75	500	219	300	4	15.7	7.7	2.09E-11	1.83E-11
304	SMAW HAZ	As welded	10285	85-7A	0.75	500	221	1,000	12	16.4	8.2	1.50E-12	6.71E-12
304	SMAW HAZ	As welded	10285	85-7A	0.75	500	211	1,000	12	17.2	8.1	4.65E-11	6.66E-12
304	SMAW HAZ	As welded	10285	85-7A	0.75	500	209	1,000	12	18.3	9.1	4.28E-10	9.69E-12
304	SMAW HAZ	As welded	10285	85-XA	2.16	500	205	0.16	0.5	13.3	7.7	1.86E-08	3.17E-08
304	SMAW HAZ	As welded	10285	85-XA	2.16	500	240	26	4	13.9	3.6	2.21E-09	2.13E-11
304	SMAW HAZ	As welded	10285	85-XA	2.16	500	236	433	4	13.0	3.6	7.07E-10	1.28E-12
304	SMAW HAZ	AW + TT	10285	85-1A-TT	0.75	200	163	0.25	0.25	13.9	11.6	2.64E-08	5.81E-08
304	SMAW HAZ	AW + TT	10285	85-1A-TT	0.75	200	161	0.5	0.5	13.3	10.1	2.10E-08	2.04E-08
304	SMAW HAZ	AW + TT	10285	85-1A-TT	0.75	200	166	60	4	14.6	7.3	1.50E-12	7.76E-11
304	SMAW HAZ	AW + TT	10285	85-1A-TT	0.75	200	175	1,000	4	15.1	7.6	4.80E-10	5.20E-12
304	SMAW HAZ	AW + TT	10285	85-1A-TT	0.75	250	178	300	4	16.1	4.8	3.55E-10	4.66E-12
304	SMAW HAZ	AW + TT	10285	85-1A-TT	0.75	250	172	1,000	12	16.4	4.7	3.37E-10	1.33E-12
CF-8M	Cast SS	Aged	75	75-11TT	2.46	600	201	0.14	0.14	11.3	6.1	2.70E-08	1.76E-08
CF-8M	Cast SS	Aged	75	75-11TT	2.46	600	234	0.14	0.14	11.2	6.2	2.69E-09	1.79E-08
CF-8M	Cast SS	Aged	75	75-11TT	2.46	600	232	14.3	14.3	11.2	6.1	5.35E-11	1.73E-10
CF-8M	Cast SS	Aged	75	75-11TT	2.46	600	236	0.13	0.13	11.2	4.7	3.52E-09	9.02E-09
CF-8M	Cast SS	Aged	75	75-11TT	2.46	600	232	18	4	10.8	1.9	1.48E-10	7.08E-12
CF-8M	Cast SS	Aged	75	75-11TT	2.46	600	233	17.2	2.3	13.4	6.3	4.38E-10	1.70E-10
CF-8M	Cast SS	Aged	75	75-11TT	2.46	600	229	34.8	7	13.5	6.4	5.69E-11	8.61E-11
CF-8M	Cast SS	Aged	75	75-11TT	2.46	600	221	155	6.2	15.4	4.9	1.39E-11	9.49E-12
CF-8M	Cast SS	Aged	75	75-11TT	2.46	600	222	7.7	1.3	17.1	8.5	8.55E-10	1.00E-09
CF-8M	Cast SS	Aged	75	75-11TT	2.46	600	225	177	7	17.1	6.9	3.10E-11	2.32E-11
CF-8M	Cast SS	Aged	75	75-11TT	2.46	600	225	7.7	1.3	17.1	8.5	9.64E-10	1.00E-09
CF-8M	Cast SS	Aged	75	75-11TT	2.46	600	224	77	2.6	17.3	8.6	2.50E-10	1.05E-10
CF-8M	Cast SS	Aged	75	75-11TM	2.46	600	229	0.17	0.17	15.0	7.6	3.02E-08	3.12E-08
CF-8M	Cast SS	Aged	75	75-11TM	2.46	600	230	37	2.5	14.6	6.0	6.43E-10	7.10E-11
CF-8M	Cast SS	Aged	75	75-11TM	2.46	600	229	159	6.4	14.8	4.1	3.61E-10	5.40E-12
CF-8M	Cast SS	Aged	75	75-11TM	2.46	600	228	435	5.2	14.9	2.8	2.84E-10	8.80E-13

[a]SAW = submerged arc weld; SMAW = shielded metal arc weld; HAZ = heat affected zone.
[b]AW = as welded; TT = thermally treated.
[c]GG = Grand Gulf core shroud shell.
[d]Measured with an SS electrode located in the exit of the autoclave; the values within parentheses are estimated values.

4.2.1   Solution-Annealed Materials

Under continuous cyclic loading, the experimental CGRs and those predicted in air for the same loading conditions for solution-annealed Types 304 and 316 SSs irradiated up to 3 dpa and tested in high- and low-DO environments are plotted in Fig. 65. The curves in the figures are based on the superposition model (Eq. 10). The cyclic CGRs in air ($\dot{a}_{air}$) were determined from Eq. 11 developed by James and Jones.[58] The corrosion fatigue contribution ($\dot{a}_{cf}$) was determined from the Shack/Kassner model for nonirradiated SSs in high-purity water with either 8 or 0.2 ppm DO (Eqs. 14 and 15, respectively),[59] and

the SCC contribution ($\dot{a}_{scc}$) was determined from Eq. 16.[60] As discussed in the previous section, the CGR for SCC in SSs irradiated to >0.75 dpa was assumed to be a factor of six higher than that predicted by Eq. 16; as a result, the constant A in the equation was taken to be 1.26 x 10^{-12} for irradiated SSs. For cyclic loading using either a triangular or a slow/fast sawtooth waveform, $\dot{a}_{scc}$ is determined by considering the contribution of SCC during the slow rise time of the cycle; an equivalent K_{max} is computed to determine the contribution of fatigue loading. The average values of K_{max} used in calculating the superposition curves are given in the figure.
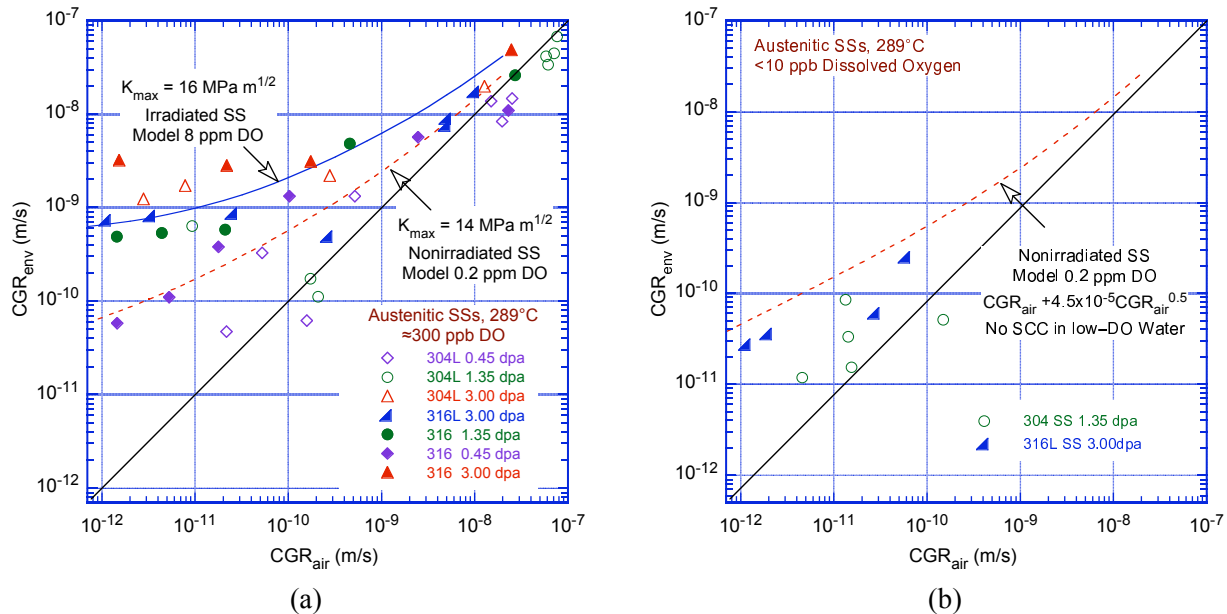
Figure 65. CGR for irradiated specimens of austenitic SSs under continuous cycling at 289°C in high-purity water with (a) ≈300 ppb and (b) <30 ppb dissolved oxygen.

In these figures, the data points that lie along the diagonal represent predominantly mechanical fatigue, and those that lie close to the model curve indicate environmentally enhanced crack growth. Austenitic SS irradiated to 0.45 dpa shows very little environmental enhancement of CGRs in high-DO water (open and closed diamonds in Fig. 65a). For austenitic SSs irradiated to less than 0.5 dpa, the fatigue CGRs in water with ≈ 300 ppb DO may be represented by superposition of the NUREG-0313 curve for nonirradiated SSs[60] and by the Shack/Kassner model for nonirradiated austenitic SSs in high-purity water with 0.2 ppm DO.[59]

The results for SSs irradiated to 1.35 or 3.0 dpa indicate significant enhancement of the CGRs in high-DO water under cyclic loading with long rise times. For austenitic SSs irradiated to 0.75-3.0 dpa, the fatigue CGRs in water with ≈ 300 ppb DO may be represented by superposition of the SCC curve for irradiated SSs (i.e., six times the NUREG-0313 curve) and by the Shack/Kassner model for nonirradiated SSs in high-purity water with 8 ppm DO.[59]

For continuous cyclic loading, decreasing the DO level has a beneficial effect on the CGRs of irradiated SSs; for example, decreasing the DO from ≈300 ppb DO to <30 ppb DO lowers the CGR by a factor of 25. At 289°C, the fatigue CGRs for irradiated austenitic SSs in water with <30 ppb DO are lower than those predicted by the Shack/Kassner model for nonirradiated austenitic SSs in high-purity water with 0.2 ppm DO (Fig. 65b);[59] there is no contribution of SCC in low-DO water.

4.2.2   Stainless Steel Weld HAZ Materials

4.2.2.1   Air Environment

The experimental CGRs for SS weld HAZ materials under continuous cycling in air and those predicted for austenitic SSs under the same loading conditions are plotted in Fig. 66. Data obtained in the NWC BWR environment on the same materials are also included in the figure for comparison (open symbols). The results indicate that irradiation up to ≈2.16 dpa has no effect on the fatigue CGRs of SS weld HAZ materials in air. In fact, the CGRs of irradiated material are slightly lower than those predicted by the correlations developed by James and Jones[58] for nonirradiated solution-annealed SSs (i.e., the experimental CGRs of irradiated SS weld HAZ are below the diagonal in Fig. 66).
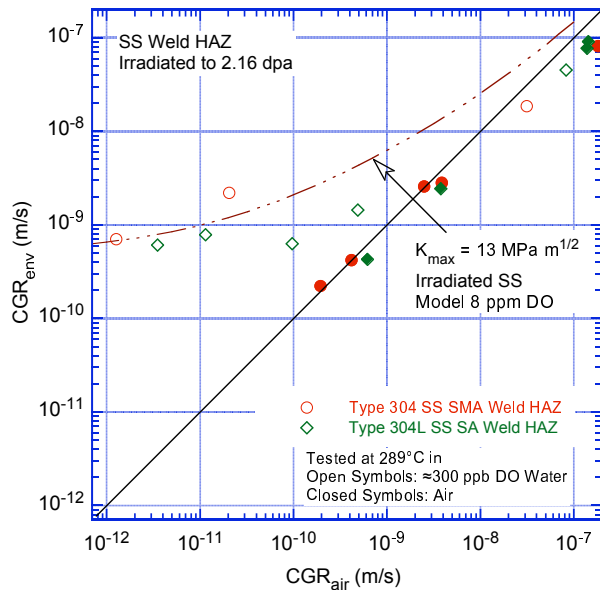
Figure 66.
CGR data under cyclic loading for irradiated SS weld HAZ materials in air and high-purity water at 289°C.

4.2.2.2   Simulated BWR Environment

The experimental CGRs for nonirradiated SS weld HAZ materials in high-DO water[54] and those predicted in air for the same loading conditions are plotted in Fig. 67; the loading conditions for the data points shown with a "+" did not satisfy the K/size criterion of ASTM E-647. The two curves in the figure are based on the superposition model. For the nonirradiated HAZ materials, the growth rate did not increase readily when the load ratio and rise time were increased. For example, a large number of data points lie along or below the diagonal in Fig. 67. The applied K_{max} had to be increased for environmental enhancement.

In general, the fatigue CGRs of the nonirradiated HAZ materials in water with 300-500 ppb DO are greater than those predicted by the Shack/Kassner model in high-purity water with 0.2 ppm DO and lower than those predicted with 8 ppm DO.[59] The fatigue CGRs of nonirradiated SS weld HAZ materials may be conservatively represented by superposition of the SCC curve for nonirradiated SSs and the Shack/Kassner model for austenitic SSs in high-purity water with 8 ppm DO. The results also indicate that thermal treatment of the material for 24 h at 500°C has little or no effect on growth rates.
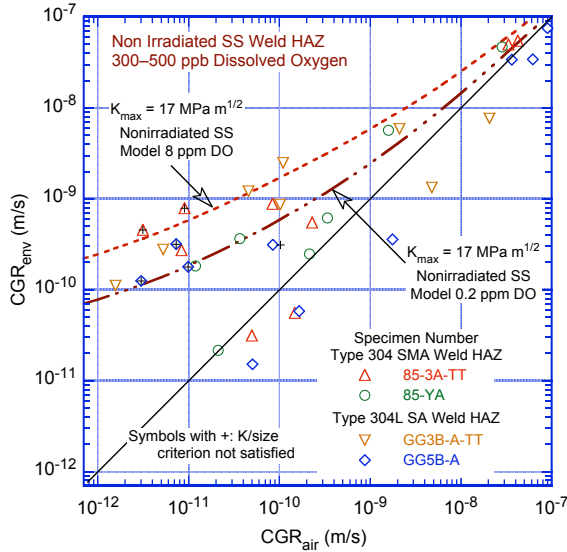
Figure 67.
CGR data under cyclic loading for nonirradiated SS weld HAZ materials in high-purity water at 289°C.

The experimental CGRs for irradiated GG Type 304L SA weld HAZ and laboratory-prepared Type 304 SMA weld HAZ in high-DO water and those predicted in air for the same loading conditions are plotted in Figs. 68a and 68b, respectively. The curve in the figures is based on the superposition model (Eq. 10). The results indicate significant environmental enhancement of CGRs for HAZ materials irradiated to 0.75 or 2.16 dpa. The CGRs of the GG Type 304L weld HAZ are slightly lower than those of the Type 304 SMA weld HAZ. The fatigue CGRs of SS weld HAZ materials irradiated to 0.75-2.16 dpa in water containing ≈ 500 ppb DO can be represented by superposition of the SCC curve for irradiated SSs (i.e., six times the NUREG-0313 curve) and the Shack/Kassner model for nonirradiated austenitic SSs in high-purity water with 8 ppm DO.[59] The estimates may be somewhat conservative for Type 304L weld HAZ materials.

(a)

(b)
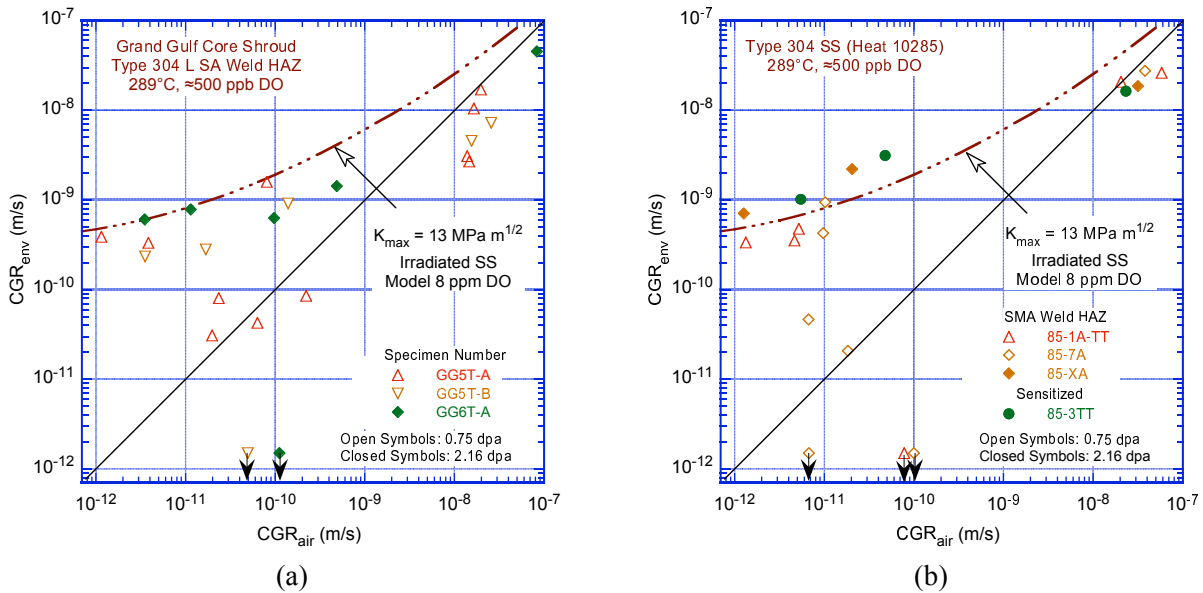
Figure 68. CGR for irradiated specimens of (a) Type 304L SA weld HAZ from the Grand Gulf core shroud and (b) laboratory-prepared Type 304 SS SMA weld HAZ under continuous cycling in high-purity water at 289°C.

67

4.2.3   Cast Austenitic Stainless Steels

The experimental CGRs for CF-8M cast austenitic SS under continuous cycling in the NWC BWR environment and those predicted for austenitic SSs under the same loading conditions in air are plotted in Fig. 69. The two curves in the figure are based on the superposition model. The material was thermally aged for 10,000 h at 400°C and then irradiated to 2.46 dpa at ≈300°C. As seen before for nonirradiated HAZ materials (Fig. 67), environmental enhancement of CGRs did not occur readily for Specimen 75-11TT when the load ratio and rise time were increased; for this specimen, a large number of data points lie along the diagonal in Fig. 69. The applied K_{max} had to be increased for environmental enhancement.

Under similar loading and environmental conditions, the fatigue CGRs of CF-8M cast austenitic SS appear to be lower than those of wrought SSs or SS weld HAZ materials. Limited data indicate that the fatigue CGRs of SS weld HAZ materials irradiated to 0.75-2.46 dpa in water containing ≈ 300 ppb DO can be represented by superposition of the SCC curve for irradiated SSs (i.e., six times the NUREG-0313 curve) and the Shack/Kassner model for nonirradiated austenitic SSs in high-purity water with 0.2 ppm DO.[59]
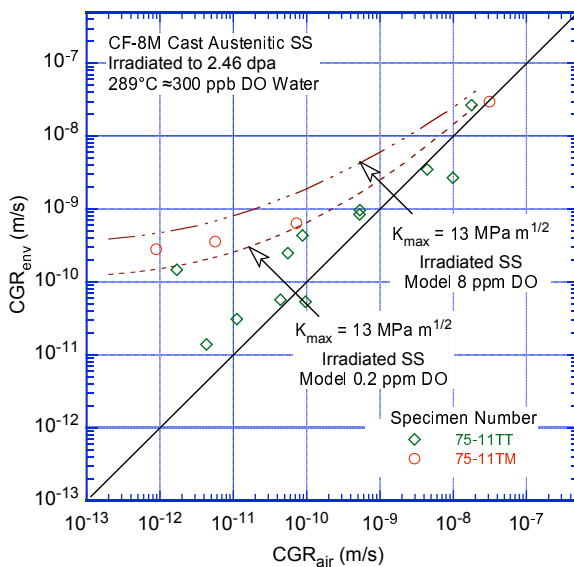
Figure 69.
CGR data under cyclic loading for irradiated CF-8M cast austenitic SS in high-purity water at 289°C.

4.3   Fracture Toughness of Irradiated Austenitic SSs

Fracture toughness is typically characterized by the initiation toughness J_{Ic} and tearing modulus T for materials that fail after substantial plastic deformation (conditions of EPFM) and by the critical stress intensity factor K_{Ic} for materials that fail after little or no deformation (conditions of LEFM). Austenitic SSs have been divided into three broad categories of fracture toughness.[3] Category III corresponds to high toughness materials with J_{Ic} above 150 kJ/cm^2 (857 in.-lb/in.^{2}). In these materials, fracture occurs after stable crack extension at stresses well above the yield stress. Category II corresponds to materials with intermediate toughness with J_{Ic} in the range of 30-150 kJ/cm^2 (171-857 in.-lb/in.^{2}). In these materials, fracture occurs by stable or unstable crack extension at stress levels close to the yield stress. Category I corresponds to low-toughness materials with K_{Ic} less than 75 MPa m$^{1/2}$ (68.2 ksi in.$^{1/2}$) [$J_{Ic} < 30$ kJ/cm^2 (< 171 in.-lb/in.^{2})]. In these materials, fracture occurs by unstable crack extension at stress levels well below the yield stress.

Nonirradiated wrought and cast austenitic SSs and their welds fall in Category III. The J_{Ic} values for Types 304 and 316 SS at temperatures up to 125°C (257°F) vary between 169 and 1660 kJ/cm^2 (965 and 9479 in.-lb/in.^{2}), with a median value of 672 kJ/cm^2 (3837 in.-lb/in.^{2}).[3] The J_{Ic} values at 400-550°C (752-1022°F) are ≈ 35% lower, with a median value of 421 kJ/cm^2 (2404 in.-lb/in.^{2}). Fracture in such high-toughness materials is by the nucleation and coalescence of microvoids and is characterized by a dimpled fracture morphology.

Although cast austenitic SSs and SS welds also exhibit ductile fracture at temperatures up to 550°C (1022°F), their fracture toughness is lower than that of the wrought SSs. A dimpled fracture morphology is also observed in SS welds. Because of a high density of inclusions in the weld, the dimples are relatively small and shallow. Also, dimples are often associated with an inclusion and are initiated by a decohesion of the particle/matrix interface. The overall fracture toughness of cast austenitic SSs and SS welds is controlled by the density and morphology of second-phase inclusions in these materials and varies with the cast or weld process. For example, static cast products have lower fracture toughness than centrifugally cast pipes. Gas tungsten arc (GTA) welds exhibit the highest toughness; SMA welds have intermediate toughness; and SA welds have the lowest toughness.[3] The median value of J_{Ic} is 492 kJ/cm^2 (2809 in.-lb/in.^{2}) for GTA welds and 147 kJ/cm^2 (839 in.-lb/in.^{2}) for SA welds for temperatures up to 125°C (257°F).

Welding of austenitic SSs results in a HAZ adjacent to the fusion zone, where the material microstructure and microchemistry are greatly altered because of the precipitation of Cr-rich carbides at the grain boundaries. The formation of the carbides depletes Cr from the grain-boundary region, thereby creating a region that is susceptible to SCC. However, the fracture toughness of HAZ material is generally superior to that of the weld metal and may be comparable to that of the base metal.

Neutron irradiation can degrade fracture toughness of austenitic SSs to the level of Category II or I. The initiation toughness data (J_{Ic}) of irradiated SSs obtained in the present study, as well as those obtained earlier at ANL,[27] are compared with similar data from other studies in Fig. 70. The scatter band for the data from fast reactor irradiations is also plotted in the figure. The results on BWR irradiated materials fall within the scatter band of the data obtained on materials irradiated in fast reactors at
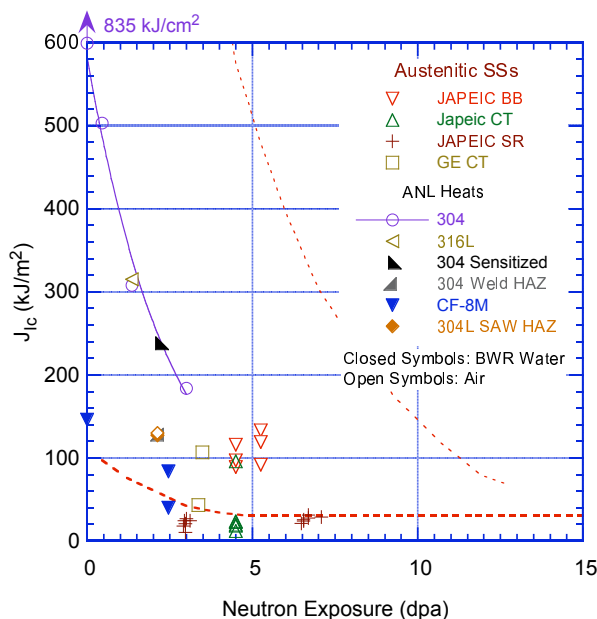
Figure 70.
Change in fracture toughness J_{Ic} as a function of neutron exposure for irradiated austenitic SSs. Dashed lines represent the scatter band for the fast reactor data on austenitic SSs irradiated at 350-450°C (662-843°F).

GE = General Electric Nuclear Energy, JAPEIC = Japan Power Engineering and Inspection Corporation, CT = compact tension, BB = bend bar, and SR = short rod.

temperatures higher than 288°C (550°F). Also, the data for BWR irradiated materials indicate that the J_{Ic} of austenitic SSs can decrease to ≈15 kJ/m^2 [corresponding to K_{Ic} value of 54 MPa m $^{1/2}$ (38 ksi in.$^{1/2}$)] at neutron dose as low as 3-5 dpa. The significant results from the ANL study are summarized as follows:

(a) Neutron irradiation decreases the fracture toughness of SSs. The change in the fracture toughness J-R curve for irradiated Type 304 SS and CF-8M cast SS is shown in Figs. 71a and b, respectively.

(b) For the same irradiation conditions, the fracture toughness of the weld HAZ materials is lower than that of the solution-annealed materials, and the toughness of the thermally aged cast SS is lower than that of the HAZ material.

(c) Limited data indicate that the fracture toughness is approximately the same in air and simulated BWR environments. The use of an IG starter crack instead of a TG fatigue crack and the corrosion/oxidation reaction during crack extension had little or no effect on the fracture toughness of irradiated SSs. The fracture toughness J-R curves for SS weld HAZ materials in air and water environments are shown in Fig. 72.

(a)   (b)
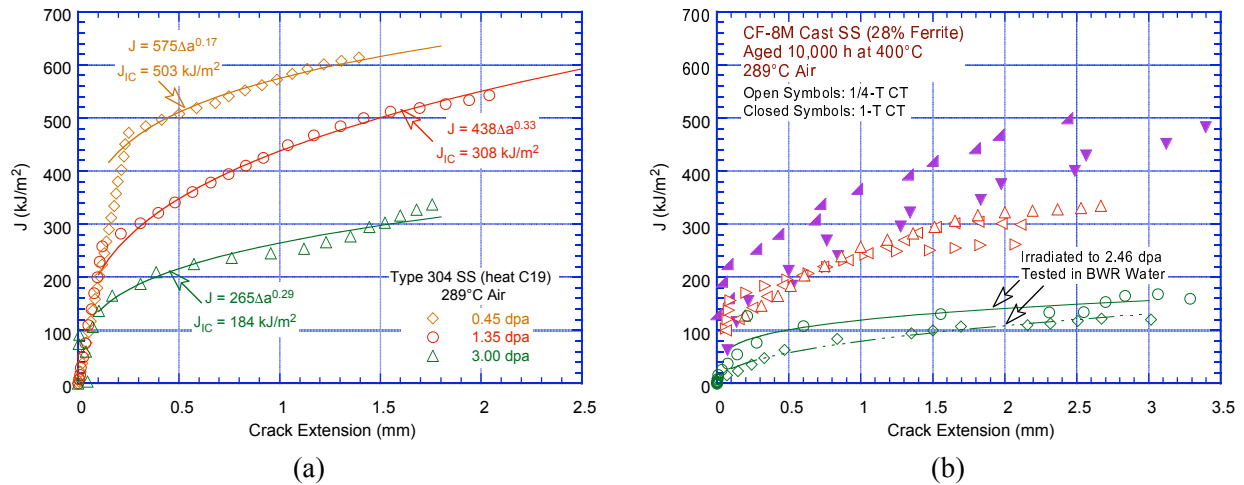
Figure 71.   J-R curves for irradiated (a) Type 304 SS and (b) thermally aged CF-8M cast SS at 289°C.

(a)   (b)
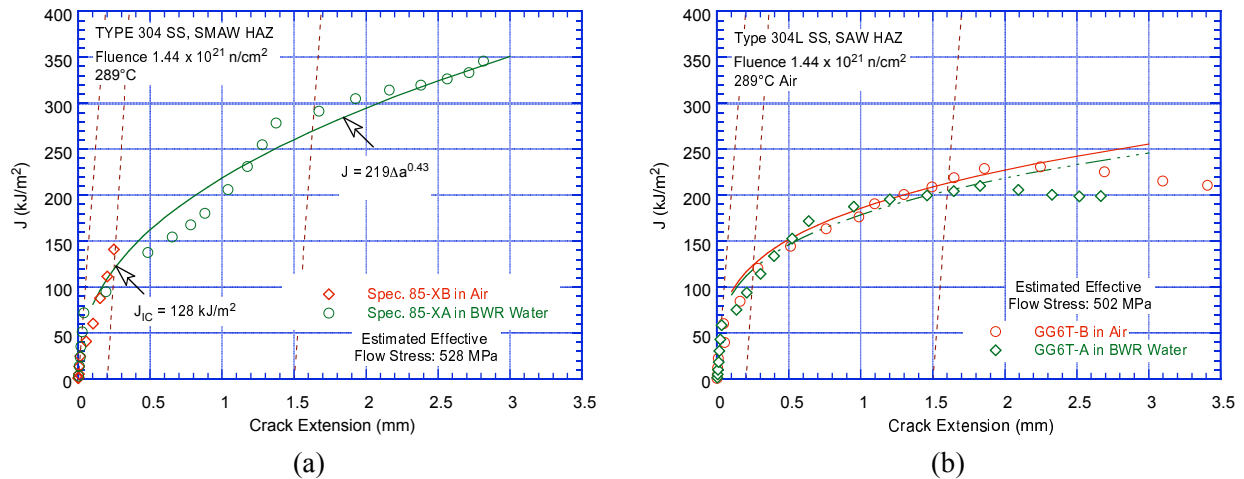
Figure 72.   J-R curves for irradiated specimens of (a) Type 304 SS SMA weld HAZ and (b) Type 304L SA weld HAZ in air and BWR water environments.

4.3.1   Comparison with Fracture Toughness Data in the Literature

The change in initiation toughness J_{Ic} of wrought austenitic SSs and cast SSs and weld metals is shown in Fig. 73 as a function of neutron exposure (in dpa). The fracture toughness data from both fast reactor and LWR irradiations are included in the figures. The irradiation temperatures range from 90 to 427°C (194-800°F) and test temperatures from 100 to 427°C (212-800°F); some of the tests were conducted at room temperature. The procedures for determining J_{Ic} vary among these studies. For example, in earlier studies a bilinear J-R curve was used to fit the data, whereas a power-law curve was used in the more recent studies. Different expressions have also been used for the blunting line. For example, for high-strain-hardening materials such as austenitic SSs, a slope of $4\sigma_f$ is generally used for the blunting line, while the ASTM specifications define it as $2\sigma_f$. A slope of $4\sigma_f$ will yield lower J_{Ic} values. Also, in the present study, to account for possible strain softening that may occur in irradiated materials, an effective flow stress (defined as the average of the nonirradiated and irradiated flow stress) was used in J-R curve data analysis. Earlier studies have used the irradiated flow stress.

(a)

(b)
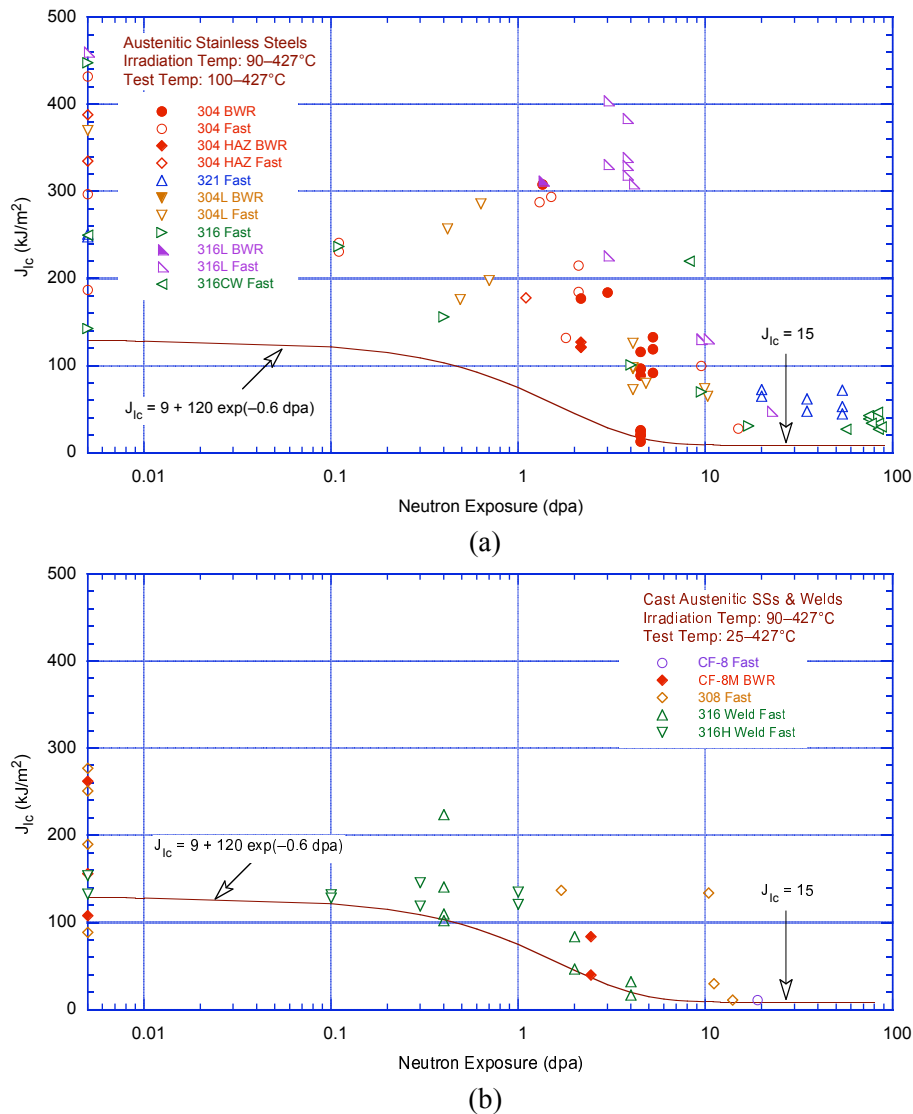
Figure 73.   The change in initiation toughness J_{Ic} of (a) wrought austenitic SSs and (b) cast austenitic SSs and weld metals as a function of neutron exposure (in dpa).

71

The data in Fig. 73a indicate some differences in behavior between subsets of the data. The average J_{Ic} of the Type 304 SS drops from ≈ 350 kJ/m^2 (1999 in.-lb/in.^{2}) at 1 dpa to ≈ 75 kJ/m^2 (≈ 428 in.-lb/in.^{2}) at 5 dpa. The sharp drop in J_{Ic} for Type 316L SS appears to occur at a somewhat higher fluence range (3 dpa to 10 dpa). The drop in Type 304L SS appears to occur at a somewhat lower fluence. Overall, the results indicate little or no change in toughness below 0.5 dpa, a rapid decrease between 1 and 5 dpa, and no further change (saturation) beyond 10 dpa. The overall pattern is that with increasing fluence, the decrease in toughness is the earliest for Type 304L SS, followed by Type 304 SS, and then Type 316 SS. The data in Fig. 73b also show that the toughness of cast SSs and welds is lower than that of the wrought SSs for all fluences less than the 10-dpa saturation level. The existing data for welds indicate that ≈ 0.3 dpa can be considered a threshold neutron dose below which irradiation has little or no effect on fracture toughness. The fracture toughness of austenitic SSs irradiated at less than the threshold dose will have a minimum J_{Ic} of 135 kJ/m^2 (771 in.-lb/in.^{2}).

The following summarizes the conclusions regarding the effects of parameters such as material type and heat treatment; irradiation conditions such as spectrum, flux, temperature, and dose; and test temperature.

Irradiation Facility: Fast reactor irradiations are at fluxes and temperatures higher than those typically observed in LWRs and have a different spectrum. All of the high neutron exposure data (≥ 20 dpa) are from fast reactor irradiations at $\geq 400°$C ($\geq 752°$F). An accurate determination of the effects of neutron spectrum, flux, and temperature on the fracture properties of these materials requires data on the same heat of material irradiated in a fast reactor and an LWR to comparable neutron dose. Such information is not available. However, the general data trends appear to be similar for fast reactor and LWR irradiations.

Material Type: Some differences in the fracture toughness data trends appear for the various grades of wrought austenitic SSs, but these differences may be artifacts of the limited data. The heat-to-heat variation for a particular grade may be comparable to the apparent differences between grades in the current data. Although the fracture toughness of nonirradiated cold-worked (CW) steels is lower than that of nonirradiated solution-annealed steels, the decrease in toughness of CW steels with neutron exposure is slower and the J_{Ic} value at saturation is higher than that of irradiated solution-annealed steels. However, the data for CW steels are from fast reactor irradiations and at relatively high temperatures, 400-427°C (752-800°F). As discussed below, the saturation J_{Ic} for CW SSs is likely to be lower for irradiations at LWR operating temperatures, which are 290-320°C (554-608°F), so the differences may be smaller than indicated in Fig. 73b.

Nonirradiated weld metals and thermally aged cast SSs have lower fracture toughness than wrought materials, and the toughness may decrease somewhat more rapidly with neutron fluence than that of solution-annealed material. However, the saturation toughness for the welds is not significantly different from that of solution-annealed SSs, and the same bounding curve for J_{Ic} appears applicable to both wrought and weld and cast materials. Although LWR core internals are typically constructed of CF-8 or CF-3 steels, the only data for LWR irradiation of cast SS are for CF-8M steel. For thermal embrittlement of cast SSs the fracture toughness of CF-8M steel represents the worst-case scenario.[28,30] It thus might represent a bounding case also for the synergistic effects of irradiation and thermal aging.

Irradiation Temperature: The available data are inadequate to establish accurately the effects of the irradiation temperature on the fracture toughness of austenitic SSs. However, tensile data for austenitic SSs indicate that irradiation hardening is the highest, and ductility loss is maximum, at an irradiation temperature of $\approx 300°$C ($\approx 572°$F).[10] In Fig. 73, the J_{Ic} values for all of the data at neutron exposures

greater than 20 dpa may overestimate the toughness for irradiation temperatures of 290-320°C (554-608°F) because the irradiation temperatures were above 300°C (572°F).

Test Temperature: The fracture toughness of nonirradiated austenitic SSs is known to decrease as the test temperature is increased. The change in the J_{Ic} of irradiated SSs as a function of test temperature is plotted in Fig. 74 for several grades of SSs and welds. The fracture toughness of steels irradiated to relatively low dose (less than 5 dpa) also decreases with increasing test temperature in most cases. However, for steels irradiated to more than 12 dpa, test temperature has little effect on fracture toughness. Similar data on materials irradiated in LWRs are not available in the open literature.
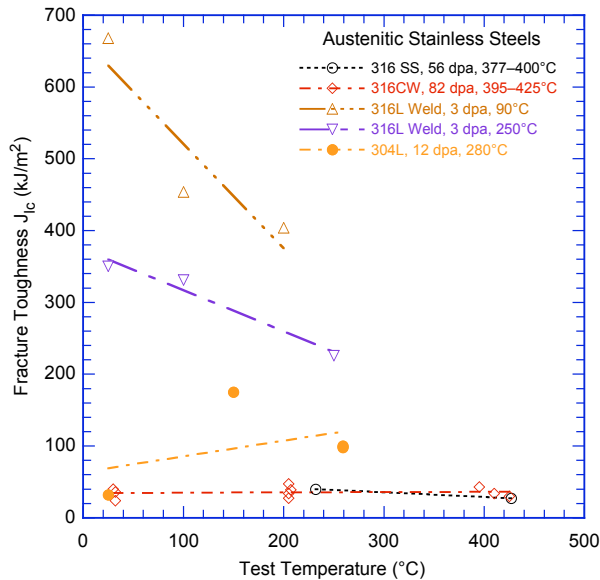
Figure 74.
Fracture toughness J_{Ic} of irradiated austenitic stainless steels and welds as a function of test temperature.

The effect of test temperature is also reflected in the fracture morphology of highly irradiated materials. At temperatures above 230°C (446°F) the failure mode is predominantly channel fracture characterized by a faceted fracture surface. It is caused by highly localized deformation along a narrow band of slip planes whereby dislocation motion along the narrow band clears the irradiation-induced defect structure, creating a defect-free channel that offers less resistance to subsequent dislocation motion. The localization of the deformation ultimately leads to channel failure. At temperatures ≤ 205°C (≤ 400°F), Hamilton et al.[23] observed quasi-cleavage fracture in 20% CW Type 316 SS irradiated to 77-87 dpa at 395-425°C (743-797°F) in a fast reactor. The brittle fracture was believed to be an indirect consequence of the onset of void swelling in the material. The segregation of Ni to the void surfaces depletes Ni and enriches Cr in the region between voids, leading to extensive formation of ε-martensite and an embrittlement failure mode.

Test Environment: Nearly all of the existing fracture toughness data have been obtained from tests in air and on specimens that were fatigue precracked at relatively low load ratios (typically 0.1-0.2) in room-temperature air. However, in reactor core components cracks are initiated primarily by SCC and have IG morphology, whereas the fatigue precracks in fracture toughness tests are always TG. Also, the corrosion/oxidation reaction could influence fracture toughness. For example, hydrogen generated from the oxidation reaction could diffuse into the material and change the deformation behavior by changing the stacking-fault energy of the material. However, limited data on irradiated SS weld HAZ materials (Fig. 72) indicate that an NWC BWR environment has little or no effect on the fracture toughness J-R curves. Similar tests in air and water environments have not been conducted on irradiated wrought or

cast SSs. In the present study, large load drops were observed at the onset of crack extension during the two tests on irradiated CF-8M cast SS. Such load drops, typically, are not observed during tests in air.[28]

The effect of neutron irradiation on the fracture toughness of austenitic SSs can also be represented by the decrease in the coefficient C of the power-law correlation for the J-R curve with neutron dose. The change in coefficient C for wrought and cast SSs and welds is plotted as a function of neutron dose in Fig. 75. The results indicate that, even for fluence levels above 10 dpa, most heats of wrought austenitic SSs show ductile crack extension in the toughness tests. Under similar irradiation conditions, coefficient C of cast SSs and welds is lower than that of wrought SSs. There are less data at high fluences for cast SSs and weld metals. However, since most of the data are from irradiations in fast reactors and at temperatures of 370-427°C (698-800°F), the values of C are likely to be lower for irradiations at LWR operating temperatures.
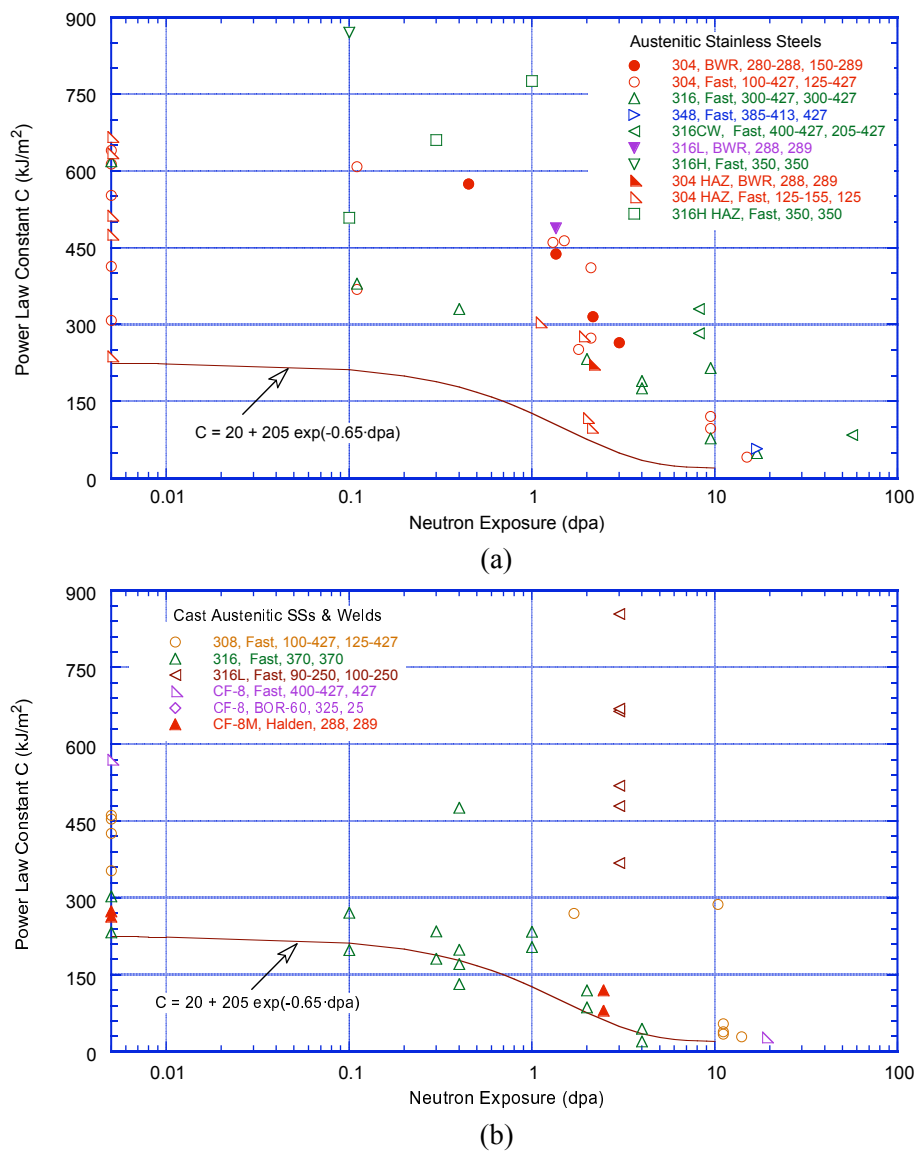
Figure 75. The change in coefficient C of the power-law J-R curve for (a) wrought austenitic SSs and (b) cast austenitic SSs and weld metals as a function of neutron exposure (in dpa).

Figure 73a shows that CT specimens of Type 304 SS irradiated to ≈4.5 dpa in a BWR (closed circles in Fig. 73a) have very low J_{Ic} values [corresponding to K_{Ic} of 52-74 MPa m $^{1/2}$ (37-50 ksi in.$^{1/2}$)] and exhibit no ductile crack extension in the toughness tests. These results indicate that BWR irradiated materials can have very poor fracture toughness, with little or no ductile crack extension, at neutron dose as low as 3-5 dpa. Additional tests on SSs irradiated to 3-10 dpa are needed to validate these results.

Ductile crack extension was also not observed for some specimens of a 20% CW Type 316 SS irradiated to 74-88 dpa in a fast reactor at 410-425°C (770-797°F); the K_{Ic} values were 74-90 MPa m$^{1/2}$ (67-82 ksi in.$^{1/2}$). However, the specimens failed by a quasi-cleavage fracture believed to be an indirect consequence of the onset of void swelling in the material.

The exponent n of the power law curve typically ranges from 0.35 to 0.70 for nonirradiated materials and 0.16 to 0.65 for irradiated materials. No obvious trend of n with fluence is evident. For irradiated materials, the median value is 0.37.

4.3.2 Fracture Toughness Trend Curve

A fracture toughness trend curve that bounds the existing data has been developed. It includes (a) a threshold neutron exposure for radiation embrittlement of austenitic SSs and a minimum fracture toughness for these materials irradiated to less than the threshold value, (b) a saturation neutron exposure and a saturation fracture toughness for materials irradiated to greater than this value, and (c) a description of the change in fracture toughness between the threshold and saturation neutron exposures. For fluences less than 5 dpa, as shown in Fig. 73, a fracture toughness trend curve that bounds the existing fracture toughness data for J_{Ic} as a function of neutron exposure in dpa may be represented by

$$J_{Ic} = 9 + 120 \exp(-0.6 \text{ dpa}). \tag{25}$$

A fracture toughness J-R curve may be used to analyze behavior beyond J_{Ic}. The curve is expressed in terms of the J integral and crack extension (Δa) by the power law $J = C(\Delta a)^n$. For fluences less than 5 dpa, as shown in Fig. 75, the existing fracture toughness data can be bounded by a power-law J-R curve with coefficient C expressed as

$$C = 20 + 205 \exp(-0.65 \text{ dpa}), \tag{26}$$

and an exponent n equal to 0.37 (the median value of the experimental data). This equation yields a bounding C value of ≈ 225 kJ/m^2 (1285 in.-lb/in.^{2}) for materials irradiated to less than 0.5 dpa and ≈ 28 kJ/m^2 (≈ 160 in.-lb/in.^{2}) for materials irradiated to ≈ 5 dpa.

Although the toughness of welds and cast SS is somewhat less than that of wrought materials, Fig. 75 shows that the proposed trend curves also provide an adequate description of the toughness of these materials.

An Electric Power Research Institute (EPRI) report on thermal aging embrittlement of cast SS components proposed using the fracture toughness J at a crack extension of 2.5 mm (0.1 in.), $J_{2.5}$, to differentiate between nonsignificant and potentially significant reductions in fracture toughness of cast austenitic SSs.[64] Flaw tolerance evaluations were presented in Appendices A and B of the EPRI report to support the choice of a threshold value of $J_{2.5} = 255$ kJ/m^2 (1456 in.-lb/in.^{2}). The NRC staff has found that using $J_{2.5} = 255$ kJ/m^2 is an acceptable screening approach for fracture toughness of cast SSs.[65] For the coefficient C data shown in Fig. 75 for wrought and cast austenitic SSs and welds, the experimental
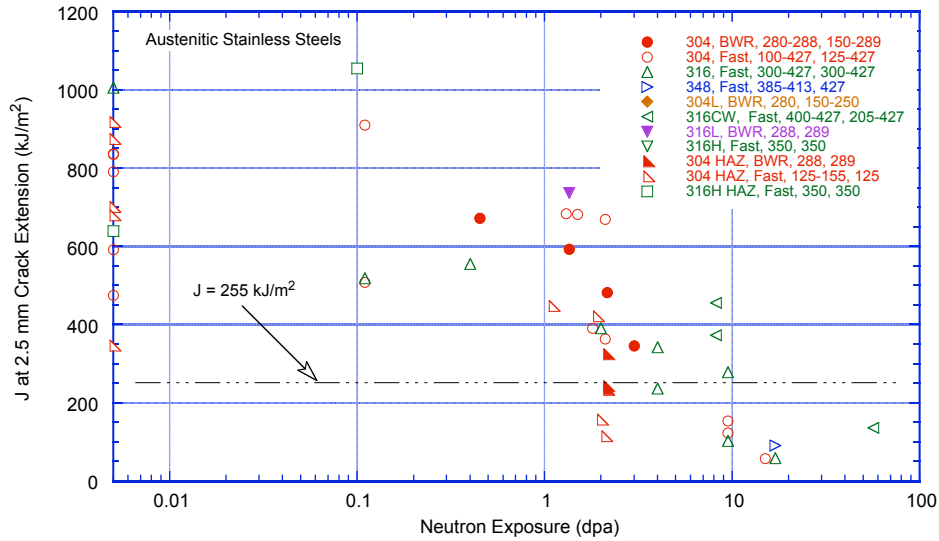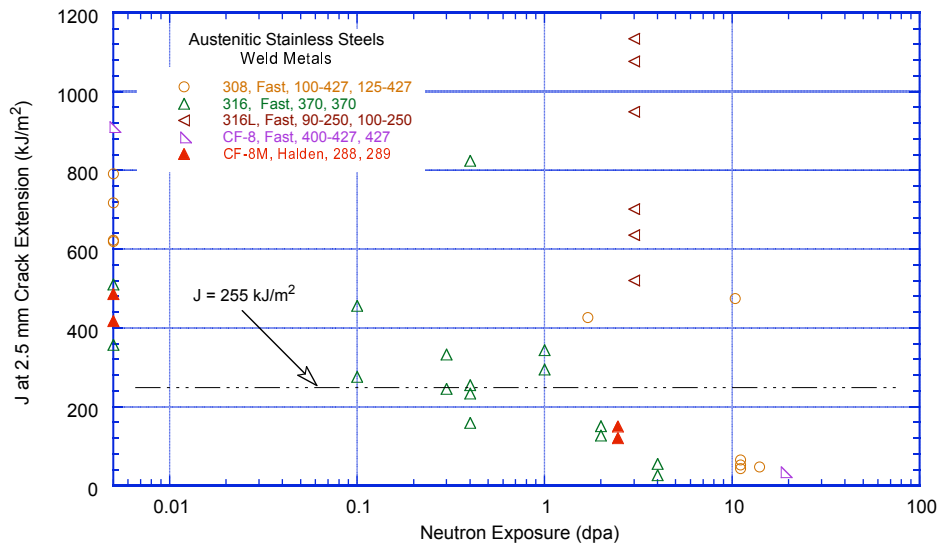
Figure 76. Experimental values of J-integral at a crack extension of 2.5 mm for (a) wrought austenitic SSs and (b) cast austenitic SSs and weld metals plotted as a function of neutron exposure. The legend gives the grade of material, irradiation source (in fast reactor or LWR), and irradiation and test temperatures.

J-integral values at a crack extension of 2.5 mm are plotted as a function of neutron exposure in Fig. 76. The results indicate that the value of $J_{2.5}$ for austenitic SSs and welds irradiated up to 0.3 dpa is above the screening value of 255 kJ/m^2 (1456 in.-lb/in.^{2}). However, the applicability of the flaw tolerance evaluations in Appendices A and B of the EPRI report would have to be demonstrated to support the use of the $J_{2.5}$ parameter for evaluating the toughness of irradiated materials.

4.3.3 Synergistic Effect of Thermal and Neutron Irradiation

Thermal aging of cast austenitic SSs at reactor operating temperatures of 280-350°C (536-662°F) can lead to degradation of the fracture properties of these materials, depending on the characteristics of the material and the environment to which they are exposed.[28-30] Thermal aging increases the tensile

strength, hardness, and Charpy-impact transition temperature, and it decreases the ductility, fracture toughness, and impact strength. The extent of mechanical-property degradation is essentially determined by the chemical composition of the steel, the casting process used to construct the component, the ferrite content and ferrite morphology of the steel, and the time and temperature of service for the component. Cast SSs with high levels of Mo (e.g., CF-8M) show greater susceptibility to thermal embrittlement than steels with low Mo content (e.g., CF-3 or CF-8). Also, static cast steels are more susceptible to thermal embrittlement than centrifugally cast components.

As part of the evaluation of passive, long-lived reactor structures for license renewal, the NRC staff has proposed screening criteria to determine the susceptibility of cast SS components to thermal aging embrittlement;[65] the criteria are outlined in Table 16. For components found or assumed to be potentially susceptible, an aging management program is required for the license renewal period. However, for reactor core internal components, concurrent exposure to neutron irradiation can result in a synergistic effect wherein the service-degraded fracture toughness can be less than that predicted for either of these processes independently.

Table 16.　Screening criteria for thermal-aging susceptibility of cast austenitic stainless steels.

Mo Content (wt.%)	Casting Method	Ferrite Content	Susceptibility Determination
High (2.0-3.0)	Static	$\leq 14\%$	Not susceptible
		$> 14\%$	Potentially susceptible
	Centrifugal	$\leq 20\%$	Not susceptible
		$> 20\%$	Potentially susceptible
Low (0.5 max.)	Static	$\leq 20\%$	Not susceptible
		$> 20\%$	Potentially susceptible
	Centrifugal	All	Not susceptible

In the proposed resolution regarding the issue of thermal aging embrittlement of cast SS components,[65] the NRC staff recommends that, to account for the synergistic loss of fracture toughness, "a program should be implemented consisting of either a supplemental examination of the affected components as part of the applicant's 10-year inservice inspection program during the license renewal term, or a component-specific evaluation to determine the susceptibility to loss of fracture toughness." The component-specific evaluation is based on the neutron fluence. The current guidance[65] suggests that, if the fluence is greater than 1×10^{17} n/cm^2 (E > 1 MeV) (or 0.00015 dpa) for a component, a mechanical loading assessment should be conducted to determine whether a supplemental inspection program is required for the component.

It is useful to consider the potential effects of irradiation in terms of its effect on the rate of embrittlement and on the minimum value of toughness that can occur after long-term thermal aging. Formation of Cr-rich α' phase in the ferrite is the primary mechanism for thermal embrittlement of cast austenitic SSs;[28-36] thermal aging has little or no effect on the austenite phase. Embrittlement of ferrite phase from neutron irradiation occurs at lower fluences than does embrittlement of the austenite phase. A shift in the NDT temperature of up to 150°C (302°F) has been observed in pressure vessel steels irradiated to 0.07-0.15 dpa.[37] As discussed in Section 4.3.1, any significant effect of neutron irradiation on embrittlement of the austenite phase occurs only above ≈ 0.5 dpa (see Figs. 73 and 75).

The minimum value of fracture toughness that can occur due to thermal embrittlement depends primarily on the ferrite content and morphology. A globular ferrite morphology in which the brittle ferrite phase is isolated in an austenitic matrix will have a higher toughness than a lacy morphology where a more continuous path through the brittle ferrite is possible. The minimum toughness due to thermal aging occurs when the ferrite is fully embrittled, and the remaining toughness depends on the toughness

provided by the ductile matrix surrounding the embrittled phase. Based on an ANL study,[28] the predicted saturation fracture toughness J-R curves for the various cast materials in the thermally aged condition (i.e., the lowest fracture toughness that could be achieved for the steel after thermal aging) are expressed as $J \approx 264 \, \Delta a^{0.35}$, $\approx 251 \, \Delta a^{0.34}$, and $\approx 167 \, \Delta a^{0.31}$, respectively, for CF-3, CF-8, and CF-8M steels at 290°C (554°F).

For fluences greater than 1.5 x 10^{-4} dpa, but less than ≈ 0.5 dpa, irradiation is expected to affect the rate at which cast SSs embrittle, because the ferrite phase is being embrittled both by thermal aging and radiation damage. However, the minimum toughness after long thermal aging would be similar to that observed in the nonirradiated case since the toughness of the austenitic phase does not change. For fluences greater than ≈ 0.5 dpa, the minimum toughness will be lower than can be achieved by thermal aging alone, since both the ferrite and the austenitic phases are embrittled.

No data are available in the open literature to quantify the effect of irradiation on the rate of embrittlement, and only very limited data are available to assess the effect of irradiation on the minimum toughness. The data developed in this program were obtained on a CF-8M steel that was thermally aged for 10,000 h at 400°C and then irradiated to well above the threshold fluence. The resulting toughness is bounded by the curve for other SSs irradiated to a similar level, i.e., thermal aging doesn't seem to lower the toughness below that expected for irradiation alone at these fluences. Based on these very limited data and the general mechanism of embrittlement for cast SSs, the minimum fracture toughness of cast SSs can be taken as (a) the minimum predicted toughness for thermal aging for fluences less than 0.3 dpa and (b) the lesser of the minimum predicted toughness for thermal aging or the lower bound curves in Fig. 75 for irradiated SSs. The threshold fluence, taken as 0.3 dpa, is a slightly conservative value in light of the limited data and corresponding uncertainty.

The kinetics of thermal aging are reasonably well known.[28] Irradiation is expected to accelerate the embrittlement of the ferrite phase so the results in Ref. 28 may be nonconservative for fluences greater than 1.5 x 10^{-4} dpa. Additional study and testing are needed to quantify this effect. Additional tests on cast CF-3 and CF-8 steels are also needed to better establish the potential for synergistic loss of toughness in these materials in the transition fluence range from 0.3 to 2 dpa. Although cast CF-8M steels are not used in LWR core internal components because of the difficulty of testing irradiated materials, it may be useful to study this material as a "worst-case" material in lieu of testing a number of heats of CF-3 and CF-8.

5. Summary

Crack growth tests have been conducted in BWR environments at 289°C on Type 316 SS irradiated to 0.3, 0.9, and 2.0 x 10^{21} n/cm^2 (0.45, 1.35, and 3.0 dpa); sensitized Type 304 SS and SS weld HAZ materials irradiated to 1.44 x 10^{21} n/cm^2 (2.16 dpa); and CF-8M cast SS irradiated to 1.63 x 10^{21} n/cm^2 (2.46 dpa). The CGR tests on materials irradiated to 2.16 or 2.46 dpa were followed by a fracture toughness J-R curve test in the BWR environment. Fracture toughness tests have also been conducted in air at 289°C to obtain baseline data. The weld HAZ specimens were obtained from a Type 304L SA weld and a Type 304 SS SMA weld. Also compiled in this report are crack growth rate data from earlier ANL studies on Types 304L and 316L SS irradiated to 0.45, 1.35, and 3.0 dpa and SS weld HAZ materials irradiated to 5 x 10^{20} n/cm^2 (0.75 dpa) in BWR environments, as well as fracture toughness data on Types 304 and 316L SS irradiated up to 2 x 10^{21} n/cm^2 (3.0 dpa) in air at 289°C. The results from the ANL study are compared with the data available in the literature.

The results indicate that in an NWC BWR environment, the constant-load CGRs (i.e., under SCC loading) of nonirradiated SSs or materials irradiated to ≈3 x 10^{20} n/cm^2 (≈0.45 dpa) are either comparable to or slightly lower than the disposition curve in NUREG-0313 for sensitized SSs in water with 8 ppm DO. Neutron irradiation increases the CGRs significantly. The CGRs of austenitic SSs irradiated to 5 x 10^{20}-2.67 x 10^{21} n/cm^2 (0.75-4.0 dpa) are a factor of 2-7 higher than the NUREG-0313 disposition curve. For these irradiation dose levels, the CGRs of austenitic SSs can be represented by a curve that is a factor of 6 higher than the NUREG-0313 disposition curve. A different SCC behavior is observed for austenitic SSs irradiated to higher neutron dose. The CGRs of SSs irradiated to 13 dpa show a strong dependence on K and are up to a factor of 30 higher than the NUREG-0313 disposition curve for nonirradiated SSs.

The results also indicate a benefit from a low-DO environment. In general, the CGRs of nonirradiated SSs and steels irradiated up to 4.0 dpa decreased more than an order of magnitude when the DO level was decreased from the NWC to the HWC BWR environment. The beneficial effect of low corrosion potential (i.e., HWC chemistry) is not observed for steels irradiated to 8.67 x 10^{21} n/cm^2 (13.0 dpa) or similar high fluences, and a determination of the maximum fluence level for which HWC is effective would be of great interest.

In the current tests a few specimens, irradiated to ≈2 x 10^{21} n/cm^2 (≈3.0 dpa), did not show the benefit of the low-DO environment. It is not clear if specimen constraint had been lost for these specimens; the adequacy of the proposed K/size criterion is not well–established. A loss of specimen constraint is also likely to influence the fracture mode and morphology. For example, if the thickness criterion is exceeded, the crack plane, typically, is out-of-normal near the edges of the specimen, and if the specimen ligament criterion is exceeded the crack propagates away from the normal plane at an angle of 45°. No fractographic indication of a change in fracture morphology due to a loss in specimen constraint, however, was evident in the test specimens that did not show the benefit of HWC. The fracture planes were straight and normal to the stress axis. In these specimens, although the specimen K/size criterion was exceeded in high-DO water, the expected increase in growth rate was not observed. The loading conditions seemed to have had no effect on the growth rates until the DO level in the environment was decreased. Additional tests and analyses are needed to ensure that the unusually high growth rates, or the lack of a benefit of HWC on growth rates, in these irradiated austenitic SSs were not caused by processes other than the loss of specimen constraint due to high loads.

The limited data on SS weld HAZ materials indicate that neutron irradiation to $\approx 1.47 \times 10^{21}$ n/cm^2 (≈ 2.2 dpa) has little or no effect on cyclic CGRs in air. The experimental CGRs are slightly lower than those predicted by the correlations developed by James and Jones for solution-annealed SSs.

In the NWC BWR environment, the cyclic CGRs of SSs irradiated to $\approx 3 \times 10^{20}$ n/cm^2 (≈ 0.45 dpa) are the same as those for nonirradiated materials, whereas the CGRs of SSs irradiated to 5×10^{20}-2.67×10^{21} n/cm^2 (0.75-4.0 dpa) are higher. Limited data indicate that the growth rates of irradiated CF-8M cast SS and Type 304L SS weld HAZ material are lower than those of wrought materials irradiated to the same neutron dose. The cyclic CGRs at low frequencies are decreased by more than an order of magnitude when the DO level is decreased by changing from NWC to HWC. A superposition model has been used to represent the cyclic CGRs of austenitic SSs. The CGR in the environment is expressed as the superposition of the rate in air (mechanical fatigue) and the rates due to corrosion fatigue and SCC. The correlations for the various material and environmental conditions are listed in Table 17.

Table 17. Cyclic CGR correlations for wrought and cast austenitic stainless steels in BWR environments at 289°C.

CGR (m/s)	Correlations		Material and Environmental Conditions
$\dot{a}_{air}$	$\dot{a}_{air} = 3.443 \times 10^{-12}\, S(R) \Delta K^{3.3} / t_{rise}$		Nonirradiated or irradiated
	$S(R) = 1.0$	$R < 0$	
	$S(R) = 1.0 + 1.8R$	$0 < R < 0.79$	
	$S(R) = -43.35 + 57.97R$	$0.79 < R < 1.0$	
$\dot{a}_{CF}$			Nonirradiated and irradiated <0.5 dpa
	$\dot{a}_{CF} = 4.5 \times 10^{-5}\left(\dot{a}_{air}\right)^{0.5}$		≤ 0.3 ppm DO
	$\dot{a}_{CF} = 1.5 \times 10^{-4}\left(\dot{a}_{air}\right)^{0.5}$		8.0 ppm DO
			Irradiated >0.5 & ≤ 3.0 dpa
	$\dot{a}_{CF} = 1.5 \times 10^{-4}\left(\dot{a}_{air}\right)^{0.5}$		0.2 - 0.5 ppm DO[a]
$\dot{a}_{SCC}$			Nonirradiated and irradiated <0.5 dpa
	$\dot{a}_{SCC} = 2.1 \times 10^{-13}\left(K\right)^{2.161}$		0.2 - 0.5 ppm DO
	$\dot{a}_{SCC} = 7.0 \times 10^{-14}\left(K\right)^{2.161}$		≤ 0.2 ppm DO
			Irradiated >0.5 & ≤ 3.0 dpa
	$\dot{a}_{SCC} = 1.26 \times 10^{-12}\left(K\right)^{2.161}$		0.2 - 0.5 ppm DO

[a]Correlation may yield conservative estimates of CGR for cast austenitic SSs and low-C Type 304L SS weld HAZ materials.

Neutron irradiation decreases the fracture toughness of wrought and cast austenitic SSs. For the same irradiation conditions, fracture toughness of the weld HAZ materials is lower than that of the solution-annealed materials, and the toughness of the thermally aged cast SS is lower than that of the HAZ material. Limited data on irradiated SS weld HAZ materials indicate that an NWC BWR environment has little or no effect on their fracture toughness J-R curves. In addition, the fracture toughness J-R curves in air and BWR environments are comparable. Similar tests in air and water environments have not been conducted on irradiated wrought or cast SSs. In the present study, large load drops were observed at the onset of crack extension during the two tests on thermally aged and irradiated CF-8M cast SS. Such load drops, typically, are not observed during J-R curve tests in air. Additional tests on the fracture toughness of wrought and cast SSs are needed to investigate the possible effects of an IG starter crack compared to the TG fatigue crack generally used in nearly all the fracture toughness tests and the corrosion/oxidation reaction during crack extension.

The available fracture toughness data in the open literature on wrought and cast austenitic SSs and their welds have been reviewed. Most of the experimental data on neutron embrittlement of austenitic SSs have been obtained in high flux fast reactors; similar test results that are relevant to LWRs are very limited. Summarized in this report are the effects of neutron irradiation on the fracture toughness of these steels, as well as the effects of material and irradiation conditions and test temperature.

The existing fracture toughness data on austenitic SSs indicate little or no change in toughness below 3.3×10^{20} n/cm^2 (0.5 dpa), rapid decrease between 6.6×10^{20} and 3.3×10^{21} n/cm^2 (1 and 5 dpa) to reach a saturation toughness value, and no further change beyond 6.6×10^{21} n/cm^2 (10 dpa). In general, the data trend appears to be similar for the fast reactor and LWR irradiations. There are no apparent differences in the fracture toughness data trends for the various grades of wrought austenitic SSs. In general, the fracture toughness of nonirradiated solution-annealed materials is relatively high, but it decreases rapidly with increasing neutron exposure above 1 dpa and reaches a saturation value beyond 10 dpa. For cold-worked SSs, although the fracture toughness of nonirradiated materials is lower than that of solution-annealed steels, the decrease with neutron exposure is slower, and the saturation toughness is higher. The fracture toughness of nonirradiated weld metals and thermally aged cast SSs is also lower, but it decreases more rapidly than that for solution-annealed steels. For example, the fracture toughness for Type 316 SS welds appears to saturate at 2.67×10^{21} or 3.3×10^{21} n/cm^2 (4 or 5 dpa).

Both irradiation and test temperature can influence fracture toughness. Available data for austenitic SSs indicate that irradiation hardening is the highest, and ductility loss is maximum at $\approx 300°C$ (572°F). Also, the fracture toughness of austenitic SSs is known to decrease as the test temperature is increased. Steels irradiated to less than 3.3×10^{21} n/cm^2 (5 dpa) show a similar behavior. However, for irradiation levels of 8×10^{21} n/cm^2 (12 dpa) or greater, test temperature has little or no effect on fracture toughness.

The existing fracture toughness data have been evaluated to define (a) the threshold neutron exposure for radiation embrittlement of austenitic SSs and the minimum fracture toughness of austenitic SSs irradiated to less than the threshold value, (b) the saturation neutron exposure and the saturation fracture toughness of these materials, and (c) the change in fracture toughness between the threshold and saturation neutron exposures. The results indicate that fracture toughness properties (J_{Ic} and J-R curve) exhibit (a) a threshold neutron dose of $\approx 2 \times 10^{20}$ n/cm^2 (≈ 0.3 dpa) below which irradiation has little or no effect on fracture toughness and (b) a saturation neutron dose of $\approx 3.3 \times 10^{21}$ n/cm^2 (≈ 5 dpa). Conservatively, no ductile crack extension is assumed to occur at or above the saturation neutron dose. The available data indicate a K_{Ic} of 50 MPa m$^{1/2}$ [or J_{Ic} of 15 kJ/m^2 (86 in.-lb/in.^{2})] for austenitic SSs irradiated to 5 dpa. However, the existing data are inadequate to determine whether K_{Ic} decreases further at higher neutron dose. A fracture toughness trend curve that bounds the existing data has been defined in terms of J_{Ic} vs. neutron dose (in dpa) and coefficient C of the power-law J-R curve vs. dose.

Potential synergistic effects of thermal and radiation embrittlement of cast austenitic SS internal components have also been evaluated. Such effects could affect both the rate of embrittlement and the degree of embrittlement. Cast austenitic SSs have a duplex structure consisting of both ferrite and austenite phases and are susceptible to thermal embrittlement even in the absence of irradiation. Thermal aging affects primarily the ferrite phase and has little or no effect on the austenite phase. It is estimated that effects on the rate of embrittlement could occur for fluences greater than 1×10^{17} n/cm^2 (0.00015 dpa). However, synergistic effects on the minimum toughness would occur only for fluences greater than 2×10^{20} n/cm^2 (0.3 dpa). Below 0.3 dpa, the minimum toughness can be estimated from the correlations available for thermal embrittlement of cast SS. For fluences > 0.3 dpa, the minimum fracture toughness of cast SSs can be assumed to be given by the lesser of the minimum predicted toughness for thermal aging or the lower bound curves for the fracture toughness of irradiated stainless steels.

This page is intentionally left blank.

References

1. Bruemmer, S. M., et al., "Critical Issue Reviews for the Understanding and Evaluation of Irradiation-Assisted Stress Corrosion Cracking," EPRI TR-107159, Electric Power Research Institute, Palo Alto, CA, 1996.

2. Herrera, M. L., et al., "Evaluation of the Effects of Irradiation on the Fracture Toughness of BWR Internal Components," Proc. ASME/JSME 4th Intl. Conf. on Nucl. Eng. (ICONE-4), Vol. 5, A. S. Rao, R. M. Duffey, and D. Elias, eds., American Society of Mechanical Engineers, New York, pp. 245-251, 1996.

3. Mills, W. J., "Fracture Toughness of Type 304 and 316 Stainless Steels and Their Welds," Intl. Mater. Rev. **42**, 45-82, 1997.

4. Kanasaki, H., I. Satoh, M. Koyama, T. Okubo, T. R. Mager, and R. G. Lott, "Fatigue and Stress Corrosion Cracking Behaviors of Irradiated Stainless Steels in PWR Primary Water," Proc. 5th Intl. Conf. on Nuclear Engineering, ICONE5-2372, pp. 1-7, 1997.

5. Andresen, P. L., F. P. Ford, S. M. Murphy, and J. M. Perks, "State of Knowledge of Radiation Effects on Environmental Cracking in Light Water Reactor Core Materials," Proc. 4th Intl. Symp. on Environmental Degradation of Materials in Nuclear Power Systems - Water Reactors, NACE, Houston, TX, pp. 1.83-1.121, 1990.

6. Jenssen, A., and L. G. Ljungberg, "Irradiation Assisted Stress Corrosion Cracking of Stainless Alloys in BWR Normal Water Chemistry and Hydrogen Water Chemistry," Proc. Sixth Intl. Symp. on Environmental Degradation of Materials in Nuclear Power Systems - Water Reactor, R. E. Gold and E. P. Simonen, eds., Minerals, Metals & Materials Society, Warrendale, PA, pp. 547-553, 1993.

7. Maziasz, P. J., and C. J. McHargue, "Microstructural Evolution in Annealed Austenitic Steels during Neutron Irradiation," Int. Met. Rev. **32**, 190, 1987.

8. Maziasz, P. J., "Overview of Microstructural Evolution in Neutron-Irradiated Austenitic Stainless Steels," J. Nucl. Mater. **205**, 118-145, 1993.

9. Garner, F. A., "Evolution of Microstructures in Face-Centered Cubic Metals during Neutron Irradiation," J. Nucl. Mater. **205**, 98-111, 1993.

10. Lucas, G. E., "The Evolution of Mechanical Property Change in Irradiated Austenitic Stainless Steels," J. Nucl. Mater. **206**, 287-305, 1993.

11. Dufresne, J., B. Henry, and H. Larsson, "Fracture Toughness of Irradiated AISI 304 and 316L Stainless Steels," Effects of Radiation on Structural Materials, ASTM STP 683, J. A. Sprague and D. Kramer, eds., American Society for Testing and Materials, Philadelphia, PA, pp. 511-528, 1979.

12. Picker, C., A. L. Stott, and H. Cocks, "Effects of Low-Dose Fast Neutron Irradiation on the Fracture Toughness of Type 316 Stainless Steel and Weld Metal," Proc. Specialists Meeting on Mechanical Properties of Fast Reactor Structural Materials, Chester, UK, Paper IWGFR 49/440-4, 1983.

13.	Huang, F. H., "The Fracture Characterization of Highly Irradiated Type 316 Stainless Steel," Int. J. Fracture **25**, 181-193, 1984.

14.	Bernard, J., and G. Verzeletti, "Elasto-Plastic Fracture Mechanics Characterization of Type 316H Irradiated Stainless Steel up to 1 dpa," Effects of Radiation on Materials: 12th Intl. Symp., ASTM STP 870, F. A. Garner and J. S. Perrin, eds., American Society for Testing and Materials, Philadelphia, PA, pp. 619-641, 1985.

15.	Mills, W. J., L. A. James, and L. D. Blackburn, "Results of Fracture Mechanics Tests on PNC SU 304 Plate," Westinghouse Hanford Report HEDL-7544, Hanford Engineering Development Laboratory, Richland, WA, 1985.

16.	Mills, W. J., "Fracture Toughness of Irradiated Stainless Steel Alloys," Nucl. Technol. **82**, 290-303, 1988.

17.	Michel, D. J., and R. A. Gray, "Effects of Irradiation on the Fracture Toughness of FBR Structural Materials," J. Nucl. Mater. **148**, 194-203, 1987.

18.	Ould, P., P. Balladon, and Y. Meyzaud, Bull. Cercle Etud. Metaux **15**, 31.1-31.12, 1988.

19.	Van Osch, E. V., M. G. Horsten, and M. I. De Vries, "Fracture Toughness of PWR Internals," ECN Contribution to CEC Contract on PWR Internals-Part 2 (ETNU/CT/94/0136-F), ECN-I-97-010 (71747/NUC/EvO/mh/006274), Netherlands Energy Research Foundation ECN, Petten, the Netherlands, 1997.

20.	De Vries, M. I., "Fatigue Crack Growth and Fracture Toughness Properties of Low Fluence Neutron-Irradiated Type 316 and Type 304 Stainless Steels," Influence of Radiation on Mechanical Properties: 13th Symposium (Part II), ASTM STP 956, F. A. Garner et al., eds., American Society of Testing and Materials, Philadelphia, PA, pp. 174-190, 1987.

21.	Alexander, D. J., J. E. Pawel, L. M. Grossbeck, A. F. Rowcliffe, and K. Shiba, "Fracture Toughness of Irradiated Candidate Materials for ITER First Wall/Blanket Structures," Effect of Radiation on Materials: 17th Intl. Symp., ASTM STP 1270, American Society of Testing and Materials, Philadelphia, PA, pp. 945-970, 1996.

22.	Sindelar, R. L., G. R. Caskey, Jr., J. K. Thomas, J. R. Hawthorne, A. L. Hiser, R. A. Lott, J. A. Begley, and R. P. Shogan, "Mechanical Properties of 1950s Vintage Type 304 Stainless Steel Weldment Components after Low Temperature Neutron Irradiation," 16th Intl. Symp. on Effects of Radiation on Materials, ASTM STP 1175, American Society of Testing and Materials, Philadelphia, PA, pp. 714-746, 1993.

23.	Hamilton, M. L., F. H. Huang, W. J. S. Yang, and F. A. Garner, "Mechanical Properties and Fracture Behavior of 20% Cold-Worked 316 Stainless Steel Irradiated to Very High Neutron Exposures," Influence of Radiation in Material, Properties: 13th Intl. Symp. (Part II), ASTM STP 956, American Society of Testing and Materials, Philadelphia, PA, pp. 245-270, 1987.

24.	Little, E. A., "Dynamic J-Integral Toughness and Fractographic Studies of Fast Reactor Irradiated Type 321 Stainless Steel," Effects of Radiation on Material, Properties: 12th Intl. Symp., ASTM STP 870, American Society of Testing and Materials, Philadelphia, PA, pp. 563-579, 1985.

25. Haggag, F. J., W. L. Server, W. G. Reuter, and J. M. Beeston, "Effects of Irradiation Fluence and Creep on Fracture Toughness of Type 347/348 Stainless Steels," ASTM STP 870, American Society of Testing and Materials, Philadelphia, PA, pp. 548-562, 1985.

26. O'Donnell, I. J., H. Huthmann, and A. A. Tavassoli, "The Fracture Toughness Behaviour of Austenitic Steels and Weld Metal Including the Effects of Thermal Aging and Irradiation," Intl. J of Pressure Vessels and Piping **65** (3), 209-220, 1996.

27. Chopra, O. K., E. E. Gruber, and W. J. Shack, "Fracture Toughness and Crack Growth Rates of Austenitic Stainless Steels," NUREG/CR-6826, ANL-03/22, 2004.

28. Chopra, O. K., "Estimation of Fracture Toughness of Cast Stainless Steels during Thermal Aging in LWR Systems," NUREG/CR-4513 Rev. 1, ANL-93/22, 1994.

29. Chopra, O. K. and W. J. Shack, "Mechanical Properties of Thermally Aged Cast Stainless Steels from Shippingport Reactor Components," NUREG/CR-6275, 1995.

30. Gavenda, D. J., W. F. Michaud, T. M. Galvin, W. F. Burke, and O. K. Chopra, "Effects of Thermal Aging on Fracture Toughness and Charpy-Impact Strength of Stainless Steel Pipe Welds," NUREG/CR-6428, ANL-95/47, 1996.

31. Bonnet, S., J. Bourgoin, J. Champredonde, D. Guttmann, and M. Guttmann, "Relationship between Evolution of Mechanical Properties of Various Cast Duplex Stainless Steels and Metallurgical and Aging Parameters: An Outline of Current EdF Programmes," Mater. Sci. Technol. **6**, 221-229, 1990.

32. Slama, G., P. Petrequin, and T. Mager, "Effect of Aging on Mechanical Properties of Austenitic Stainless Steel Castings and Welds," SMiRT Post-Conference Seminar 6, Assuring Structural Integrity of Steel Reactor Pressure Boundary Components, Aug. 29-30, 1983, Monterey, CA, 1983.

33. Chung, H. M., and O. K. Chopra, "Kinetics and Mechanism of Thermal Aging Embrittlement of Duplex Stainless Steels," Environmental Degradation of Materials in Nuclear Power Systems - Water Reactors, G. J. Theus and J. R. Weeks, eds., The Metallurgical Society, Warrendale, PA, pp. 359-370, 1988.

34. Auger, P., F. Danoix, A. Menand, S. Bonnet, J. Bourgoin, and M. Guttmann, "Atom Probe and Transmission Electron Microscopy Study of Aging of Cast Duplex Stainless Steels," Mater. Sci. Technol. **6**, 301-313, 1990.

35. Brown, J. E., A. Cerezo, T. J. Godfrey, M. G. Hetherington, and G. D. W. Smith, "Quantitative Atom Probe Analysis of Spinodal Reaction in Ferrite Phase of Duplex Stainless Steel," Mater. Sci. Technol. **6**, 293-300, 1990.

36. Miller, M. K., and J. Bentley, "Characterization of Fine-Scale Microstructures in Aged Primary Coolant Pipe Steels," Environmental Degradation of Materials in Nuclear Power Systems - Water Reactors, G. J. Theus and J. R. Weeks, eds., The Metallurgical Society, Warrendale, PA, pp. 341-349, 1988.

37. Hawthorne, J. R., and L. E. Steele, "Metallurgical Variables as Possible Factors Controlling Irradiation Response of Structural Steels," Effects of Radiation on Structural Metals, ASTM STP 426, American Society of Testing and Materials, Philadelphia, PA, pp. 534-572, 1967.

38. Brown, K. S., and G. M. Gordon, "Effects of BWR Coolant Chemistry on the Propensity for IGSCC Initiation and Growth in Creviced Reactor Internals Components," Proc. Third Intl. Symp. on Environmental Degradation of Materials in Nuclear Power Systems - Water Reactor, The Metallurgical Society, Warrendale, PA, pp. 243-248, 1987.

39. Gordon, G. M., and K. S. Brown, "Dependence of Creviced BWR Component IGSCC Behavior on Coolant Chemistry," Proc. 4th Intl. Symp. on Environmental Degradation of Materials in Nuclear Power Systems - Water Reactor, Daniel Cubicciotti, ed., NACE, Houston, TX, pp. 14.46-14.61, 1990.

40. Garzarolli, F., D. Alter, and P. Dewes, "Deformability of Austenitic Stainless Steels and Nickel-Base Alloys in the Core of a Boiling and a Pressurized Water Reactor," Proc. Intl. Symp. on Environmental Degradation of Materials in Nuclear Power Systems - Water Reactor, American Nuclear Society, Lagrange, IL, pp. 131-138, 1986.

41. Kodama, M., et al., "IASCC Susceptibility of Austenitic Stainless Steels Irradiated to High Neutron Fluence," Proc. Sixth Intl. Symp. on Environmental Degradation of Materials in Nuclear Power Systems - Water Reactor, R. E. Gold and E. P. Simonen, eds., Minerals, Metals & Materials Society, Warrendale, PA, pp. 583-588, 1993.

42. Kodama, M., et al., "Effects of Fluence and Dissolved Oxygen on IASCC in Austenitic Stainless Steels," Proc. Fifth Intl. Symp. on Environmental Degradation of Materials in Nuclear Power Systems - Water Reactor, American Nuclear Society, Lagrange, IL, pp. 948-954, 1991.

43. Clark, W. L., and A. J. Jacobs, "Effect of Radiation Environment on SCC of Austenitic Materials," Proc. First Intl. Symp. on Environmental Degradation of Materials in Nuclear Power Systems - Water Reactor, NACE, Houston, TX, p. 451, 1983.

44. Jacobs, A. J., G. P. Wozadlo, K. Nakata, T. Yoshida, and I. Masaoka, "Radiation Effects on the Stress Corrosion and Other Selected Properties of Type-304 and Type-316 Stainless Steels," Proc. Third Intl. Symp. on Environmental Degradation of Materials in Nuclear Power Systems - Water Reactor, The Metallurgical Society, Warrendale, PA, pp. 673-681, 1987.

45. Chung, H. M., R. V. Strain, and R. W. Clark, "Slow-Strain-Rate-Tensile Test of Model Austenitic Stainless Steels Irradiated in the Halden Reactor," in Environmentally Assisted Cracking in Light Water Reactors Semiannual Report July 2000 - December 2000, NUREG/CR-4667, Vol. 31, ANL-01/09, pp. 22-32, 2002.

46. Chung, H. M., R. V. Strain, and R. W. Clark, "Slow-Strain-Rate-Tensile Test of Model Austenitic Stainless Steels Irradiated in the Halden Reactor," in Environmentally Assisted Cracking in Light Water Reactors Semiannual Report January-December 2001, NUREG/CR-4667, Vol. 32, ANL-02/33, pp. 19-28, 2003.

47. Andresen, P. L., and F. P. Ford, "Irradiation Assisted Stress Corrosion Cracking: From Modeling and Prediction of Laboratory & In-Core Response to Component Life Prediction," Corrosion/95, NACE, Houston TX, Paper No. 419, 1995.

48. Jenssen, A., and L. G. Ljungberg, "Irradiation Assisted Stress Corrosion Cracking: Post Irradiation CERT Tests of Stainless Steels in a BWR Test Loop," Proc. Seventh Intl. Symp. on Environmental Degradation of Materials in Nuclear Power Systems - Water Reactor, G. Airey et al., eds., NACE, Houston, TX, pp. 1043-1052, 1995.

49. Angeliu, T. M., P. L. Andresen, E. Hall, J. A. Sutliff, and S. Sitzman, "Strain and Microstructure Characterization of Austenitic Stainless Steel Weld HAZs," Corrosion/2000, Paper 00186, NACE, Houston, TX, 2000.

50. Angeliu, T. M., P. L. Andresen, J. A. Sutliff, and R. M. Horn, "Intergranular Stress Corrosion Cracking of Unsensitized Stainless Steels in BWR Environments," Proc. Ninth Intl. Symp. on Environmental Degradation of Materials in Nuclear Power Systems - Water Reactor, The Metallurgical Society, Warrendale, PA, pp. 311-318, 1999.

51. Andresen, P. L., T. M. Angeliu, W. R. Catlin, L. M. Young, and R. M. Horn, "Effect of Deformation on SCC of Unsensitized Stainless Steel," Corrosion/2000, Paper 00203, NACE, Houston, TX, 2000.

52. Andresen, P. L., T. M. Angeliu, L. M. Young, W. R. Catlin, and R. M. Horn, "Mechanism and Kinetics of SCC in Stainless Steels," Proc. Tenth Intl. Symp. on Environmental Degradation of Materials in Nuclear Power Systems - Water Reactor, NACE, Houston, TX, 2001.

53. Chung, H. M., and W. J. Shack, "Irradiation-Assisted Stress Corrosion Cracking Behavior of Austenitic Stainless Steels Applicable to LWR Core Internals," NUREG/CR-6892, ANL-04/10, 2006.

54. Chopra, O. K., B. Alexandreanu, E. E. Gruber, R. S. Daum, and W. J. Shack, "Crack Growth Rates of Irradiated Austenitic Stainless Steel Weld Heat Affected Zone in BWR Environments," NUREG/CR-6891, ANL-04/20, 2006.

55. Odette, G. R., and G. E. Lucas, "The Effects of Intermediate Temperature Irradiation on the Mechanical Behavior of 300-Series Austenitic Stainless Steels," J. Nucl. Mater. **179-181**, 572-576, 1991.

56. Andresen, P. L., "Similarity of Cold Work and Radiation Hardening in Enhancing Yield Strength and SCC Growth of Stainless Steel in Hot Water," Corrosion/02, NACE, Houston, TX, Paper No. 02509, 2002.

57. Jenssen, A., K. Gott, P. Efsing, and P. O. Andersson, "Crack Growth Behavior of Irradiated Type 304L Stainless Steel in Simulated BWR Environment," Proc. 11th Intl. Symp. on Environmental Degradation of Materials in Nuclear Power Systems - Water Reactor, pp. 1015-1024, 2003.

58. James, L. A., and D. P. Jones, "Fatigue Crack Growth Correlation for Austenitic Stainless Steels in Air," Proc. Conf. on Predictive Capabilities in Environmentally-Assisted Cracking, PVP Vol. 99, R. Rungta, ed., American Society of Mechanical Engineers, New York, pp. 363-414, 1985.

59. Shack, W. J., and T. F. Kassner, "Review of Environmental Effects on Fatigue Crack Growth of Austenitic Stainless Steels," NUREG/CR-6176, ANL-94/1, 1994.

60. Hazelton, W. S., and W. H. Koo, "Technical Report on Material Selection and Processing Guidelines for BWR Coolant Pressure Boundary Piping, Final Report," NUREG-0313, Rev. 2, 1988.

61. Balladon, P., J. Heritier, and P. Rabbe, "Influence of Microstructure on the Ductile Rupture Mechanisms of a 316L Steel at Room and Elevated Temperatures," Fracture Mechanics: 14th Symp., Vol. II: Testing and Applications, ASTM STP 791, American Society for Testing and Materials, Philadelphia, PA, pp. 496-516, 1983.

62. Mills, W. J., "On the Relationship Between Stretch Zone Formation and the J Integral for High Strain-Hardening Materials," J. of Testing and Evaluation **9**, 56-62, 1981.

63. Karlsen, T. M., P. Bennett, and N. W. Hogberg, "In-Core Crack Growth Rate Studies on Irradiated Austenitic Stainless Steels in BWR and PWR Conditions in the Halden Reactor," Proc. 12th Intl. Conf. on Environmental Degradation of Materials in Nuclear Power Systems - Water Reactors, T. R. Allen, P. J. King, and L. Nelson, eds., The Minerals, Metals & Materials Society, Warrendale, PA, pp. 337-348, 2005.

64. Nickell, R. E., and M. A. Rinckel, "Evaluation of Thermal Aging Embrittlement for Cast Austenitic Stainless Steels Components in LWR Reactor Coolant Systems," EPRI TR-106092, Electric Power Research Institute, Palo Alto, CA, 1997.

65. U.S. Nuclear Regulatory Commission, "Thermal Aging Embrittlement of Cast Austenitic Stainless Steel Components," License Renewal Issue No. 98-0030, U.S. Nuclear Regulatory Commission, May 19, 2000.

Appendix A

Appendix A: Crack Growth Rate Data for Irradiated Austenitic SSs

A.1 Specimen C3-A of Type 304L SS Irradiated to 0.45 dpa at 288°C, Test CGRI-12

Table A1. Crack growth data for Specimen C3-A[a] of Type 304L SS in BWR water at 289°C.

Test Period[b]	Test Time, h	ECP,[c] mV (SHE) Pt	ECP,[c] mV (SHE) Steel	O$_2$ Conc.,[c] ppb	R Load Ratio	Rise Time, s	Return Time, s	Hold Time, s	K$_{max}$, MPa m$^{1/2}$	ΔK, MPa m$^{1/2}$	Growth Rate, m/s	Allowed K$_{max}$,[d] MPa m$^{1/2}$	Crack Length,[e] mm
													6.000
Pre	55	226	167	300	0.31	0.50	0.50	0	12.9	8.9	2.94E-09	18.4	6.037
1	165	212	166	300	0.30	0.50	0.50	0	14.0	9.8	8.37E-09	17.9	6.350
2a	189	221	169	300	0.50	5.00	5.00	0	13.9	6.9	negligible	17.9	6.364
2b	193	211	169	300	0.50	0.50	0.50	0	13.8	6.9	negligible	17.9	6.363
2c	214	211	163	300	0.30	0.50	0.50	0	13.9	9.7	negligible	17.9	6.358
2d	219	218	171	300	0.30	0.50	0.50	0	15.0	10.5	1.48E-08	17.7	6.499
3	364	218	171	300	0.30	1	1	0	15.9	11.1	1.39E-08	17.5	6.598
4	380	218	171	300	0.30	30	4	0	16.0	11.2	1.33E-09	17.4	6.663
5*	404	219	177	300	0.29	300	4	0	15.9	11.3	3.29E-10	17.4	6.690
6	479	204	173	300	0.48	300	4	0	15.7	8.2	4.75E-11	17.4	6.704
7	596	235	187	300	0.70	12	12	0	15.7	4.7	negligible	17.4	6.704
8	670	228	188	300	0.70	12	12	0	17.6	5.3	6.23E-11	17.3	6.720
9	717	231	186	300	0.70	12	12	3600	17.9	-	-	17.3	6.741
10*	910	134	197	300	0.70	500	12	3600	17.9	-	8.65E-11	17.2	6.796
11	1080	232	200	300	0.70	500	12	3600	22.0	-	1.11E-10	17.1	6.873
12	1175	226	203	300	0.70	500	12	9500	22.3	-	1.13E-10	17.0	6.916

[a]Heat C3, irradiated to 0.3 x 10^{21} n/cm^2 (0.45 dpa) at ≈288°C.
[b]An asterisk indicates environmental enhancement of growth rates under cyclic loading.
[c]Represents values in the effluent. Conductivity was ≈0.07 and 0.30-0.45 μS/cm in the feedwater and effluent, respectively. Feedwater pH at room temperature was 6.5.
[d]Based on effective flow stress, defined as the average of irradiated and nonirradiated flow stresses.
[e]The difference between the measured crack extension and that determined from the DC potential drop measurements was <5%.
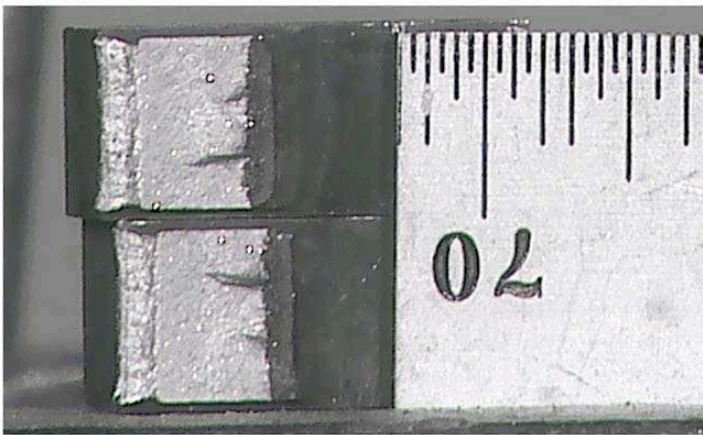
Figure A1.
Photograph of the fracture surfaces of the two halves of the fractured Specimen C3-A.

A.2 Specimen C3-B of Type 304L SS Irradiated to 1.35 dpa at 288°C, Test CGRI-07

Table A2.   Crack growth data for Specimen C3-B[a] of Type 304L SS in BWR water at 289°C.

Test Period[b]	Test Time, h	ECP,[c] mV (SHE) Pt	ECP,[c] mV (SHE) Steel	O_2 Conc.,[c] ppb	R Load Ratio	Rise Time, s	Return Time, s	Hold Time, s	K_{max}, MPa m$^{1/2}$	ΔK, MPa m$^{1/2}$	Growth Rate, m/s	Allowed K_{max},[d] MPa m$^{1/2}$	Crack Length,[e] mm
													6.000
Pre a	2	222	147	300	0.20	0.5	0.5	0	18.7	15.0	4.51E-08	19.5	6.188
Pre b	4	223	148	300	0.20	0.5	0.5	0	17.6	14.1	4.17E-08	19.2	6.391
Pre c	23	-	-	300	0.53	30	2	0	16.9	7.9	1.12E-10	19.2	6.393
Pre d	26	-	-	300	0.20	0.5	0.5	0	17.9	14.3	3.41E-08	18.8	6.590
1	28	230	154	300	0.20	0.5	0.5	0	19.1	15.3	6.83E-08	18.4	6.817
2*	172	239	189	300	0.51	60	2	0	19.0	9.3	1.75E-10	18.3	6.873
3*	287	233	187	300	0.70	300	2	0	19.8	5.9	6.38E-10	18.0	7.046
4	335	235	191	300	0.70	2	2	7200	20.1	-	1.06E-09	17.7	7.229
5	376	238	195	300	0.70	2	2	7200	22.1	-	1.04E-09	17.4	7.400
6	624	-475	-595	≈10	0.70	2	2	7200	22.3	-	4.02E-11	17.2	7.503
7	696	-482	-607	≈10	0.70	300	2	0	22.1	6.6	8.56E-11	17.1	7.534
8	935	-495	-614	≈10	0.70	2	2	3600	22.7	-	6.42E-12	17.1	7.540
9	1031	-499	-609	≈10	0.70	300	2	0	22.5	6.8	3.37E-11	17.1	7.550
10a	1127	-495	-613	≈10	0.70	1000	2	0	22.2	6.7	negligible	17.1	7.548
10b	1271	-507	-620	≈10	0.70	1000	2	0	23.0	6.9	1.20E-11	17.1	7.552
11	1295	-507	-624	≈10	0.70	30	2	0	22.9	6.9	5.17E-11	17.1	7.561
12	1343	-498	-617	≈10	0.70	300	2	0	23.1	6.9	1.55E-11	17.1	7.568
14	1608	248	151	250	0.70	1000	2	0	24.2	7.3	5.93E-10	16.7	7.768
15	1655	244	155	250	0.70	2	2	3600	24.4	-	8.70E-10	16.4	7.916

[a]Heat C3, irradiated to 0.9 x 10^{21} n/cm^2 (1.35 dpa) at ≈288°C.
[b]An asterisk indicates environmental enhancement of growth rates under cyclic loading.
[c]Represents values in the effluent. Conductivity was ≈0.07 and 0.30-0.45 μS/cm in the feedwater and effluent, respectively. Feedwater pH at room temperature was 6.5.
[d]Based on effective yield stress, defined as the average of irradiated and nonirradiated yield stresses.
[e]The difference between the measured crack extension and that determined from the DC potential drop measurements was <5%.
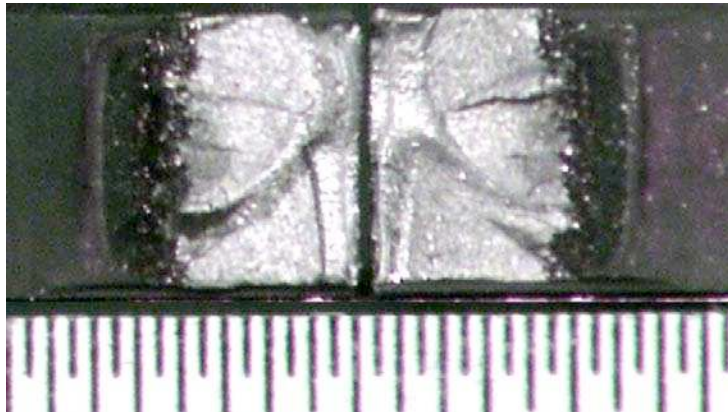
Figure A2.
Photomicrographs of the fracture surface of Specimen C3-B.

A.3   Specimen C3-C of Type 304L SS Irradiated to 3.0 dpa at 288°C, Test CGRI-08

Table A3.   Crack growth data for Specimen C3-C[a] of Type 304L SS in BWR water at 289°C.

Test Period[b]	Test Time, h	ECP,[c] mV (SHE) Pt	ECP,[c] mV (SHE) Steel	O_2 Conc.,[c] ppb	R Load Ratio	Rise Time, s	Return Time, s	Hold Time, s	K_{max}, MPa m$^{1/2}$	ΔK, MPa m$^{1/2}$	Growth Rate, m/s	Allowed K_{max},[d] MPa m$^{1/2}$	Crack Length,[e] mm
													6.000
1	46	241	164	300	0.26	2	2	0	17.9	13.2	2.00E-08	22.4	6.702
2	71	223	155	300	0.53	30	2	0	18.4	8.7	2.22E-09	22.1	6.830
3[*]	99	235	167	300	0.70	300	2	0	18.8	5.6	1.73E-09	21.8	6.977
4[*]	142	232	164	300	0.69	1000	2	0	19.2	6.0	1.25E-09	21.4	7.167
5	191	233	164	300	0.70	2	2	3600	19.4	-	6.83E-10	21.1	7.294
6	311	200	150	100	0.70	2	2	3600	23.7	-	5.07E-10	20.5	7.572
7	560	-547	-294	≈10	0.70	2	2	3600	27.5	-	6.91E-10	19.1	8.171
8	706	-551	-502	≈10	0.70	2	2	3600	34.7	-	2.04E-09	16.4	9.154
9	724	-557	-457	≈10	0.70	2	2	3600	37.0	-	3.70E-09	15.8	9.367

[a]Heat C3, irradiated to 2.0 x 10^{21} n/cm^2 (3.0 dpa) at ≈288°C.
[b]An asterisk indicates environmental enhancement of growth rates under cyclic loading.
[c]Represents values in the effluent. Conductivity was ≈0.07 and 0.30-0.45 μS/cm in the feedwater and effluent, respectively. Feedwater pH at room temperature was 6.5.
[d]Based on effective yield stress, defined as the average of irradiated and nonirradiated yield stresses.
[e]Actual crack extension was 40% greater than the value determined from the DC potential drop measurements.
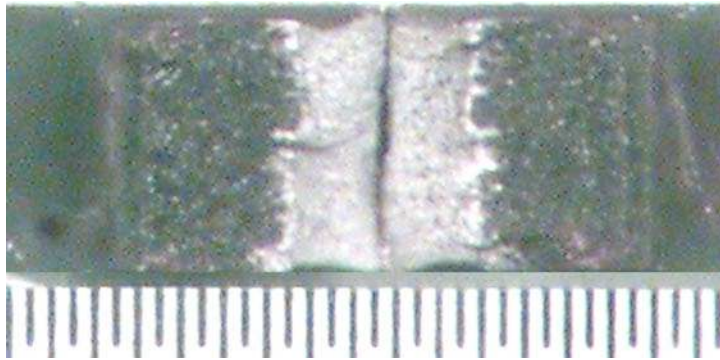
Figure A3.
Photograph of the fracture surfaces of the two halves of the fractured Specimen C3-C.

A.4   Specimen C16-B of Type 316L SS Irradiated to 3.00 dpa at 288°C, Test CGRI-09

Table A4.   Crack growth data for Specimen C16-B[a] of Type 316L SS in BWR water at 289°C.

Test Period[b]	Test Time, h	ECP, mV (SHE) Pt	ECP, mV (SHE) Steel	O_2 Conc.,[c] ppb	R Load Ratio	Rise Time, s	Return Time, s	Hold Time, s	K_{max}, MPa m$^{1/2}$	ΔK, MPa m$^{1/2}$	Growth Rate, m/s	Allowed K_{max},[d] MPa m$^{1/2}$	Crack Length,[e] mm
													6.000
Pre a	6	-	-	250	0.32	1	1	0	14.3	9.8	1.75E-08	22.9	6.132
Pre b	30	232	144	250	0.30	2	2	0	14.0	9.8	7.54E-09	22.5	6.328
Pre c	52	227	144	250	0.31	2	2	0	14.2	9.8	8.94E-09	22.3	6.417
1	94	224	148	250	0.56	12	2	0	14.6	6.4	4.94E-10	22.2	6.450
2	132	226	147	250	0.73	30	2	0	14.8	4.0	8.65E-10	22.0	6.546
3*	173	228	151	250	0.71	300	2	0	15.0	4.4	8.16E-10	21.8	6.666
4*	198	224	153	250	0.70	1,000	12	0	15.0	4.5	7.33E-10	21.7	6.728
5	265	162	117	250	0.70	12	12	3600	15.2	-	4.62E-10	21.4	6.877
6	410	-547	-298	<30	0.70	12	12	3600	15.3	-	1.90E-11	21.3	6.908
7	504	-562	-410	<30	0.70	1,000	12	0	15.1	4.5	2.76E-11	21.3	6.914
8	527	-560	-449	<30	0.73	30	2	0	15.2	4.1	6.07E-11	21.3	6.920
9	552	-557	-502	<30	0.70	30	2	0	17.3	5.2	2.51E-10	21.2	6.971
10	600	-554	-545	<30	0.69	1,000	12	0	17.2	5.3	3.59E-11	21.2	6.977
11	672	-557	-554	<30	0.70	12	12	3600	17.3	-	1.73E-11	21.1	6.983
12	792	-438	-597	<30	0.70	12	12	3600	19.7	-	4.11E-11	21.1	7.011
13	866	219	139	250	0.70	12	12	3600	19.6	-	7.14E-10	21.0	7.071
14	871	224	148	250	0.70	12	12	3600	21.9	-	1.10E-09	20.9	7.088
15	888	224	148	250	1.00[f]	-	-	-	21.9	-	5.27E-10	20.9	7.118

[a]Heat C16, irradiated to 2.0 x 10^{21} n/cm^2 (3.0 dpa) at ≈288°C.
[b]An asterisk indicates environmental enhancement of growth rates under cyclic loading.
[c]Represents values in the effluent. Effluent conductivity was ≈0.45 μS/cm and DO was ≈250 ppb during high-DO test and <30 ppb during low-DO test. Feedwater conductivity was 0.07 μS/cm and pH at room temperature was 6.5.
[d]Based on effective yield stress, defined as the average of irradiated and nonirradiated yield stresses.
[e]The difference between the measured crack extension and that determined from the DC potential drop measurements was <5%.
[f]Constant-displacement test.
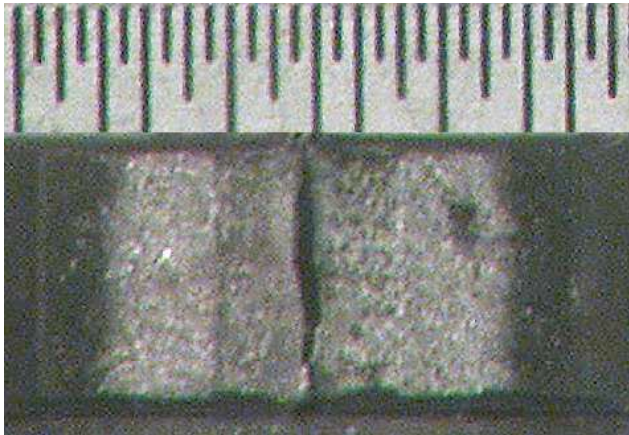
Figure A4.
Photograph of the fracture surfaces of the two halves of the fractured Specimen C16-B.

A.5   Specimen GG5B-A of Type 304L SA weld HAZ as-welded, Test CGR-10.

Table A5.   Crack growth results for Specimen GG5B-A[a] of Type 304L HAZ in high-purity water at 289°C.

Test Period[b]	Test Time, h	ECP,[c] mV (SHE) Pt	ECP,[c] mV (SHE) Steel	O_2 Conc.,[c] ppb	R Load Ratio	Rise Time, s	Return Time, s	Hold Time, s	K_{max}, MPa m$^{1/2}$	ΔK, MPa m$^{1/2}$	Growth Rate, m/s	Allowed K_{max},[d] MPa m$^{1/2}$	Crack Length,[e] mm
													5.797
Pre a	97	f	f	580	0.23	0.25	0.25	0	16.7	12.9	7.57E-08	19.3	6.411
Pre b	98	f	f	580	0.23	0.25	0.25	0	15.0	11.5	3.42E-08	19.1	6.498
Pre c	114	f	f	590	0.23	7.5	7.5	0	14.2	11.0	3.59E-10	19.1	6.518
Pre d	120	f	f	590	0.23	0.50	0.50	0	15.7	12.1	3.40E-08	18.7	6.746
1	143	f	f	485	0.52	30	2	0	15.5	7.4	5.85E-11	18.6	6.764
2a	259	f	f	440	0.71	30	2	0	17.0	4.9	negligible	18.6	6.771
2b	306	f	f	450	0.71	30	2	0	17.0	4.9	1.52E-11	18.6	6.772
2c*	337	f	f	465	0.72	30	2	0	20.6	5.8	3.15E-10	18.6	6.795
3*	407	f	f	460	0.71	300	2	0	20.8	6.0	1.81E-10	18.5	6.842
4*	455	f	f	500	0.71	1,000	2	0	20.9	6.1	1.26E-10	18.5	6.866
5	572	f	f	500	0.71	12	12	3600	21.1	6.1	6.01E-11	18.4	6.893
6	646	f	f	500	0.71	12	12	3600	26.5	7.7	1.72E-10	18.3	6.957
7	692	f	f	500	0.71	12	12	3600	26.9	7.8	1.55E-10	18.2	6.985
8	767	f	f	500	0.71	1000	2	0	27.4	7.9	3.18E-10	18.1	7.067

[a]Nonirradiated Grand Gulf H5 SA weld bottom shell HAZ, as-welded condition.
[b]An asterisk indicates environmental enhancement of growth rates under cyclic loading.
[c]Represents values in the effluent.
[d]Based on ASTM 647 criterion and flow stress.
[e]The difference between the measured crack extension and that determined from the DC potential drop measurements was <5%.
[f]Could not be measured because of a faulty reference electrode.
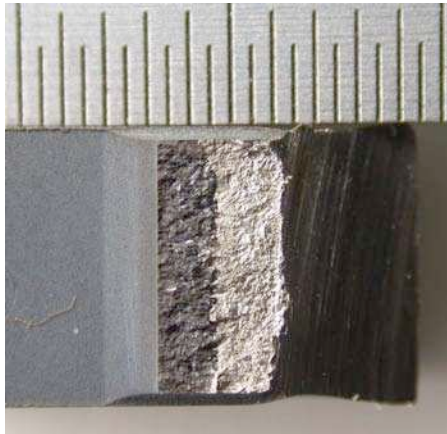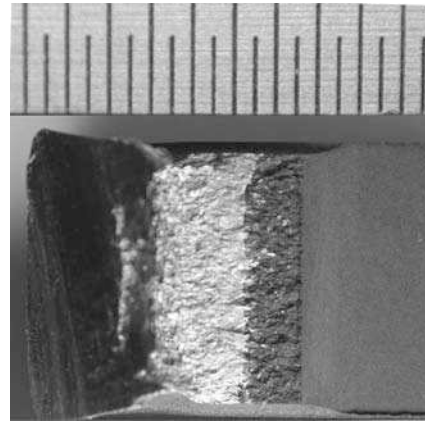
(a)   (b)
Figure A5.   Photomicrograph of the fracture surface of Specimen GG5B-A.

A.6   Specimen 85-3A-TT of Type 304 SMA weld HAZ thermally treated, Test CGR-11.

Table A6.   Crack growth results for Specimen 85-3A-TT[a] of nonirradiated Type 304 SS SMA weld HAZ in high-purity water at 289°C.

Test Period[b]	Test Time, h	ECP, [c] mV (SHE) Pt	Steel	O_2 Conc.,[c] ppb	R Load Ratio	Rise Time, s	Return Time, s	Hold Time, s	K_{max}, MPa m$^{1/2}$	ΔK, MPa m$^{1/2}$	Growth Rate, m/s	Allowed K_{max},[d] MPa m$^{1/2}$	Crack Length,[e] mm
													5.786
Pre a	144	-	-	690	0.21	0.50	0.50	0	16.1	12.7	5.46E-08	22.0	6.237
Pre b	148	183	27	650	0.21	0.50	0.50	0	15.0	11.9	5.00E-08	21.6	6.480
1	166	182	32	600	0.51	30	2	0	14.6	7.2	5.61E-11	21.5	6.507
2	190	184	41	600	0.51	30	2	0	16.7	8.2	5.50E-10	21.4	6.550
3	215	182	45	600	0.71	30	2	0	16.9	4.9	3.16E-11	21.4	6.555
4*	264	184	60	600	0.71	30	2	0	19.8	5.8	8.85E-10	21.1	6.709
5a*	298	188	68	600	0.71	300	2	0	19.8	5.7	2.75E-10	21.0	6.744
5b*	338	187	79	600	0.71	300	2	0	20.2	5.9	7.91E-10	20.8	6.862
6*	384	188	87	600	0.70	1,000	2	0	20.5	6.2	4.57E-10	20.6	6.937
7	478	192	106	600	0.70	12	12	3600	21.2	-	6.60E-10	20.2	7.150
8	646	-482	-633	45	0.70	12	12	3600	21.4	-	9.13E-11	20.0	7.227
9	862	-483	-627	<40	0.70	12	12	3600	25.0	-	4.29E-11	19.9	7.293

[a]Nonirradiated Type 304 SS (Heat 10285) SMA weld HAZ, as-welded plus thermally treated for 24 h at 500°C.
[b]An asterisk indicates environmental enhancement of growth rates under cyclic loading.
[c]Represents values in the effluent. Water flow rate was maintained at ≈105 mL/min.
[d]Based on ASTM 647 criterion and flow stress.
[e]Actual crack extension was 40% greater than the value determined from the DC potential drop measurements.
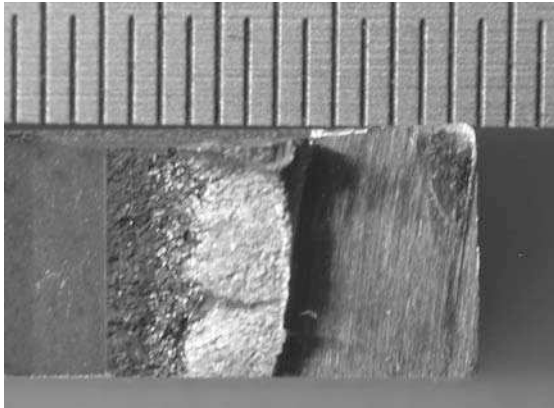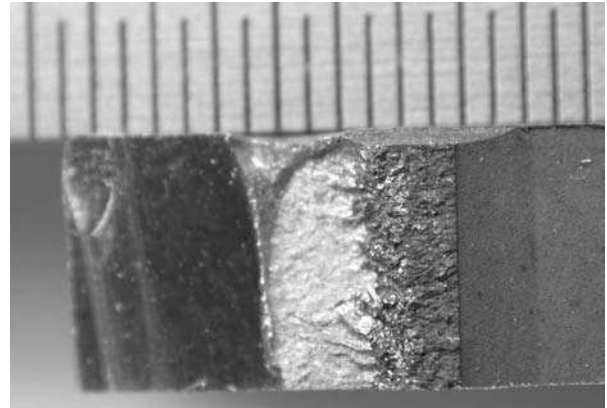
(a)   (b)

Figure A6.   Photomicrographs of the fracture surfaces of the two halves of Specimen 85-3A-TT.

A.7 Specimen GG3B-A-TT of Type 304L SA weld HAZ thermally treated, Test CGR-14.

Table A7. Crack growth results for Specimen GG3B-A-TT[a] of Type 304L HAZ in high-purity water at 289°C.

Test Period[b]	Test Time, h	ECP,[c] mV (SHE) Pt	ECP,[c] mV (SHE) Steel	O_2 Conc.,[c] ppb	R Load Ratio	Rise Time, s	Return Time, s	Hold Time, s	K_{max}, MPa m$^{1/2}$	ΔK, MPa m$^{1/2}$	Growth Rate, m/s	Allowed K_{max},[d] MPa m$^{1/2}$	Crack Length,[e] mm
													5.788
Pre a	120	181	20	450	0.31	0.5	0.5	0	14.3	9.9	7.71E-09	20.2	5.856
Pre b	143	185	25	450	0.31	5	5	0	14.4	10.0	5.91E-09	20.0	5.991
Pre c	238	192	36	450	0.51	1	1	0	15.0	7.4	1.34E-09	19.5	6.255
1a*	275	192	40	470	0.71	12	2	0	16.0	4.6	8.66E-10	19.4	6.307
1b*	305	193	42	470	0.71	12	2	0	16.3	4.7	2.50E-09	19.2	6.475
2*	328	194	44	470	0.71	30	2	0	16.5	4.8	1.22E-09	19.0	6.579
3*	403	195	53	450	0.70	300	2	0	16.7	5.0	2.80E-10	18.8	6.659
4*	522	198	65	400	0.70	1,000	12	0	16.7	5.0	1.12E-10	18.8	6.706
5a	580	203	79	400	0.70	12	12	3600	16.4	4.9	4.34E-11	18.7	6.717
5b	765	202	87	400	0.70	12	12	3600	16.7	5.0	9.60E-12	18.4	6.882
6	1000	202	88	400	0.70	500	12	3600	18.5	5.6	9.06E-12	18.4	6.890
7	1094	204	90	400	0.70	500	12	3600	20.4	6.1	4.47E-12	18.4	6.894

[a]Nonirradiated Grand Gulf H5 SA weld bottom shell HAZ, as-welded plus thermally treated for 24 h at 500°C.
[b]An asterisk indicates environmental enhancement of growth rates under cyclic loading.
[c]Represents values in the effluent. Water flow rate was ≈100 mL/min.
[d]Based on ASTM 647 criterion and flow stress.
[e]Actual crack extension was 30% greater than the value determined from the DC potential drop measurements.
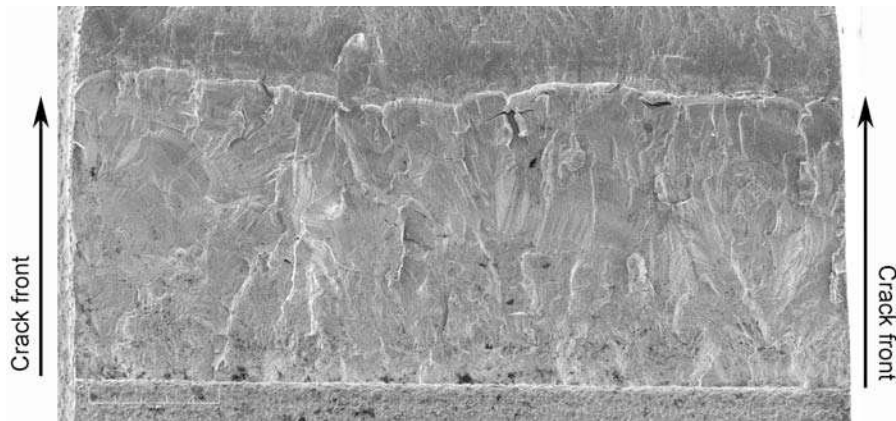
Figure A7. Micrograph of the fracture surface of Specimen GG3B-A-TT tested in high-DO water at 289°C.

A.8   Specimen 85-YA of Type 304 SMA weld HAZ as-welded, Test CGR-22.

Table A8.   Crack growth results for Specimen 85-YA[a] of nonirradiated Type 304 SS SMA weld HAZ in high-purity water at 289°C.

Test Period[b]	Test Time, h	ECP,[c] mV (SHE) Pt	ECP,[c] mV (SHE) Steel	O_2 Conc.,[c] ppb	R Load Ratio	Rise Time, s	Return Time, s	Hold Time, s	K_{max}, MPa m$^{1/2}$	ΔK, MPa m$^{1/2}$	Growth Rate, m/s	Allowed K_{max},[d] MPa m$^{1/2}$	Crack Length,[e] mm
													5.799
Pre a	149	f	f	300	0.33	0.50	0.5	0	16.2	10.8	4.73E-08	22.1	6.181
Pre b	192	f	f	300	0.33	10	10	0	16.7	11.2	5.72E-09	21.6	6.477
1	263	f	f	300	0.52	300	12	0	16.7	8.0	2.19E-11	21.6	6.482
2	288	f	f	300	0.52	30	12	0	16.7	8.0	2.51E-10	21.5	6.500
3	318	f	f	300	0.52	30	12	0	19.2	9.2	6.21E-10	21.3	6.607
4*	384	f	f	300	0.51	300	12	0	19.3	9.5	3.68E-10	21.1	6.693
5*	551	f	f	300	0.51	1,000	12	0	19.8	9.7	1.85E-10	20.9	6.795
6	768	f	f	300	1.00	-	-	-	19.7	-	negligible	20.9	6.788

[a]Nonirradiated laboratory-prepared Type 304 SS (Heat 10285) SMA weld HAZ, as-welded condition.
[b]An asterisk indicates environmental enhancement of growth rates under cyclic loading.
[c]Represents values in the effluent. Conductivity was ≈0.07 and 0.2 μS/cm in feedwater and effluent, respectively.
[d]Based on ASTM 647 criterion and flow stress.
[e]Actual crack extension was 80% greater than the value determined from the DC potential drop measurements.
[f]Could not be measured because of faulty temperature controller
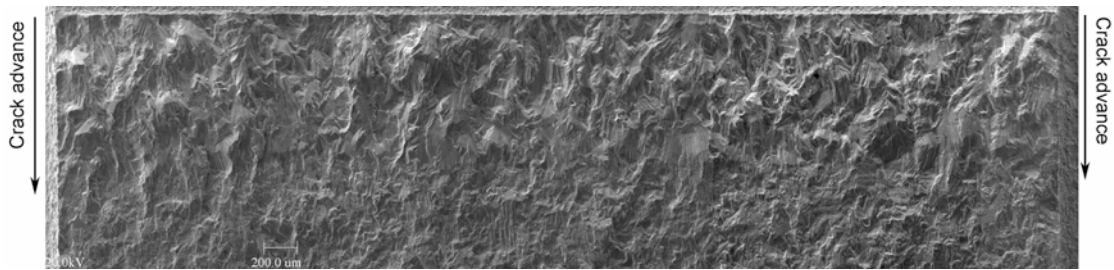
Figure A8.   Micrograph of the fracture surface of Specimen 85-YA tested in BWR environment at 289°C.

A.9   Specimen GG5T-A of Type 304L SA weld HAZ as-welded and irradiated to 0.75 dpa, Test CGRI-15.

Table A9.   Crack growth results for Specimen GG5T-A[a] of Type 304L HAZ in high-purity water at 289°C.

Test Period[b]	Test Time, h	ECP, mV (SHE) Pt	Steel	O_2 Conc.,[c] ppb	R Load Ratio	Rise Time, s	Return Time, s	Hold Time, s	K_{max}, MPa m$^{1/2}$	ΔK, MPa m$^{1/2}$	Growth Rate, m/s	Allowed K_{max},[d] MPa m$^{1/2}$	Crack Length,[e] mm
													5.806
1	69	212	205	250	0.17	0.50	0.50	0	12.4	10.3	1.71E-08	28.1	5.923
2a	74	212	205	250	0.28	0.50	0.50	0	12.3	8.9	3.11E-09	28.0	5.956
2b	144	214	201	250	0.30	0.50	0.50	0	12.8	8.9	2.70E-09	28.0	5.972
2c	165	214	201	250	0.32	0.50	0.50	0	13.5	9.2	1.06E-08	27.8	6.036
3a	195	213	195	250	0.52	60	4	0	14.3	6.9	4.30E-11	27.8	6.045
3b[*]	215	213	195	250	0.52	60	4	0	15.3	7.4	1.61E-09	27.6	6.118
4[*]	260	209	196	250	0.69	300	4	0	14.7	4.6	3.34E-10	27.5	6.173
5[*]	305	207	196	250	0.69	1,000	12	0	14.7	4.6	3.89E-10	27.4	6.235
6	355	206	196	250	0.70	60	12	0	15.3	4.6	3.10E-11	27.3	6.276
7	378	205	199	250	0.71	60	12	0	16.6	4.8	8.03E-11	27.2	6.285
8	482	199	193	250	0.51	30	4	0	16.6	8.1	8.57E-11	27.2	6.308

[a]Grand Gulf H5 SA weld top shell HAZ, irradiated to 5.0 x 10^{20} n cm^{-2} (0.75 dpa) at ≈297°C.
[b]An asterisk indicates environmental enhancement of growth rates under cyclic loading.
[c]Represents values in the effluent. Conductivity was ≈0.07 and 0.2 μS/cm in feedwater and effluent, respectively.
[d]Based on ASTM 1681 criterion and flow stress.
[e]The specimen was not fractured and the DC potential drop measurements were not corrected.

A.10 Specimen GG5T-B of Type 304L SA weld HAZ as-welded and irradiated to 0.75 dpa, Test CGRI-16.

Table A10. Crack growth results for Specimen GG5T-B[a] of Type 304L HAZ in high-purity water at 289°C.

Test Period[b]	Test Time, h	ECP,[c] mV (SHE) Pt	ECP,[c] mV (SHE) Steel	O_2 Conc.,[d] ppb	R Load Ratio	Rise Time, s	Return Time, s	Hold Time, s	K_{max}, MPa m$^{1/2}$	ΔK, MPa m$^{1/2}$	Growth Rate, m/s	Allowed K_{max},[d] MPa m$^{1/2}$	Crack Length,[e] mm
													5.823
Pre	81	225	211	400	0.20	0.50	0.50	0	13.8	11.0	7.24E-09	28.1	5.930
1	105	218	200	400	0.30	0.50	0.50	0	13.0	9.1	4.59E-09	28.0	5.982
2a	122	216	206	350	0.50	60	4	0	12.8	6.4	negligible	28.0	5.980
2b*	154	214	199	350	0.51	30	4	0	14.4	7.1	9.13E-10	27.8	6.075
3*	221	211	199	350	0.49	300	4	0	14.7	7.5	2.82E-10	27.6	6.155
4*	296	204	200	350	0.70	300	4	0	14.8	4.4	2.35E-10	27.4	6.229
5*	362	229	200	350	0.68	1,000	12	0	14.7	4.7	2.98E-10	27.2	6.305
6	433	201	176	350	0.69	300	12	3600	14.7	4.6	6.75E-10	26.7	6.501
7	530	220	204	350	1.00	-	-	-	15.0	-	4.24E-10	26.4	6.644
8	584	215	202	350	0.69	300	12	9700	15.2	4.7	5.62E-10	26.1	6.774
9	724	-532	-285	<50	0.69	300	12	9700	14.9	4.6	negligible	26.0	6.777
10	893	-533	-530	<50	0.69	300	122	0	15.0	4.6	negligible	26.0	6.781

[a]Grand Gulf H5 SA weld top shell HAZ, irradiated to 5.0 x 10^{20} n cm^{-2} (0.75 dpa) at ≈297°C.
[b]An asterisk indicates environmental enhancement of growth rates under cyclic loading.
[c]Represents values in the effluent. Conductivity was ≈0.07 and 0.2 μS/cm in feedwater and effluent, respectively.
[d]Based on ASTM 1681 criterion and flow stress.
[e]The difference between the measured crack extension and that determined from the DC potential drop measurements was <5%.

Figure A9.
Photomicrograph of the fracture surface of Specimen GG5T-B.

A.11 Specimen 85-1A-TT of Type 304 SMA weld HAZ thermally treated and irradiated to 0.75 dpa, Test CGRI-18.

Table A11. Crack growth results for Specimen 85-1A-TT[a] of Type 304 SS SMA weld HAZ in high-purity water at 289°C.

Test Period[b]	Test Time, h	ECP,[c] mV (SHE) Pt	Steel	O_2 Conc.,[c] ppb	R Load Ratio	Rise Time, s	Return Time, s	Hold Time, s	K_{max}, MPa m$^{1/2}$	ΔK, MPa m$^{1/2}$	Growth Rate, m/s	Allowed K_{max},[d] MPa m$^{1/2}$	Crack Length,[e] mm
													5.837
Pre a	98	229	163	200	0.17	0.25	0.25	0	13.9	11.6	2.64E-08	29.8	5.965
Pre b	101	228	161	200	0.24	0.50	0.50	0	13.3	10.1	2.10E-08	29.6	6.065
1a	145	213	166	200	0.50	60	4	0	14.6	7.3	negligible	29.6	6.065
1b*	217	203	175	200	0.50	1,000	4	0	15.1	7.6	4.80E-10	29.5	6.100
2*	262	201	178	250	0.70	300	4	0	16.1	4.8	3.55E-10	29.2	6.204
3*	314	199	172	250	0.71	1,000	12	0	16.4	4.7	3.37E-10	29.1	6.261
4	411	197	182	250	0.70	300	12	3600	16.6	5.0	2.55E-10	28.8	6.358
5	479	203	188	250	0.70	300	12	9700	16.7	5.0	1.74E-10	28.7	6.404
6	605	175	185	250	0.70	300	12	9700	18.7	5.6	2.78E-10	28.4	6.520
7	746	-526	-258	<30	0.70	300	12	9700	19.3	5.8	5.73E-11	28.3	6.550

[a]Laboratory-prepared SMA weld HAZ thermally treated 24 h at 500°C, irradiated to 5.0 x 10^{20} n cm^{-2} (0.75 dpa) at ≈297°C.
[b]An asterisk indicates environmental enhancement of growth rates under cyclic loading.
[c]Represents values in the effluent. Conductivity was ≈0.07 and 0.2 μS/cm in feedwater and effluent, respectively.
[d]Based on ASTM 1681 criterion and flow stress.
[e]The difference between the measured crack extension and that determined from the DC potential drop measurements was <5%.
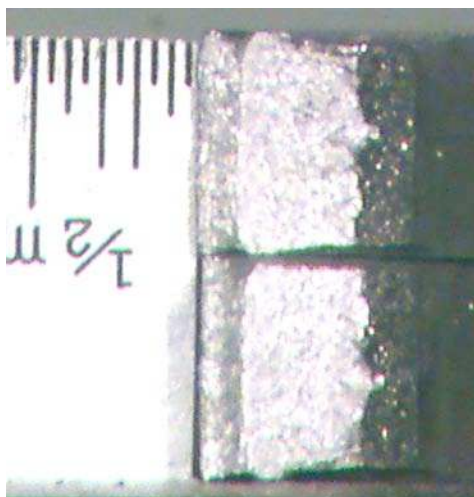
Figure A10.
Photomicrograph of the fracture surface of Specimen 85-1A TT.

A.12 Specimen 85-7A of Type 304 SMA weld HAZ as-welded and irradiated to 0.75 dpa, Test CGRI-20.

Table A12. Crack growth data for specimen 85-7A of SS SMA Weld HAZ in high-purity water[a] at 289°C.

Test Period[b]	Test Time, h	ECP,[c] mV (SHE) Pt	ECP,[c] mV (SHE) Steel	O_2 Conc.,[c] ppb	R Load Ratio	Rise Time, s	Return Time, s	Hold Time, s	K_{max}, MPa m$^{1/2}$	ΔK, MPa m$^{1/2}$	Growth Rate, m/s	Allowed K_{max},[d] MPa m$^{1/2}$	Crack Length,[e] mm
													5.806
Pre	166	261	224	500	0.23	0.50	0.50	0	15.9	12.2	2.77E-08	29.7	5.951
1	187	258	225	500	0.50	60	4	0	15.8	7.9	negligible	29.7	5.969
2	428	244	219	500	0.51	300	4	0	15.7	7.7	2.09E-11	29.6	5.999
3	499	245	221	500	0.50	1,000	12	0	16.4	8.2	negligible	29.6	5.998
4	608	234	211	500	0.53	1,000	12	0	17.2	8.1	4.65E-11	29.6	6.013
5*	763	229	209	500	0.50	1,000	12	0	18.3	9.1	4.28E-10	29.1	6.219
6*	788	231	212	500	0.50	1,000	12	3600	18.6	9.3	9.51E-10	28.8	6.310
7	845	221	214	500	1.00	-	-	-	19.4	-	9.46E-10	28.3	6.502
8	1100	-527	-252	<50	1.00	-	-	-	19.8	-	1.55E-11	28.0	6.625

[a]Laboratory-prepared SMA weld HAZ, irradiated to 0.5 x 10^{21} n cm^{-2} (0.75 dpa) at ≈297°C.
[b]An asterisk indicates environmental enhancement of growth rates under cyclic loading.
[c]Represents values in the effluent. Conductivity was ≈0.07 and 0.3 μS/cm in feedwater and effluent, respectively.
[d]Based on ASTM 1681 criterion and flow stress.
[e]Actual crack extension was 80% greater than the value determined from the DC potential drop measurements.
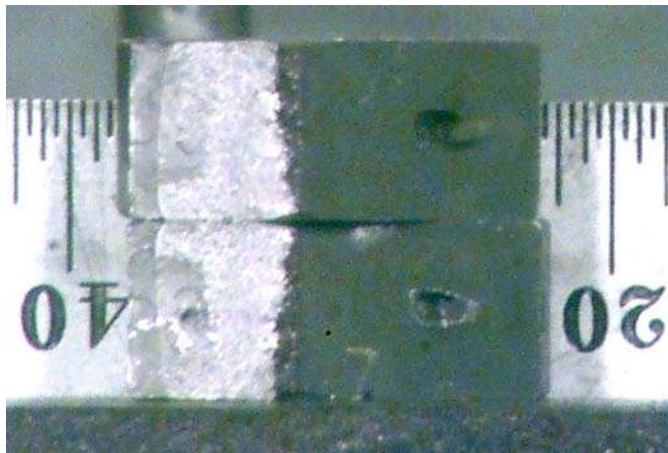
Figure A11.
Photomicrograph of the fracture surface of Specimen 85-7A.

Appendix B

Appendix B: Fracture Toughness J-R Curve Data for Irradiated Austenitic SSs

Table B1.   Fracture toughness data for specimen C19-A in air at 289°C.

Test Number   : JRI-21   Test Temp.   : 288°C
Test Environment : Air
Material Type   : Type 304 SS   Heat Number   : C19
Aging Temp.   : -   Aging Time   : -
Irradiation Temp. : 288°C   Fluence   : 0.30 x 10^{21} n/cm^2 (0.45 dpa)
Thickness   : 6.500 mm   Net Thickness   : 5.850 mm
Width   : 12.000 mm   Flow Stress   : 618 MPa
Modulus E   : 175 GPa   Effective Flow Stress : 479 MPa
Initial Crack   : 6.000 mm   Init. a/W   : 0.500
Final Crack   : 8.843 mm   Final a/W   : 0.737

No.	Load (kN)	Deflection (mm)	J (kJ/m^2)	Δa (mm)
0	0.0881	0.000	0.0	0.000
1	1.6218	0.154	11.4	0.006
2	2.3126	0.304	38.3	0.021
3	2.4287	0.499	76.9	0.041
4	2.5052	0.696	117.2	0.062
5	2.5640	0.895	159.1	0.084
6	2.6182	1.094	201.9	0.107
7	2.6583	1.295	245.6	0.130
8	2.6729	1.395	267.5	0.140
9	2.6872	1.497	290.1	0.153
10	2.7023	1.597	312.3	0.164
11	2.7005	1.699	334.4	0.179
12	2.7059	1.802	357.6	0.188
13	2.7045	1.902	380.1	0.196
14	2.7076	2.004	402.3	0.213
15	2.7054	2.104	427.3	0.227
16	2.6978	2.207	450.7	0.232
17	2.6796	2.310	472.3	0.251
18	2.6663	2.414	484.5	0.336
19	2.6449	2.516	496.7	0.415
20	2.6129	2.619	507.6	0.502
21	2.5889	2.723	518.5	0.587
22	2.5617	2.827	527.8	0.681
23	2.5261	2.931	540.6	0.748
24	2.4599	3.037	551.9	0.829
25	2.4252	3.143	561.6	0.913
26	2.3949	3.246	572.0	0.987
27	2.3544	3.351	582.6	1.062
28	2.3318	3.454	592.0	1.138
29	2.2673	3.561	600.8	1.220
30	2.2183	3.666	607.3	1.307
31	2.1663	3.771	613.2	1.393

Crack extension determined from DC potential drop method.

Power-Law Fit $J = C(\Delta a)^n$
DC Potential Method J_{Ic} : 503 kJ/m^2 (17 Data)
Coeff. C   : 575 kJ/m^2 Exponent n   : 0.17   Fit Coeff. R   : 0.974

Table B2.   Fracture toughness data for specimen C19-B in air at 289°C.

Test Number   : JRI-23   Test Temp.   : 288°C
Test Environment : Air
Material Type   : Type 304 SS   Heat Number   : C19
Aging Temp.   : -   Aging Time   : -
Irradiation Temp.   : 288°C   Fluence   : 0.90 x 10^{21} n/cm^2 (1.35 dpa)
Thickness   : 6.500 mm   Net Thickness   : 5.850 mm
Width   : 12.000 mm   Flow Stress   : 760 MPa
Modulus E   : 175 GPa   Effective Flow Stress : 550 MPa
Initial Crack   : 6.000 mm   Init. a/W   : 0.500
Final Crack   : 9.399 mm   Final a/W   : 0.783

No.	Load (kN)	Deflection (mm)	J (kJ/m^2)	Δa (mm)
0	0.0876	0.000	0.0	0.000
1	1.9710	0.125	8.6	0.004
2	2.6302	0.176	17.1	0.009
3	3.1849	0.236	24.3	0.012
4	3.5439	0.311	48.7	0.024
5	3.6431	0.404	73.8	0.035
6	3.6364	0.519	106.2	0.050
7	3.5893	0.624	137.7	0.065
8	3.5270	0.729	168.2	0.078
9	3.4687	0.836	201.8	0.094
10	3.4260	0.941	230.1	0.106
11	3.3411	1.047	255.7	0.118
12	3.2659	1.153	277.6	0.210
13	3.1947	1.259	305.5	0.309
14	3.1244	1.366	331.4	0.397
15	3.0582	1.472	354.1	0.479
16	2.9590	1.581	380.7	0.566
17	2.8802	1.689	401.5	0.657
18	2.7935	1.796	413.0	0.746
19	2.7094	1.903	437.0	0.832
20	2.6471	2.009	457.9	0.918
21	2.5386	2.169	483.0	1.040
22	2.4310	2.329	505.5	1.169
23	2.2842	2.491	521.3	1.301
24	2.1836	2.649	535.8	1.416
25	2.0595	2.811	547.5	1.550
26	1.9510	2.970	550.1	1.694
27	1.8340	3.131	557.1	1.823
28	1.7433	3.290	566.9	1.939
29	1.6570	3.449	572.2	2.041

Crack extension determined from DC potential drop method.

Power-Law Fit   **J = C(Δa)^n**
DC Potential Method J_{Ic} : 308 kJ/m^2 (17 Data)
Coeff. C   : 438 kJ/m^2 Exponent n   : 0.33   Fit Coeff. R   : 0.996

Table B3. Fracture toughness data for specimen C19-C in air at 289°C.

Test Number   : JRI-33   Test Temp.   : 288°C
Test Environment : Air
Material Type   : Type 304 SS   Heat Number   : C19
Aging Temp.   : -   Aging Time   : -
Irradiation Temp. : 288°C   Fluence   : 2.00 x 10^{21} n/cm^2 (3.00 dpa)
Thickness   : 6.500 mm   Net Thickness   : 5.850 mm
Width   : 11.996 mm   Flow Stress   : 794 MPa
Modulus E   : 175 GPa   Effective Flow Stress : 567 MPa
Initial Crack   : 6.000 mm   Init. a/W   : 0.500
Final Crack   : 10.359 mm   Final a/W   : 0.863

No.	Load (kN)	Deflection (mm)	J (kJ/m^2)	Δa (mm)
0	0.0890	0.000	0.0	0.000
1	0.6210	0.040	1.0	-0.254
2	0.9301	0.061	1.9	-0.011
3	1.2508	0.082	3.8	0.047
4	1.5862	0.106	6.5	-0.034
5	1.9114	0.129	9.2	-0.078
6	3.6676	0.350	48.5	-0.044
7	3.7183	0.397	60.4	0.038
8	3.6907	0.449	74.7	0.003
9	3.6266	0.504	92.2	0.006
10	3.5461	0.558	106.9	0.072
11	3.4118	0.668	136.7	0.102
12	3.2316	0.781	165.4	0.168
13	3.0697	0.893	187.5	0.311
14	2.9260	1.004	209.7	0.387
15	2.7459	1.118	225.4	0.575
16	2.5693	1.232	236.9	0.762
17	2.4256	1.343	245.3	0.956
18	2.2944	1.453	253.6	1.122
19	2.1663	1.564	266.4	1.230
20	2.0733	1.672	277.5	1.351
21	1.9630	1.780	294.9	1.445
22	1.8709	1.889	303.1	1.523
23	1.7949	1.997	316.1	1.599
24	1.7001	2.105	327.2	1.680
25	1.6249	2.212	337.3	1.757

Crack extension determined from elastic unloading compliance method.

Power-Law Fit   **J = C(Δa)^n**
DC Potential Method J_{Ic} : 184 kJ/m^2 (15 Data)
Coeff. C   : 265 kJ/m^2 Exponent n   : 0.29   Fit Coeff. R   : 0.967

Table B4. Fracture toughness data for specimen C16-A in air at 289°C.

Test Number   : JRI-26   Test Temp.   : 288°C
Test Environment : Air
Material Type   : Type 316L SS   Heat Number   : C16
Aging Temp.   : -   Aging Time   : -
Irradiation Temp. : 288°C   Fluence   : 0.90 x 10^{21} n/cm^2 (1.35 dpa)
Thickness   : 6.500 mm   Net Thickness   : 5.850 mm
Width   : 12.000 mm   Flow Stress   : 590 MPa
Modulus E   : 175 GPa   Effective Flow Stress : 463 MPa
Initial Crack   : 6.000 mm   Init. a/W   : 0.500
Final Crack   : 8.730 mm   Final a/W   : 0.728

No.	Load (kN)	Deflection (mm)	J (kJ/m^2)	Δa (mm)
0	0.0885	0.000	0.0	0.000
1	1.7602	0.117	8.6	0.007
2	2.5266	0.212	24.8	0.018
3	2.7552	0.347	53.4	0.032
4	2.8068	0.496	86.4	0.048
5	2.8104	0.572	103.2	0.057
6	2.8117	0.649	120.6	0.066
7	2.8206	0.725	137.5	0.076
8	2.8322	0.801	154.6	0.086
9	2.8179	0.880	172.2	0.095
10	2.8228	0.955	189.2	0.103
11	2.8206	1.031	206.0	0.112
12	2.8002	1.136	228.7	0.139
13	2.8050	1.236	248.5	0.183
14	2.7837	1.338	268.1	0.234
15	2.7846	1.441	287.4	0.290
16	2.7704	1.544	306.2	0.346
17	2.7450	1.647	325.4	0.397
18	2.7196	1.751	344.0	0.456
19	2.6925	1.853	361.5	0.515
20	2.6551	1.957	378.8	0.576
21	2.6187	2.063	396.1	0.638
22	2.5729	2.169	412.6	0.703
23	2.5395	2.273	428.2	0.767
24	2.5124	2.378	443.2	0.834
25	2.4799	2.482	459.2	0.888
26	2.4439	2.588	475.6	0.941
27	2.3931	2.693	491.6	0.994
28	2.3513	2.797	503.9	1.051
29	2.2922	2.904	518.7	1.111
30	2.2299	3.010	530.0	1.188
31	2.1801	3.117	540.6	1.260
32	2.1285	3.223	552.1	1.325
33	2.0813	3.328	562.9	1.390
34	2.0395	3.429	572.9	1.453

Crack extension determined from DC potential drop method.

Power-Law Fit $J = C(\Delta a)^n$
DC Potential Method J_{Ic} : 312 kJ/m^2 (14 Data)
Coeff. C   : 488 kJ/m^2 Exponent n : 0.45   Fit Coeff. R   : 0.997

Table B5. Fracture toughness data for specimen 85-3TT in high-purity water at 289°C.

Test Number : CGRI JR-31 Test Temp. : 289°C
Test Environment : High-purity water with ≈ 300 ppb dissolved oxygen
Material Type : Type 304 SS Heat Number : 10285
Aging Temp. : 600°C Aging Time : 10.5 h
Irradiation Temp. : 297°C Fluence : 1.44 x 10^{21} n/cm^2 (2.16 dpa)
Thickness : 6.523 mm Net Thickness : 5.817 mm
Width : 11.996 mm Flow Stress : 725 MPa (Estimated)
Modulus E : 175 GPa Effective Flow Stress : 527 MPa (Estimated)
Initial Crack : 6.161 mm Init. a/W : 0.514
Final Crack : 8.880 mm Final a/W : 0.740 (Measured)

No.	Load (kN)	Deflection (mm)	J (kJ/m^2)	Δa (mm)
0	0.000	0.000	0.0	0.000
1	0.976	0.021	0.7	0.000
2	1.647	0.040	2.2	0.001
3	2.259	0.074	6.5	0.003
4	2.899	0.111	12.7	0.007
5	3.474	0.153	21.4	0.011
6	3.938	0.207	34.3	0.017
7	4.321	0.267	50.4	0.025
8	4.525	0.347	73.8	0.024
9	4.583	0.443	99.5	0.142
10	4.560	0.547	128.1	0.234
11	4.511	0.605	151.9	0.097
12	4.490	0.708	170.6	0.354
13	4.385	0.821	200.0	0.456
14	4.273	0.932	228.6	0.543
15	4.182	1.044	261.8	0.553
16	4.046	1.160	290.2	0.633
17	3.863	1.280	307.2	0.833
18	3.761	1.394	331.6	0.923
19	3.570	1.567	356.6	1.147
20	3.366	1.741	384.5	1.323
21	3.154	1.914	408.9	1.499
22	2.833	2.149	432.4	1.761
23	2.542	2.381	445.1	2.047
24	2.340	2.605	452.8	2.317
25	2.169	2.829	469.0	2.519
26	2.020	3.047	479.2	2.723

Power-Law Fit $J = C(\Delta a)^n$
DC Potential Method J_{Ic} : 176 kJ/m^2 (18 Data)
Coeff. C : 316 kJ/m^2 Exponent n : 0.45 Fit Coeff. R : 0.959

Table B6.   Fracture toughness data for specimen 85-XA in high-purity water at 289°C.

Test Number   : CGRI JR-32   Test Temp.   : 289°C
Test Environment : High-purity water with ≈ 400 ppb dissolved oxygen
Material Type   : HAZ of 304 SS SMAW Heat Number   : 10285
Aging Temp.   : -   Aging Time   : -
Irradiation Temp. : 297°C   Fluence   : 1.44×10^{21} n/cm^2 (2.16 dpa)
Thickness   : 6.502 mm   Net Thickness   : 5.410 mm
Width   : 11.981 mm   Flow Stress   : 725 MPa (Estimated)
Modulus E   : 175 GPa   Effective Flow Stress : 527 MPa (Estimated)
Initial Crack   : 6.263 mm   Init. a/W   : 0.523
Final Crack   : 9.080 mm   Final a/W   : 0.758 (Measured)

No.	Load (kN)	Deflection (mm)	J (kJ/m^2)	Δa (mm)
0	0.000	0.000	0.0	0.000
1	0.911	0.040	1.2	0.001
2	1.479	0.070	3.7	0.002
3	2.104	0.105	8.1	0.004
4	2.689	0.142	14.4	0.007
5	3.249	0.189	24.2	0.012
6	3.758	0.237	36.0	0.018
7	4.200	0.293	51.6	0.026
8	4.536	0.360	72.4	0.038
9	4.708	0.442	95.2	0.192
10	4.135	0.608	137.9	0.484
11	3.833	0.686	154.8	0.652
12	3.712	0.751	168.1	0.780
13	3.627	0.811	180.7	0.878
14	3.431	0.932	206.5	1.041
15	3.243	1.052	231.6	1.174
16	3.131	1.164	255.1	1.278
17	2.994	1.278	278.7	1.372
18	2.667	1.439	291.7	1.672
19	2.338	1.602	305.2	1.926
20	2.055	1.759	314.5	2.161
21	1.842	1.908	320.0	2.380
22	1.719	2.054	326.8	2.562
23	1.630	2.190	333.7	2.714
24	1.558	2.324	346.2	2.817

Power-Law Fit $J = C(\Delta a)^n$
DC Potential Method J_{Ic} : 128 kJ/m^2 (16 Data)
Coeff. C   : 219 kJ/m^2 Exponent n   : 0.43   Fit Coeff. R   : 0.902

Table B7.   Fracture toughness data for specimen GG6T-A in high-purity water at 289°C.

Test Number   : CGRI JR-35   Test Temp.   : 289°C
Test Environment : High-purity water with ≈ 400 ppb dissolved oxygen
Material Type   : Type 304L SAWeld HAZ Heat Number   : Grand Gulf core shroud shell
Aging Temp.   : -   Aging Time   : -
Irradiation Temp.   : 297°C   Fluence   : 1.44×10^{21} n/cm^2 (2.16 dpa)
Thickness   : 6.533 mm   Net Thickness   : 5.791 mm
Width   : 11.999 mm   Flow Stress   : 711 MPa
Modulus E   : 175 GPa   Effective Flow Stress : 502 MPa
Initial Crack   : 6.747 mm   Init. a/W   : 0.562
Final Crack   : 9.412 mm   Final a/W   : 0.784

No.	Load (kN)	Deflection (mm)	J (kJ/m^2)	Δa (mm)
0	0.000	0.000	0.0	0.000
1	0.963	0.051	1.7	0.001
2	1.711	0.091	5.3	0.003
3	2.295	0.129	10.6	0.006
4	2.838	0.175	18.8	0.010
5	3.290	0.231	31.0	0.016
6	3.544	0.283	43.5	0.023
7	3.708	0.343	59.0	0.031
8	3.764	0.413	75.7	0.133
9	3.762	0.487	94.3	0.205
10	3.698	0.571	114.6	0.300
11	3.622	0.655	134.1	0.396
12	3.502	0.743	152.9	0.521
13	3.340	0.835	172.0	0.636
14	2.720	0.974	187.9	0.949
15	2.426	1.082	195.7	1.200
16	2.121	1.187	200.1	1.458
17	1.983	1.280	204.8	1.645
18	1.742	1.383	210.3	1.828
19	1.542	1.482	206.1	2.092
20	1.449	1.567	200.5	2.328
21	1.349	1.654	198.7	2.516
22	1.279	1.740	199.4	2.665

Crack extension determined from DC potential drop method.

Power-Law Fit   **J = C(Δa)^n**
DC Potential Method J_{Ic} : 121 kJ/m^2 (10 Data)
Coeff. C   : 179 kJ/m^2 Exponent n   : 0.29   Fit Coeff. R   : 0.923

Table B8.   Fracture toughness data for specimen 85-XB in air at 289°C.

Test Number   : JRI-35   Test Temp.   : 289°C
Test Environment : Air
Material Type   : Type 304 SMA Weld HAZ   Heat Number : 10285
Aging Temp.   : -   Aging Time   : -
Irradiation Temp.   : 297°C   Fluence   : 1.44 x 10^{21} n/cm^2 (2.16 dpa)
Thickness   : 6.523 mm   Net Thickness   : 5.664 mm
Width   : 11.944 mm   Flow Stress   : 725 MPa
Modulus E   : 175 GPa   Effective Flow Stress : 527 MPa
Initial Crack   : 6.442 mm   Init. a/W   : 0.539
Final Crack   : not measured   Final a/W   :

No.	Load (kN)	Deflection (mm)	J (kJ/m^2)	Δa (mm)
0	0.000	0.000	0.00	0.000
1	0.726	0.040	1.00	0.000
2	1.658	0.058	2.31	0.001
3	2.434	0.084	5.86	0.003
4	3.083	0.127	13.98	0.007
5	3.721	0.174	25.06	0.013
6	4.282	0.234	41.26	0.053
7	4.777	0.298	60.43	0.101
8	5.128	0.380	88.22	0.151
9	5.310	0.448	111.84	0.200
10	5.305	0.528	141.05	0.247
11	5.423	0.548	-	-

Crack extension determined from DC potential drop method.

Power-Law Fit   **J = C(Δa)^n**

J-R curve not determined because of uncontrolled crack advance at J = 141 kJ/m^2.

Table B9.   Fracture toughness data for specimen GG6T-B in air at 289°C.

Test Number   : JRI-36   Test Temp.   : 289°C
Test Environment : Air
Material Type   : Type 304L SAWeld HAZ Heat Number   : Grand Gulf core shroud shell
Aging Temp.   : -   Aging Time   : -
Irradiation Temp.   : 297°C   Fluence   : 1.44 x 10^{21} n/cm^2 (2.16 dpa)
Thickness   : 6.543 mm   Net Thickness   : 5.728 mm
Width   : 11.993 mm   Flow Stress   : 711 MPa
Modulus E   : 175 GPa   Effective Flow Stress : 502 MPa
Initial Crack   : 6.426 mm   Init. a/W   : 0.536
Final Crack   : 9.833 mm   Final a/W   : 0.820

No.	Load (kN)	Deflection (mm)	J (kJ/m^2)	Δa (mm)
0	0.0000		0.0	0.000
1	1.283	0.022	0.9	0.000
2	2.195	0.056	4.8	0.001
3	3.102	0.101	12.6	0.003
4	3.794	0.145	22.8	0.008
5	4.258	0.210	40.3	0.051
6	4.792	0.274	60.4	0.045
7	5.113	0.354	84.8	0.158
8	4.952	0.467	120.9	0.281
9	4.618	0.564	144.7	0.512
10	4.182	0.659	163.9	0.757
11	3.854	0.738	176.6	0.985
12	3.635	0.805	191.0	1.095
13	3.351	0.883	200.8	1.298
14	3.179	0.961	209.4	1.492
15	3.028	1.036	219.3	1.647
16	2.786	1.134	229.3	1.857
17	2.286	1.281	231.2	2.248
18	1.883	1.447	225.6	2.691
19	1.635	1.599	215.7	3.096
20	1.501	1.740	211.0	3.407

Crack extension determined from DC potential drop method.

Power-Law Fit $J = C(\Delta a)^n$
DC Potential Method J_{Ic} : 125 kJ/m^2 (11 Data)
Coeff. C   : 186 kJ/m^2 Exponent n   : 0.29   Fit Coeff. R   : 0.757

Table B10. Fracture toughness data for specimen 75-11TT in high-purity water at 289°C.

Test Number   : CGRI JR-33   Test Temp.   : 289°C
Test Environment : High-purity water with ≈ 400 ppb dissolved oxygen
Material Type   : CF-8M   Heat Number   : 75
Aging Temp.   : 400°C   Aging Time   : 10,000 h
Irradiation Temp.   : 297°C   Fluence   : 1.63×10^{21} n/cm^2 (2.46 dpa)
Thickness   : 6.515 mm   Net Thickness   : 5.685 mm
Width   : 12.022 mm   Flow Stress   : 760 MPa (Estimated)
Modulus E   : 170 GPa   Effective Flow Stress : 585 MPa (Estimated)
Initial Crack   : 6.338 mm   Init. a/W   : 0.527
Final Crack   : 9.626 mm   Final a/W   : 0.801 (Measured)

No.	Load (kN)	Deflection (mm)	J (kJ/m^2)	Δa (mm)
0	0.000	0.000	0.0	0.000
1	1.0206	0.0606	2.1	0.001
2	1.7444	0.0845	4.2	0.002
3	2.3543	0.1203	9.1	0.005
4	2.9476	0.1635	16.8	0.008
5	3.4982	0.2100	26.7	0.033
6	3.9856	0.2582	38.5	0.074
7	4.3593	0.3225	55.8	0.140
8	4.5293	0.4026	77.4	0.275
9	4.2455	0.5370	108.9	0.600
10	2.7523	0.7904	131.0	1.555
11	2.1877	0.9025	127.5	2.146
12	2.0009	0.9724	134.7	2.310
13	1.8502	1.0371	135.0	2.548
14	1.5426	1.1759	154.1	2.698
15	1.3853	1.2950	165.9	2.837
16	1.2231	1.4167	168.6	3.065
17	1.1405	1.4781	160.4	3.288

Power-Law Fit $J = C(\Delta a)^n$
DC Potential Method J_{Ic} : 84 kJ/m^2 (10 Data)
Coeff. C   : 120 kJ/m^2 Exponent n   : 0.24   Fit Coeff. R   : 0.709

Table B11. Fracture toughness data for specimen 75-11TM in high-purity water at 289°C.

Test Number   : CGRI JR-34   Test Temp.   : 289°C
Test Environment : High-purity water with ≈ 400 ppb dissolved oxygen
Material Type   : CF-8M   Heat Number   : 75
Aging Temp.   : 400°C   Aging Time   : 10,000 h
Irradiation Temp.   : 3297°C   Fluence   : 1.63 x 10^{21} n/cm^2 (2.46 dpa)
Thickness   : 6.502 mm   Net Thickness   : 5.702 mm
Width   : 12.012 mm   Flow Stress   : 760 MPa (Estimated)
Modulus E   : 170 GPa   Effective Flow Stress : 585 MPa (Estimated)
Initial Crack   : 6.384 mm   Init. a/W   : 0.531
Final Crack   : 9.400 mm   Final a/W   : 0.783 (Measured)

No.	Load (kN)	Deflection (mm)	J (kJ/m^2)	Δa (mm)
0	0.000	0.000	0.0	0.000
1	0.8584	0.0531	1.5	0.001
2	1.4541	0.0907	4.5	0.002
3	2.0252	0.1287	8.9	0.005
4	2.5912	0.1725	15.5	0.070
5	3.1271	0.2163	23.5	0.146
6	3.5783	0.2749	36.0	0.241
7	3.7969	0.3269	48.3	0.329
8	3.7874	0.3923	63.5	0.470
9	3.1409	0.5099	84.4	0.835
10	2.4692	0.6285	94.6	1.352
11	2.3553	0.6780	100.3	1.501
12	2.1794	0.7470	107.3	1.697
13	1.5461	0.8658	109.6	2.157
14	1.4229	0.9311	113.1	2.318
15	1.2923	1.0225	118.1	2.508
16	1.2152	1.1085	122.4	2.672
17	1.0075	1.2352	120.4	3.016

Power-Law Fit $J = C(\Delta a)^n$
DC Potential Method J_{Ic} : 40 kJ/m^2 (12 Data)
Coeff. C   : 80 kJ/m^2 Exponent n   : 0.45   Fit Coeff. R   : 0.959

This page is intentionally left blank.

BIBLIOGRAPHIC DATA SHEET

(See instructions on the reverse)

2. TITLE AND SUBTITLE

Crack Growth Rates and Fracture Toughness of Irradiated Austenitic Stainless Steels in BWR Environments

5. AUTHOR(S)

O. K. Chopra and W. J. Shack

8. PERFORMING ORGANIZATION – NAME AND ADDRESS *(If NRC, provide Division, Office or Region, U.S. Nuclear Regulatory Commission, and mailing address; if contractor, provide name and mailing address.)*

Argonne National Laboratory
9700 South Cass Avenue
Argonne, IL 60439

11. ABSTRACT (200 words or less)

In light water reactors, austenitic stainless steels (SSs) are used extensively as structural alloys in reactor core internal components because of their high strength, ductility, and fracture toughness. However, exposure to high levels of neutron irradiation for extended periods degrades the fracture properties of these steels by changing the material microstructure (e.g., radiation hardening) and microchemistry (e.g., radiation–induced segregation). Experimental data are presented on the fracture toughness and crack growth rates (CGRs) of wrought and cast austenitic SSs, including weld heat-affected-zone materials, that were irradiated to fluence levels as high as $\approx 2 \times 10^{21}$ n/cm^2 (E > 1 MeV) ($\approx$3 dpa) in a boiling heavy water reactor at $\approx$288-300 °C. The results are compared with the data available in the literature. The effects of material composition, irradiation dose, and water chemistry on CGRs under cyclic and stress corrosion cracking conditions were determined. A superposition model was used to represent the cyclic CGRs of austenitic SSs. The effects of neutron irradiation on the fracture toughness of these steels, as well as the effects of material and irradiation conditions and test temperature, have been evaluated. A fracture toughness trend curve that bounds the existing data has been defined. The synergistic effects of thermal and radiation embrittlement of cast austenitic SS internal components have also been evaluated.

12. KEY WORDS/DESCRIPTORS *(List words or phrases that will assist researchers in locating this report.)*

Crack Growth Rate
Fracture Toughness
J-R Curve
Irradiation–Assisted Stress Corrosion Cracking
Radiation–Induced Segregation
Neutron Irradiation
Dissolved Oxygen
Stress Corrosion Cracking
Austenitic Stainless Steels